UNIVERSITÀ DEGLI STUDI DI MILANO

FACOLTÀ DI SCIENZE AGRARIE E ALIMENTARI

DOTTORATO DI RICERCA IN AGRICOLTURA,

AMBIENTE E BIOENERGIA

XXXVII Ciclo

Dipartimento di Scienze Agrarie e Ambientali - Produzione, Territorio, Agroenergia

3D sensing approaches for Precision Agriculture: applications to plant features characterization and to weed control in maize

Settore Disciplinare: AGRI-04/B

Dottorando: Marco Davide Michel TORRENTE

Matricola: R13214

Tutor: Prof. Roberto OBERTI

Co-tutor: Prof. Aldo CALCANTE

Coordinatore: Prof. Salvatore Roberto PILU

A.A. 2023/2024

Torrente Marco Davide Michel
PhD Course in Agriculture, Environment and Bioenergy - XXXVII cycle -
"3D Sensing Approaches for Precision Agriculture: applications to plant features characterization and to weed control in maize"
September, 2024
Supervisors: Oberti Roberto & Calcante Aldo
University of Milan
Faculty of Agricultural Sciences for Sustainability
Department of Agricultural and Environmental Sciences
Via Celoria, 2 - 20133 Milano, ITALY.

Declaration

I, Torrente Marco Davide Michel, whose signature appears below hereby declare that:

- I have written this thesis by myself, except for the help and guidance offered by my thesis advisors.

- The scientific materials included in this thesis are products of my own research, culled from the period during which I was a PhD student.

Milano, September 2024

Marco Davide Michel Torrente

Acknowledgment

First and foremost, I want to thank my wife and my daughter, who was born during this doctoral journey. I know that pursuing this goal took time and energy that would otherwise have been theirs, and I am incredibly grateful for their love, patience, and unwavering support.

A heartfelt thanks also goes to my parents, whose encouragement and belief in me have been constant in my life. Their support has been a foundation for all my achievements, and I am deeply thankful.

I also wish to thank my supervisors, especially Prof. Oberti and Prof. Calcante, for their constructive guidance and exceptional kindness. Their belief in me from the very beginning has been invaluable, and their encouragement and trust have made this achievement possible.

My sincere thanks also go to the external reviewers, whose insights and suggestions helped refine this work and bring it to its best possible version.

Finally, I am grateful to my colleagues, who have shared this journey with me, and particularly to Daniele Manenti, who has been an indispensable partner in this endeavor. His collaboration and dedication have made a meaningful difference, both personally and professionally.

Contents

LIST OF FIGURES **8**

LIST OF TABLES **12**

LIST OF PUBLICATION **13**

ABSTRACT **14**

1 INTRODUCTION **17**

1.1 Future Challenges of Agriculture 17

1.2 Purpose of the work 19

1.3 Contents of the Dissertation 21

1.4 Plant Phenotyping 24

1.4.1 Phenotyping Applied to Precision Agriculture *25*

1.4.2 Lettuce a Ready-To-Eat (RTE) Salads Crop *26*

1.4.3 Automated Data Collection Management *28*

1.4.3.1 Examples of Marketed Models 29

1.5 The Problem of Weeds in Agriculture 33

1.5.1 Main Weed Control Techniques *35*

1.5.2 Chemical Weeds Control *36*

1.5.3 The Herbicide Resistance Phenomenon *38*

1.5.4 European Regulations on the Use of Plant Protection Products *39*

1.5.5 Digital Technologies for Weeds Sensing *41*

1.5.6 Site-Specific Weeds Management (SSWM) *42*

1.5.7 Field-Scale Data Acquisition for SSWM Management *43*

1.5.8 3D Sensing in Agriculture *45*

1.6.9 3D Weed-Crop Characterization for Target Detection *48*

1.6.10 Actuation in Precision Spraying *50*

1.6.11 Technological Steps of Actuation in Precision Spraying *52*

2 MATERIALS USED DURING PHD ACTIVITIES **55**

2.1 ToF 3D Camera (Microsoft KINECT V2) 55

2.1.1 Operational Principles of Time-of-Flight (ToF) Sensors *55*

2.1.2 Pros and Cons of using ToF sensors *56*

2.1.3 Data Output *56*

2.1.4 Common Measurement Errors *57*

2.2 3D Stereo Camera (Stereolabs ZED 2i) 57

2.2.1 Operational Principles of Stereo Cameras *59*

2.2.2 Pros and Cons of using Stereo Cameras *59*
2.2.3 Data Output *60*
2.3 Color Camera (GoPro Hero 8) 60
2.4 Digital Processing and Hardware Management 61
2.5 MATLAB Programming Environment 61
2.6 Microcontroller (Arduino Uno) 62
2.7 AprilTags 63
3 LABORATORY-SCALE PHENOTYPING TEST WITH 3D SENSOR 65
3.1 Aim of the Experiment 65
3.2 Material and Methods 65
3.2.1 Plant Management *65*
3.2.2 Data Acquisition *66*
3.2.3 Foreground Segmentation *66*
3.2.4 2D Projected Area Measurements *67*
3.2.5 3D Volumetric Object Reconstruction *69*
3.3 Results 74
3.4 Research Objective Achieved 76
4 FIELD-SCALE APPLICATION PHENOTYPING ON LETTUCE PLANTS 77
4.1 Aim of the Experiment 77
4.2 Materials and Methods 78
4.2.1 Plants Management *78*
4.2.2 Autonomous Vehicle *79*
4.2.2.1 Workspace Occupancy Map 83
4.2.2.2 Mission planning 84
4.2.3 Data Processing *86*
4.3 Results 91
4.4 Research Objective Achieved 94
5 COMPARISON TEST OF PROXIMAL AND REMOTE SENSING DATA 95
5.1 Aim of the Experiment 95
5.2 Materials and Methods 95
5.2.1 Experimental Site *95*
5.2.2 Determination of Fractional Green Canopy Cover (FC) *95*
5.2.3 Remote (UAV) Aerial Survey and Generation of FC Map *96*
5.2.4 Proximal Surveys and Generation of the Infestation Map *97*
5.2.5 Treatment Scale -- Remote (UAV) and Proximal Sensing Validation *98*
5.2.6 Proximal Scale --- Remote (UAV) and Proximal Imaging Comparison *99*

5.2.7 Field Scale --- Remote (UAV) and Proximal Imaging Comparison 99
5.3 RESULTS 100
5.3.1 Treatment Scale -- Remote (UAV) and Proximal Sensing Validation 100
5.3.2 Proximal Scale -- Remote (UAV) and Proximal Imaging Comparison 101
5.3.3 Field Scale -- Remote (UAV) and Proximal Imaging Comparison 103
5.4 RESEARCH OBJECTIVE ACHIEVED 104
6 2D-BASED ALGORITHMS FOR WEED SENSING IN MAIZE 106
6.1 AIM OF THE EXPERIMENT 106
6.2 MATERIAL AND METHODS 107
6.2.1 Image Acquisition and Setup 107
6.2.2 Image pre-processing 107
6.2.3 A Patch-spraying Approach Simulation [Management Zones] 108
6.2.4 A Micro-spraying Approach Simulation [Local Cover Fraction] 110
6.2.4.1 Determining the single crop row space with 2D images 111
6.2.4.2 Classification of inter-row weeds and local cover fraction 112
6.2.4.3 Determination of Thresholds 114
6.2.5 Ground Truth Image Labelling 115
6.2.6 Results Metrics and Environmental Impacts 116
6.2.7 FC-dependent Intervention Modulation 117
6.2.8 Field Capacity Estimation 118
6.3 RESULTS 118
6.3.1 Ground Truth Images Labelling 118
6.3.2 Treated Area 119
6.3.3 Evaluation of Treatment Efficacy 120
6.3.4 FC-dependent Intervention Modulation 121
6.3.5 Environmental Impact Index 123
6.3.6 Field Capacity Results 123
6.4 RESEARCH OBJECTIVES ACHIEVED 124
7 LABORATORY-SCALE 3D PLANT CHARACTERIZATION 126
7.1 AIM OF THE EXPERIMENT 127
7.2 MATERIALS AND METHODS 127
7.2.1 Plants Management 127
7.2.2 Plants Material 127
7.2.3 Sensor Carrier 130
7.2.4 Data Processing 137
7.3 RESULTS 142
7.3.1 Segmented point cloud 142

7.3.2 Morphological parameter extraction ... *143*
7.4 Research Objective Achieved ... 145
8 3D-BASED ALGORITHM FOR WEED DETECTION IN MAIZE ... 146
8.1 Aim of the Experiment ... 146
8.2 Materials and Methods ... 148
8.2.1 Experimental Site ... *148*
8.2.2 Sensor Management ... *148*
8.2.3 Crop and Weeds Binary Classification ... *149*
8.2.4 Data Pre-processing ... *150*
8.2.5 Crop Row Detection ... *152*
8.2.6 Detection of the Near Crop Row Volume ... *154*
8.2.7 Binary Classification ... *155*
8.2.8 Treatments Simulations and Intervention Strategies ... *157*
8.2.9 Results Metrics ... *160*
8.2.10 Field Capacity Estimation ... *161*
8.2.11 Precision Biostimulant Application ... *161*
8.3 Results ... 162
8.3.1 Binary Classification ... *162*
8.3.2 Treatments Simulations and Intervention Strategies ... *163*
8.3.3 Biostimulant distribution ... *165*
8.3.4 Field capacity ... *165*
8.4 Comparability between results obtained with RGB and RGB-D sensors ... *166*
8.5 Significance Test of the Results ... *167*
8.6 Conclusions ... *170*
9 PRECISION ACTUATION ... 172
9.1 Aim of the Experiment ... 172
9.2 Materials and Methods ... 172
9.2.1 Calibration Procedures ... *174*
9.2.2 Prescription Map Generation ... *178*
9.2.3 Distributed Control Operating Logic ... *179*
9.2.4 Overall Operating Logic ... *181*
9.3 Conclusions and Future Prospectives ... 182
10 CONCLUSIONS ... 184
REFERENCE ... 187
SITOGRAPHY ... 200

List of figures

Figure 1. Patent and articles trend related to agricultural robots [Zhao et al., 2020]. 28
Figure 2. Coefficient of variation of objects [Source: Bechar et al., 2021] 30
Figure 3. Examples of agricultural robots currently on the market 32
Figure 4. ToF Microsoft Kinect V2 sensor [Source: Brancati et al., 2018] 55
Figure 5. Example of flying pixels issue [Source: Reynolds et al., 2011] 57
Figure 6. Go Pro Hero 8 Camera 60
Figure 7. Example of an AprilTag 64
Figure 8. Laboratory scale RGB-D top-view acquisition setup. 66
Figure 9. Single pixel ExG value distribution 67
Figure 10. Color-based segmentation process 67
Figure 11. MATLAB camera calibration App checkboard pattern 68
Figure 12. Gradient magnitude filtering example 70
Figure 13. Example of point cloud rectification process result 71
Figure 14. Example of a 3D binary occupancy grid 71
Figure 15. Preliminary voxelization object (PVO), algorithm pseudocode 72
Figure 16. Preliminary volumetric object 73
Figure 17. Pseudocode of the last step of the reconstruction algorithm 73
Figure 18. Samples characterization with frequency distribution 74
Figure 19. Result of the volumetric reconstruction process 74
Figure 20. Results of plant DM estimation 75
Figure 21. Example of volumetric reconstruction of a sample 76
Figure 22. Arrangement of plants within plots 78
Figure 23. Different UGV configurations 80
Figure 24. Manual controller and safety device used of the UGV 80
Figure 25. LiDAR sensor and its field of view 81
Figure 26. Example of navigation within a map. 81
Figure 27. User interface for the control of the rover (Moliris by InfoSolution) 82
Figure 28. Example of a rover workspace occupancy map. 84
Figure 29. Example of the creation of a mission profile through the GCS 85
Figure 30. Graphical representation of the data acquisition mission 86

Figure 31. Example of noise filtering in depth measurement 87
Figure 32. Example of ground plane fitting. 88
Figure 33. Result of the reconstruction process of a single plot..... 89
Figure 34. Transplant layout 90
Figure 35. Outdoor augmented reality data visualization 91
Figure 36. Characterization of samples DM at harvest..... 91
Figure 37. DM estimation model based on the volume 92
Figure 38. Biomass development kinetics 93
Figure 39. Graphical representation of plant development 94
Figure 40. Setup for proximal image acquisition mounted at the rear of the tractor. 97
Figure 41. Aerial image of the experimental field 99
Figure 43. Validation results.....100
Figure 42. Comparison of images used for FC validation 100
Figure 44. FC estimated over an area of 3 by 2 m at 90 GCP. 101
Figure 45. Comparison of color-based segmentation 102
Figure 46. Comparison of color-based segmentation (2) 102
Figure 47. FC map of the experimental field.....103
Figure 48. Map of FC differences between UAV and proximal sensing 104
Figure 49. Calibration image 108
Figure 50. Example of a color image acquired with the experimental setup.....108
Figure 51. Diagram of the setup used to simulate treatment with the MZ method ...109
Figure 52. Labelling of individual treatment zones for MZ algorithm.....110
Figure 53. Diagram of the setup used to simulate treatment with the LCF method .110
Figure 54. Labelling of individual treatment zones for LCF algorithm 111
Figure 55. Example crop rows position detection 112
Figure 56. Results of first classification phase for LCF algorithm.....113
Figure 57. Segmentation of critical areas with LCF method 113
Figure 58. Frequency distribution of ExG single pixel values 114
Figure 59. Determination of thresholds used for treatment.....115
Figure 60. Manually labelled ground truth image.....116
Figure 61. Pseudocode of the logical operations.....116
Figure 62. Results labeling on low level of FC images (FC < 22%) 118

Figure 63. Results labeling on low medium of FC images (22% ≤ FC ≤ 30%) 119
Figure 64. Results labeling on high level of FC images (FC >30%). 119
Figure 65. Average percentage of the sampled area treated.....120
Figure 66. Confusion matrices of treatments based on 2D images 120
Figure 67. RGB-based algorithm performance indexes summary. 121
Figure 68. Point of indifference between the LCF and UD method 122
Figure 69. Intervention modulation using RGB-based algorithms 122
Figure 70. Environmental impact of the spraying operation 123
Figure 71. RGB top-view image of maize plants.....128
Figure 72. RGB top-view image of weeds plants. 130
Figure 73. Overview of the linear actuator 131
Figure 74. Components of the control module.....132
Figure 75. Main components and operating diagram of the automated platform 135
Figure 76. Example of target value casted for sending via serial communication 135
Figure 77. Automated platform components and operational diagram 136
Figure 78. Pseudocode of platform management 137
Figure 79. Example of color-based vegetation segmentation. 138
Figure 80. Distance-based individual clustering 139
Figure 81. Example of geometric feature extraction 140
Figure 82. Example of semi-automatic validation interface output.....141
Figure 83. Example of feature extraction output.....141
Figure 84. Example of point cloud extraction 142
Figure 85. Example of horizontal and vertical shapes 143
Figure 86. Evolution of height mode in the first 12 days after emergence 144
Figure 87. Evolution of vertical extent ratio in the first 12 days after emergence 144
Figure 88. Evolution of horizontal extent ratio in the first 12 days after emergence .144
Figure 89. Adjustable sensor support, design diagram 149
Figure 90. Adjustable sensor support, design diagram..... 149
Figure 91. RGB image and depth map acquired with Zed 2i in field conditions.....150
Figure 92. Overlay of the color mask shown in yellow on the RGB image.....151
Figure 93. Segmenting with stereo camera 152
Figure 94. Result of segmentation based on height. 153

Figure 95. Example of estimating the position of crop line in high weed infestation 154
Figure 96. Estimated crop-row distance map 154
Figure 97. Segmentation of the near crop-row volume 155
Figure 98. Overlay of the near crop row volume mask.....156
Figure 99. Example of binary crop-weed segmentation 156
Figure 100. Micro-spraying design used for treatments simulations. 157
Figure 101. Implementation rules 159
Figure 102. Examples of treatments simulation output 159
Figure 103. Evaluation of treatment performance 160
Figure 104. Results of binary classification.....162
Figure 105. Confusion matrices of results obtained with TAW and TWM strategies.163
Figure 106. 3D based precision spraying treatments performance indexes results. 164
Figure 107. Result of environmental impact 164
Figure 108. Biostimulant treatment performance index results.....165
Figure 109. FC levels observed in samples 167
Figure 110. Comparisonof the sensitivity 168
Figure 111. Comparison of the quantity of herbicides distributed 168
Figure 112. Comparison of the impact on soil.....169
Figure 113. Machine components summary.....174
Figure 114. Display of marker detection for individual actuators 175
Figure 115. Procedure for segmentation of individual zones 176
Figure 116. Total spatial memory stored from the master 177
Figure 117. Diagram of the components used to build the machine 177
Figure 118. Summary of the procedure for converting the prescription map 179
Figure 119. Summary of the procedure for converting the prescription map 179
Figure 120. Summary of the procedure for converting data received 180
Figure 121. Pseudocode representing operation logic management by the slave ...181
Figure 122. Pseudocode representing operation logic management by the master 182
Figure 123. Actuators triggered at a target according to the prescription map..... 183

List of Tables

Table 1. Field capacity estimation results for MZ and LCF methods. 124
Table 2. List of waypoints of a mission reported in metric unit 136
Table 3. Summary of all the steps needed to get the binary classification. 157
Table 4. Individual nozzle workspace masks. 157
Table 5. Summary of the actuation rules 158
Table 6. Method for calculating treatment performance. 160
Table 7. Field capacity estimation results for 3D methods 165

List of Publication

Journal publication:

- Calcante, A., Manenti, D., Torrente, M. D. M., & Oberti, R. (2024). Comparison of the Effectiveness of Different Mechanical Tools for the Termination of Cover Crops Using a Modular Prototype. In Applied Engineering in Agriculture (Vol. 40, Issue 2, pp. 211–223). American Society of Agricultural and Biological Engineers (ASABE). https://doi.org/10.13031/aea.15714

Conference Presentation:

- Biosystems engineering promoting resilience to climate change. Mid-Term Conference of the Italian Association of Agricultural Engineering (AIIA), held at the University of Padova, Italy, from June 17 to 19, 2024. The Comparison between proximal and UAV sensing methods for detecting weeds infestation in maize work has been presented and awaiting publication in conference proceedings.

- Berto, F., Ardagna, C., Torrente, M., Manenti, D., Ferrari, E., Calcante, A., Oberti, R., Fra', C., & Ciani, L. (2022). A 5G-IoT enabled Big Data infrastructure for data-driven agronomy. In 2022 IEEE Globecom Workshops (GC Wkshps) (pp. 588–594). 2022 IEEE Globecom Workshops (GC Wkshps). IEEE. https://doi.org/10.1109/gcwkshps56602.2022.10008727

- Characterization of morphological parameters of growth in leafy vegetables using 3D sensors on a robotic platform / D. Manenti, M. Torrente, P. Pasta, A. Calcante, R. Oberti (ACTA ITALUS HORTUS). - In: Digital sensing and agromotics in horticulture / [edited by] A. Galieni, C. Pane, M. Savona. - First edition. - Sesto Fiorentino : Società di Ortoflorofrutticoltura Italiana, 2023. - ISBN 978-88-32054-06-4. - pp. 13-14 ((conference SOI Technical Days : Digital sensing and agromotics in horticulture : 4-5-October held in Pontecagnano (SA), 2023.

- Preliminary studies on the development of an advanced detection method for the early detection of different diseases on Solanum lycopersicum and Capsicum annuum A. Follador, A. Passera, D. Manenti, M. Torrente, R. Oberti, G. Cocetta, P. Casati (Acta Italus Hortus). - In: Digital sensing and agromotics in horticulture. A. Galieni, C. Pane, M. Savona. - First edition. - Sesto Fiorentino : Società di Ortoflorofrutticoltura Italiana, 2023. - ISBN 978-88-32054-06-4. - pp. 13-14.

Additional publications not related to this thesis:

- Weed control by hot vegetable oil and eugenol spray / R. Oberti, A. Calcante, E. Ferrari, M. Torrente, S. Vitalini, T. Tadiello, M. Iriti, L. Bechini. In: Biosystems Engineering Towards the Green Deal. Improving the resilience of agriculture, forestry and food systems in the post-Covid era. Book of Abstracts / G. Giordano, P. Catania. AIDIC Associazione Italiana di Ingegneria Chimica, 2022. ISBN 978-0-13-601970-1.pp. 115-115 (Presented at the XII Conference Biosystems Engineering Towards the Green Deal. Improving the resilience of agriculture, forestry and food systems in the post-Covid era held in Palermo : September 19-22, 2022.

- Mechanical termination of cover crops / A. Calcante, D. Manenti, M. Torrente, D. Reginelli, R. Oberti. - In: L'INFORMATORE AGRARIO. - ISSN 0020-0689. - 40(2022), pp. 66-68.

Abstract

This PhD thesis investigates the application of 3D data acquired by Time-of-Flight (ToF) sensors and stereo cameras for agronomic measurements. The main objectives are the characterization of plant geometric properties, biomass estimation with non-destructive methods and discrimination between crops and weeds for use in precision agriculture applications.

Following an introductory section, the first part of the work, which corresponds to Chapters 3 and 4, involves the volumetric characterization of lettuce plants to estimate biomass using non-destructive measurements. This was performed both in preliminary laboratory trials and in a field application. In the field application the depth sensor was integrated with a robotic platform to ensure the possibility to collect data at the individual plant level, with all data that can be stored in a data lake. In both cases, the assumed volumetric reconstruction algorithms achieved very satisfactory results, obtaining accurate dry biomass weight (DM) estimates from the developed models for both laboratory scale (with a root mean square error (RMSE) of 0.12 g and a mean absolute percentage error (MAPE) of 12%.) and greenhouse conditions (with a RMSE of 1.07 g and MAPE 16%). The different ability to estimate the DM obtained in the two contexts, although minimal, depends mainly on the different spatial resolutions obtainable with the acquisition setups designed for the two experiments and on the conditions under which the measurements were carried out. Considering the technological characteristics of the ToF sensors, under field conditions they are disturbed by solar radiation, which contributes to decreasing the level of accuracy of the measurement obtained.

The second part of the thesis, which corresponds to Chapters 5, 6, 7 and 8, deals with the comparison of two sensing techniques, two-dimensional based on color (RGB) and three-dimensional that consider distance in addition to color (RGBD) to optimize the process of target identification for use in precision weed control spraying that aims to reduce chemical inputs using advanced techniques. Regarding 2D imagery, a comparative analysis was conducted on images captured using drones (UAV – Remote sensing) and those obtained in proximity to vegetation (proximal sensing). The

objective was to assess the capacity of these approaches to estimate soil cover, a critical driver that can indirectly indicate the degree of weed infestation. Proximal images demonstrated superior accuracy in estimating this phenomenon, achieving a coefficient of determination (R^2) of 0.93, compared to UAV-acquired images, which yielded an R^2 of 0.8 in validation tests based on 90 ground control points established within the field. When comparing the two monitoring techniques at a field scale, UAV imagery was found to provide an estimate of soil cover that, in 75% of the sampled area, was lower than that derived from proximal images under experimental conditions.

In this context, which highlights the superior representativeness of information obtainable through proximal monitoring, the contribution of 3D sensing techniques to estimating weed presence was subsequently evaluated in comparison to proximal 2D images. To this end, several algorithms specifically designed to utilize both sensing techniques were developed.

Using 2D images, two algorithms were developed. The first is a simpler approach that enables uniform treatment decisions across areas of 0.75 m^2 (Management Zones - MZ) based on assessing vegetation soil cover. The second, an innovative algorithm known as Local Cover Fraction (LCF), is more complex, employing a hybrid technique to simultaneously detect weeds between rows and subsequently characterize the spatial distribution of remaining soil cover along each crop row. This allows identification of areas where biomass distribution deviates from the clean-field conditions recorded at the experiment's start.

In parallel, a classification algorithm based on 3D sensing was developed, with two distinct implementation strategies proposed. The first, Treat All Weeds (TAW), aims to target all areas identified as weeds and the second, Treat Weed in Majority (TWM), activates actuators only when they can cover a greater surface area classified as weeds than of crops.

To evaluate the results and quantify the contribution of these methods compared to traditional uniformly distributed (UD) techniques, precision spraying treatments

based on the MZ, LCF, and 3D-based algorithms were simulated, and the outcomes were compared.

Simulations yielded promising results, forecasting a reduction in both the quantity of herbicide applied and the environmental impact for most developed algorithms. Herbicide reductions were observed as follows: 10% for the MZ method, 45% for the LCF method, and for the 3D sensing approach, a 22% reduction for the TAW strategy and 28% for TWM. However, the TAW strategy was the only approach to achieve a statistically significant reduction in both herbicide quantity and environmental impacts without a notable decrease in treatment effectiveness, which remained statistically comparable to the uniformly distributed (UD3D) treatment simulation.

The results obtained with both imaging techniques surpassed expectations. Compared to the 2D imaging-based method for estimating weed control treatments, the 3D survey produced even more favorable results, owing to its enhanced capability for target classification, which proved more robust than the 2D method. This advanced classification capability enabled the design of crop-targeted treatments through simulations of localized biostimulant distribution, achieving full crop surface coverage with a sensitivity of 0.99. This approach reduced product waste from ground distribution by 85% and minimized the undesired effect of weed biostimulation by 75%.

Finally, in Chapter 9, a low-cost simulator prototype is proposed for the hardware and software management of highly precise, localized treatments based on proximal imaging. This simulator is designed to perform real-time monitoring and execute the required treatment actions.

In general, considering the results obtained in both fields of application investigated in this thesis work, the use of 3D sensors demonstrated significant outcomes across all evaluated contexts, both in initial laboratory tests and in field application trials.

1 Introduction

1.1 Future Challenges of Agriculture

According to data reported by the United Nations (UN), the world population reached 8 billion in November 2022 and a further increase is expected in the coming years and future growth estimates predict that this could reach 10 billion by 2050 (UN World Population Prospect, 2022). In parallel, the climate is undergoing and will probably continue to undergo major changes (Anderson et al., 2020) that will make it more difficult to achieve the goal of ensuring food security by that date. Climate change poses significant challenges to agriculture globally, with impacts varying across regions (Yohannes, 2015). Rising temperatures are expected to reduce crop yields, increase pest proliferation, and alter precipitation patterns, threatening food security (Liaqat et al., 2022). While increased CO_2 levels may enhance plant productivity, this benefit is outweighed by negative effects such as increased evapotranspiration and extreme weather events (Liaqat et al., 2022). Agriculture also contributes to climate change through greenhouse gas emissions from fossil fuel use, soil management, and livestock. However, the sector can potentially mitigate climate change through optimizing input management and adopting best management practices (Yohannes, 2015). Developing countries are particularly vulnerable due to their faster population growth, dependence on agriculture and limited adaptation infrastructure (Yohannes, 2015). Adaptation strategies and urgent policy changes are needed to address these challenges (Liaqat et al., 2022).

For the European Commission (EC) these adversities lead to a substantial reduction in potential yields, areas suitable for cultivation, and production, in terms of quality and quantity. To ensure food security, both in terms of food safety and food security, it will be necessary to reduce waste, increase crop production and improve the efficiency of resource use. This approach might help to lower economic costs and reduce environmental impacts. Precision Agriculture (PA), which in its most contemporary and digital modern conception is defined as smart farming. has gained prominence as an essential strategy to address these needs (Stafford, 2000). Smart farming leverages advanced technologies to enhance agricultural productivity and

sustainability. Internet of Things (IoT) applications in agriculture enable remote monitoring and management of farming activities, reducing labor and improving resource utilization (Terence & Purushothaman, 2020). These systems incorporate various technologies, including sensors, data mining, and Artificial Intelligence (AI) to facilitate informed decision-making regarding crop management, such as weather tracking, water usage, and fertilizer applications (Priyanka, 2017). The integration of IoT, cloud computing, and robotics in agriculture is anticipated to drive innovation and transform conventional farming practices (Dhanaraju et al., 2022). As the global population increases and the demand for healthier products grows, smart farming techniques are becoming essential for ensuring sustainable agricultural practices and maintaining competitiveness in the global market (Moysiadis et al., 2021).

Data analysis, sensor automation, and robotics applications can significantly enhance crop production, improving the overall efficiency of agricultural processes. By enabling farmers to make informed decisions based on real-time data, smart farming contributes to increased yields while promoting more sustainable and efficient farming practices (Gebbers & Adamchuk, 2010). Higher education also will play a crucial role in developing the agricultural sector by providing up-to-date knowledge and skills to farmers and professionals, adapting curricula to include precision agriculture techniques, and offering lifelong learning opportunities (Kőmíves et al., 2019).

Regarding the reduction of the environmental impact of field operations, caused from the use of synthetic chemicals which are proven to have negative effects on human health like herbicide (Mohd Ghazi, 2023), to this aim the EC have begun to envisage mechanisms to reduce significantly its inputs, especially with regard to weeding operations applying the European Green Deal, which provides for a regulatory framework in this regard and, although not yet implemented, represent a likely future trend direction for institutions and public opinion.

Unmanned Aerial Vehicles (UAVs) have emerged as valuable tools for precision agriculture, offering efficient crop monitoring and management capabilities (Ronchetti, 2020; Ganesan et al., 2023), these can be equipped with various sensors

can collect multispectral data for crop health assessment, weed detection, and soil analysis (Alsalam et al., 2017; Popescu et al., 2020). The integration of UAVs in PA offers a cost-effective, reliable, and efficient method for monitoring large agricultural areas and optimizing crop management practices (Ronchetti, 2020; Popescu et al., 2020).

Modern 3D sensing technologies have emerged as valuable tools in agricultural applications, offering advantages over traditional 2D imaging methods because offers unique shape and localization data (Vázquez-Arellano et al., 2016) and can be useful to make sensing more powerful in the agricultural field to solve problems such as weed detection, which can become particularly difficult under high infestation conditions, or to make possible more accurate non-destructive measurements than 2D images.

1.2 Purpose of the work

The aim of this work is to integrate low-cost 3D (RGB-D) sensing systems into Precision Agriculture applications. The goal is to employ these sensors in particularly demanding and critical tasks like precision spraying and single plant phenotyping for optimizing crop management by experimenting with applications both in laboratory settings and in open-field environments.

The first area of application considered is crop monitoring, which has been addressed in various ways in the literature (Virlet et al., 2017; Rose et al., 2016; Sampaio et al., 2021). It benefits from the use of non-invasive methods that offer high-throughput, accurate, and objective measurements of plant traits (Liu et al., 2020), enabling complex investigations into plant growth, water balance, drought responses, and QTL analysis. According to Paulus (2019), future research will focus on high-resolution point clouds and the automated extraction of plant traits at both experimental and field scales. Consequently, part of this work will explore the application of this sensing technique at the laboratory and field levels, aiming to develop algorithms that can be executed in a short time a frame, while operating on low-cost hardware, and potentially run in real time, thereby reducing the cost of data collection and analysis without compromising data and results quality.

The second case study addresses the optimization of input management in site-specific chemical weed management (SSWM). Recent advancements in 3D imaging technology have opened new opportunities for SSWM by overcoming the limitations of traditional 2D imaging methods (Dobbs et al., 2022). While remote sensing can detect large patches of weeds, it struggles to identify individual weeds due to spectral mixing and low spatial resolution (Brown & Noble, 2005; Shaw, 2005). Ground-based systems utilizing multispectral imaging sensors show promise for weed identification by extracting spectral and spatial features but face challenges in image processing and computational power (Brown & Noble, 2005; Shaw, 2005). Despite the potential economic and environmental benefits of SSWM, its widespread adoption has been hindered by the lack of robust weed recognition methods and limited understanding of the economic and environmental potential of improved weed control resolution (Christensen et al., 2009). Current research is focused on enhancing weed sensing systems, weed management models, and precision weed control tools to overcome these barriers (Christensen et al., 2009; Dobbs et al., 2022). For this reason, much of this work will also focus on using these sensors to improve weed detection capabilities compared to RGB images. This effort will concentrate on a crop critical to global agriculture, maize, as it is a major crop used for food, animal feed, and biofuel production (Revilla et al., 2022; Shiferaw et al., 2011).

Targets detection is a crucial step in the effective application of SSWM principles, but it cannot be fully realized without an appropriate actuation system to support the developed detection algorithms and their spatial accuracy. Current technologies can detect green vegetation and activate herbicide sprayers, and research is exploring ground-based, aerial, and satellite sensor systems for weed detection (Shaw, 2005). However, barriers to widespread adoption remain, including the lack of robust weed recognition methods and limited knowledge of the economic and environmental potential of increased weed control resolution (Christensen et al., 2009). Recent advances in remote and ground platforms, sensors, and decision algorithms are improving information collection and processing for SSWM (Fernández-Quintanilla et al., 2020). As technology improves and costs decrease, real-time, sensor-driven SSWM may overcome the challenges of scouting and map-making (Swinton, 2005).

Therefore, the last part of this work will be dedicated to developing and testing a prototype actuation system that is effective, scalable, and low-cost, with the goal of achieving single-nozzle control with high spatial accuracy.

To evaluate the impact of introducing this sensing technology in these application contexts, the results will also be compared to those obtained using more commonly employed 2D (RGB) imaging techniques.

1.3 Contents of the Dissertation

In the context of applying the principles of PA, the use of 3D sensors, or better RGB-D sensors, is being investigated for developing innovative algorithms in crop phenotyping and weed detection applied in precision spraying. These two major topics were chosen for in-depth study because they can be most effectively addressed using the capabilities of these sensors. They are current and relevant issues that are crucial for supporting agriculture in its future challenges.

With the aim of making the reading of the chapters dealing with the experimental tests easier and clearer, the following introductory paragraphs provide a general overview of the issues addressed in the experiments proposed in the subsequent sections of the thesis.

One of the most widely used RGB-D sensors is produced by Microsoft® (Kinect V2). Originally designed for use with the Microsoft® Xbox gaming console to allow players to interact without using the controller, solely through body movements, it has been utilized in various academic studies across fields ranging from engineering (Jabely et al., 2017; Fankauser et al., 2015) to agriculture (Hu et al., 2018) due to its compatibility with other systems and development environments, as well as its low cost.

Crop morphological characterization of individual plants can be instrumental in optimizing agricultural inputs. Its three-dimensional characterization capability, which significantly surpasses that of RGB images, is useful for accurately quantifying the morphological traits and growth rates of plants. This enables precise, non-destructive measurements and the automation of harvesting and processing in high-value crops, such as those in the ready-to-eat (RTE) vegetable market, a sector that is

well-developed in the Italian and European economies (Eurostat). In this application, Chapter 3 considers the use of a 3D sensor to estimate the dry weight biomass of lettuce plants under controlled laboratory conditions. In Chapter 4, the same sensor was installed on an autonomous ground vehicle (UGV) to perform automatic data collection at various stages of crop development, thereby characterizing growth dynamics in a real field application.

In Chapters 6 and 8 the topic of precision spraying has been considered to explore the potential for reducing the amount of chemicals used in this process, thereby decreasing environmental impact and minimizing harmful effects on consumer health and the health of operators performing the treatment. Traditionally, this operation involves uniformly distributing herbicides across the entire field. This method is employed because the product typically has selective action and is relatively inexpensive. This approach yields satisfactory results in controlling weeds compared to not applying any treatment. However, it also leaves significant room for optimization to reduce the quantity of herbicides used, enhancing environmental sustainability without compromising crop yield.

Precision spraying can be executed based on prescription maps created from surveys typically conducted using unmanned aerial vehicles (UAVs) or by performing the intervention in real-time concurrently with the survey. In Chapter 5, a comparison will be presented between the quality of information obtained through proximal imaging, which is typically used for real-time applications, and remote sensing via UAV-acquired images. The latter is the more commonly employed method in PA for data acquisition and generating prescription maps used in site-specific treatments.

The precision spraying on-the-go workflow encompasses four primary phases: sensing, data processing, result interpretation and actuation. This process involves regulating the nozzles to deliver the treatment at the right moment and with the right dose. All these critical phases have been thoroughly examined and discussed in the following sections.

In Chapter 6, proximal RGB images were used to develop two distinct algorithms based on soil coverage to create real-time prescription maps for concurrent treatment

during the survey. The two algorithms vary in complexity and spatial accuracy. The first method, termed uniform Management Zones (MZ), implements site-specific weed management through patch-spraying, with a working width of 0.75 m and a length of 1 meter. The second method, called Local Cover Fraction (LCF), is a more sophisticated algorithm that offers higher spatial accuracy, characterized by a working width of 0.2 m and variable length, thus categorized as micro-spraying. Unlike the first method, the LFC algorithm can perform a preliminary classification of potential targets and subsequently identify other problematic areas near the rows of crops to be treated.

In Chapter 7 will be explored the use of 3D sensors to characterize various morphological features of both monocot and dicot weed species, as well as a crop (in this case, maize) during its early growth stages, specifically from sowing until the post-emergence weed control intervention period. The significance of this trial lies not only in testing potential solutions for plant classification but also in the automation of the monitoring process and the collection and registration of multiple point clouds. In this experiment, acquisitions were conducted using a custom-built belt-driven linear actuator designed specifically for this purpose.

Chapter 8 presents a field application of 3D sensing on maize, employing a stereo camera to collect field data. For this purpose, an algorithm was developed to discriminate between weeds and the crop, focusing on conditions of medium-to-high infestation intensity, which are challenging to address using only RGB images. The algorithm outputs a binary classification (crop vs. weeds) of the images. Various actuation strategies were assessed for implementation, and their effects on the quality of the simulated intervention were evaluated. Furthermore, the treatment simulations include a further and innovative localized treatment which involves the application of a biostimulant to the crop, thus avoiding product waste and the possible stimulation of weed development.

In conclusion, Chapter 9 proposes an example of hardware and software architecture designed for managing high-precision treatments. This system is based on prescription maps generated in real-time by the algorithms discussed in the previous sections.

1.4 Plant Phenotyping

Phenotyping in agriculture refers to the systematic measurement of observable plant characteristics (phenotypes), which include traits such as size, growth, development and responses to various stresses. This process is pivotal for the development of improved crop varieties, particularly in enhancing yield, resilience to climate change, and resource-use efficiency.

Recent research trends demonstrate a growing interest in this area, with a notable increase in publications since 2010, driven by technological advancements in imaging, automation, and data management (Costa et al., 2019). While early studies primarily focused on model organisms like *Arabidopsis thaliana L.*, contemporary research increasingly targets diverse crop species and field-based conditions (Costa et al., 2019).

Traditional phenotyping methods have been characterized by labor-intensive, time-consuming processes, especially in field settings where manual measurements can be both challenging and prone to inaccuracies. These measurements are often gathered by different individuals over extended periods, further complicating data consistency and reliability.

Latest technological advances have shifted the focus toward non-destructive, high-throughput phenotyping methods, particularly with 3D imaging technologies (Liu et al., 2020). These methods enable precise measurement of critical plant traits, such as plant height, leaf area, and canopy cover, offering powerful tools for monitoring growth and health in agricultural environments. Moreover, the integration of robotics and sensor fusion techniques has expanded phenotyping capabilities, facilitating the generation of 3D plant models and the mapping of environmental variables onto these models (Sampaio et al., 2021).

These developments in sensor technology and imaging techniques have revolutionized phenotyping by enabling high-throughput data collection on a large scale. This approach provides a comprehensive understanding of plant behavior across diverse environmental conditions, thereby supporting future efforts in plant breeding and Precision Agriculture.

1.4.1 Phenotyping Applied to Precision Agriculture

Phenotyping within PA has become an essential tool for addressing global food security challenges and enhancing crop productivity (Yandun Narvaez et al., 2017). High-throughput field phenotyping techniques, which employ a range of sensors and imaging methods, facilitate the evaluation of plant traits for both breeding and cultivation purposes (Chawade et al., 2019). These non-invasive, imaging-based methods have significantly transformed phenotyping by enabling more efficient and accurate data collection compared to traditional manual approaches (Minervini et al., 2015). However, despite these advances, the pace of phenotypic data extraction is still slower than genotyping, creating a bottleneck in plant research (Minervini et al., 2015). To address this challenge, cutting-edge technologies incorporating AI and machine learning are being developed to enhance data acquisition, analysis, and management in next-generation plant phenotyping (Tripodi et al., 2022). These advancements are designed to bridge the gap between phenomics and genomics, facilitating more efficient crop breeding and PA practices (Tripodi et al., 2022). Furthermore, they enable large-scale, precise data collection on plant traits, significantly contributing to breeding programs and improving our understanding of plant-environment interactions (Fiorani & Schurr, 2013). PA, which relies on data-driven decision-making, stands to benefit from these advanced phenotyping techniques. By integrating high-throughput phenotyping data with Geographic Information Systems (GIS) and multi-scale sensing technologies, researchers and farmers can monitor plant health, optimize inputs such as water and fertilizer, and enhance crop management practices on a site-specific basis. This integration supports precise interventions, reducing the environmental impact of farming while maximizing productivity. Additionally, the continuous stream of phenotypic data provides real-time insights into crop performance, enabling more adaptive and responsive agricultural systems. This capability to create accurate growth models represents a cornerstone of modern PA, as it offers detailed, scalable, and timely information about plant traits. Such information is essential for promoting sustainable and efficient farming practices. By harnessing phenotypic data, PA can contribute to addressing global food security challenges while simultaneously reducing the environmental footprint of agriculture.

The integration of phenotyping with PA thus forms a powerful synergy, enhancing the ability to manage crops at fine spatial and temporal scales.

Phenotyping at the individual plant level is a high labor-intensive process that can be justified when applied to high-value crops. This approach is suitable due to the plant's size during its developmental stages and its field arrangement, which allows for top-view imaging. For these reasons, lettuce was selected as the crop for the volumetric development characterization trials.

1.4.2 Lettuce a Ready-To-Eat (RTE) Salads Crop

Ready-To-Eat (RTE) salads consumption is continuously increasing worldwide and is expected to further grow because of the change of food habits and lifestyle in developing countries. Fresh-cut industry is nowadays the most expanding sector of all the fruit and vegetable markets (Gullino et al. 2019, Losio et al. 2015). These vegetables are thus particularly requested by consumers for their convenience and quality but also for the increased awareness about the relations between health status and consumption of fresh vegetables (Tomasi et al., 2015). RTE salads, immediately after the harvest, undergo to different technological operations intended to keep the freshness of the products up to the consumer. Most of the leafy vegetables are minimally processed (cutted, sorted, washed, dried), packed in air or modified atmosphere, refrigerated and consumed within a few days from harvest, constantly keeping them in cold chain storage (2-4°C) (Tomasi et al., 2015). The cultivation of salads for RTE market is generally conducted in greenhouse where plants are sown in rows and carefully managed according to production protocols aimed at obtaining a suitable final quality. Indeed, the RTE salads market requires to meet specific quality standards in terms of external appearance, organoleptic features, texture of the tissue, nutritional value and food safety (Francesca et al. 2019, Saini et al., 2017). A crucial aspect for market value and shelf life of RTE salads is the growth stage and the homogeneity of plants at the harvest, which can be negatively affected by different factors (genetic variability of seeds, spatial heterogeneity in greenhouse microclimate or in water and nutrients availability etc., (Nicola et al., 2003).

In the last decades, the availability of relatively inexpensive and high-performance optical devices and cameras has boosted the development of non-invasive measurement systems for estimating macroscopic parameters of the plant related to growth. Early applications of color imaging to monitor lettuce growth were aimed to investigate the possible use of sensed plant-projected area extracted from top-view images to identify nutrient stress in hydroponic cultivation (Giacomelli et al., 1998). More recently, similar approaches have been applied to evaluate lettuce growth-rate data extracted from greenhouse imaging, to be used as state-variable to feedback control of nutrient solution in hydroponic system (Jung et al., 2015). Bumgarner et al. (2012), by conducting an extensive study on imaging of lettuce plants grown in different environments, concluded that a top-view approach is an accurate method to indirectly measure lettuce biomass during the early stages of growth, while on canopy closure the correlation is weakened by occlusions in plant's top-view due to leaves overlapping. This limitation, also reported by Jung et al. (2015) for lettuce plants at advanced stages of development, is encountered with any plant with erectophyle architecture (Tackenberg, 2007), and it has been addressed by deploying different approaches, as: by side-view imaging configurations, or, rarely, in combination with top-view (Pereyra-Irujo et al., 2012); by the use of three dimensional measuring instrumentation such as LIDAR (Friedli et al., 2016), stereoscopic or multi-view cameras (Rose et al., 2015; Golbach et al., 2016) or ToF cameras (Chéné et al., 2012). Mortensen (Mortensen et al., 2018) proposed a proximal sensing using stereo color cameras mounted on an agricultural robot for fresh weight estimation of lettuce. The obtained sequences of stereo image pairs were used to generate high density lettuce 3D colored point cloud showed a good correlation with the lettuce fresh biomass weight. Therefore, there are several high-time and cost methods focused on the detailed 3D reconstruction of plants which, however, require a lot of computational time and which are often not applicable in field conditions, especially in real-time, because they require the reconstruction of data taken from different views.

Field-scale data collection with a high level of detail cannot be carried out by one or more operators but must be entrusted as a task to an automated unit capable of carrying it out autonomously.

1.4.3 Automated Data Collection Management

The integration of automation technologies into agricultural production processes has garnered increasing attention in recent years. According to Zhao et al. (Zhao et al., 2020), this growing interest is evident in their historical analysis (1950-2017), which examined the number of patent and scientific articles related to agricultural robots. Their findings indicate that experimental and academic interest in this field began to rise significantly around 2009. This increased interest in the subject is also being reflected in the market. According to the "Market Report, Agricultural Robots Forecasts" by Global Industry Analysts Inc., the global market for agricultural robots reached a value of 13.5 billion USD in 2023. The market is expected to continue its upward trajectory, with projections estimating a significant growth to 40 billion USD by 2028, driven by a Compounded Annual Growth Rate (CAGR) of 24.3%.

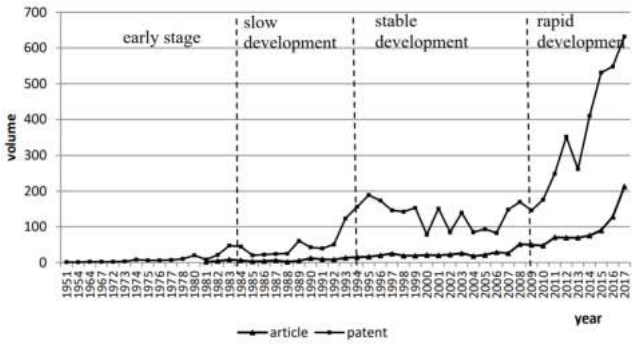

Figure 1. Patent and articles trend related to agricultural robots over the last 50 years [Zhao et al., 2020].

The use of automated vehicles in agriculture, compared to traditional machinery, offers several advantages. For instance, it extends the operational window for agricultural tasks by enabling work both during the day and at night. Additionally, these vehicles can operate in fields sub-optimal soil moisture conditions without damaging the soil structure, thereby minimizing soil compaction due to their generally lower mass compared to traditional agricultural machinery (Duckett et al., 2018). The implementation of robots in certain tasks can also yield economic benefits. For example, Perez-Ruiz et al. (2014) estimate that the introduction of weeding robots could reduce operational costs by approximately 170 USD per hectare.

In addition to performing physical tasks such as cultivation, treatments, or harvesting, agricultural robots can also be employed for continuous monitoring to collect crop, environmental, and operational data. This capability enables the optimization of farm management, improves the efficiency of input use, supports internal decision-making processes, and ensures the quality and safety of agricultural products (Buelvas et al.,

2019). The large volume of data on crop morphological characteristics, acquired with high temporal resolution, is also utilized in experimental trials, for instance, in genetic improvement studies (Pauli et al., 2016).

The availability of low-cost commercial 3D sensors allows for their integration at a reasonable expense, enhancing the monitoring process by providing detailed insights into the dynamics of agronomically significant variables such as growth rate, health status, and weed infestation levels. This approach offers extremely high spatial and temporal resolution and greater accuracy compared to manual data collection.

Protected environment horticulture, such as tunnel greenhouses, is a high-income sector with greater potential for investment, even for farms of similar sizes (Bagagiolo et al., 2022). Specific features of this cultivation system, such as physical structures that shield crops from rainfall, the regular layout and division of plots, and the presence of technological infrastructure, make the integration of automation systems more feasible. These characteristics also attract research and development efforts aimed at implementing such systems. The European Union's framework program launched in 2010, known as "CROPS" (Clever RObots of croPS), along with other initiatives by the United States Department of Agriculture (USDA) that has supported a significant number of research efforts aimed at designing intelligent vehicles for greenhouse applications. Recent research outputs from both the United States and the European Union have contributed to advancements in this field (Zhao et al., 2020).

The protected cultivation sector is highly diverse in terms of agricultural practices, presenting a significant challenge for designers and researchers. Ensuring the economic viability of robotic systems will require developing solutions that are reconfigurable and adaptable to various production environments. This reconfigurability will be crucial for making such technologies feasible to a wide range of farms, including those involved in niche markets with lower production volumes (Van Henten et al., 2013).

1.4.3.1 Examples of Marketed Models

Despite the diverse range of prototypes developed, the number of agricultural robots capable of monitoring crops and performing tasks of limited complexity that are

currently available on the market remains quite small. One of the main challenges is the difficulty in mass-producing machines whose tasks cannot be easily standardized and adapted to different agricultural environments. The medium-to-low profitability associated with these machines is largely due to the low market value of many agricultural products and the strong seasonality in many production areas, which would limit the use of such robots (Urrea & Munoz, 2015). Furthermore, these vehicles face significant challenges in interacting with human operators, identifying and reaching targets, and, most critically, developing truly effective artificial vision systems. The improvement of these vision systems is closely tied to advances in information integration (Jin Y. et al., 2021).

For instance, Bechar et al. (2021) compared the coefficient of variation (CV) derived from sample distributions of weight estimates produced by machine vision algorithms applied to inert targets and agricultural products. The CV was significantly higher for the agricultural domain, highlighting the difficulties in recognizing and characterizing biological objects, which are inherently more complex and variable than inert targets.

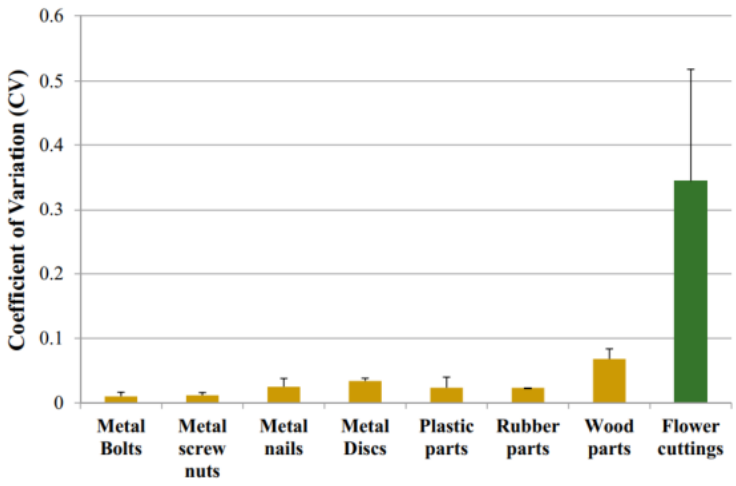

Figure 2. Coefficient of variation of objects in different domains [Source: Bechar et al., 2021].

Despite their limited number, some of the most interesting and advanced semi-commercial robot models, designed for data collection in horticulture, are briefly presented below. The information provided is based on claims made by their respective manufacturers.

EcoRobotix, a Swiss company, has developed AVO (see Fig. 3a), a robot designed to identify weeds and apply herbicides in a localized and precise manner. AVO moves autonomously over cultivated areas, operating for up to 8 hours on a single battery charge, during which it can cover an area of 5 hectares. Its operational time is further extended through the integration of solar panels that support the robot's energy system. Another advanced robot is Dino (see Fig. 3b), developed by the French company Naïo Technologies. Dino is capable of recognizing weeds using RGB stereo cameras and performing mechanical weeding between crop rows with an accuracy of 50 mm. Its positioning is ensured by an RTK-GPS receiver, and it has a working capacity of 4 hectares per day. In the Netherlands, HortiKey has introduced the Plantalyzer (see Fig. 3c), a monitoring system designed to estimate key parameters such as the quantity and ripeness of tomatoes. This system uses color and depth image processing powered by machine-learning algorithms. The price of the Plantalyzer is available upon request. Korechi Innovations Inc. offers the RoamIO Series (see Fig. 3d), a robot capable of collecting soil data using electromagnetic induction probes, assessing crop health, and producing yield estimates through multispectral sensors. Navigation is based on an RTK-GPS receiver, supported by a LiDAR sensor, and the robot has a working capacity of 4 hectares per day. In Australia, AGERRIS has developed The Digital Farmhand (see Fig. 3e), a robot that collects crop data, assesses crop health and yield, and uses deep-learning models to process stereo RGB images. This system also enables the identification of weed species. When equipped with solar panels, the robot’s battery can achieve an autonomy of 15 hours, with a working capacity of 3 hectares per day, supported by RTK-GPS corrected GNSS signals. Lastly, the Small Robot Company from the UK has introduced Tom (see Fig. 3f), a robot that monitors crop health, growth parameters, yield predictions, and weed pressure using reprocessed RGB and hyperspectral images through machine-learning systems. Tom has a working capacity of 20 hectares per day.

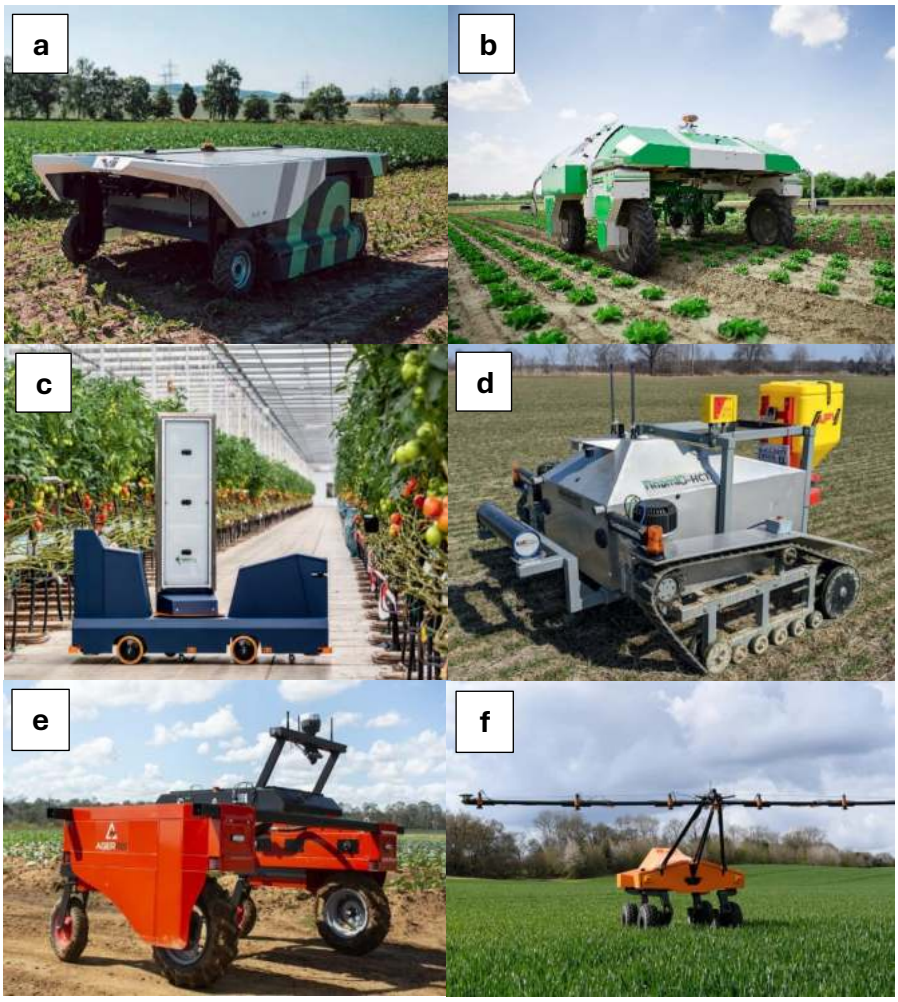

Figure 3. Examples of agricultural robots currently on the market.

1.5 The Problem of Weeds in Agriculture

Weed control has been a critical challenge in agricultural practices since ancient times (Scavo & Mauromicale, 2020) and remains a pertinent issue today. Weeds are among the primary factors contributing to potential yield reductions in crops, alongside pathogens such as fungi, bacteria, viruses, and animal pests including insects, rodents, nematodes, and mites. On a global scale, average potential losses in agricultural production due to weed pressure have been estimated at approximately 34%, which is nearly double the losses attributed to animal pests (18%) and those caused by other pathogens (16%) (Oerke, 2005). The yield reduction primarily arises from the ability of weeds to directly compete with crops for essential resources needed for growth, such as nutrients, water, sunlight, and space (Slaughter et al., 2008). However, the extent of yield reduction varies depending on several factors, including the crop species, weed population, weed density, the timing of weed emergence relative to the crop, and the cultivation practices employed.

In addition to direct competition, the presence of weeds can lead to other indirect management challenges. One of the key challenges posed by weeds is the presence of a seed bank in the soil, which consists of all the potentially viable seeds that have accumulated over time and can remain dormant for several years until conditions become favorable for germination (Trognitz et al., 2016). Seeds of weed species often exhibit dormancy, leading to staggered seedling emergence, which complicates the timing and planning of effective control measures and prolongs the persistence of weeds in the field. Therefore, it is crucial to effectively and promptly manage weed growth, ensuring that they are controlled before reaching the reproductive phenological stage. If weeds are allowed to produce seeds, this would further refill the seed bank, exacerbating the problem.

Additionally, weeds can release secondary metabolites into the soil, known as allelopathic substances, which can interfere with the physiology of crops and reduce their vigor (Farooq et al., 2020). Weeds can also serve as intermediate hosts for various pests, providing a refuge for overwintering and subsequently attacking subsequent crops. Furthermore, they possess the ability to thrive across a wide range of environmental conditions, including those that are potentially unfavorable (Chauhan,

2020). This adaptability suggests that, in the future, considering the impacts of ongoing climate change weeds may further enhance their competitive ability. Consequently, it is anticipated that greater quantities of herbicides will be required, and their effectiveness will become increasingly crucial (Tudi et al., 2021), alongside the diversification of weed management strategies.

Another critical issue is the potential health risk to consumers due to the accidental contamination of crops by weeds. In horticulture, particularly in the production of leafy greens, there is a concern about the contamination of harvests by weed species that contain toxic compounds (Stephens, 1982). If these toxic substances are ingested, they can pose serious health risks, leading to the rejection of entire production batches if contaminated weeds are detected, resulting in significant economic losses. In addition, insufficient weed management can elevate the risk of food contamination by mycotoxins, which are compounds with harmful health effects (Peles et al., 2021).

These challenges underscore the ability of weeds to compete with crops, leading not only to reduced yields but also to increased production costs and management complexity. Achieving effective weed control is therefore essential for sustainable production, both in terms of quantity and quality, especially considering the goals set for 2050 (Westwood et al., 2018).

Regarding the quantitative aspect of agricultural production, weed-related yield reductions have been estimated at around 23% for wheat, 37% for both rice and soybean, 40% for maize, 36% for cotton, and 30% for potatoes (Esposito et al., 2021). Some studies suggest that these percentages could be even higher. For instance, Zohaib (2016) estimates that wheat yield losses due to weed competition can range between 25% and 30%. Similarly, uncontrolled weed growth during the critical phase of wheat development can lead to yield reductions of up to 60% (Gharde et al., 2018). Other studies indicate that intense weed pressure can reduce maize yields by up to 60%, and under certain conditions, even by as much as 85% (Jain et al., 2022; Pant et al., 2021). This yield reduction phenomenon affects food prices and has implications for food security. The anticipated population growth in the coming decades will certainly increase the demand for food, a demand that will be challenging to meet

given the current global agricultural production system. Increasing crop yields is therefore crucial, as land is a limiting factor while demographic growth continues unabated.

1.5.1 Main Weed Control Techniques

The most commonly used techniques for controlling weed development and reducing competition with crops are categorized primarily based on the type of action performed, and are classified into mechanical, physical, biological, and chemical methods.

Mechanical control methods involve the use of tools to manage weed growth through direct contact with the weed or the soil. The number of interventions required and their intensity depend on the quantity and developmental stage of the weeds (Vijayakumar et al., 2023). These interventions can be performed either in the absence of crops (such as plowing and rotary tilling) or in the presence of crops (such as harrowing and hoeing) and are often part of broader field operations necessary for crop management (Scavo & Mauromicale, 2020). Generally, mechanical methods have some limitations, such as high initial costs for purchasing specialized machinery, labor and fuel costs, limited effectiveness on weeds between rows, and a strong dependence on soil and climatic conditions which can affect the timeliness of interventions, as well as the weed species and their growth stage (Scavo & Mauromicale, 2020).

The main factors leading to the use of mechanical methods include the emergence of resistance in weeds to chemical molecules and the lack of effective active ingredients for certain crops or with new mechanisms of action (Busi et al., 2013). Despite its complexity, mechanical weeding can still be considered a valuable tool in complementing chemical weed control within an integrated crop management system.

The most adopted physical method for weed control is mulching. This technique involves covering the soil with plant residues or, more often, with plastic material to physically prevent or obstruct the germination and emergence of weeds. The use of plastic film mulching is frequently employed to contrast weeds in the cultivation of

horticultural crops such as tomatoes, peppers, or eggplants. This method is much more effective against annual weeds compared to perennial (Gnanavel, 2015) and has some operational drawbacks that may limit its applicability in all contexts. For instance, the need to remove the plastic material at the end of the growing season requires additional manual labor for installation and disposal, making it not always economically sustainable. Furthermore, plastic films must be disposed of in dumps, and their contamination often necessitates further washing and purification before recycling, thereby increasing the environmental impact of these solutions (Cozzolino et al., 2014).

Other physical methods also exist, which utilize heat to alter the physiological functions of weeds. These methods can be applied through direct and indirect approaches. Direct methods include flame weeding, solarization, and steam application (Chauhan, 2020). Indirect methods do not involve physical contact; instead, heat transfer is achieved using microwaves, ultraviolet light sources, or lasers, although the latter are still in experimental stages.

Regarding biological methods, cover crops (living mulch) are used. These are intercultural crops that provide a wide range of ecological services to the cropping system, including nutrient enrichment, capture and recycling, organic matter addition, soil erosion reduction, and control of pathogens and weeds. During the vegetative phase of the cover crop, the weed suppression effect occurs mainly in two ways: the first is through direct competition with the weeds, while the second is due to potential allelopathic interactions between the weed population and the cover crop (Scavo et al., 2019). Chemical control methods will be addressed in a dedicated section with more in-depth analysis.

1.5.2 Chemical Weeds Control

Chemical control methods comprehend plant protection products, a category of substances commonly referred to as agrochemicals, which includes herbicides, insecticides, fungicides, rodenticides, molluscicides, and nematicides. Agrochemicals have historically played a crucial role in the advancement of agriculture by mitigating crop losses and enhancing yields. Global production of

agrochemicals has grown at an annual rate of approximately 11%, increasing from 0.2 Mt in the 1950s to over 5 Mt by 2000 (Tudi et al., 2021).

Following their introduction in the 1950s, herbicides quickly became the predominant method for controlling weeds in conventional agricultural practices (Kudsk et al., 2003). The significant advantage of chemical weed control lies in the ability of herbicides to selectively remove weeds from cultivated fields, thereby improving productivity efficiency and reducing both costs and management complexity. Consequently, their use is widespread on a global scale (Oerke, 2005).

In conventional agricultural practices, herbicide application can be performed either on the soil or via foliar methods. Soil applications include surface applications, aimed at preventing weed germination in the upper soil layer; subsurface applications, where herbicides are injected into the lower soil layers at various points, either manually or with machinery; and band applications, utilizing bar sprayers. Foliar applications are carried out using a sprayer and can be either uniformly distributed over the entire treatment area (non-localized distribution) or localized directly between crop rows. Uniform spraying generally requires less investment in equipment compared to site-specific management methods, which may involve procedures that could delay intervention. However, a significant drawback of this method is the use of large quantities of herbicides, which consequently increases environmental impact and may cause potential damage to the crop (Vijayakumar et al., 2023). This excess application is a function of the percentage of the product that does not reach the target and depends on various factors, such as the type of product used, the method of application, and the weather conditions at the time of treatment. The portion of the product that does not hit the target may affect nearby organisms or disperse into the environment, potentially causing adverse effects on non-target organisms within an ecosystem, including humans (Bernardes et al., 2015).

The severity of the issue becomes more apparent considering that many of these pesticides have the characteristic of being highly persistent in the environment, leading to severe and lasting contamination of agricultural ecosystems. For example, chlorinated insecticides can remain detectable on water surfaces even 20 years after

their ban (Bachetti et al., 2021). All pesticides present in groundwater and many found in surface water bodies pass through the soil. Therefore, in Chapters 6 and 8, where algorithms are developed to simulate herbicide treatments, an index was designed to assess the amount of herbicide distributed off-target with the aim of assessing the environmental impact on soil. This approach seems sensible considering that only 0.1% of the product applied to the crop reaches the target site where it exerts its function; the remainder disperses into the environment (Pimentel & Levitan, 1986). The responsible use of herbicides should therefore be as limited and efficient as possible to enhance their sustainability (Partel et al., 2019). This concept will be explored further in Section 8.5.

1.5.3 The Herbicide Resistance Phenomenon

Herbicide resistance is the ability of a weed to survive the application of herbicide (The International Herbicide-Resistant Weed, HRAC 2021). This resistance is a natural consequence of the selective pressure introduced artificially, which over time favors the fitness of populations with genetic configurations that enable survival. The issue of herbicide resistance is a significant concern, with approximately 250 weed species confirmed to be resistant to one or more active ingredients to date.

The most crucial classification to address this phenomenon is the one that groups and categorizes herbicides based on their site or mode of action. The official body responsible for this classification is the Herbicide Resistance Action Committee (HRAC), which provides comprehensive guidelines on the potential resistance of weeds to the various active ingredients available in the market. This phenomenon necessitates farmers carefully consider and evaluate agronomic practices and the susceptibility of weeds to herbicides. It is also essential to avoid agronomic practices that increase the risk of resistance development, such as the repeated use of herbicides with similar mechanisms of action across different seasons, monocultures, or crop rotations that rely on herbicides with similar action for weed control. Additionally, the lack of integrated weed management practices that incorporate non-chemical methods, such as mechanical and physical control, should be avoided.

The use of herbicide mixtures and the rotation of active ingredients can reduce the risk of herbicide resistance in weeds. Additionally, employing new techniques that decrease the amount of product applied while increasing the accuracy of distribution to the target can also help mitigate this risk (Chauhan, 2020).

1.5.4 European Regulations on the Use of Plant Protection Products

To reduce the use of plant protection products in favor of sustainable agronomic practices for pest control, the United Nations Conference on Environment and Development in 1991 identified Integrated Pest Management (IPM) as the preferred strategy for sustainable agriculture (Agenda 21). Following this, the European Union pursued a more sustainable use of pesticides through the 2006 Thematic Strategy on the Sustainable Use of Pesticides and the adoption of the 'pesticide package' in 2009. Since 2009, the European Union (EU) has implemented Directive 2009/128/EC on the Sustainable Use of Pesticides (SUD). This regulatory framework aims to reduce risks to human health and the environment by introducing Integrated Pest Management (IPM) to decrease agricultural dependence on plant protection products in EU member states. Each member state is required to develop a National Action Plan (NAP) to propose measures for achieving the objectives set by the legislation.

Since 2014, professional users of plant protection products have been required to apply the principles of IPM established by the EU (Riemens et al., 2022). IPM, mandated by Directive 2009/128/EC, also includes Integrated Weed Management (IWM), which plays a crucial role in managing weeds in EU cropping systems. However, this approach remains relatively underutilized in developing countries (Scavo et al., 2020). The goals outlined in the Strategic Plan of Directive 2009/128/EC can be achieved through various solutions and complementary approaches, including crop rotation, selection of resistant varieties, cultivation techniques, appropriate scouting practices, setting treatment thresholds, and applying biocides and beneficial organisms (Tona et al., 2017).

Despite these regulatory interventions, the excessive simplification of cropping systems in weed management and the reliance on chemical control methods, exacerbated by the continuous and extensive use of a few modes of action, have led

to the spread of herbicide resistance and other severe side effects such as soil and groundwater contamination, and adverse impacts on non-target organisms (Busi et al., 2013). Additionally, the decreasing number of active substances available may contribute to the emergence of resistance. The rate of introduction of new active ingredients and modes of action is declining, and an increasing number of registered herbicides could be banned. According to the European Commission, there were over a thousand approved active ingredients in 2001, but this number had reduced to around 250 by 2009, and this trend continues to decline. The future of agricultural production is therefore threatened both by the emergence of resistance and by the reduction in the number of active substances allowed on the market, which could further exacerbate the problem.

The EU's objective also includes ensuring that European citizens have access to healthy and sustainable food, setting several targets presented in December 2019 within the framework of the European Green Deal. This deal aims to mitigate the impacts of activities in EU member states to combat climate change and achieve the set goals by 2050. Specifically, in December 2019, the European Commission introduced the European Green Deal as directly connected to the Commission's strategy for implementing the UN Agenda 2030.

Within this framework, the "Farm to Fork" strategy, published in May 2020, was introduced. This strategy addresses environmental and public health issues that European society faces, aiming to create a food system that is fair, healthy, and environmentally friendly. The key areas of focus are:

- Achieving more sustainable food production
- Enhancing the sustainability of food processing and distribution
- Promoting sustainable food consumption
- Preventing food losses and waste.

The strategy sets several targets to be achieved by 2030, such as: a 50% reduction in the use of plant protection products; a 20% reduction in fertilizer use; dedicating 25% of the EU's arable land to organic farming and a 50% reduction in antimicrobial sales.

The impacts of implementing this strategy could be significant in terms of agricultural production, use of natural resources such as water, land, and chemical inputs (Cortignani et al., 2022).

The real challenge for modern agriculture is thus to maintain adequate agricultural production levels while reducing the use of plant protection products by 50%. However, the implementation of the 50% reduction target by 2030 has been suspended. On November 22, 2023, the European Parliament rejected the EU Regulation proposal on the sustainable use of plant protection products advanced by the European Commission with 299 votes against, 207 in favor, and 121 abstentions. Efforts have been made to reach an agreement for a more gradual reduction, postponing the halving to 2035 instead of 2030, and providing member states with some flexibility, with a mandatory national reduction target of 35%. Currently, solutions for this issue are still being reviewed.

1.5.5 Digital Technologies for Weeds Sensing

Digitalization in agriculture began with the implementation of precision farming techniques. The objective of precision agriculture is to optimize crop yields by increasing the efficiency of input use, thereby reducing environmental impact and input costs. When applied to chemical weed control, precision agriculture maximizes the efficiency of herbicide use by employing a combination of sensors and actuators. Sensors capture the spatial variability of weed infestations, while actuators precisely control the distribution of the herbicide, applying it only where necessary.

The more recent development of Agriculture 4.0 continues to follow the principles of sustainability, efficiency, and Site-Specific Weed Management (SSWM) introduced by PA. However, it incorporates advanced digital technologies, including IoT and AI. These technologies interconnect sensors deployed in the field, on machinery, and within the farm enterprise to analyze large volumes of data at high speeds. They support strategic planning and decision-making across the entire agricultural supply chain, from the field to the consumer. The analysis of this data aims to enhance not only the efficiency of specific processes but also the overall operational effectiveness of the farm system. Given the importance of these advancements, regulations are

already in place to encourage the adoption of such technologies through targeted funding.

Additionally, the use of agricultural robots is gaining traction, particularly in countries such as the United States, France, and the Netherlands. These robots are designed to optimize crop management and reduce costs by performing tasks that require minimal decision-making. They can automate and schedule various agricultural operations, including mechanical weeding, where they are most used, harvesting, and, in some cases, soil tillage (Sozzi, 2021; Hunter et al., 2020).

1.5.6 Site-Specific Weeds Management (SSWM)

Site-Specific Weed Management primarily relies on technologies capable of analyzing weed infestation levels in the field and assessing their spatial and temporal variability to plan precision weeding treatments. This type of analysis has been the subject of various studies (Gerhards & Oebel, 2006; Berge et al., 2012) that aimed to employ different technologies to detect weeds and apply herbicides with variable and spatially differentiated doses based on presence, concentration or group. Improved treatment localization increases its effectiveness and reduces the environmental impact of the operation.

The application of this methodology involves conducting monitoring using various types of sensors to assess crop development and the level of infestation. Unmanned Aerial Vehicles (UAVs) are commonly used for this purpose (Rasmussen et al., 2013; Torres-Sánchez et al., 2013). UAVs, which are now relatively inexpensive, are employed for aerial surveys to quantify weed pressure or provide an indication of crop vigor through related vegetative indices (Hunter et al., 2020), aiding in the creation of prescription maps for subsequent interventions. The delay between data collection, processing, and actual treatment can negatively impact the timeliness of the intervention. Post-processing methods are associated with high costs because they require, both for the survey and during implementation, high-accuracy positioning systems (GPS-RTK) that are costly.

Conversely, real-time data processing (online or on-the-go) is now more feasible thanks to technological advances in areas such as sensor technology, microcontrollers, computers and hardware. These advancements have made it possible to obtain setups that can acquire and process field images in real-time at reasonable costs, making the process economically sustainable, flexible, and rapid.

Weed detection algorithms involve two main processing steps. The first step is thematic segmentation, which separates vegetation (foreground) from the background based on color information or spectral signatures obtained from multi- or hyperspectral sensors. The second step involves classifying the vegetation pixels into two categories: crops and weeds. This classification is achieved using various algorithms that can consider color features (identifying spectral differences between weeds and crops), morphological features (such as shape, structure, and size), and positional features (e.g., the relative position within the field).

The following sections will present comparisons regarding the two main methods used in digital image processing. Chapter 5 will compare the segmentation capabilities of images acquired via UAV at an altitude of 40 m with those obtained from proximal images taken from 2 m from the ground. The topic of vegetation pixel classification will be addressed by presenting two algorithms that use RGB images in Chapter 6, while another algorithm using a 3D stereo camera to enhance segmentation capabilities, particularly in scenarios with high weed presence, will be discussed in Chapter 8.

1.5.7 Field-Scale Data Acquisition for SSWM Management

In recent years, the public's interest in reducing the environmental impact of production activities (van Bussel et al., 2022) has led consumers to become more aware and attentive in their product choices, favoring those characterized by greater sustainability.

In the agricultural production sector, the introduction of PA techniques has enabled the planning of field operations with a high degree of localization, as exemplified by precision spraying during chemical weeding operations. Such operations require the use of machinery, either mounted or self-propelled, needs highly representative and

spatially accurate data inputs to function correctly and achieve their intended purpose.

Currently, one commonly used technique for collecting field-scale data in this context involves the use of unmanned aerial vehicles (UAVs) to conduct aerial surveys and generate thematic maps based on information obtained from onboard sensors. The purpose of the aerial survey is to generate a map of the area through the ortho-mosaic of images acquired during the flight. This map must then be processed using geostatistical software - such as ArcGIS or QGIS - to obtain useful information for the localized management of subsequent high-precision operations.

A variable considered in literature for estimating weed pressure in the field is the Fractional Green Canopy Cover (FC) (Zhang et al., 2018). FC is based on calculating the percentage of surface area covered by vegetation at a given time by discretizing the overall area into homogeneous sub-areas, that represent the spatial resolution of the treatment. Generally, the trend of this variable is a function of the crop type and its phenological stage at the time of the survey. The degree of infestation within each sampled area is estimated by observing the excess deviations of FC levels compared to those measured in a control area, where weeds have been removed. Depending on how much infestation can be tolerated by the farmer, a maximum FC threshold is determined, and all sampled sub-areas with a value exceeding this threshold are considered critical and thus require treatment. This generates the prescription map containing all the information needed to manage the localized intervention by the precision machinery.

Although the use of UAVs ensures a short monitoring operation time, it presents certain challenges, primarily the high cost required by a specialized operator, usually external to the farm (> 1 k€), for conducting the survey and creating the map. If the operation is performed by internal farm personnel, the costs remain high due to the potential purchase of the UAV, necessary licenses and insurance, and the acquisition of a high-performance computer needed to reduce the map processing time, which remains relatively high, on the order of hours per hectare, delaying the subsequent intervention.

1.5.8 3D Sensing in Agriculture

Recent advancements in 3D sensing technologies have shown significant potential for agricultural applications (Gregorio & Llorens, 2021). These sensors provide essential depth information, enabling automation and robotics in agriculture, particularly in areas such as crop management, vehicle navigation, and livestock management (Vázquez-Arellano et al., 2016).

3D imaging techniques in agricultural applications include various sensors that use different technologies and operational principles. These techniques primarily include Light Detection And Ranging (LiDAR), multiview 3D imaging systems (such as Structure from Motion (SfM) or stereo vision systems), and Time of Flight (ToF) based 3D imaging (Xiang, 2023). However, some of these techniques are not suitable for field surveys intended for real-time image processing.

LiDAR sensors offer a long working distance, but high-resolution systems are expensive and generally have lower point cloud density. These sensors are used in autonomous vehicle navigation applications, particularly for Simultaneous Localization And Mapping (SLAM) (Xiang, 2023). In this study, LiDAR sensors were employed for the same purposes, specifically in Chapter 4**,** which involves automated data collection using an Unmanned Ground Vehicle (UGV) navigating within a map using the SLAM method. However, a significant limitation of LiDAR technology for vegetation sensing is its inability to capture color information, which makes it challenging to accurately segment vegetation points based solely on spatial location. Nonetheless, LiDAR has been utilized in various studies for less complex measurements, such as crop height estimation (Liu, 2018) with an error of 12.7%, crop row detection algorithms for under-canopy navigation (Gai et al., 2021) capable of identifying the position of crop rows with an mean error of 3.4 cm and 3.6 cm in maize and sorghum fields, yield estimation (Feng et al., 2019) with an error of 12.7% and biomass estimation (Hütt et al., 2022).

Regarding the SfM technique, 3D reconstruction is achieved by using a series of sequentially captured RGB images to generate a full surface profile of the object of interest. These systems are commonly used in acquisitions performed with UAVs to

monitor large areas quickly using RGB or multispectral sensors (Remondino et al., 2012). The primary limitation of SfM is its requirement for a substantial number of images from different viewpoints and a considerable amount of computational time, making it suitable only for post-processing applications.

Given the characteristics of the primary 3D sensing methods, only those capable of real-time data processing will be considered for this work: specifically, stereo vision systems and Time of Flight (ToF) based imaging. ToF sensors were chosen due to their low cost (ranging from €100 for the Kinect V2 to €400 for the latest high-resolution Microsoft® Azure Kinect). Typically, depth images acquired with these sensors have limited resolution and moderate measurement accuracy, and performance can be affected by the material properties of the object's surface and environmental lighting conditions.

Stereo imaging systems are also relatively affordable (ranging from € 300 to € 800 depending on the manufacturer and the performance of the device) and, unlike ToF sensors, can be used both indoors and outdoors. These systems acquire depth information by using the disparity between images captured from two different viewpoints (in this case, the left and right cameras), based on triangulation principles. Traditional stereo matching algorithms can be classified into three categories: local, global, and semi-global methods (Zhou et al., 2020), each with varying execution times and result quality. Additionally, recent advancements have introduced deep learning-based stereo matching algorithms to improve performance, although these methods still produce relatively inaccurate reconstruction results in texture-less, reflective, and occluded regions (Zhang et al., 2019). The accuracy of measurements depends on the stereo matching results, which are influenced not only by the chosen method but also by the lighting conditions and the type and abundance of visible textures in the scene.

The integration of RGB-D technology into the agricultural domain holds significant potential for enhancing performance in common vision-based tasks such as object detection and semantic segmentation (Kurtser & Lowry, 2023). Literature provides several examples of applying these sensors in agriculture. Depth information is utilized

for autonomous navigation and robotic applications to detect obstacles (Skoczeń et al., 2021). Wang employed RGB-D data to model the workspace of harvesting robots in apple orchards (Wang et al., 2022) and You developed a pruning robot for apple orchards using RGB-D technology (You et al., 2020). Similar robotic harvesting approaches have been explored for other crops, including grapes (Peng et al., 2021), cotton (Fue et al., 2020), and bananas (Lin et al., 2022 [1]). Additionally, Lin utilized RGB-D data to perform cone and cylinder fitting for maize organ segmentation in high-throughput phenotyping (Lin et al., 2022 [2]).

3D sensors have shown also promising applications in weed management and research. These sensors can overcome limitations of 2D imaging by providing depth data for accurate plant modeling (Dobbs et al., 2022). The RGB-D data has also demonstrated higher recognition rates for weeds in wheat fields, particularly for grass weeds that are visually like wheat (Xu et al., 2020). These advancements in RGB-D-based weed detection contribute to the development of more accurate and robust computer vision systems for smart farming applications.

Some studies have utilized plant height and spacing information to distinguish between crops and weeds (Yong Chen et al., 2013). These systems have shown high detection rates for crop species such as broccoli and soybean, facilitating automated weeding operations. The technology enables spatiotemporal mapping of weed populations, targeted site-specific weed management, and monitoring of cover crop performance for weed suppression. Such advancements offer significant potential for reducing herbicide use, mitigating herbicide resistance, and enhancing environmental health in agricultural systems (Dobbs et al., 2022; Andújar et al., 2016). Systems based on Convolutional Neural Networks (CNNs) have achieved high accuracy in identifying various crops and weed species, with accuracy rates ranging from 77% to 98% (Peteinatos et al., 2020).

Moreover, in addition to high-throughput crop phenotyping applications, 3D imaging techniques have also been employed in the animal science sector to enhance animal production management (Vázquez-Arellano et al., 2016). Bezen utilized RGB-D cameras to monitor individual cow feed intake in open cowshed conditions (Bezen et

al., 2020). Na, instead, applied 3D sensing to predict cattle weights (Na et al., 2022), while Mortensen developed a system for predicting broiler chicken weights in the poultry industry (Mortensen et al., 2016).

1.6.9 3D Weed-Crop Characterization for Target Detection

To classify and discriminate between a crop and the weeds present, it is necessary to characterize its salient geometric features, which can make this process more accurate than using 2D images. In this sense, 3D sensors can be useful for the geometric characterization of vegetation. In this work, it was chosen to characterize maize as a crop and some of the most common weeds.

Maize occupies a pivotal role in global agricultural production (Yu et al., 2021). This versatile crop is utilized for various purposes, including food and animal feed production, as well as energy generation (Klopfenstein et al., 2013). Maize is typically grown in rows with a spacing of approximately 0.7 - 0.75 m, depending on sowing density. This wide inter-row spacing increases the crop's vulnerability to weed competition, particularly during the early stages of growth (Iqbal et al., 2020). Weeds can significantly threaten maize yields by competing for space and environmental resources (Sharma et al., 2022). Weed control in maize is commonly managed by means of herbicides, which can be applied either pre-emergence or post-emergence. Pre-emergence treatments protect the developing corn plants from early weed competition (Abdallah et al., 2021), whereas post-emergence applications allow for adjustments based on the observed weed spectrum and overall pressure at the time of treatment (Alptekin et al., 2023). Timing is critical, as herbicides are most effective when weeds are not too advanced in their growth (Klopfenstein et al., 2013; Dewar, 2009). Therefore, the timeliness and localization of herbicide application are crucial factors for effective weed management. The objective of an effective weed control intervention involves, following pre-emergence treatment, the precise and localized application of herbicides during the post-emergence phase. This approach aims to reduce chemical inputs, enhance efficiency, and ensure greater economic and environmental sustainability.

To achieve automated high-precision treatments, such as patch or micro-spraying, it is essential to develop algorithms capable of distinguishing between weeds and crops with both accuracy and speed, suitable for real-time applications. This method offers improved accuracy compared to using color channels alone, particularly in scenarios with significant weed presence.

Characterization of plant structure is possible by extracting geometric features from individual plants or from specific sampled areas as in the case of monocots where isolation of a single individual is not always achievable. The morphological data used in the process of discriminating between crops and weeds could also be used to assess the vigor of the crop or to identify areas where planting or emergence has not taken place by monitoring in conjunction with the herbicide application process.

In the phenotyping experiment in Chapter 4, a ToF sensor was used in greenhouse conditions, which serves as an intermediate environment between full-field and indoor conditions. The high solar radiation, which interferes with the sensor's operation by introducing noise and reducing measurement accuracy, is partially mitigated by the plastic film covering the structure. Additionally, during the analysis phase, a gradient-based filter and a suitable region of interest (ROI) are applied to reduce the impact of noise. This approach helps to exclude edge areas, which are known to be more affected by noise.

In the field experiment in Chapter 8 aimed at weed detection, the Stereolabs ZED 2i stereo camera was used, equipped with polarizing filters to minimize glare. The environment in this scenario features high granularity due to the abundant textures of plants and soil, making the images suitable for this type of processing. This sensor is already utilized in PA applications, installed on commercial Monarch Tractors Mark-V models, and is currently integrated into operations at vineyards, orchards, and dairy farms for various purposes including automated management and safety at work. The use of the RGB-D sensor significantly contributes to characterizing the overall structure of the various species providing morphological parameters to complement colorimetric data. In field trials, these parameters will be used together with positional

parameters - such as row position and regularity, typically used in the discrimination process with RGB images - to optimize the discrimination process.

1.6.10 Actuation in Precision Spraying

In the context of precision chemical weeding, the ability to detect the presence of potentially infested areas or individual targets for treatment is, by itself, not quite to effectively address the issue of weeds. This capability must be coupled with an implementation system capable of delivering the appropriate amount of herbicide with a high degree of spatial accuracy. This is a critical factor for the successful execution of the weeding operation and for enhancing the environmental sustainability of such interventions.

This task in the field is assigned to precision sprayers, machines designed to transport, dose, and distribute a liquid mixture of water and herbicide. Broadly, two families of sprayers can be distinguished, each suited to different types of crops: boom sprayers, which are used for herbaceous crops, and atomizers, which are employed in treatments for tree crops. For the purposes of this work, reference will be made to machines dedicated to herbaceous crops.

The main components that constitute a sprayer are common across all types and primarily include the following:

- The tank, typically made of corrosion-resistant plastic, contains internal agitation mechanisms designed to maintain the homogeneity of the mixture to be distributed. These agitation systems are usually hydraulic, utilizing a portion of the flow that is recirculated within the tank itself, or in some cases, agitation is achieved through the activation of mechanical devices specifically designed for this purpose. The machine is also equipped with one or more auxiliary tanks containing clean water for washing and ensuring operator safety. Additionally, there is a pre-mixing tank that facilitates the loading of the active ingredient and its mixing with dilution water, as well as a cleaning tank connected to the hydraulic circuit, which is used at the end of the operation.

- The hydraulic circuit, whose function is to transport the mixture from the tank to the spray nozzles. This circuit may include manually or electrically actuated valves to isolate branches of the system from the flow, as well as filters both at the pump intake and along the supply lines to the individual distribution branches.
- The pump, driven by the tractor's power take-off (PTO), provides the necessary energy for the liquid to reach the distribution components, overcoming the resistance and friction encountered by the fluid along its path.
- The regulation system, which is essential for controlling the flow rate and distribution pressure, can be either mechanical or electronic. Among mechanical systems, the most common is a constant pressure system based on a pressure regulation valve (pressure switch) that, in combination with a constant flow rate, ensures uniformity and accuracy in dosage distribution. When the circuit pressure exceeds the set value, the valve opens, releasing the excess flow into the tank's return circuit.

  Electronic regulation systems, on the other hand, are based on electronic control units connected to sensors that monitor the machine’s forward speed and the circulating flow rate (flow meter). In these cases, excess flow regulation is managed by electrically operated valves that control the return flow recirculated into the tank. Such systems can maintain a constant dose even with variations in the tractor’s speed, and they allow for real-time adjustments to the dose during operation, as the configuration can be modified directly from the tractor cab.
- The spray nozzles, located at the terminal parts of the system, are mounted on the distribution boom and serve to atomize the mixture into a spray. This atomization can occur through various methods, with the most common being the pressurized passage of the liquid through the nozzle orifice. Different types of nozzles correspond to varying droplet sizes (diameters) and droplet population. Once a specific nozzle model is selected, it is possible to adjust, within certain limits, the dosage and the characteristics of the droplet population by regulating the pressure. Increasing the pressure typically results

in smaller droplet diameters, while decreasing the pressure produces the opposite effect.

Nozzles can be classified according to the shape of the spray they produce, with flat fan nozzles and cone nozzles being the most common. Additionally, there are specialized nozzles, such as double fan nozzles, designed to enhance penetration of the treatment in dense vegetation or when vertical surface coverage is required.

Anti-drift nozzles are also available, which significantly reduce the fine droplet population by incorporating air into the spray. This reduces the drift effect, which can cause a mismatch between the intended treatment area and the actual distribution, thereby increasing environmental impact due to off-target application and compromising weeding efficacy. To further mitigate drift, pneumatic spray nozzles can be used, where the liquid exits at low pressure from a slit and is propelled by a high-velocity airstream generated by a fan. The airflow both atomizes the mixture and transports it to the target, minimizing drift. Pneumatic atomization is particularly used in mist blowers, as it allows for the formation of spray patterns tailored to the specific needs of dense crop canopies.

1.6.11 Technological Steps of Actuation in Precision Spraying

In recent years, research on these machines, in line with the broader trend of reducing the environmental impact of agricultural activities, has led to various innovations aimed primarily at increasing input efficiency. This improvement in efficiency is achieved through enhanced spatial accuracy in the distribution process using variable rate technology, which in turn enables a reduction in both the cost of the distribution operation and its associated environmental impact.

Technology that has been applied across various operations, from planting to the distribution of phytosanitary products, involves the use of assisted guidance systems. Assisted steering enable the operator to accurately maintain a predetermined straight trajectory during operations, aiming to reduce overlaps and avoid leaving gaps between passes. This effectively prevents the application of a double dose in

overlapping areas and ensures that no treatments are missed in the gaps between separate passes, ensuring a high degree of optimization of the distribution process and thus a reduction in the quantities used without limiting the treatment effect. A similar effect has also been achieved through the more modern spatial control of individual boom sections (Scarafone et al., 2021).

Other technological applications have focused on optimizing management at the individual nozzle level. For example, the introduction of solenoid valves within the circuit allows for automated control of individual nozzles, adjusting their operation based on feedback from forward speed (obtained through sensors such as encoders, ultrasonic devices, or high-accuracy GPS-RTK receivers). This enables proportional adjustment of the distributed volume in relation to the tractor's speed, ensuring uniformity in the applied dose (Electronic Proportional Application Distribution, or DPAE). This method is also employed during the execution of curvilinear trajectories, allowing for volume adjustment at each nozzle based on the tangential speed relative to the center of rotation of the trajectory (Fabula et al., 2021).

Advanced nozzles are individually controlled to manage and modulate their opening through Pulse Width Modulation (PWM) signals. PWM is a widely used technique for controlling the power delivered to electrical devices, particularly motors, LEDs, and other components reliant on power. It functions by varying the duty cycle of a digital signal, which represents the ratio of "high" time to the total period of the signal. In a typical PWM signal, power is rapidly switched between high and low states, allowing the output to approximate an analog voltage through time-averaged signaling. The key parameter in PWM is the duty cycle, expressed as a percentage; a higher duty cycle indicates that the signal remains high for a larger portion of the period, resulting in greater power output.

Precision spraying treatments require algorithms for recognizing weeds based on their location, vegetation indices, or artificial intelligence systems. Recent field applications focus on solutions aimed at enhancing the localization and spatial resolution of treatments, primarily addressing this issue through two sensing methodologies discussed in the comparative study conducted in Chapter 5.

The first sensing strategy involves the post-processing of images obtained from aerial surveys using UAVs to generate georeferenced maps, which serve as the basis for creating prescription maps for targeted interventions. These prescription maps typically allow uniform treatment of areas approximately one square meter or slightly larger, depending on the spatial resolution of the sprayer, which is influenced by the distance between nozzles and their responsiveness.

The second strategy, named micro-spraying, is more sophisticated and involves ensuring that each actuator has a narrower working width while being capable of activating nozzles selectively along the direction of travel. This approach enables targeting of identified weeds with significantly higher accuracy, moving away from the fixed grid pattern typical of patch-spraying.

The increased computational capacity of microcontrollers and single-board computers, which are now relatively inexpensive (e.g., Raspberry Pi, Jetson Orin, etc.), has facilitated the experimental development and integration of complex algorithms capable of performing imaging techniques, incorporating classifiers, object detectors, and artificial intelligence models with relative ease. This hardware can also directly control the operation of end effectors by generating digital signals or transmitting information via standardized protocols such as USB, I^2C, SPI, as well as CAN BUS and ISO BUS, which are the standards adopted in agricultural machinery.

2 Materials used during PhD activities

In this general materials section, only the sensors and other hardware components and software tools used in the various experiments are presented. These are introduced once in the introductory part of the thesis.

2.1 ToF 3D Camera (Microsoft KINECT V2)

The Kinect is a low-cost depth sensor originally designed as an interactive controller for video games. However, due to the availability of libraries, drivers, and a dedicated Software Development Kit (SDK), it is frequently used in experimental contexts. This device features both a color camera (RGB) and a depth camera (D), which measures distance using a signal emitted by an infrared projector.

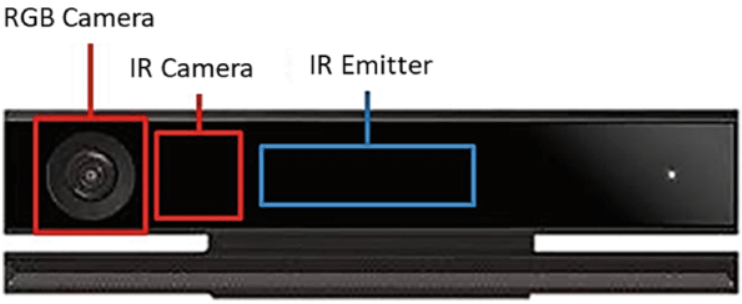

Figure 4. ToF Microsoft Kinect V2 sensor [Source: Brancati et al., 2018].

2.1.1 Operational Principles of Time-of-Flight (ToF) Sensors

Time-of-Flight (ToF) sensors measure distance (d) by determining the time it takes for a light signal to travel from the sensor to an object and back. Specifically, infrared (IR) ToF sensors, such as those used in the Kinect V2, utilize IR light for distance measurement. The sensor emits a modulated infrared light signal, which travels through the air, reflects off the object's surface, and returns to the sensor. The sensor then detects the returned light and measures the time interval (Δt) between the emission and reception of the signal. The distance (d) to the object is calculated using the speed of light (c), based on the following formula:

$$d = \frac{c \cdot \Delta t}{2}$$

2.1.2 Pros and Cons of using ToF sensors

The main advantages of ToF sensors include their ability to achieve high-precision distance measurements, often with millimeter-level accuracy. Additionally, they can measure distances with a high frequency, which makes them ideal for real-time applications. Unlike stereo vision systems, ToF sensors offer direct distance measurements without the need for complex image processing algorithms, simplifying the data acquisition process and enhancing efficiency.

However, the primary drawbacks of ToF sensors include a limited range, particularly when dealing with highly reflective or absorptive materials. While they are generally less affected by ambient conditions than passive systems, strong IR light sources such as sunlight can still interfere with their performance. Moreover, the constant emission and detection of IR signals can result in higher power consumption compared to some other distance measurement methods and typically have lower resolution compared to high-resolution color cameras, which can reduce their effectiveness in applications requiring detailed imaging.

In summary, these sensors offer a reliable solution for distance measurement and 3D mapping, with a balance between accuracy, speed, and functionality across different lighting conditions. Nonetheless, their performance may be affected by limitations in range, susceptibility to ambient light interference, and lower resolution.

2.1.3 Data Output

The raw output generated by the sensor is organized into two matrices: one representing color information (RGB) with dimensions 1080 by 1920 by 3 and a *'uint8'* format, and another matrix representing distance data (D) with dimensions 424 by 512 and a 'uint16' format, derived from the sensor's respective optical channels. By merging the data from these two matrices, a point cloud can be created where each individual point in space is characterized by a vector containing both spatial coordinates [X,Y,Z] and colorimetric coordinates [R,G,B].

Given that the RGB and depth sensors have different positions, optical characteristics and resolutions, the point cloud can be generated in two different ways. The first

method, known as depth-centric, involves registering the color image onto the depth image, resulting in an output with the same dimensions as the depth matrix. The second method, called color-centric, involves the registration of the depth image onto the color image, making the output size match that of the RGB image. The choice of output depends on the experiment's objectives, the relative importance of the two data channels, and any constraints regarding processing time.

2.1.4 Common Measurement Errors

Raw depth data often contains artifacts and inaccuracies caused by measurement errors, missing data, and noise due to lighting conditions during capture. These issues necessitate a preliminary data filtering phase before further processing. Some of these measurement errors result in clusters of points scattered in space with lower density compared to actual surfaces. This phenomenon, known in the literature as "*flying pixels*" (Reynolds et al., 2011), tends to occur most frequently in transition zones and along the edges of objects, potentially altering their true dimensions and shape and creating connections between different clusters, which complicates effective clustering.

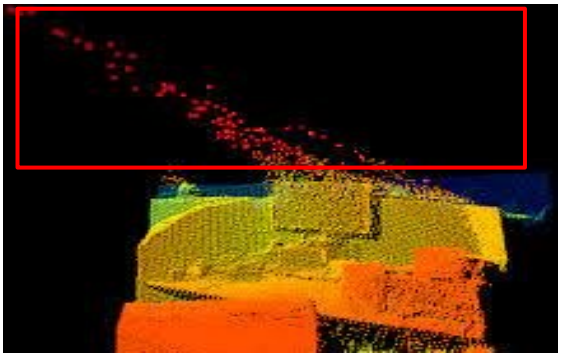

Figure 5. Example of flying pixels issue [Source: Reynolds et al., 2011].

To address flying pixels in this work, a gradient-based filter was applied to the depth matrix. This filter eliminates points with a gradient variation relative to neighboring pixels that exceed a certain threshold. By doing so, it preserves surfaces with higher point density and lower measurement error.

2.2 3D Stereo Camera (Stereolabs ZED 2i)

The Stereolabs ZED 2i is an advanced stereo camera designed to capture 3D images and provide real-time depth data that can be deployed in most environments. ZED 2i is an IP66-rated Rolling Shutter camera built for spatial analytics, resistant to dust, water, humidity, and is designed for outdoor applications and challenging medical,

industrial, agricultural environments. It incorporates dual 4-megapixel (MP) RGB cameras, an Inertial Measurement Unit (IMU) and it utilizes a combination of hardware and software techniques to enhance depth perception. The camera can acquire images with different resolutions (2K, 1080p, 720p, 376p) and with a frequency that depends on the resolution selected and which can vary from 100 frame per second (fps) to 15 fps. Additionally, the sensor is equipped with various onboard components, including an accelerometer and a gyroscope with an acquisition rate of up to 400 Hz. It also features a barometer, a magnetometer, and a thermometer. This sensor can be integrated with a range of third-party software and platforms, allowing developers to harness its capabilities for diverse applications. Some key third-party integrations include:

- Robot Operating System (ROS) that supports features such as SLAM (Simultaneous Localization and Mapping) and obstacle detection.
- Software Development Kits (SDKs) like Unity or Unreal Engine for developing Augmented Reality (AR) and Virtual Reality (VR) applications.
- Computer Vision Libraries like OpenCV a popular computer vision library, for image processing and analysis.
- TensorFlow for machine learning and neural network-based applications enabling the deployment of AI models for tasks like object detection and classification.
- 3D Mapping and simulation like Gazebo for robotics simulation and virtual environment allowing for testing and development of robotic systems before deploying in real-world scenarios, or RTAB-Map (Real-Time Appearance-Based Mapping) for real-time 3D mapping and localization that is useful for SLAM applications in robotics and autonomous systems.

In this work, the stereo camera was integrated with MATLAB for data analysis, visualization, and algorithm development, a method particularly useful for research and academic purposes. These third-party integrations enhance the versatility and functionality of the Stereolabs ZED 2i, making it a powerful tool for a wide range of applications, from robotics and industrial automation to AR/VR development and AI-based projects.

2.2.1 Operational Principles of Stereo Cameras

Stereo cameras measure distance by comparing two images captured from slightly different perspectives, like human binocular vision. This process is known as stereo vision or stereopsis.

The stereo camera consists of two lenses positioned a fixed distance apart, and this distance is named baseline (B = 0.12 m). Each lens captures an image from a slightly different viewpoint and after the acquisition, images are analyzed to identify corresponding points (features) in both images. This involves finding points in the left image that match points in the right image. For each matched pair of points, the disparity, or the difference in their positions between the two images, is calculated. This disparity is inversely proportional to the distance of the object from the camera. The depth is calculated using the disparity value according to the formula and f represent the focal length:

$$d = \frac{B \cdot \mathrm{f}}{disparity}$$

2.2.2 Pros and Cons of using Stereo Cameras

Stereo cameras do not emit any signals, so they do passive measurements that rely on ambient light making them less intrusive and reducing power consumption. They provide both depth information and high-resolution color images, which can be useful for a variety of applications, including object recognition and tracking. Compared to the camera ToF, stereo cameras have a much wider measuring range, from a few centimeters (0.3 m) to several meters (20 m), depending on the baseline distance and resolution. A key advantage is that these cameras are more robust to different ambient light conditions. The disadvantages of using these sensors compared to ToF are that the process of feature matching and disparity calculation can be computationally demanding, requiring more powerful processors and optimized algorithms.

Accurate depth measurement relies on identifying matching features in both images and for this reason homogeneous surfaces or poor lighting conditions can lead to errors. Moreover, this kind of sensor has limited close-range accuracy.

In conclusion, stereo cameras like the Stereolabs ZED 2i provide detailed depth and color information, making them suitable for a wide range of applications, including robotics, augmented reality, and 3D mapping. However, their performance can be influenced by computational requirements, texture and lighting conditions, occlusion, and the need for precise calibration.

2.2.3 Data Output

The output of this sensor is organized similarly to the Kinect V2 described in Section 2.1.3, with the resolution determined by the data acquisition settings. Unlike the Kinect V2, the registration between color and depth is not necessary and the depth will always have the same resolution as the image of the left lens which is the one used for the alignment and calculation of disparity compared to the right one.

2.3 Color Camera (GoPro Hero 8)

The GoPro Hero 8 Black, introduced by GoPro Inc., is an advanced action camera renowned for its versatility and high-performance capabilities, making it suitable for both amateur and professional applications. This camera is engineered to offer robust performance in demanding conditions, integrating several technological advancements that enhance its usability and image quality.

The camera is equipped with a 12 MP CMOS sensor, which delivers high-resolution images and video capture. The sensor is paired with an advanced image processor that supports a maximum video resolution of 4K at 60 fps. Additionally, the camera can capture Full HD (1080p) video at up to 240 fps, allowing for high-quality slow-motion footage. The lens features an ultra-wide field of view (FOV) of approximately 170 degrees, providing a broad perspective ideal for capturing immersive action shots.

Figure 6. Go Pro Hero 8 Camera

One of the key innovations in the Hero 8 Black is its built-in Hyper-Smooth 2.0 image stabilization technology. This advanced stabilization system offers gimbal-like performance without the need for additional hardware, significantly reducing camera shake and ensuring smooth video footage even during dynamic movements.

2.4 Digital Processing and Hardware Management

The acquisition and processing of the images as well as the management of the hardware peripherals interfaced in the experiments was controlled by a Notebook (PC1) ASUS Notebook equipped with AMD A10-9600P, 2.40 GHz frequency, integrated Radeon R5 and 16 GB RAM). The analytics were handled with customized software routines developed in MATLAB.

The real-time operation of the stereo camera (discussed in Chapter 8) required the use of a notebook equipped with a suitable graphics card. In this case the notebook Lenovo ThinkPad P16s Gen 2 (PC2) was used. This is powered by an Intel Core i7 processor, providing robust performance for multitasking and complex tasks. The device is equipped with 32GB of DDR5 RAM and a GPU NVIDIA T550, allowing for smooth operation of memory-intensive applications.

2.5 MATLAB Programming Environment

MATLAB (MATrix LABoratory) (Mathworks, Natick, MA, United States) is a high-level programming language and interactive environment developed by MathWorks. It is commonly used for numerical computing, data analysis, algorithm development, and visualization. For these reasons MATLAB is widely adopted in academia, research, and various industries due to its powerful computational capabilities and ease of use for matrix and vector operations. The key features are:

- provides a high-level language for matrix and array mathematics. Its syntax is designed to be intuitive and easy to learn, making it accessible to users with a background in mathematics and engineering. It is optimized for matrix and array operations, which are fundamental to many scientific and engineering calculations. Built-in functions allow for efficient manipulation and

computation with large datasets (it may not be as fast as lower-level programming languages (e.g., C, C++) for certain computational tasks).

- offers an integrated development environment (IDE) with a command window, workspace, and various tools for debugging and profiling code. The interactive nature allows users to test and visualize their results immediately.
- has a wide range of specialized toolboxes that extend its functionality. These toolboxes cover areas such as signal processing, control systems, image processing, machine learning, and more, providing pre-built functions and algorithms for specific applications.
- excels in data visualization, offering a variety of plotting functions to create 2D and 3D graphs, charts, and animations.
- supports the development and testing of algorithms, enabling users to implement complex mathematical models and simulations. It also provides tools for optimizing and refining these algorithms.
- can interface with other programming languages such as C, C++, Java, and Python. It can also interact with hardware and software systems, making it suitable for real-world applications and embedded systems.
- has a large user base, extensive documentation, and a supportive community. MathWorks provides regular updates, technical support, and training resources.

In summary, MATLAB is a versatile and powerful tool for numerical computing, widely used across various fields for its ease of use, extensive functionality, and strong visualization capabilities. However, its cost and proprietary nature can be limiting factors for some users.

2.6 Microcontroller (Arduino Uno)

Arduino is an open-source hardware platform based on a microcontroller, designed to simplify the use of interactive electronics in multidisciplinary projects. The board was developed in 2005 by members of the Interaction Design Institute in Ivrea, Italy. The platform integrates a programmable microcontroller with an Integrated Development Environment (IDE).

The Arduino IDE is a free, open-source software that allows users to write, compile, and upload code to the board. It is Java-based and supports Windows, macOS, and Linux operating systems. The programming language used in Arduino is based on Wiring, a simplified version of C/C++. This, combined with various libraries, facilitates easier interaction with hardware components.

Arduino boards come preloaded with a bootloader, enabling microcontroller programming via a simple USB connection, thereby eliminating the need for an external programmer. The core component of the Arduino UNO board is the microcontroller, typically an 8-bit AVR series model from Atmel, such as the ATmega328.

The Arduino UNO board features 14 digital input/output pins and 6 analog inputs, which allow the connection of sensors, actuators, and other electronic devices. It also supports multiple communication interfaces, including UART, I^2C, and SPI, facilitating communication with other devices such as sensor modules, displays, or network.

Arduino is widely used for various purposes, including education, rapid prototyping, the development of interactive projects, and both home and industrial automation.

2.7 AprilTags

AprilTags are a type of fiducial marker used in computer vision applications to detect and identify objects. They are specifically designed for robust and efficient detection in a wide variety of conditions. AprilTags are like QR-codes but are optimized for applications where precise spatial localization is required, such as robotics, augmented reality, and computer vision research.

These tags consist of a square grid of black and white cells encoding a unique identifier. The simplicity of their design makes it easy to detect and decode. The detection algorithm for AprilTags is designed to be robust to lighting variations, partial occlusions, and perspective distortions. This makes them suitable for use in dynamic and cluttered environments. Each marker encodes a unique ID, allowing multiple tags to be used simultaneously in a scene. This is useful for applications that require tracking multiple objects or landmarks. These markers can be used for estimating the

pose (position and orientation) of the tag relative to the camera and for this purpose were used for example in the field experiment in Chapter 4 and for the machine calibration discussed in Chapter 9. This is achieved through the known geometry of the tag and the projective properties of the camera. Its library is open source and widely available, making it accessible for both academic and commercial use. The library includes tools for tag generation, detection, and pose estimation. The main applications of these tags are:

- Robotics: they are commonly used in robotics for navigation, localization, and mapping. Robots can detect and identify tags placed in the environment to understand their position and orientation.
- Augmented Reality (AR): in these applications, AprilTags can serve as markers to overlay digital content accurately on physical objects or surfaces.
- Object Tracking: AprilTags can be attached to objects to facilitate tracking in computer vision systems. This is useful in scenarios such as motion capture, inventory management, and interactive installations.
- Calibration: AprilTags are used in the calibration of cameras and other sensors. They provide a reliable reference for determining the geometric properties of a camera setup or even the equivalent pixel-surface conversion.

AprilTags are an effective and versatile tool for computer vision applications requiring robust detection and precise localization. Despite some limitations related to visibility and environmental constraints, their ease of use and open-source nature make them a popular choice for both research and practical applications.

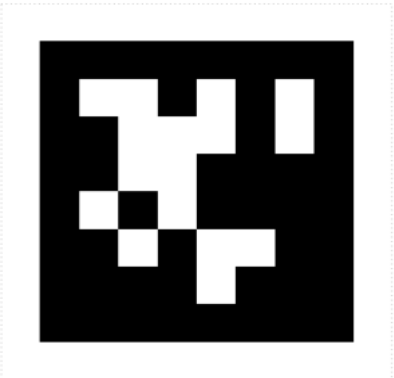

Figure 7. Example of an AprilTag with ID equal to 0.

3 Laboratory-scale phenotyping test with 3D sensor

3.1 Aim of the Experiment

This study was conducted to develop a single frame top-view analysis to predict the fresh weights of one of the most popular species for RTE salads that is the Romaine lettuce (*Lactuca sativa L. cv. 'Longifolia'*) at different growth stages using two different image processing methods, i.e., morphological analysis (for RGB-D images) and pixel-value analysis (for RGB images) done with a low-cost 3D sensor Microsoft Kinect V2.

The goals of this experiment are to advance understanding of the use of RGB-D sensors to characterize individual plants to accurately estimate their biomass in a controlled laboratory environment, with potential for future field applications. Furthermore, the algorithm must be optimized to ensure that the execution time will be fast enough to be usable in field applications.

The contribution of this technology, along with the implementation of an innovative, simplified voxelization-based reconstruction method, will be assessed by comparing its results with those obtained using a commonly employed method for estimating biomass weight based on RGB images, specifically the top-view projected area approach. This comparison aims to evaluate the effectiveness of the simplified volumetric reconstruction technique in estimating plant biomass.

3.2 Material and Methods

3.2.1 Plant Management

A total of 100 Romain lettuce (*Lactuca sativa L.* cv. '*Longifolia'*) plants were cultivated in a greenhouse at the Department of Agricultural and Environmental Sciences of the University of Milan (Italy) under controlled conditions at 24/20°C day/night temperature, with 60-75% relative humidity and 16 h photoperiod. One week-old plantlets were transplanted in 0.1 m diameter plastic pots on a peaty substrate, regularly watered and fertilized until reaching a predefined growth stage (from 3 leaves up to more than 20 leaves), to obtain a set of plants with a wide range of variation in

size and biomass. Among all the plants only 70 were selected and transplanted for the measurements based on their regular shape and healthy appearance of lettuce plants aimed to the RTE chain.

Immediately after image acquisition, the plants were destructively harvested to determine the dry matter weight of the leaves (DM). Leaves were cut at the height of the plant collar and the dry weight of the biomass was determined by drying the plants material in an oven at 105° until reaching a constant weight and then measured with a precision weighing scale (50 g ± 0.001 g).

3.2.2 Data Acquisition

The Kinect V2 sensor was employed during the tests to estimate the growth vigour of the seedlings. In this study, color and depth images of lettuce were acquired in an experimental cabinet under light-controlled conditions. To reduce the complexity of the color segmentation a black background was used to reduce the disturbance. Sensor is positioned perpendicular and near to the growth axis of the plant at 1 m to the pot base. The acquisition setup is shown in Figure 8.

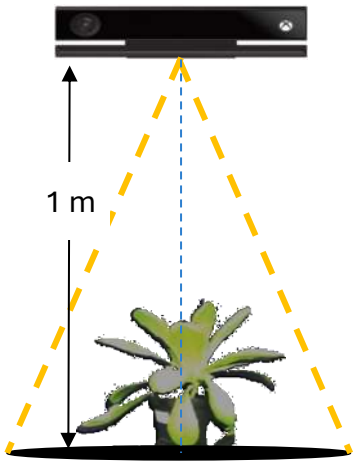

Figure 8. Laboratory scale RGB-D top-view acquisition setup.

3.2.3 Foreground Segmentation

First, both methods require to segment the foreground (plants) from the background (rest of the image), and this was done by calculating the excess green index (ExG) at single pixel level. Distance was not used in this trial to carry out the segmentation process because some leaves fell to the side of the pot and to avoid overlooking some of them or even segmenting parts of the pot or growing medium, it was decided to use colour as the main feature. This is achieved by multiplying the green component of the RGB image by two and subtracting the red and blue components thus highlighting the green component of the image. In this case it was not deemed necessary to carry out a colour normalization given that the lighting conditions and the acquisition setup ensured homogeneous conditions in the different acquisitions.

$$ExG_{(x,y)} = 2 \cdot G_{(x,y)} - R_{(x,y)} - B_{(x,y)}$$

This converts the RGB image to a grayscale one that contains the ExG index information. The segmentation is performed by calculating a threshold and all the pixels that have an ExG value greater than this are considered as foreground. The threshold is determined using the Otsu's method. This method is useful for calculating a threshold value capable of separate a bimodal distribution or better the values of predominantly green pixels of the plants from the rest of the background pixels. To segment the color image and obtain a binary or logical array, (Color Mask) containing set as *'true'* (1) only pixels that have an ExG value higher than the set threshold. Below is reported the pseudocode used for generating the color mask and an example of a color image and the related color mask. Colorimetric segmentation is useful for both segmenting 2D and 3D images.

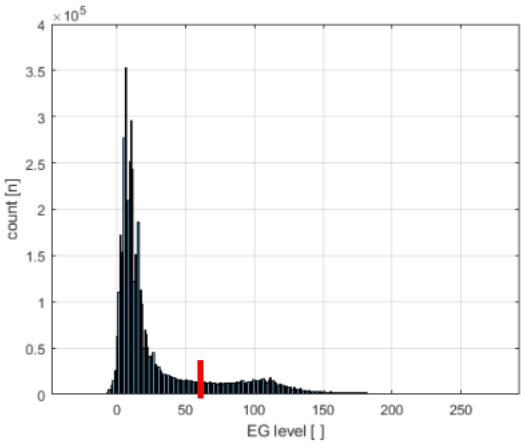

Figure 9. Single pixel ExG value distribution. The red line indicates the threshold determined with the Otsu's method.

```
Input 1: ExG image
Input 2: Threshold value
Output: Color Mask

for each pixel in image
 if ExG(x,y)> Threshold
      ColorMask(x,y)= 1;
 else
      ColorMask (x,y)= 0;
 end
end
```

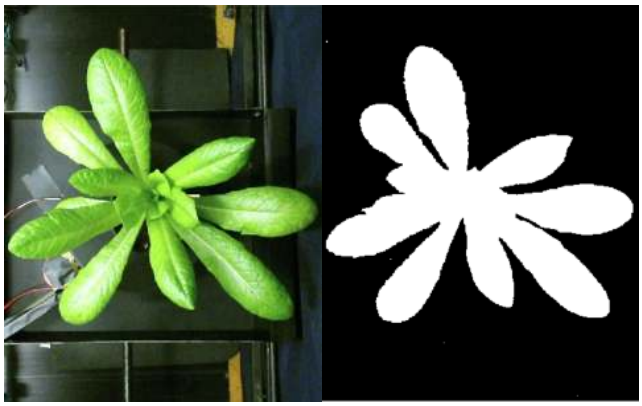

Figure 10. Color-based segmentation process. On the left: color segmentation pseudocode; on the center: RGB image captured with Kinect V2; on the right: binary mask used for plant segmentation.

3.2.4 2D Projected Area Measurements

To calculate the leaves top-view projected area by RGB images it was necessary first to eliminate lens distortion, carry out a geometric calibration and then convert the number of pixels segmented as vegetation in m^2 of surface.

To correct the lens distortion, the MATLAB Camera Calibrator app was employed. This application is designed to estimate the camera's intrinsic parameters and correct lens distortion by processing a series of at least twenty images featuring a special chessboard pattern (shown in Fig. 11), which can be downloaded and printed for this purpose. The chessboard must be fully visible in the images, and the photos should capture the pattern from various distances and angles relative to the camera. The app automatically detects the edges of the chessboard squares, enabling it to estimate the lens distortion. The result of this process is a calibration variable that can be applied to rectify images captured afterward.

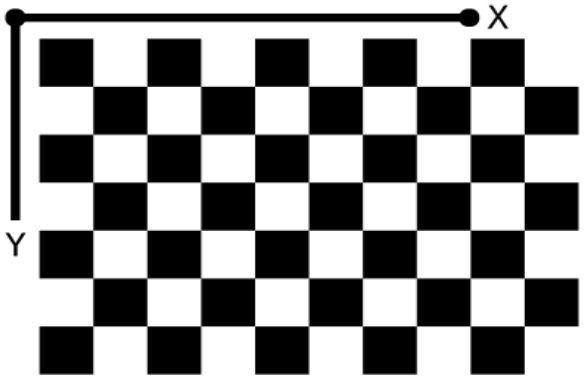

Figure 11. MATLAB camera calibration App checkboard pattern (with dimension of 7 by 10 squares).

After correcting for lens distortion, converting pixel count to surface area requires positioning the calibration pattern at the level of the pot's soil. Once the image is captured and distortion corrected, each individual square of the checkerboard pattern is segmented to count the number of pixels within it. The conversion factor (m^2/pixel) is then calculated by dividing the known area of a square by the number of pixels counted and averaging the results across all squares. This conversion factor is subsequently used to estimate the projected leaf area by multiplying the number of plant pixels segmented in each binary image by the conversion parameter, thereby converting the pixel count into m^2.

$$KConv = \frac{\sum_{i=1}^{n} \frac{square\ Area}{N\ Pixels_{(i)}}}{n} \quad \left[\frac{m^2}{pix}\right]$$

$$Projected\ Leaf\ Area = Segmented\ Pixel\ \cdot Kconv \quad [m^2]$$

3.2.5 3D Volumetric Object Reconstruction

As happens in RGB imaging, where a single pixel represents a little square of a bidimensional array, in RGB-D imaging, voxel is used as a single representable element, identifiable as a little cube with his volumetric and surface extension property. An accurate 3D plant model can be obtained by several different techniques but unfortunately none of these is sufficiently fast to provide a high-throughput system (Golbach F., et al. 2015) and moreover these techniques require a setup that cannot be used in operating conditions because of their complexity and size and because they often use a turntable or multiple sensors to acquire different views of the object and this can be difficult to use in the field (Rose et al., 2015; Golbach et al., 2016).

The objective of this section is to process RGB-D data to develop a volumetric model of the plant that can deliver a sufficiently accurate estimation of the dry matter from a single top-down frame. This approach aims to enhance the accuracy of biomass estimation compared to methods relying solely on RGB images.

After the color-based segmentation, the first step to work with RGB-D images was to filter the data and eliminate outliers due to measurement inaccuracies and to this aim a gradient filter was applied. This filtering method was chosen because it is more efficient in terms of calculation time compared to a filter based on point cloud density. For this purpose, the depth image gradient magnitude (see Fig. 12 on the left) was calculated with a Sobel gradient operator. The gradient of a pixel is a weighted sum of pixels in the 3-by-3 neighborhood. Data are considered outliers if the pixel gradient is above a certain threshold.

$$\text{Sobel Operator} = \begin{vmatrix} 1 & 2 & 1 \\ 0 & 0 & 0 \\ -1 & -2 & -1 \end{vmatrix}$$

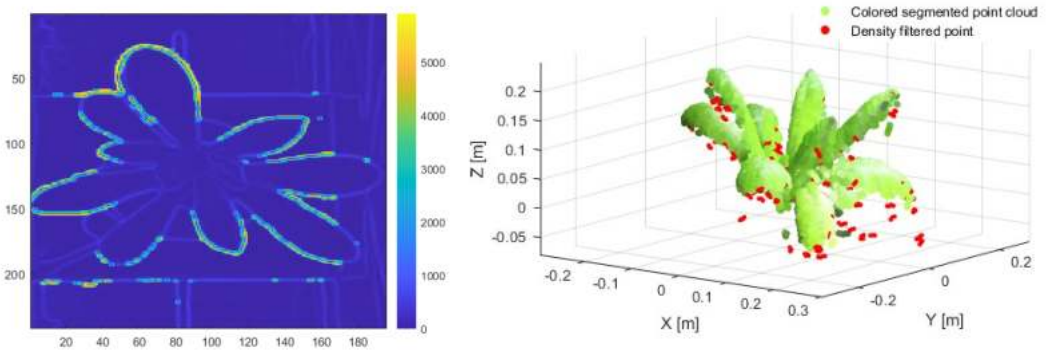

Figure 12. Gradient magnitude filtering example. On the left: depth array gradient magnitude; on the right: example of points filtering based on gradient magnitude. The points highlighted in red are filtered with this method.

The reconstruction method employed in this work can be described as an approximation using a voxel structure. It focuses on generating a simplified but representative volumetric model of the plant rather than an exact three-dimensional reconstruction. The primary aim is to create a model that provides a reliable estimate of dry matter. A significant feature of this algorithm is its ability to approximate the reconstruction of plant parts that are not visible from the top view.

The method comprises two variants, each tailored to accommodate the shape of the leaves of the plants being studied. In this instance, leaf bending compensation was employed due to the plants being grown in small, single pots. The limited diameter of these pots led to pronounced downward bending of the leaves, particularly in the more developed samples. This meant that the leaves could fall partially below the ground level while in open field conditions this does not happen and the rectification phase with this species of plant is not necessary as was done in the case of the field application of this method (see Chapter 4).

After filtering the raw data, the further step involves the determination of the centroid of the plant projected onto the ground plane. This is achieved by calculating the mean value of the X and Y coordinates of all points that belong to the plant.

$$X_{Centroid} = \frac{\sum_{i=1}^{n} X_{plant}}{n}$$

$$Y_{Centroid} = \frac{\sum_{i=1}^{n} Y_{plant}}{n}$$

$$Z_{Centroid} = 0$$

The rectification process is useful for reducing complexity and optimizing the subsequent reconstruction operation in case it is necessary. The rectification process consists of replacing the Z value of each point with the Euclidean distance from the to the centroid of the segmented plant point cloud. In this section the rectification process will be used because in this case the bending phenomenon is due to the small size of the pots used, which meant that the leaves could partially fall below the level of the ground while in the open field, with plants of this cultivar, the rectification step is not necessary as in the case of the field experiment in Chapter 4.

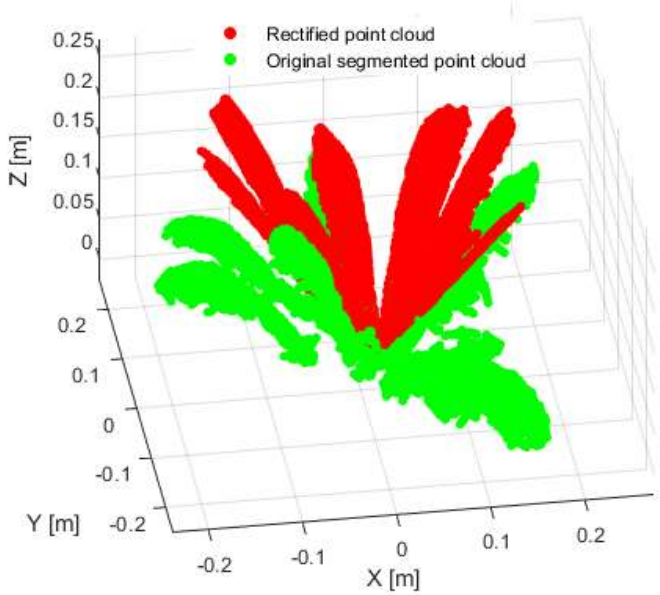

Figure 13. Example of point cloud rectification process result. In green is shown the raw point cloud of the plant before rectification and in red is reported the same point cloud after the rectification process.

The next step concerns the preliminary volumetric object representation (PVO) of the plant point cloud (rectified or not). To this aim it's necessary to compile a three-dimensional logical array (known also as binary occupancy grid) which represents the grid used for the reconstruction of the volumetric objects. Every cell in this array represents a single voxel and is set as *'true'*, hence "materialized", if it contains at least one point in the point cloud. In this case, given the resolution of the sensor, the density of the points and the size of the objects that will be represented as well as the processing time needed, a grid resolution of 5 mm (mesh size) was chosen,

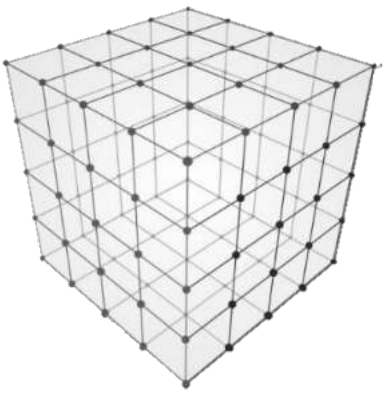

Figure 14. Example of a 3D binary occupancy grid.

so each voxel used for volumetric reconstruction has a volume equal to 125 mm^2 which is equivalent to a cubic mesh with 5 mm on each side.

To construct the logical array, a conversion between the Cartesian coordinate system used by the point cloud and the array indices was performed. This conversion involves dividing the distance from the minimum value of each axis by the mesh step size and rounding the result to the nearest integer, as illustrated below.

```
Input 1: segmented point cloud
Input 2: minimum value for each axis(X-Y-Zmin)
Input 3: mesh size
Output: Preliminary volumetric object (PVO)

for all points in segmented point cloud
  X(i)= ceil((XPc(i) - Xmin)/mesh size);
   Y(i)= ceil((YPc(i) - Ymin)/mesh size);
    Z(i)= ceil((ZPc(i) - Zmin)/mesh size);
     PVM(X(i),Y(i),Z(i)) = 1;
end
```

Figure 15. Preliminary voxelization object (PVO), algorithm pseudocode.

Additionally, a filter based on minimum region size equal to 10 voxels was applied. This size filter helps to address issues such as disturbances and imperfect distance detection that can lead to multiple contiguous regions in the reconstruction. By considering only the most consistent voxel regions, the filter enhances the accuracy of the reconstruction process.

Below, in Figure 16, an example of the preliminary volumetric reconstruction of the object without rectification and reconstruction is displayed. On the left is shown a top-view of the object, and on the right its side-view. The red-highlighted point indicates the location of the plant's collar. This illustration demonstrates that the initial reconstruction captures only the portion visible from the top but fails to reconstruct the parts that are occluded from this view. Consequently, as the plant size increases, there will be a greater underestimation of the internal biomass of the lettuce head. This limitation also illustrates the shortcomings of using two-dimensional images, which lack depth information.

The last step of the algorithm involves the reconstruction procedure of the volumetric object (RVO) - aimed to reconstruct also the occluded parts - requires that each voxel that was generated in the first reconstruction phase (PVO), compile as *'true'* all the

voxels that lie in the joining segment between the latter and the voxel in which the centroid is located, if not already compiled. The volumetric reconstruction of the parts occluded in the view from above assumes that leaves develop from the point where the plant emerges from the ground. During the volumetric reconstruction process, the algorithm generates voxels that tend to converge at the point where the plant emerges from the ground (collar), reconstructing in a simplified manner the volumes occupied by the plant in terms of both height above ground and width of the individual leaf blades.

The reconstructed volumetric object (RVO) obtained in this way is eligible to be depicted with the specific MATLAB *volshow* functions and its volumetric features can be evaluated with the function *regionprops3*. This function measures a set of properties, such as volume, surface, centroid and other geometrical features for each connected component in the volumetric object.

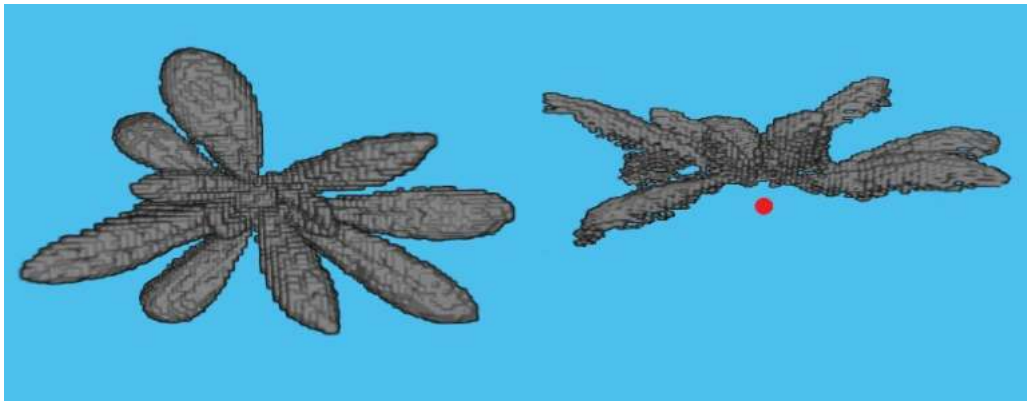

Figure 16. Preliminary volumetric object. On the left top-view. On the right: side-view of the same object. In red is indicated the place where the plant's collar is located. This view serves to highlight the lack of several plant parts that are occluded in the top-view.

```
Input 1: Preliminary volumetric object (PVO)
Input 2: Centroid position index (Cpi)
Output: Reconstructed volumetric object (RVO)

Cpi(1)= ceil((XCentr - Xmin)/mesh size);
Cpi(2)= ceil((YCentr - Ymin)/mesh size);
Cpi(3)= ceil((ZCentr - Zmin)/mesh size);

for all PVM voxels
 if PVO(X,Y,Z)==1
  for each voxel in the PVO(X,Y,Z) → Cpi joining segment
   if RVO(X,Y,Z)==0
    RVO(X,Y,Z)=1;
   end
  end
 end
end
```

Figure 17. Pseudocode of the last step of the reconstruction algorithm.

3.3 Results

The 70 plants of lettuce considered in this study have a dry weight (DM) ranging from 0.1 g to 3.05 g with a mean value of 1.29 g.

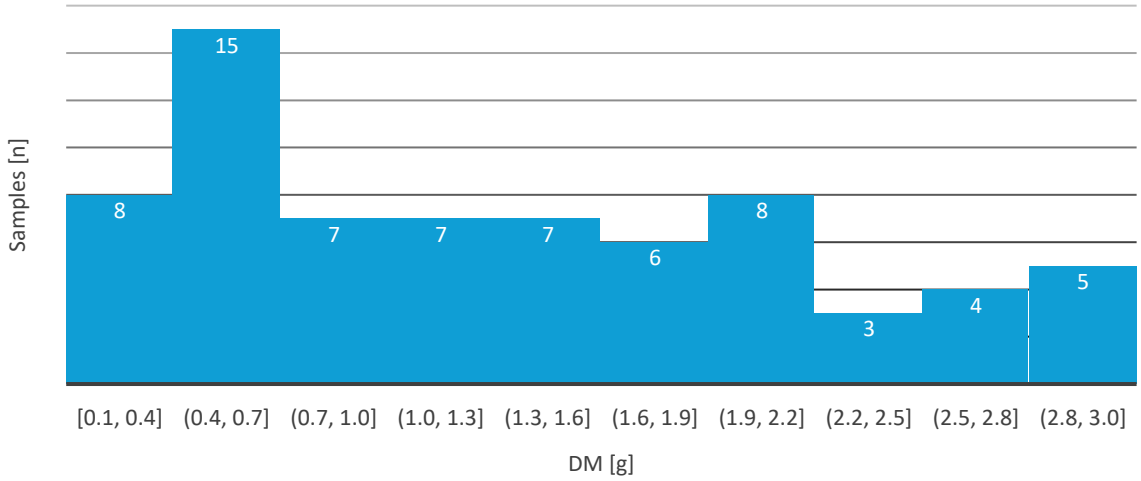

Figure 18. Samples characterization with frequency distribution.

Figure 19 displays the result of the volumetric reconstruction process, offering both top and side-views to highlight the reconstruction of occluded parts near the plant collar. The inclusion of the leaf position rectification process is evident, enhancing the model by addressing areas previously obscured. The top-view demonstrates the surface details, while the side-view reveals the depth and vertical structure, showing the improvements made in capturing the full volume of the plant.

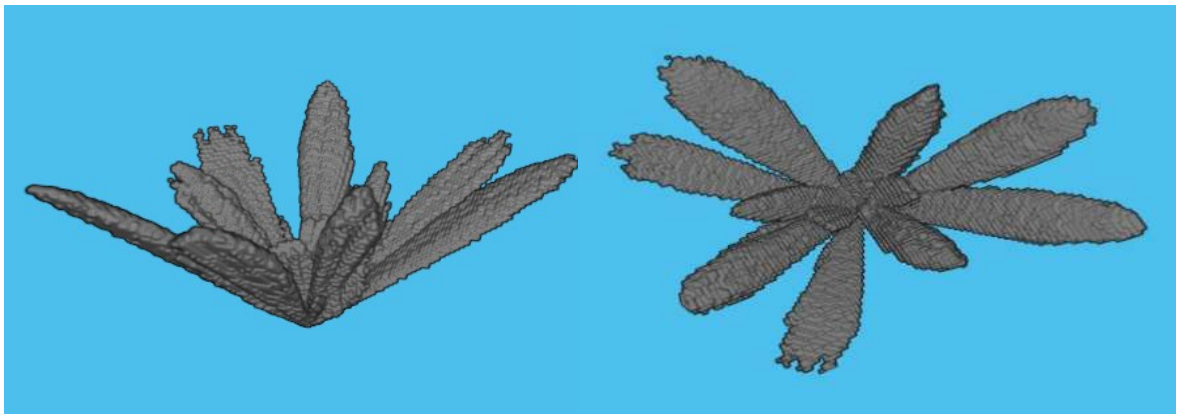

Figure 19. Result of the volumetric reconstruction process. On the left: volumetric object side-view; on the right: volumetric object top-view.

The two methods examined yielded distinct results. The RGB imaging-based approach delivers satisfactory outcomes, particularly for small plants, where the estimation error for DM is minimized. However, as plant size increases, the estimation error also increases (see Fig. 20c). This trend is corroborated by the correlation line slope of

0.059, indicating that the error grows with the plant size due to the increasing occlusion of plant parts. The model showed a correlation index of 0.89, a root mean squared error (RMSE) of 0.27 g and the mean absolute percentage error (MAPE) of 18.3%. The method that uses volume to predict the DM gives better results, especially about plants with larger dimensions which are also the most difficult to evaluate. The second method based on volumetric object showed - in this case - a correlation index of 0.98, a root mean squared error (RMSE) of 0.12 g (-55% compared to the RGB imaging) and the mean absolute percentage error (MAPE) of 12.3% (-33%). The estimation capabilities remain almost constant even in the largest plants and this is confirmed by the slope of the correlation line in Figure 20c which is equal to 0.008.

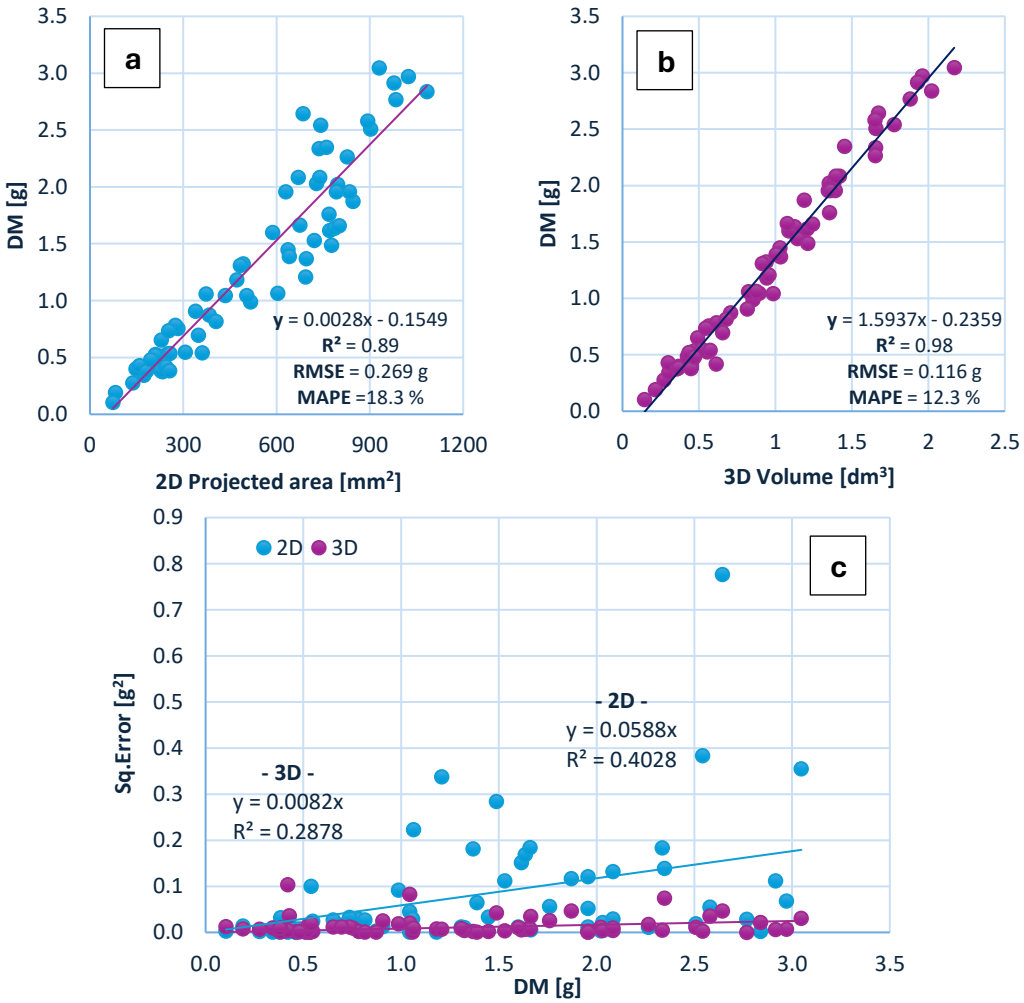

Figure 20. Results of plant DM estimation. Correlation lines of DM estimation with the 2D method (a) and the 3D method based on volumetric reconstruction (b). The 3D method is a better estimator with a determination index of 0.98, the significantly lower RMSE and MAPE values demonstrate the capability of the simplified reconstruction method to estimate the DM. c) The estimators error with samples size. The estimators error tends to increase with sample size for the 2D method while this not occur with the volumetric based method.

3.4 Research Objective Achieved

In this experiment, a key objective was accomplished: achieving accurate biomass estimates using a three-dimensional data-based algorithm, while maintaining a rapid execution time (less than 1 s) and utilizing a single RGB-D image captured from a top-down view. To conclude, the potential of the algorithm is highlighted by presenting results from the reconstruction of plants with more developed and complex structures. Figure 21 illustrates that the algorithm effectively reconstructs the plant structure, particularly the occluded parts. Even when only the tips of the basal leaves are visible from the top-view, the algorithm successfully reconstructs the full structure of the leaves.

Therefore, the algorithm demonstrated at the laboratory scale is planned for implementation in field applications, with further details available in Chapter 4.

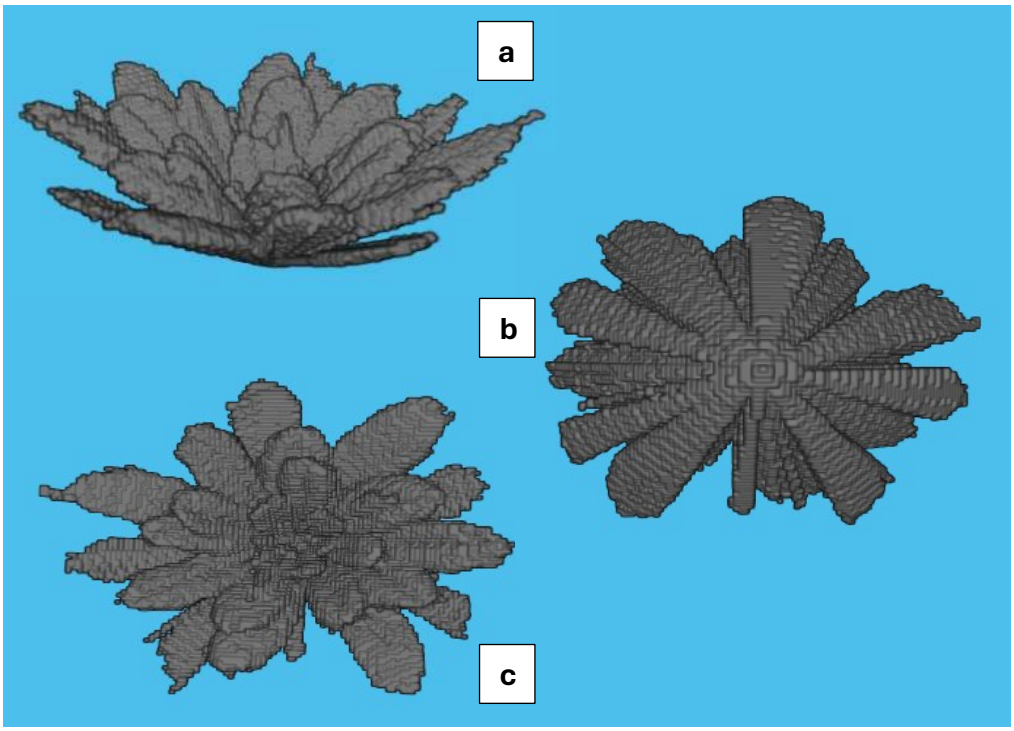

Figure 21. Example of volumetric reconstruction of a sample with a large size and number of leaves. A) side-view, C) top-view. B) bottom-view. In this view, it is possible to appreciate the reconstruction of the parts closest to the plant's collar, with the reconstruction algorithm the entire leaf structure is approximated, even those that are only partially visible from the top view.

4 Field-scale Application phenotyping on Lettuce Plants

4.1 Aim of the Experiment

The study was conducted within the framework of the Mind Foods Hub project, sponsored by Lombardy Region (institution of the Lombardy region, Italy) as part of its rural development plan (PSR). The project involved the Departments of Agricultural Engineering and Computer Science at the University of Milan, with technological support from TIM S.p.A. The field phenotyping experiment had several objectives.

The first objective was to use a robotized platform capable of autonomously navigating the environment and serving as a vehicle for conducting data collection missions on a crop.

The second objective was to employ known spatial references (AprilTags) to optimize the merging process of various point clouds acquired during the trial. This step aimed to refine the rover's positioning, allowing for the identification of experimental units and, consequently, individual plants, thereby monitoring their development over time.

The third objective was to verify the field applicability of the non-destructive biomass estimation algorithm previously discussed in Chapter 3. This algorithm involves a simplified volumetric reconstruction of plants using RGB-D images captured from a top-view perspective.

The fourth objective focused on the potential use of a high-speed network infrastructure (5G) to transmit data directly from the field, enabling data lake remote storage. This capability allows for cloud-based analytics and remote consultation of key parameters characterizing the monitored crop, such as growth rate, uniformity of development, and meteorological data, all accessible through a dedicated application.

4.2 Materials and Methods

4.2.1 Plants Management

The plantlets used in the experiment were transplanted into the plastic-film tunnel greenhouse at the University of Milan experimental farm located in Cornaredo, Milan (Lat. 45.502499, Lon. 9.015419). The experimental protocol involved cultivating two different head-forming lettuce varieties, Salanova cultivars, distinguished by different leaf pigmentation (green and red). For each cultivar, two plots were prepared, each comprising 8 replicates. One of these plots was fertilized with a higher dose by adding a complex granular NPK formulation enriched with micronutrients at a rate of 7 g per head during transplanting. This fertilizer was placed directly in the hole where the seedling was transplanted. The other plot received a lower dose, half that of the first. Each squared plot measured 1.5 m per side, with a planting distance of 0.5 m by 0.5 m. The arrangement of the plants within the plots is shown in Figure 22. A centrally located AprilTag visual marker (*family '36h11'*) was placed to uniquely and automatically identify each individual plot through RGB image analysis. In this case, the marker also served as a fiducial point to enhance the positioning accuracy of the rover and optimize the spatial aggregation (stitching) of the various RGB-D images during post-processing and additionally, it enabled the precise identification of individual plants by associating them with a unique ID.

Prior to transplanting the plantlets, a black mulching cloth was applied to the experimental area to prevent the growth of weeds that could have hindered the crop's development and made the identification of individual plants more challenging and less accurate. Given that this experiment represents an initial trial of the applied methodologies, it was decided to address potential issues

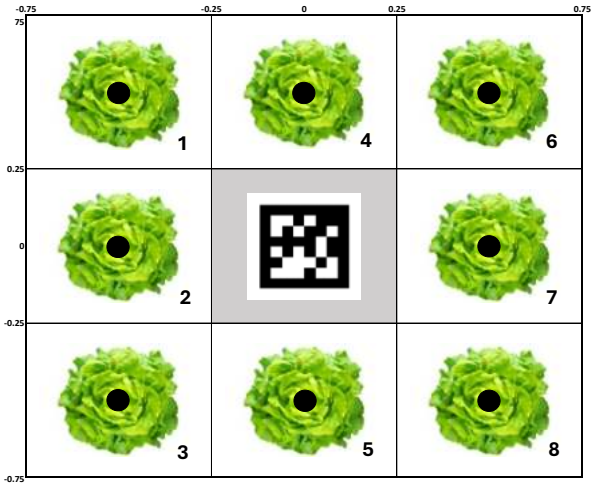

Figure 22. Arrangement of plants within plots, the marker is centrally located. Each plant is identified by the id indicated on the side.

individually to ensure a controlled and effective evaluation.

The experimental protocol involved data collection at four time points over a 20-day period. The first acquisition was conducted at the time of transplanting, followed by subsequent monitoring missions at 5, 12, and 20 days after transplanting. The experiment concluded on November 22 with the harvest of the lettuce heads. Immediately after harvesting the individual heads were weighed. They were then placed in an oven at 105°C until a constant weight was achieved to evaluate the DM.

4.2.2 Autonomous Vehicle

The AMR rover UNIMI used in this experiment is a prototype specifically designed by InfoSolution for the Department of Agricultural and Environmental Sciences (DiSAA) at the University of Milan. The rover features a base platform measuring 1.19 by 1.23 by 0.53 m and weighs 250 kg. It is a rubber-tracked, electrically powered vehicle with differential propulsion, driven by two electric motors with a maximum power output of 7.5 kW. The rover is powered by lithium-ion batteries with a nominal capacity of 8.8 kWh, which are sufficient to provide approximately 8 hours of operation or 40 kilometers of travel under the experimental conditions characterized by moderate power demands and reduced speeds.

The rover's base has a load capacity of up to 400 kg. On this base, a truss structure has been installed, allowing for two distinct operational configurations. The first is a horizontal configuration with the lateral arm extended, which is suitable for tasks such as monitoring herbaceous crops. This configuration enables the rover to access plots arranged laterally, extending up to approximately 2.6 m from the center of the track. The second configuration is vertical, with the lateral arm retracted, which is designed for monitoring vertical surfaces, such as tree crops or plants grown in rows.

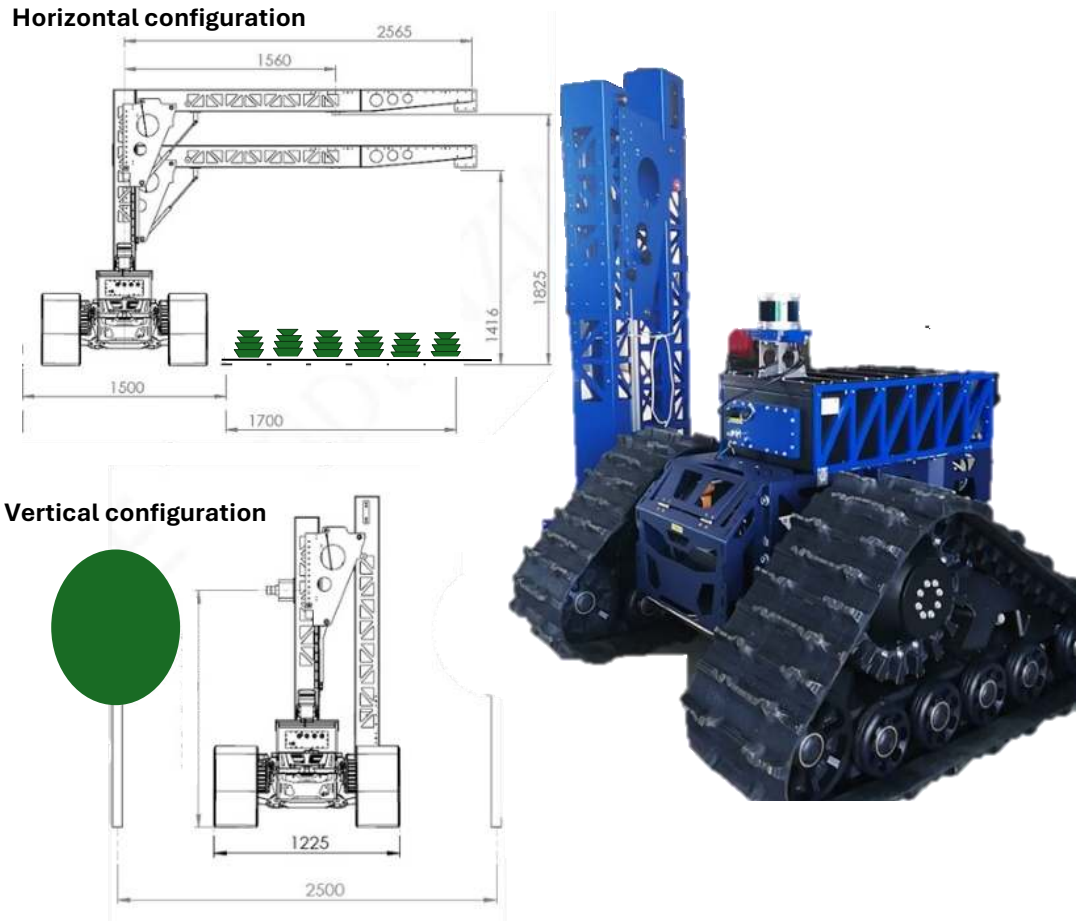

Figure 23. Different UGV configurations. The variable height horizontal configuration is useful for acquiring data with different sensors in the case of horticultural crops. The vertical configuration is designed to operate within tree-row crops such as vines.

The rover can operate in both manual and automatic modes. In manual mode, the rover is controlled via a remote controller. This controller shows the status of the radio connection with the robot, the radio channel being used, the battery levels of both devices, and the selected gear (1-4). The remote control also serves as a safety system, featuring an emergency stop red button (see Fig. 24) to immediately stop the rover if it becomes uncontrollable, thus preventing potential hazards due to the significant mass of the equipment. Given its critical safety function, maintaining constant radio contact is essential; the rover will automatically stop if it loses connection with the remote control to ensure that the emergency stop function remains operational. For safety reasons, an operator must always be present while the rover is in

Figure 24. Manual controller and safety device used of the UGV.

operation, keeping the remote control within reach. In manual mode the navigation unit, used for autonomous navigation, is disabled and which also disables the obstacle avoidance and collision prevention features. Consequently, the operator must carefully maneuver the rover, exercising increased attention.

The autonomous navigation mode is managed by the navigation unit, which estimates the rover's position within a map of the workspace. This technique integrates data from various sensors, including a LiDAR, encoder feedback from the tracks, and an Inertial Measurement Unit (IMU) that estimates the orientation in space and acceleration of rover. The LiDAR device, detailed in Figure 26b, is the CX32 model from LsLiDAR. It performs circular scans with a sampling frequency of 327,680 Hz, providing a 360° field of view across 16 horizontal planes with an angular range of ±15° and a maximum range of 50 m. However, part of the sensor's field of view has been excluded or disabled to prevent the navigation system from detecting certain components installed on the rover, such as the vertical support, the lateral arm or parts of the rover itself as obstacles. Additionally, given the geometric characteristics of the sensor's field of view, as illustrated in Figure 26a, detecting obstacles in very close proximity to the rover could be challenging.

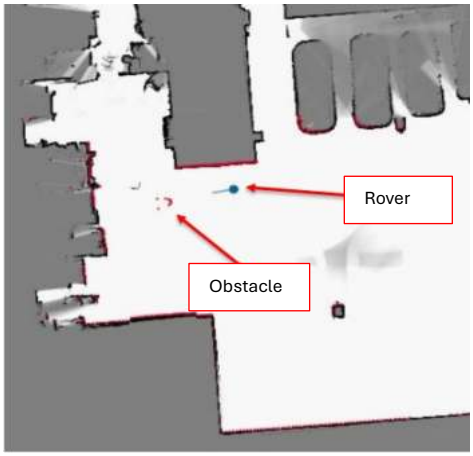

Figure 25. Example of navigation within a map. The rover uses the SLAM method and obstacle detection to avoid obstacles during autonomous navigation missions.

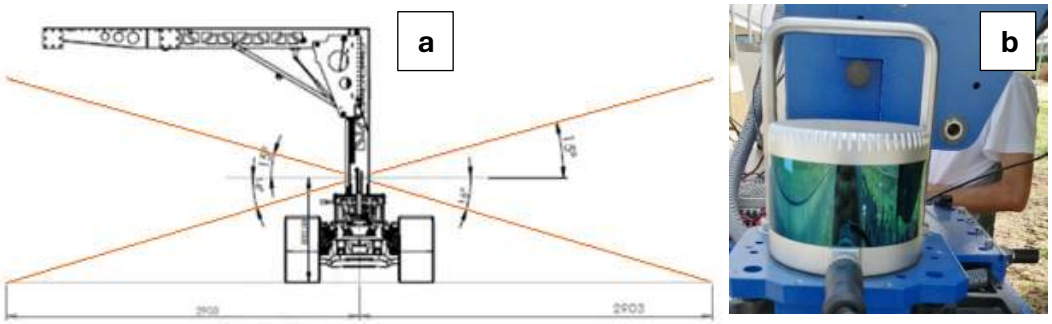

Figure 26. LiDAR sensor (b) and its field of view angle (a).

The localization system relies on measurements taken by the LiDAR, which scans the surrounding space to detect objects within the work environment and determine their

distance and spatial arrangement relative to the vehicle. This spatial characterization is used by the navigation system to estimate the rover's position by searching for geometric patterns within the mission site's map, which was created during the initial manual navigation phase. During autonomous navigation, the LiDAR helps identify obstacles along the rover’s path and calculates an alternative trajectory to enable the rover to reach the next waypoint while avoiding the detected obstacles.

The management software "MOLIRIS" is installed on a Laptop that serves as the Master or Ground Control Station (GCS). The GCS is essential for managing the rover's operations and features a graphical interface that allows users to create, modify, export, and save various mission profiles and maps. The GCS maintains constant communication with the rover via a Wi-Fi connection. It interacts with the two main units installed on the robot: the Mission Unit, which oversees the rover's actions during mission execution, and the Navigation Unit, which supports the Mission Unit by generating trajectories and avoiding obstacles. On the rear part of the rover’s base, there is an antenna for Wi-Fi signal reception. This antenna enables the rover to connect to the Ground Control Station (GCS) via a fixed IP address, which is known to authorized operators. This setup allows for unique identification of the rover's network card. Interaction with the rover is facilitated through a standard web browser by entering the rover's IP address and connecting to the Wi-Fi network generated by the rover upon startup. The 5G router was interfaced with the rover and positioned at the top of the vertical support arm to facilitate the transfer of sensor data directly from the field to a dedicated data lake. This virtual storage space was created for this purpose by researchers from the Department of Computer Science at the University of Milan.

Figure 27. User interface for the control of the rover (Moliris by InfoSolution).

4.2.2.1 Workspace Occupancy Map

Before the rover can operate in autonomous navigation mode, it is necessary to create a map of the environment in which it will operate. This mapping phase is conducted by manually driving the rover and relies on the SLAM. During this phase, the LiDAR sensor performs continuous scans allowing it to assess the rover's relative position with respect to structural elements in the surrounding environment. The operator manually pilots the rover, executing straight-line trajectories at reduced speeds and performing rotations around the Z-axis near critical areas to increase its sampling quality. The repeated scans are then incrementally added to previous scans, generating the map. This process is facilitated by the fusion of data from encoders, the IMU, and the rover's relative position estimation. The rover's position is continuously updated according to this principle, enabling the reconstruction of a scaled map of the entire workspace within a few minutes. The map is defined as an occupancy grid map, which is a regular mesh where each cell represents an area of 0.05 m per side and can be compared to a scaled image of the two-dimensional floor plan of the vertical surfaces in the environment. Each pixel in this image is filled with information about the probability whether there is an element at that point that could obstruct the rover's movement with ‘uint8’ format. White areas, those with a value of 255 on the map, identify obstacle-free zones where the rover can navigate freely, while black areas, those others with a value of 0, represent fixed obstacles or structured elements that the rover must avoid during its missions. Gray areas represent regions with varying probabilities of being transitable, ranging from 254 to 1 and values are considered by the Navigation Unit when generating trajectories.

The accuracy of rover positioning, especially the initial localization which is the most critical and is significantly improved when the geometric features of the surrounding environment are asymmetric. This allows for unique characterization of the map footprint and ensures that the surfaces of detected structures have good reflectance for accurate distance measurement.

In this study, to address the challenges of positioning in the highly symmetrical rectangular environment of the greenhouse tunnel, additional geometric elements were added to the tunnel structure to optimize rover localization.

These additional elements consisted of rigid panels made of materials with good reflectance properties, such as white plastic panels arranged to create rectangular and square shapes. Smaller objects, such as sections of PVC pipes, were also used to create circular reference points, enhancing the number of landmarks available for localization. These supplementary elements were strategically placed within space to uniquely characterize the environment, fixed to the greenhouse structure at a height that would not obstruct the rover's passage, as shown in Figure 28. The result of the mapping phase is an image in *'.jpg'* format, which can be downloaded and further edited in post-processing using any image editing software according to the user's preferences.

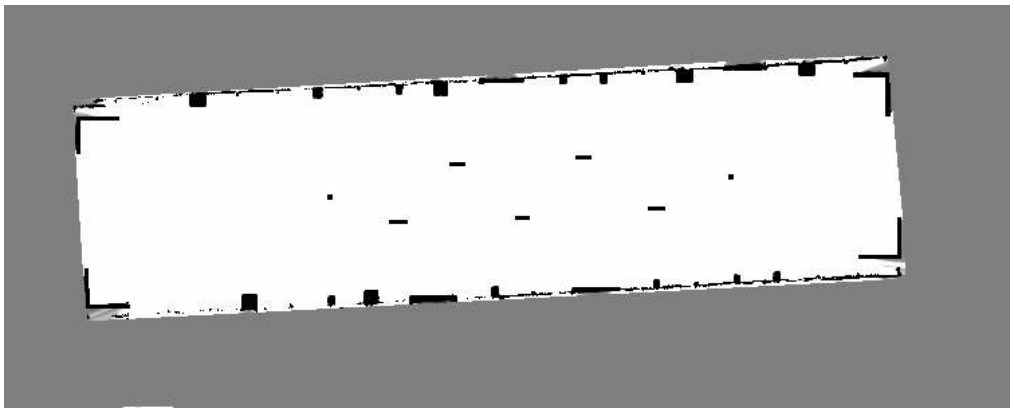

Figure 28. Example of a rover workspace occupancy map. In black are indicated the areas where obstacles are present while in white are the areas where the rover can generate trajectories and navigate autonomously. The additional elements arranged asymmetrically appear as black clusters on the side of the map.

4.2.2.2 Mission planning

After the map is created, the next phase involves programming one or more mission profiles within the map using the GCS. Through this, the user can generate, modify, or delete a mission profile. Each mission is composed of a series of waypoints that can be inserted into the map, and these waypoints correspond to four different types of tasks:

- Mission Waypoint (blue marker): This indicates a position where the rover must stop for a certain period or until a specific operation is completed. In this experiment, this type of waypoint was used to perform data acquisition and data transmission tasks.
- Transit Waypoint (green marker): This represents a position where the rover is required to pass through at a certain speed without stopping. This type of

waypoint is useful for directing the navigation unit to generate specific trajectories that might not be created solely from mission waypoints.

- Park Waypoint (yellow marker): This indicates a position on the map where the rover will halt and wait for feedback before proceeding to the next waypoint.
- Switch Waypoint (purple marker): When the rover reaches this position, it switches to another map or mission. In this case, it is necessary to define the map and mission that the robot will undertake next.

These waypoints are essential to guide the rover's movement and ensure that it completes the tasks required for each mission.

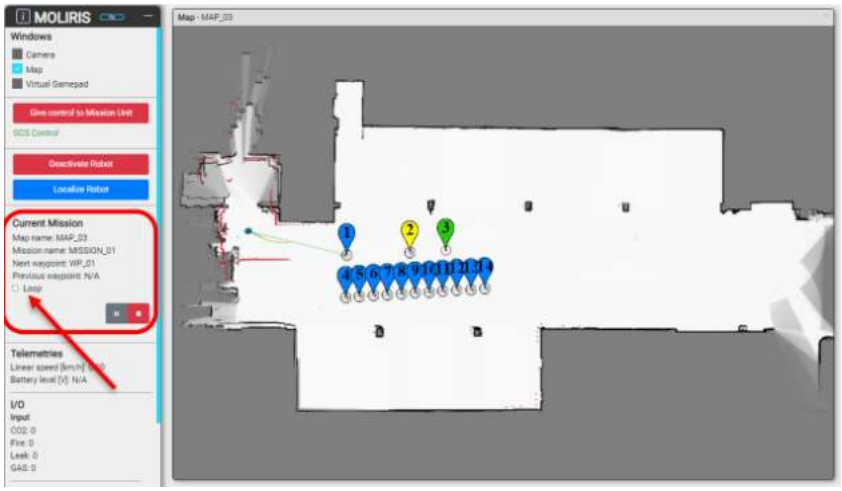

Figure 29. Example of the creation of a mission profile through the GCS.

In this experiment, the mission waypoints were strategically placed near the points where the rover needed to perform data acquisition procedures. To ensure comprehensive coverage of the RGB-D data across all four plots located in the central area of the greenhouse, six waypoints were planned for each plot: three on the left side and three on the right side (see Fig. 30). This arrangement was designed to allow the rover to adequately visit and capture data from each plot, ensuring thorough monitoring and accurate data collection.

The mission is designed for the rover to start from a homing station, which serves as the initial position from where it is launched and where the first localization within the selected map takes place.

After establishing its initial location, the rover proceeds to reach all the waypoints in the predetermined order, advancing at a defined speed of 1 m/s.

It pauses at each waypoint for the necessary time to acquire RGB-D data. The mission concludes with the rover returning to its initial homing position. At the end of the mission, the newly acquired data is sent via the network to a remote data lake.

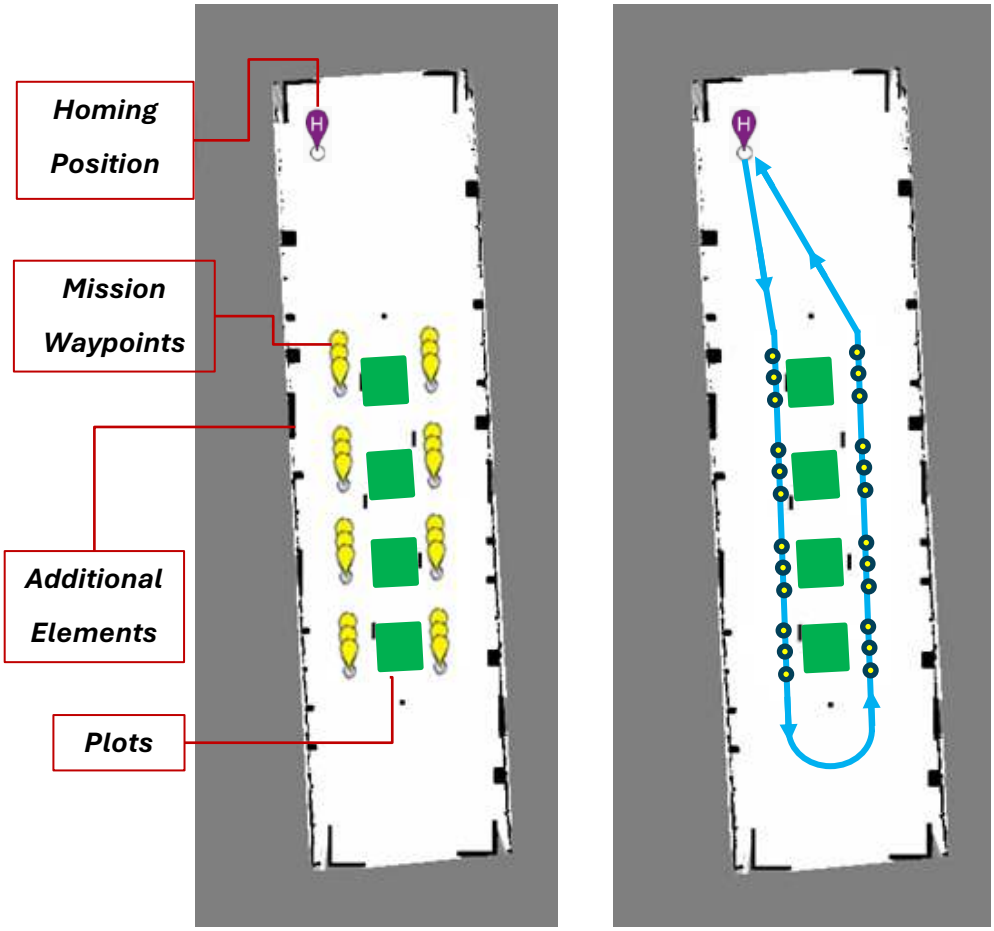

Figure 30. Graphical representation of the data acquisition mission performed by the rover. The green squares indicate the areas of the experimental plots. The points showed in yellow indicate the waypoints where the rover performs a single acquisition of an RGB-D image. The mission trajectory is highlighted in blue.

4.2.3 Data Processing

Upon reaching each waypoint, during the rover's stop, RGB-D images are captured. Immediately after, the system checks for the presence of an AprilTag in the RGB image. If no AprilTag is detected, the newly acquired data is discarded, as this would prevent certain subsequent processing steps from being carried out. In such cases, the acquisition is repeated only once more. After capturing and converting the data into a point cloud, the data is saved. While the rover moves toward the next waypoint, the recently acquired data is simultaneously transmitted to the data lake via a web call. This process involves uploading the data into three different packets: the RGB image

in *'.png'* format, the depth image as an array, and the point cloud in a specific *'.pcd'* format. Once the acquisition mission is completed, the analysis algorithm is executed.

The initial phase involves removing noise from the measurements by applying a gradient magnitude filter, following the methodology outlined in Section 3.2.5. Additionally, points at the outer edges of the sensor's field of view are filtered out, as the quality of measurements in these areas is lower, as illustrated in Figure 31. To exclude these outer points, a maximum field of view of 60° was imposed on both axes of the sensor's field of view, resulting in a region of interest (ROI) that is approximately circular in shape.

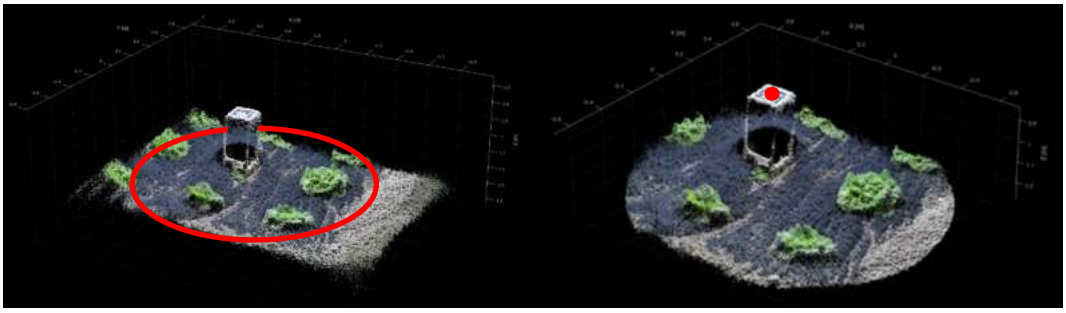

Figure 31. Example of noise filtering in depth measurement acquired in field conditions. On the left: an example of raw point cloud obtained from a single acquisition with the useful area highlighted in red where the noise in the measurement present at the edge of the frame is less present. On the right the result of applying the gradient filter and deleting the outermost part of the frame which contains the data used in the subsequent steps of the algorithm.

Subsequently, the individual point clouds are classified based on the ID contained in the graphic marker placed at the center of each plot. All point clouds belonging to the same plot are selected and processed in sequence. These point clouds are then transformed using a roto-translation aimed at reconstructing the entire plot. The first component of this transformation involves rotation, utilizing the *pcfitplane* function, which fits a plane to a point cloud with a maximum allowable distance from an inlier point to the plane, set at 5 mm in this case. To enhance the accuracy of this step, the point cloud is first down-sampled using the grid-averaged method with a box grid filter, applying a step equal to 5 mm. The function returns a geometric model that describes the plane, thereby determining the sensor's relative orientation to the ground.

$$ax + by + cz + d = 0$$

This adjustment is necessary because the rover might not always stop in a perfectly level position, making a general geometric calibration for converting the reference system ineffective. A dedicated IMU was also tested in parallel to estimate the sensor's orientation, but better results were achieved using the plane fitting method. Once the plane that best approximates the ground's position is determined, correction angles around the X and Y axes (pitch and roll) are calculated to level the ground in the point cloud. The rotation around the Z-axis (yaw) is estimated by checking the alignment of the AprilTag in the RGB image.

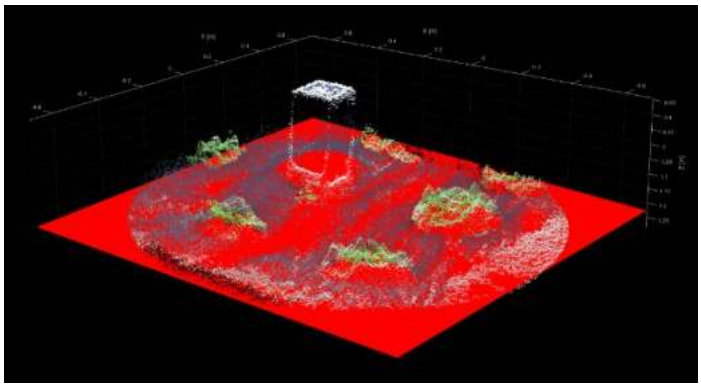

Figure 32. Example of ground plane fitting.

The second component of the transformation applied to the raw point cloud involves translation. This is determined by extracting the centroid position of the AprilTag's point cloud. This translation adjusts the position to align the centroid with the origin of the X-Y axes, setting the Z-axis to a fixed height of 0.3 m, which corresponds to the height at which the markers were installed.

After registering all the point clouds using this method, they are merged into a single representative point cloud of the parcel using the *pcmerge* function. This merged point cloud is then subjected to a smoothing and down-sampling operation to further reduce noise caused by suboptimal measurement conditions and to minimize the storage space required for the results.

The smoothing and down-sampling are achieved by interpolating the data from the merged point cloud. This is done using MATLAB's *scatteredInterpolant* function, which performs interpolation on a set of scattered data. The function returns an interpolant, denoted as F, for the given dataset. This interpolant can then be evaluated at a set of query points, such as (x_q,y_q) in 2D, to produce interpolated values $z_q = F(x_q,y_q)$. The

interpolation method used is *natural*, as it is more suitable for approximating natural surfaces compared to, for example, the linear method.

The mesh step used for down-sampling is 5 mm for both the X and Y axes, covering the entire parcel. The result is a 301-pixel wide mesh that contains the interpolated height data. Once the height matrix is obtained, the color information for each point on the mesh is determined by interpolating the RGB color channels from the point cloud onto an image with the same mesh dimensions.

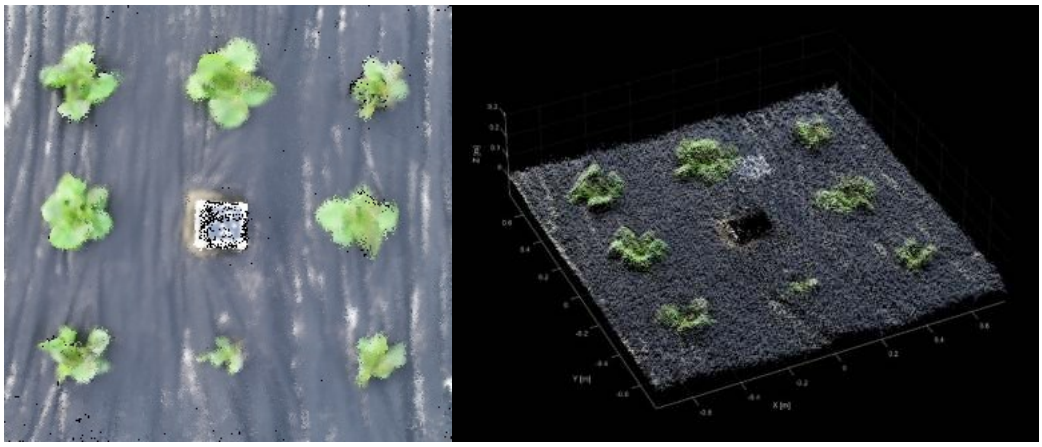

Figure 33. Result of the reconstruction process of a single plot. On the left: result obtained by observing the registered color channel of all the individual frames inherent to a single plot. On the right is showed the result of the point cloud reconstruction process.

Once the entire parcel is reconstructed and down sampled, the next step involves segmenting the individual plants and recognizing each head of lettuce. The process for identifying individual plants includes segmenting clusters containing vegetation by calculating the ExG index and applying a threshold determined using Otsu's method, as described in detail in Section 3.2.3.

When a plant is detected for the first time, it is assigned an ID based on the ideal planting scheme, considering its relative position to the marker as shown in Figure 34. For subsequent detections, the position used for assigning the ID follows the last verified position for that ID. This is necessary because, despite careful planting, the actual transplanting scheme may differ from the ideal due to the manual nature of the transplanting process.

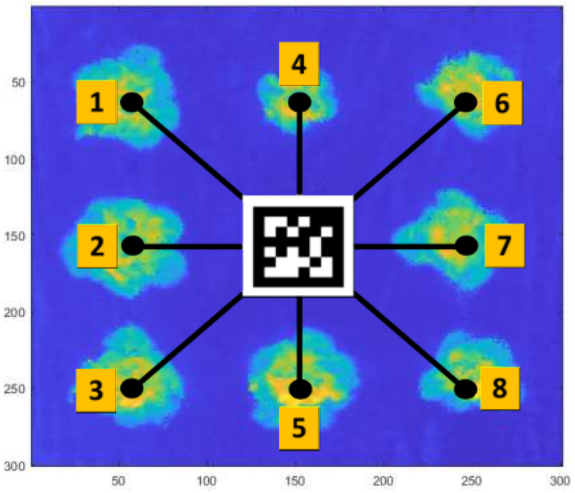

Figure 34. Transplant layout. The image shows how unique IDs between 1 and 8 were assigned based on plant relative position to the marker.

After segmenting each head of lettuce, the voxelization algorithm described in Section 3.2.5 is applied, but without compensating for leaf inclination. The resulting volumetric object is used to extract the volume feature. This procedure is repeated for each segmented individual and across all four acquisition epochs.

Following the last data acquisition, the plants were harvested, and DM was determined as described earlier in Section 3.2.1. The estimated biomass volume values and the measured ground truth weights were used to determine the correlation and apply regression to the estimated volume from all the previous acquisitions. During the acquisition campaign, three samples were discarded due to damage caused by snails.

All acquired data were uploaded to the data lake and made available for remote consultation via an application developed as part of the project, called "FoodsApp," created by the TIM S.p.A group for this purpose. After segmenting each head of lettuce, the voxelization algorithm described in laboratory-scale test is applied, but without compensating for leaf inclination. The resulting volumetric object is used to extract the volume feature. This procedure is repeated for each segmented individual and across all four acquisition epochs.

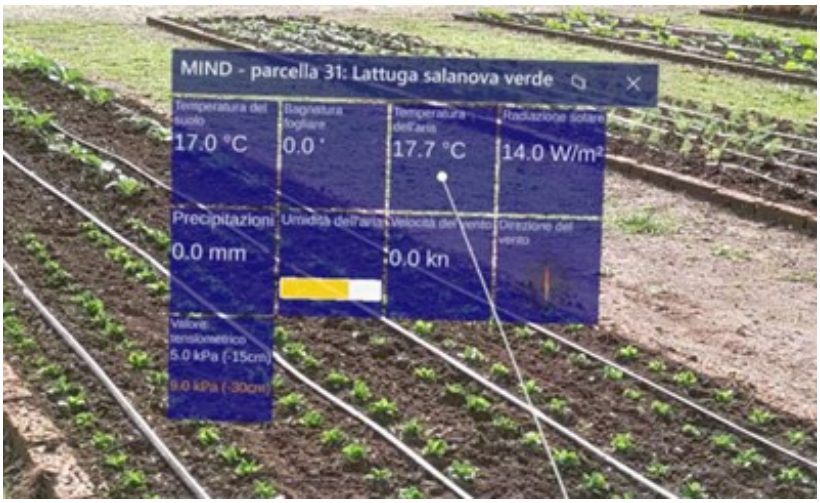

Figure 35. Outdoor augmented reality data visualization. The overlay shows the plot number, the crop species and environmental variables such as air and soil temperatures, solar radiation levels, rainfall, relative air humidity, wind speed and direction.

4.3 Results

Comparing the fresh weights at harvest with those after drying, it can be observed that the samples contained water at a concentration ranging from 92.9% to 96.8%, with an average of 94.6%. The measured DM after harvest ranged from a minimum of 0.78 g to a maximum of 14.7 g, with an average of 7.98 g.

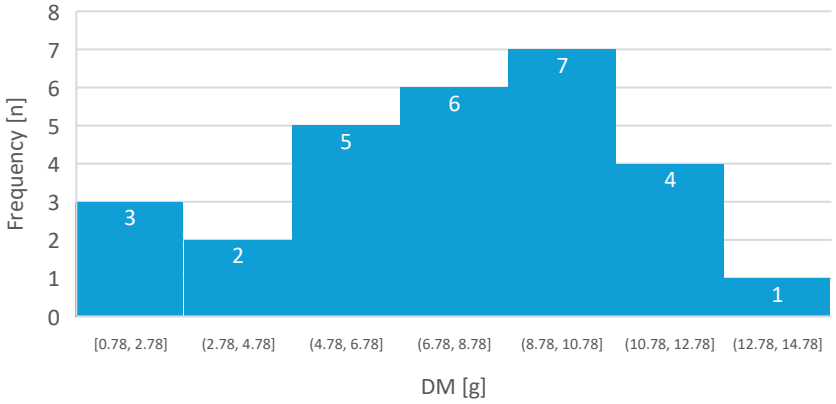

Figure 36. Characterization of samples DM at harvest.

The DM of the plants at harvest exhibits some variability, which can be attributed to several factors. These include the different fertilization doses applied, the different cultivars used, and the initial variations in plantlets sizes at transplanting, as not all plantlets were of the same dimensions due to nursery management. Additionally, post-transplant stress and other environmental factors could have influenced the samples development.

Despite this observed variability at harvest, it has been beneficial for constructing a correlation curve between dry weight and volume, consider plants of various sizes. As shown in Figure 37, the volume of the object correlates well with biomass or dry mass weight, with a coefficient of determination of 0.9 and a root mean squared error (RMSE) of 1.07 g. The performances obtained in this test, as well as those obtained in the laboratory tests discussed previously in Section 3.3, are similar to those obtained in similar work (Zhang et al., 2022), which estimates several parameters of lettuce plants including dry weight. In that case, however, the data acquisition was carried out under controlled conditions and has a higher spatial resolution than the field test.

Moreover, the estimation model obtained in this field experiment is to that observed in laboratory tests described in Section 3.3. Small differences may be attributed to the fact that the plants in the field were grown under different environmental conditions and fertilization levels compared to the lettuce plants cultivated for the laboratory tests. Additionally, the field-grown plants achieved a much higher level of development, with a maximum DM of 14.7 g compared to 3.05 g in the laboratory test.

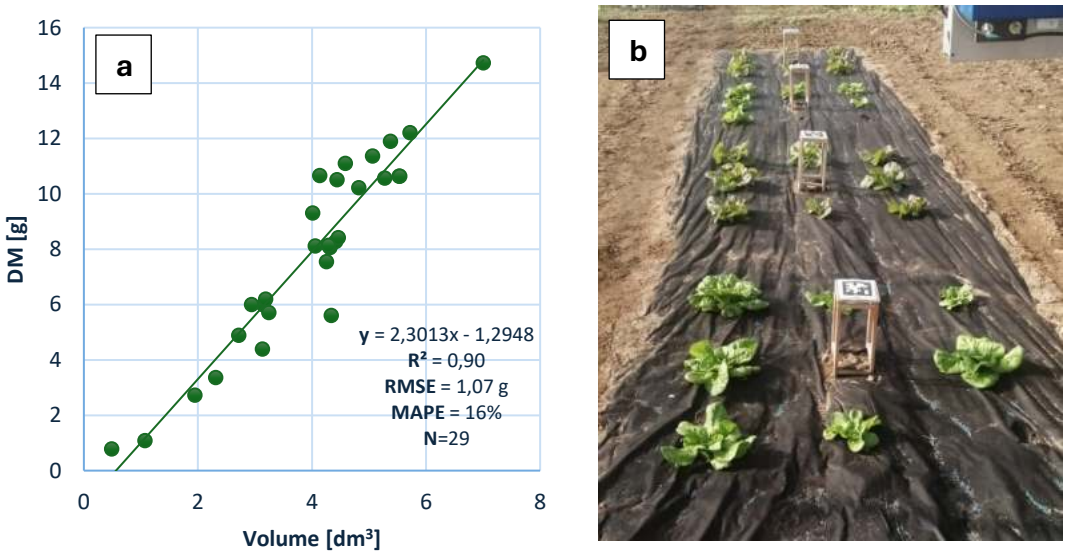

Figure 37. DM estimation model based on the volume of the reconstructed volumetric object. a) Results of correlation between estimated volume and ground truth. b) Image of the experimental setup.

Regarding the characterization of biomass throughout the growth period of the plants and considering the variability of the seedlings planted during transplantation, we have chosen to present relative biomass growth values using the volume estimated at the

first acquisition (t = 0) as the baseline. The relative growth data is calculated by dividing the estimated volume at a given time by the volume estimated at the initial acquisition.

The results are presented below in Figure 38, showing the average relative increase per plot, per cultivar and per treatment. Observing the graphs, it is evident that the red variety exhibited a greater average relative biomass increase compared to the green variety. Furthermore, fertilization had a more pronounced effect on the green cultivar, still showing visible results in both cases after approximately 20 days.

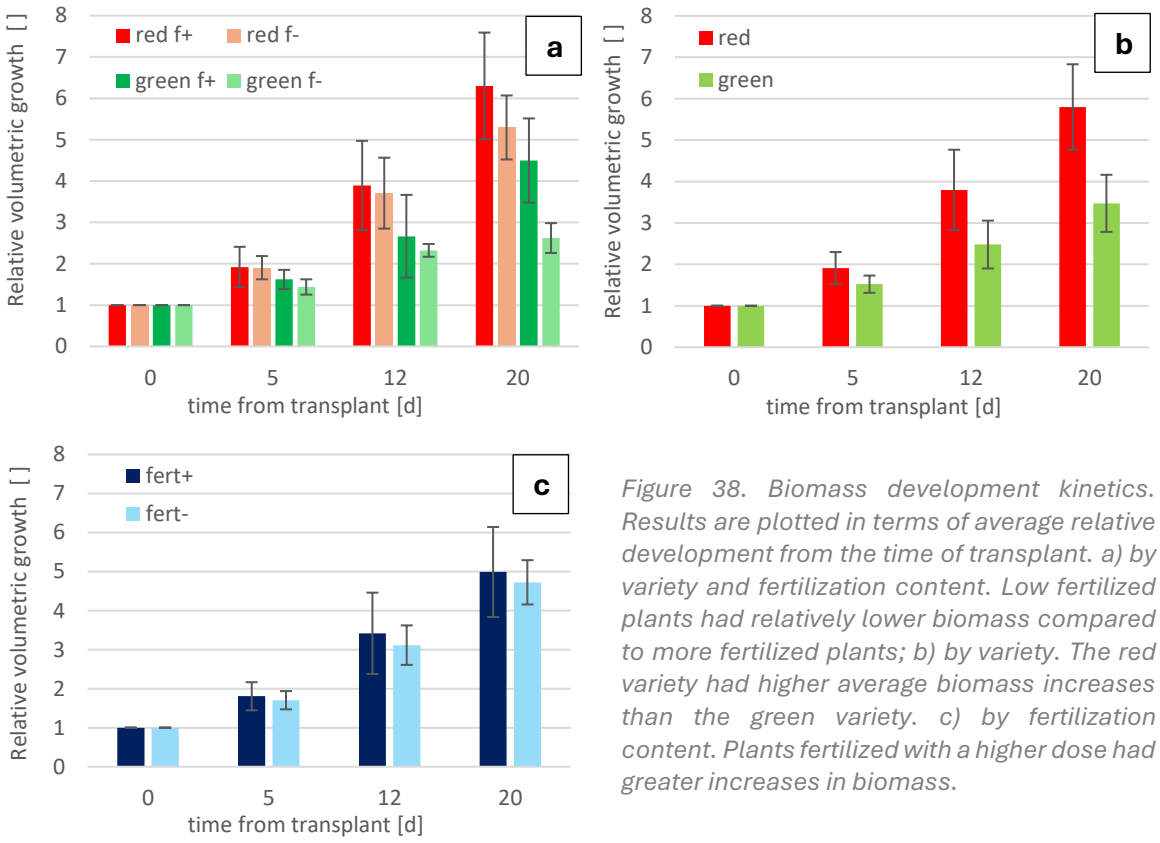

Figure 38. Biomass development kinetics. Results are plotted in terms of average relative development from the time of transplant. a) by variety and fertilization content. Low fertilized plants had relatively lower biomass compared to more fertilized plants; b) by variety. The red variety had higher average biomass increases than the green variety. c) by fertilization content. Plants fertilized with a higher dose had greater increases in biomass.

To better understand and appreciate the quality of the results obtained using this method, the graphical representation of the reconstruction of each individual plot throughout the experiment is presented below. It is interesting to observe the quality of reconstruction achieved at the level of individual plants and single plot. In this case, the quality is bit lower than that obtained at the laboratory scale due to the different sensor distance and measurement conditions. However, the algorithm provided a satisfactory level of characterization of the plants and within the individual plots which can be appreciated in Figure 39 where the results of the reconstruction process of the individual plots in the different epoch in which data acquisition happened.

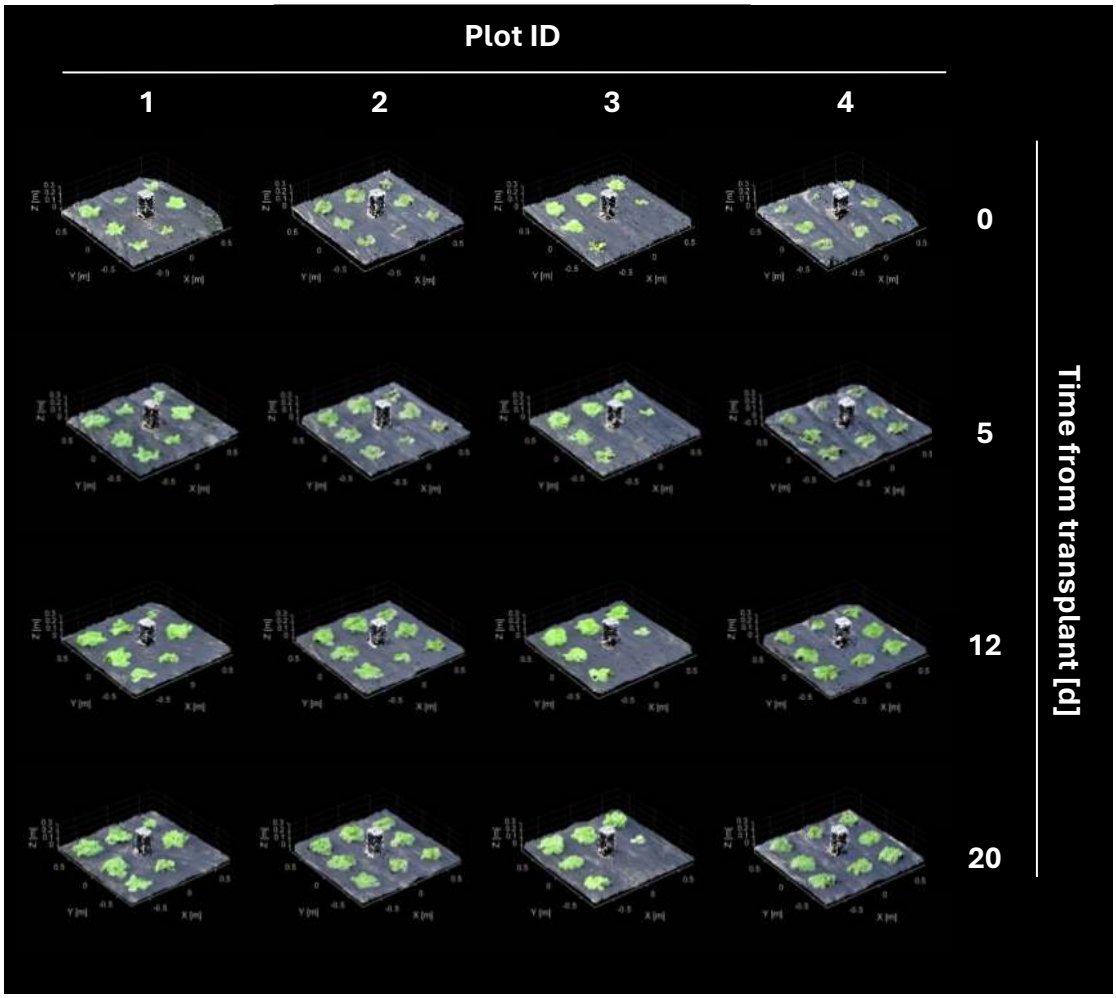

Figure 39. Graphical representation of plant development during the experiment. The rows represent the elapsed time since transplant while the columns indicate the individual plots.

4.4 Research Objective Achieved

The objectives set at the beginning of the field experiment for automated monitoring and characterization of the development of individual horticultural plants have been fully achieved. The rover was effectively used to collect data by executing programmed missions, moving the sensor within the experimental area. The spatial reference markers made possible and improved the quality of the point cloud reconstruction process for individual plots and facilitated the identification of individual plants, enabling a satisfactory characterization of their development over time. The laboratory-scale algorithm demonstrated its effectiveness even under greenhouse conditions. The collected data were archived in the data lake, and some results were accessed in augmented reality directly in the greenhouse using the Oculus headset, which, by recognizing the markers, could display data related to the plot.

5 Comparison Test of Proximal and Remote Sensing Data

5.1 Aim of the Experiment

The purpose of this work is to develop a map of soil coverage degree based on the calculation of FC and to validate and compare the results obtained from the application of a proximal imaging technique based on RGB images with those obtained using the commonly employed remote imaging method in precision agriculture, which involves the use of UAVs.

5.2 Materials and Methods

5.2.1 Experimental Site

The experimental activity was conducted within a plot of the Teaching and Experimental Agricultural Farm of the University of Milan "A. Menozzi" located in Landriano (PV), Italy (45°319 N - 9°265 E). The maize crop (*Zea mays L*. hybrid P1916 FAO 600) was sown on April 17, 2023, on an experimental area of 33.6 m in width, corresponding to 48 rows of maize with an inter-row spacing of 0.70 m and 210 m in length, ensuring an area of 7056 m^2 (0.71 ha). No chemical or physical weeding was performed prior to the survey. The monitoring of the experimental area was carried out on May 17, 2023, when the crop was at the V3-V4 stage, an ideal time to plan a post-emergence chemical weeding intervention (James et al., 2007).

5.2.2 Determination of Fractional Green Canopy Cover (FC)

The FC is defined as the vertical projection of vegetation above a defined area (*Sa*). The size of the sampled area depends on the experimental purposes and the crop considered, in this case, 0.7 m, equal to the inter-row spacing of the crop. For each sampled area, the proportion of area occupied by vegetation is determined by using a method employed in numerous studies, which involves calculating the Excess Green Index (ExG) (Zhang et al., 2018) for each pixel on the RGB channels and imposing a minimum threshold (T_{EG}). All pixels with an ExG value above this threshold are

considered as vegetation. This threshold is automatically determined using Otsu's method (Riomoros et al., 2010) on a calibration field image where no weeds are present. Otsu's method is useful for finding a value capable of separating a bimodal distribution into two parts. In this case, the bimodality is ensured by the simultaneous presence of plants, which will have higher ExG levels, and soil, which will be characterized by lower, often negative, index levels.

$$ExG = 2\,G - R - B \qquad FC = \frac{ExG > T_{EG}}{S_a} \quad [\ ]$$

The field area used for threshold calculation is located at the head of the field and has been weeded using a non-localized method, receiving two interventions, one pre-emergence and the other post-emergence. The pre-emergence intervention was carried out using Lumestra® (Syngenta®), a commercial product for controlling narrow-leaf and broad-leaf annual weeds, composed of Encarit (720 g/l dimethenamide-p, 1 l/ha) and Callisto 480 (480 g/l mesotrione, 0.3 l/ha) mixed in 300 liters of water. For the post-emergence intervention, the product used consists of a mixture of Laudis (Bayer®) (44 g/l tembotrione, 2.25 l/ha) and Ghibli (Syngenta®) (40 g/l nicosulfuron, 1.5 l/ha) in 250 liters of water.

5.2.3 Remote (UAV) Aerial Survey and Generation of FC Map

Aerial surveys using UAVs were conducted using a quadcopter (DJI Mavic 3M) equipped with a RGB digital camera with a 4/3 CMOS sensor and a resolution of 20 MP. The positioning of the aircraft is achieved through the high-precision positioning module (GPS-RTK) onboard, which is used for flight control during missions and to synchronize the position with the acquired data.

The survey involves executing a mission in automatic navigation at a constant altitude of 40 m, during which the aircraft follows a trajectory passing through a series of waypoints to capture images at a regular frequency ensuring an 80% overlap between consecutive frames and between frames belonging to adjacent trajectories. This level of overlap is necessary to ensure the generation of the map (orthophoto) allowing orthorectification and image mosaicking algorithms to work correctly. The chosen flight altitude for the experiment is lower than that commonly used in surveys of this

kind (usually around 60 m) and Huang et al., 2017, considering the use of consumer-grade RGB cameras for such purposes, indicates a reasonable altitude range between 40 m and 100 m. In this experiment, a relatively low altitude was chosen to prioritize the quality of the information used to generate the FC map.

The software used for mission planning and subsequent image processing is PIX4D. The resulting orthophoto is then divided into a regular square mesh of 0.7 m sides, and for each area, the FC is calculated.

5.2.4 Proximal Surveys and Generation of the Infestation Map

The proximal sensing monitoring utilizes a commercial RGB sensor camera (GoPro Hero 8 descripted in Sect. 2.3) with a resolution of 12 MP. The camera was positioned at a height of 2 m with the lens parallel to the ground plane, secured to a supporting structure made for this purpose using square aluminum profiles (Bosch Rexroth AG, 45 mm section), attached to the tractor via a three-point coupling to firmly support the camera and avoid excessive vibrations during tractor movement. In this configuration, the camera can capture an area of 4 m by 3 m. To minimize FC estimation errors due to perspective, the images were rectified and cropped to include 4 rows of maize with their inter-row spaces, covering an area of 3 m in width and 2 m in length parallel to the tractor's direction of motion.

The images were collected by setting the camera to time-lapse mode with an acquisition frequency of 2 Hz. This frequency, considering the tractor's set speed of 2.5 km/h, is sufficient to ensure that all areas of the field are captured. During processing, to reduce data volume and processing time, a subset of the images was automatically selected with the criterion of minimizing overlaps, thereby using the minimum number of images possible.

Figure 40. Setup for proximal image acquisition mounted at the rear of the tractor.

The infestation map is generated by processing the selected images, dividing them into 8 zones with a

width of 0.7 m equal to the inter-row distance and a length of 1 m to calculate their respective FC. For each zone, the relative position of the centroids of the individual areas with respect to the camera is transformed by imposing a rotation equivalent to the angle of the tractor's motion direction and a translation equal to the position determined by the camera's internal GPS receiver. Finally, the interpolated FC map was divided into a regular square mesh of 0.7 m sides for comparison with the map obtained through UAV survey. Image analysis was performed by developing a script in MATLAB environment. The positions of the area centroids were projected onto the map and associated with the corresponding FC attribute value, enabling the subsequent spatial interpolation of values. Finally, the interpolated FC map was divided into a regular square mesh of 0.7 m sides for comparison with the map obtained through UAV survey.

5.2.5 Treatment Scale -- Remote (UAV) and Proximal Sensing Validation

The size chosen for validation represents the treatment scale, i.e. an area that could be used as uniform management zones for high accuracy precision spraying in real-time treatments. The data collected using proximal imaging and UAV techniques were validated by comparing the FC data with ground truth, that is represented by FC determined using images captured under optimal conditions. The ground truth frames images were acquired by installing a Canon 5D camera on a tripod adjusted to maintain it at a fixed height of 1 m from the ground and oriented parallel to the ground plane [pitch and roll ~ 0] and ensuring optimal lighting conditions by using a shade cloth to make the subsequent analysis for the FC calculation as accurate as possible. In this case, for FC calculation, segmentation was obtained using software (CANOPEO - Patrignani et al., 2015) that consistently segments vegetation surfaces in an image using a combination of multiple indices based on RGB color channels. In this case, the ratios between the R and G bands and between the B and G bands, as well as the Ex-G index introduced earlier, are considered.

$$\frac{R}{G} < P_1 \ \& \ \frac{B}{G} < P_2 \ \& \ ExG > \ P_3$$

The parameters P1 and P2 typically have values close to 1 in the literature (Paruelo et al., 2000), while P3 typically assumes a value around 20 to select predominantly green pixels (Meyer and Neto, 2008). The default parameters used by Canopeo are P1 = 0.95, P2 = 0.95, and P3 = 20.

For validation purposes, 90 sampling surfaces were identified in the field, each measuring 0.7 m by 0.35 m, identified by corresponding yellow markers embedded in the ground, whose absolute positions were accurately determined using a GPS-RTK receiver.

The GPS position was used to extract from the map obtained through UAV survey all the sampled areas accurately, while the physical presence of the markers was helpful to manually extract from the rectified proximal images the same areas, as the GPS receiver in the camera did not prove to be sufficiently accurate to produce metadata useful for accurate extraction.

Figure 41. Aerial image of the experimental field. Ground control points are indicated in yellow.

5.2.6 Proximal Scale --- Remote (UAV) and Proximal Imaging Comparison

Intermediate-scale comparisons were obtained by comparing areas larger than those used for validation. For this purpose, GCPs were used to extract sample areas at a proximal scale, using the same procedure as described in Section 5.2.5. In this case, 2 m by 3 m areas were extracted to compare data at a different scale, which for proximal images represents their operational scale.

5.2.7 Field Scale --- Remote (UAV) and Proximal Imaging Comparison

The field-scale comparison was obtained through the difference map, which shows the deviations between the FC levels detected in the map obtained with proximal images and that with UAV.

5.3 Results

5.3.1 Treatment Scale -- Remote (UAV) and Proximal Sensing Validation

The results obtained in the validation of the UAV-acquired images show that the estimation of FC using this method tends to generally underestimate the ground cover, as evidenced by the slope of the correlation line (see Fig. 43b), which is 0.5. In this case, the coefficient of determination is 0.79, the RMSE is 11%, and the MAPE is 8.4%.

Regarding the validation of proximal images, again, the FC values tend to underestimate the actual field conditions, but in this case, the estimation is better as the slope of the correlation line (see Fig. 43a) is 0.92, and the coefficient of determination reaches the value of 0.93. The observed RMSE is 5.5%, and the MAPE is 4.91%.

Figure 42. Comparison of images used for FC validation. Starting from the left: proximal image acquired with Canon 5D used to calculate the FC as considered as ground truth, proximal image acquired with GoPro Hero 8 and cropped to fit with the corresponding validation sample, UAV survey orthophoto cropped to fit with the corresponding validation sample.

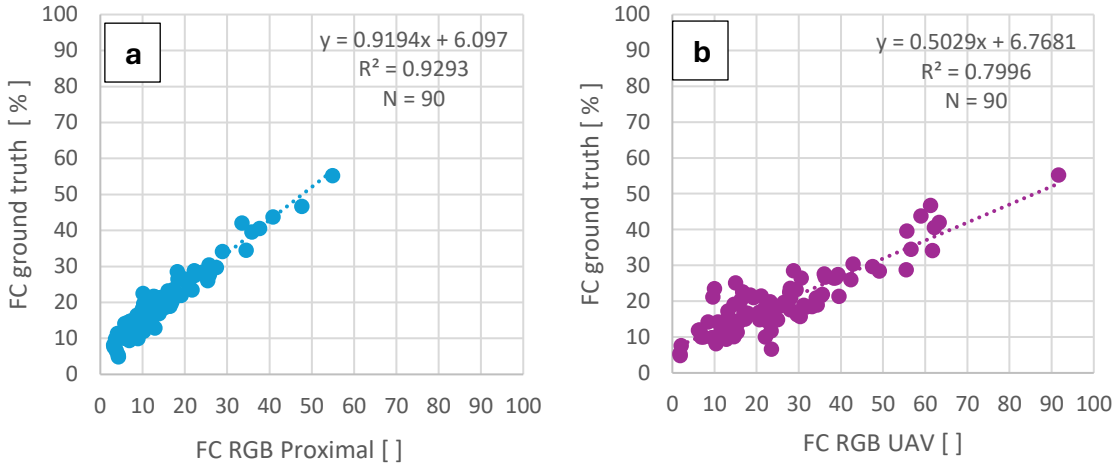

Figure 43. Validation results. FC estimated over an area of 0.7 by 0.35 m at 90 GCP.

5.3.2 Proximal Scale -- Remote (UAV) and Proximal Imaging Comparison

From an analysis of the results at an intermediate scale, the tendency to underestimate FC for data collected with UAV has been confirmed. However, there are some areas where the FC estimates made with the two methods provide very similar values and areas where, contrary to what was seen previously, the estimate made with UAV provides higher values. In Figure 44, the FC values estimated with the two analysis methods for all sampled areas are reported. To understand the causes of these FC differences, two examples were extracted corresponding to cases where UAV estimation shows maximum overestimation and maximum underestimation.

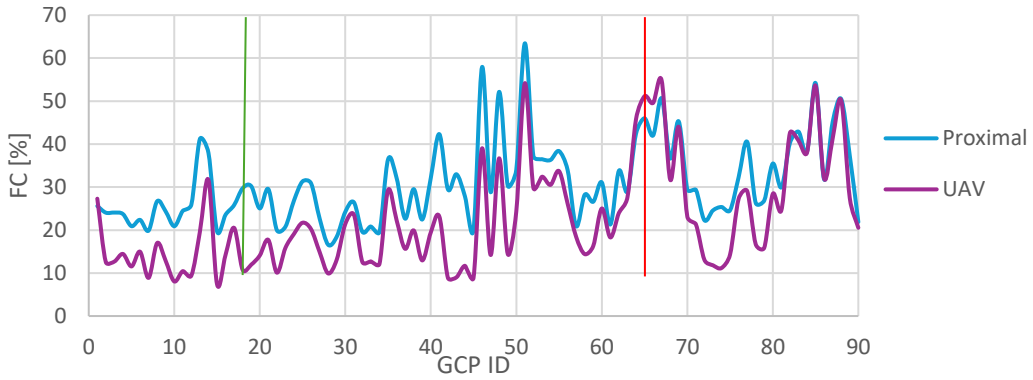

Figure 44. FC estimated over an area of 3 by 2 m at 90 GCP. The red line shows the example extracted as the case where the UAV leads to the greatest overestimation while the green line shows the case where the greatest underestimation occurs.

The first example shows a case where the UAV underestimates FC levels, which occurs when small weeds are present that are not visible at UAV resolution. As a result, the segmentation outcome tends to lose numerous details, making the generated map less accurate. This makes it difficult to detect weed in their early stages of development and those with very narrow leaf blades, such as monocots, rendering the prescription map, and consequently the treatment derived from it, less effective exposing the crop to greater weed competition.

The second example highlights a case where the UAV overestimates FC levels, which occurs when there is a higher level of infestation. In this scenario, the lower level of detail leads to the merging of nearby clusters or the closing of small empty internal areas.

Consequently, the segmentation tends to simplify the shapes of the clusters, making the generated map less accurate.

This error is less severe than the previous one regarding the management of weed competition against the crop, because in theory it ensures that the target weeds are affected, however, it can still lead to an unjustified increase in environmental impact due to the unnecessary treatment of additional areas.

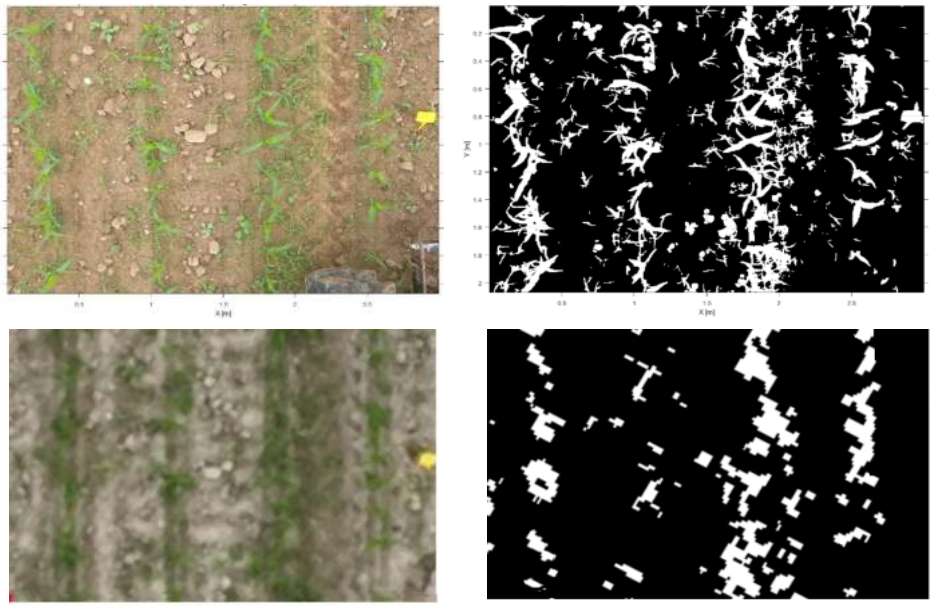

Figure 45. Comparison of color-based segmentation results obtained with proximal (top) and UAV images (bottom) under limited FC conditions.

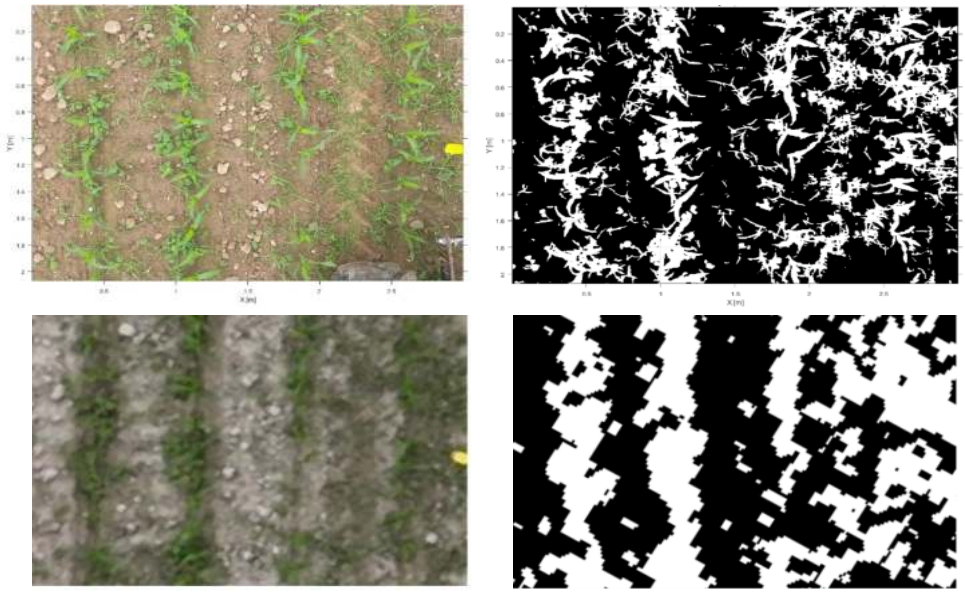

Figure 46. Comparison of color-based segmentation results obtained with proximal (top) and UAV images (bottom) under severe FC conditions.

5.3.3 Field Scale -- Remote (UAV) and Proximal Imaging Comparison

The results of the FC estimation at the field scale are depicted for each individual area in Figure 47. The maps generated using proximal images (see Fig. 47a) and those obtained with UAV acquisition (see Fig. 47b) show that there are differences between the FC values estimated with the different imaging methods. The maps obtained with the two sensing methods confirm what was observed at GCP on a smaller scale i.e. that in this case the UAV images produced FC estimates that tend to be lower, Therefore in this case, the map obtained with drone images represents a situation where the weeds pressure appears to have a lower intensity compared to the real situation

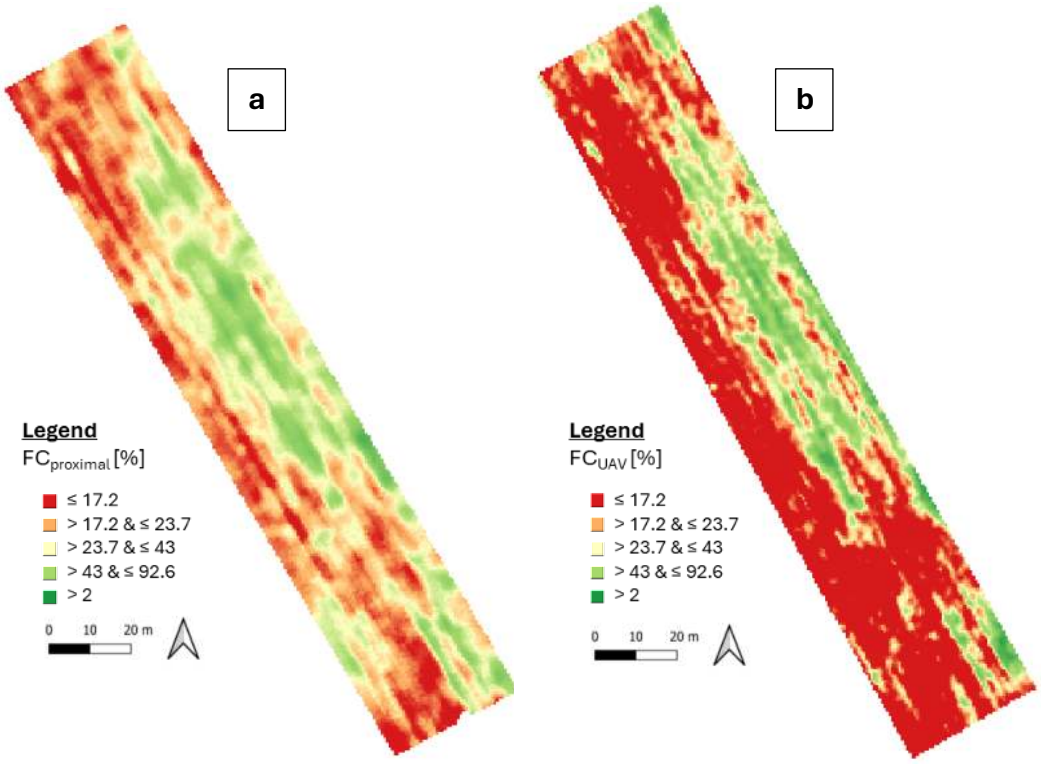

Figure 47. FC map of the experimental field obtained by proximal imaging (a) and by UAV (b).

The histogram in Figure 48 shows the probability distribution of observed differences in FC levels between the map generated with UAV images and that generated with proximal images. In 80% of cases, the estimation with proximal images provides a higher value compared to that with UAV images.

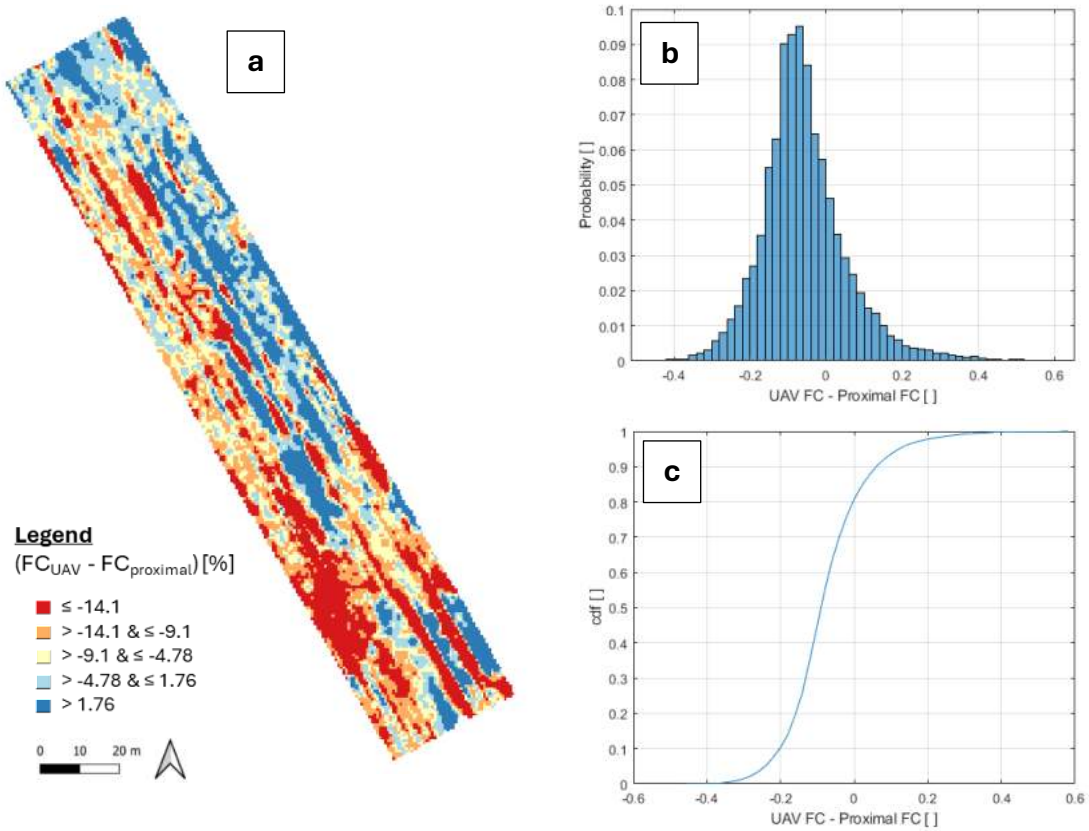

Figure 48. Map of FC differences between UAV and proximal sensing a). Deviation value distribution b) and its cumulative density function c).

Finally, regarding the time required for generating the prescription map, the one obtained with UAV images took about 8 hours of computing time, equivalent to a spatial processing capacity of 0.1 ha/h. In contrast, for proximal images, it is in the order of 16 minutes, equivalent to a spatial processing capacity of 2.6 ha/h, thus superior in comparison.

5.4 Research Objective Achieved

The proximal imaging method provided significantly higher quality information related to FC and, consequently, for estimating weed infestation pressure based on this method. Additionally, the proximal method demonstrated greater efficiency in terms of calculation time required for map creation, thereby enhancing the timeliness of any treatments based on a prescription map derived from it.

Remote sensing provided information that should be evaluated carefully. In contrast to the proximal sensing, UAV data could often provide conflicting results, which were neither systematically overestimated nor underestimated, but varied depending on

the time of detection and the type and degree of infestation and should therefore be considered less reliable.

Real-time proximal image analysis has the potential to make UAV surveys and the subsequent generation of prescription maps unnecessary. Moreover, as a critical factor in significantly reducing costs, it could also eliminate the need for highly accurate GPS-RTK positioning systems during both treatments and monitoring.

6 2D-Based Algorithms for Weed Sensing in Maize

The use of proximal images for estimating weed infestation levels in the field, based on soil cover evaluation as discussed in the previous Chapter, allows for more accurate information to be obtained. Additionally, the acquisition and processing of this information are faster. Estimating weed infestation from a single image is not enough to accurately determine the presence and location of weeds and to manage herbicide application with high precision. Therefore, it is necessary to develop algorithms capable of real-time detection of areas with a high probability of infestation and to convert the results of these algorithms into prescription maps. These maps can then be used to perform the treatment concurrently with the acquisition of information.

6.1 Aim of the Experiment

The objectives in this section focus on the development and comparison of two different algorithms based on the evaluation of FC and the use of proximal RGB images as inputs for weed detection. Additionally, these algorithms aim to generate on-the-go prescription maps that can be used to guide site-specific weeding treatments concurrently with the data collection. The evaluation of the results obtained from the two methods was carried out through the simulation of precision treatments across different scenarios, each representing field conditions with varying levels of observed weed infestation. The performance of these methods will be compared with that of a conventional herbicide treatment simulation, which involves the uniform distribution of herbicide across the entire surface, representing the standard treatment.

To conclude, the feasibility of using the tested algorithms in real-time was assessed by monitoring their execution time across scenarios of varying complexity, with the aim of evaluating their potential field capability. The execution time also depends on the hardware used to run the MATLAB script.

6.2 Material and Methods

6.2.1 Image Acquisition and Setup

The sensor used for the trial is GoPro Hero 8, mounted on the tractor using the same support structure described in detail in Section 5.2.4.

The images were acquired by programming the camera in timelapse mode to capture a frame every 0.5 s (freq. equal to 2 Hz). This acquisition frequency was chosen based on the estimated average displacement of the tractor (*Disp*). Given the tractor's forward speed (V_a) during the survey, which ranged from 2 to 2.5 m/s, this frequency ensured adequate overlap (*Ol*) between consecutive frames, thus ensuring complete coverage of the monitored area. The percentage overlap is calculated by dividing the tractor's displacement between two consecutive acquisitions (*Disp*) by the length of the frame in the direction of the tractor's movement.

$$Disp = 2.25\ ms^{-1} \cdot 0.5\ s = 1.12\ m$$

$$O_l = \frac{1.12\ m}{2\ m} = 0.56 \quad [\,]$$

6.2.2 Image pre-processing

After acquisition, the raw images were rectified to remove lens distortion and subsequently cropped to include only the relevant area for analysis using various algorithms. Considering the characteristics of the camera used and its installation height at 2 m, the effective working area in this case has a width (b_L) of 3 m and a length (b_a) of 2 m. This dimension allows for sampling an area covering 4 rows of maize along with the inter-row spaces over a length of 2 m in a single image.

The pixel-to-meter conversion was achieved by analyzing a calibration image taken after mounting the camera on the support attached to the tractor (see Sect. 3.2.4 for details). Prior to image acquisition, a checkerboard pattern (also used for estimating the camera's intrinsic parameters) was placed on a flat surface directly beneath the camera. The conversion was performed by capturing the image, rectifying it, and segmenting all the black squares of the checkerboard. Since the dimensions of the

black squares are known (30.5 mm each side), once segmented and the average area in pixels calculated, it is possible to convert each pixel into equivalent surface measurements (m^2) or linear distances (m).

Figure 49. Calibration image with visible in the center the checkboard pattern.

The vegetation visible within the images was segmented using the ExG index, with a threshold applied based on Otsu's method, as detailed in Section 3.2.3. The resulting binary masks were then processed using two different algorithms to create prescription maps, enabling precision chemical weed control interventions in real-time during the survey.

Figure 50. Example of a color image acquired with the experimental setup during the trial.

6.2.3 A Patch-spraying Approach Simulation [Management Zones]

The first algorithm, termed Uniform Management Zones (MZ), exemplifies a patch-spraying approach that provides a higher precision level and smaller patch sizes compared to UAV-based precision agriculture techniques. In this case, the algorithm

generates a real-time prescription map, rather than obtaining it via post-processing as in UAV-based workflows. This method processes one image at a time, dividing it into 8 areas that can be uniformly treated following FC assessment, allowing for immediate treatment if necessary.

The algorithm simulates a treatment using a spray bar section equipped with four fan nozzles, each with a 60° (α) angle, positioned at a height (H_n) of 0.65 m. This setup is designed to manage a work zone with a width (b_n) of 0.75 m. The selection of this type of commercial nozzle was based on preliminary sizing calculations, performed as follows:

$$b_n = 0.75\ m \qquad H_n = \frac{b_n \cdot 0.5}{\tan(\alpha \cdot 0.5)} = 0.65\ m$$

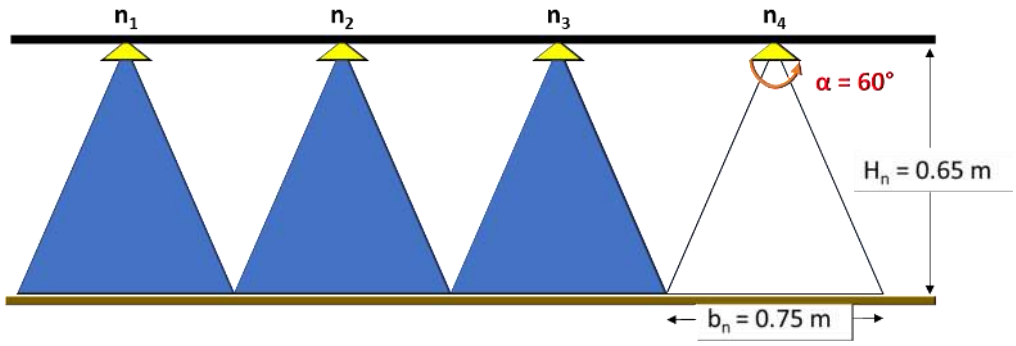

Figure 51. Diagram of the setup used to simulate treatment with the MZ method. The sprayer boom is shown in black, while the four nozzles of the simulated section are shown in yellow.

Considering this setup and the dimensions of the acquired frame, it is possible to divide the sampled area into a single image into 8 sections, each measuring 0.75 by 1 m, which can be treated uniformly. Figure 50 on the right illustrates the 8 zones individually labelled and highlighted in different colors as an example.

Within each individual zone, the cover fraction will be calculated, i.e. the ratio of the area occupied by vegetation to the area of the zone itself.

$$FC = \frac{Vegetation\ Area}{Zone\ Area}\ [\ ]$$

The logic that determines whether an area is to be treated or not is based on its FC, which if it exceeds a certain imposed threshold is to be treated. Section 6.2.4.3 will

outline the method used to determine the thresholds used in the colorimetric segmentation and that used for treatment.

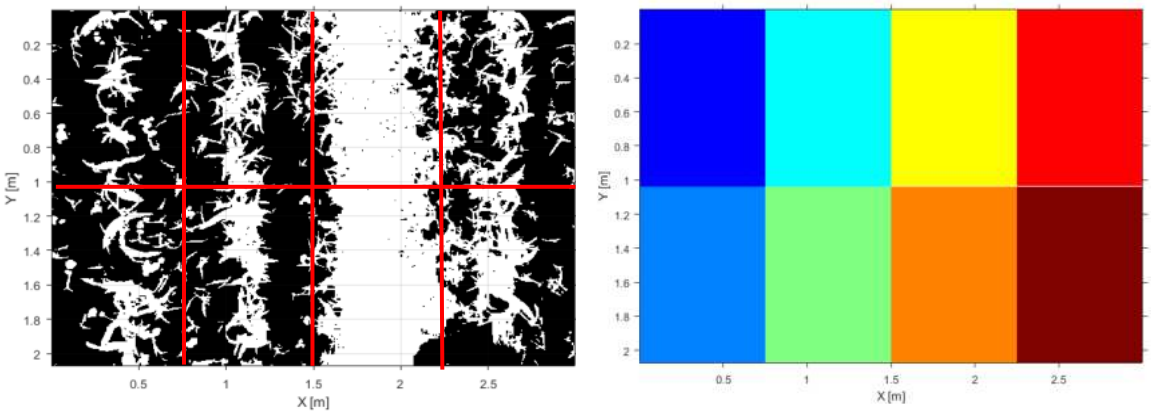

Figure 52. Labelling of individual treatment zones for MZ algorithm. On the left: binary image, result of the color-based segmentation process. This image is then divided into individual areas to determine the FC within each area. On the right: are showed the individual areas labeled individually and represented with a color representative of the unique ID associated with the area

6.2.4 A Micro-spraying Approach Simulation [Local Cover Fraction]

The second algorithm, named Local Cover Fraction (LCF) represents a micro-spraying application and is more complex because it involves evaluating local FC by differentiating between intra-row and inter-row spaces. The process begins with identifying the positions of the four visible crop rows within the image. Following this, a preliminary classification of potential weeds in the inter-row spaces is conducted, and an estimation of infestation pressure along the row (intra-row) is performed. This approach aims to generate a highly accurate prescription map that can be utilized in real-time during the survey. This algorithm simulates a treatment using a spray bar section equipped with 14 nozzles featuring a 20° fan spray pattern. These nozzles are positioned at a height (H_n) of 0.65 m and can manage a working width (b_n) of 0.2 m.

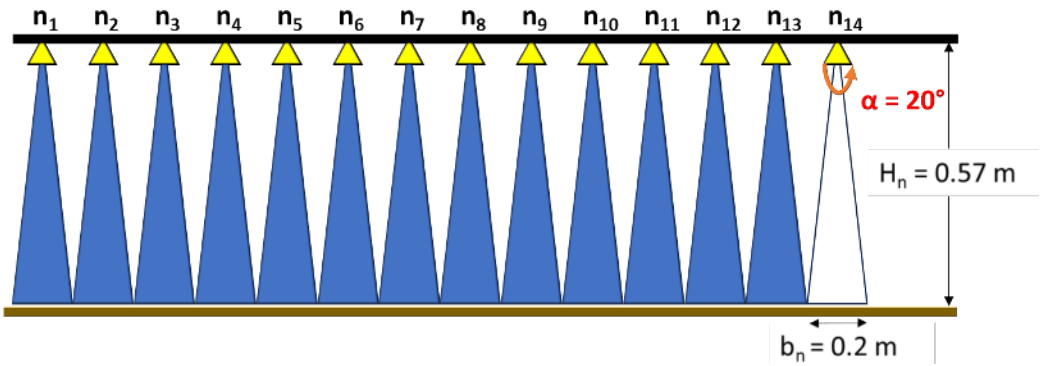

Figure 53. Diagram of the setup used to simulate treatment with the LCF method. The sprayer boom is shown in black; the nozzles of the simulated section are shown in yellow.

The selection of such commercial nozzles is based on preliminary sizing calculations as follows:

$$b_n = 0.2\ m \qquad H_n = \frac{b_n \cdot 0.5}{\tan(\alpha \cdot 0.5)} = 0.57\ m$$

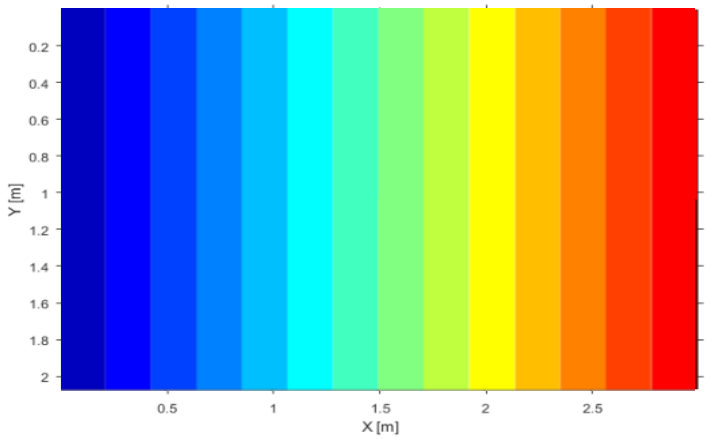

Figure 54. Labelling of individual treatment zones for LCF algorithm. The image shows the individual areas labeled individually and represented with a specific color representative of the id of each actuator workspace used in simulations to evaluate the treatment

6.2.4.1 Determining the single crop row space with 2D images

After colorimetric segmentation, the first step of the algorithm involves identifying the positions of the 4 visible crop rows within the binary mask by calculating the positional distribution of pixels segmented as vegetation. This distribution is obtained by summing 'true' pixels for each column in the binary mask, where pixels classified as vegetation are assigned a value of *'true*' or 1. The resulting distribution helps identify the positions of the 4 peaks, which represent the most probable locations of the crop rows, given that in conditions of moderate to low infestation, the crop vegetation in these positions is widely predominant. To make the identification of peaks more robust, a parameter of 0.5 m (approximated to 500 pix.) was used as the minimum distance there must be between one peak and another adjacent peak. An example of the result of this step is shown on the left in Figure 53.

In cases of high weed infestation, the 4 peaks might not be correctly identified and for this reason, when anomalies are detected in the number (4 rows) and/or position (relatively equally distributed) of the peaks, the information from all the previous

observed distributions can be used as a reference to limit the local effect of areas with high levels of infestation.

Figure 53 on the right shows an example of determining the position by averaging the current position with the peaks extracted from a single image and the estimated position, which is the average of current positions and previous ones along a straight-line trajectory of 200 m that represent a single pass, and can be updated with each direction change.

After estimating the positions of the crop rows, a single row space segmentation is performed. This process involves generating a mask composed of 3 lines positioned in the local minima that lies between the peaks highlighted above, which are subtracted to separate the 4 peaks identified (or the average position in the case of high infestation scenario). The purpose of this operation is to break the potential continuity of clusters related to the different rows within the color mask.

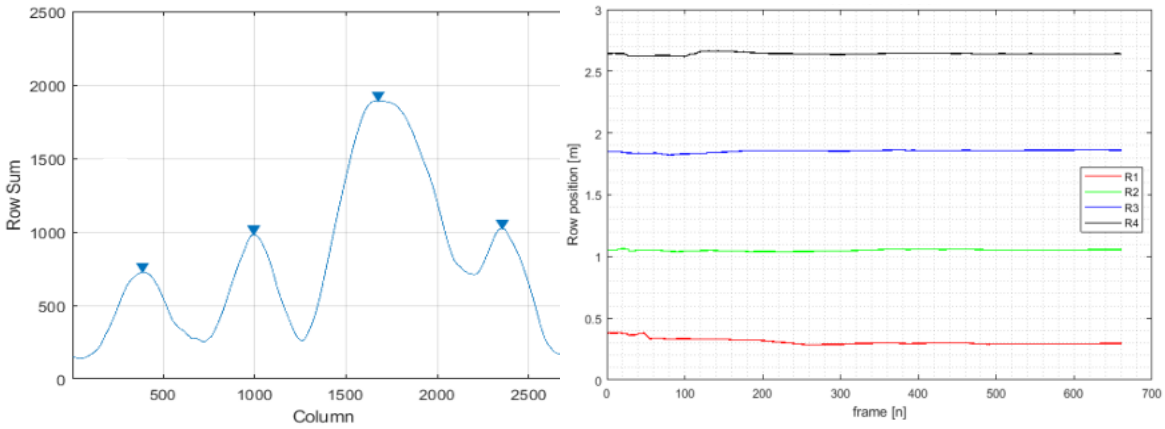

Figure 55. Example crop rows position detection. On the left: example of instantaneous crop row position detection on a single image. The plot shows the sum per column performed on the binary mask used to segment the vegetation. The blue triangles indicate peaks that represent the positions where the crop rows are most likely to be located. If their distribution is homogeneous and their number correct, the position information is correct enough to be used frame after frame. On the right: continuously detected position along a 200 m straight-line trajectory, calculating the average between the last positions detected and previous peak positions.

6.2.4.2 Classification of inter-row weeds and local cover fraction

After separating the space for each individual row, clusters that are in contact with at least one pixel of the crop lines are selected as 'potential crop'. To accomplish this, a mask composed of 4 lines is generated at the positions of the peaks previously identified in the vegetation distribution. This method allows for the selection of all clusters that are in contact with these lines as potential crops. Consequently, all other

clusters (highlighted in red in Fig. 56 right) are classified as weeds located in the inter-row spaces because they are most likely small clusters that are isolated in the inter-row space and have no contact with the center of the row.

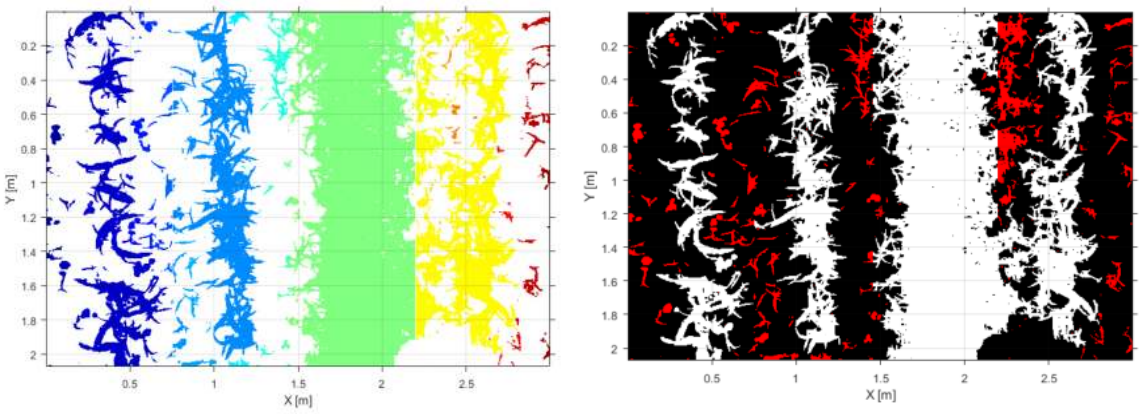

Figure 56. Results of first classification phase for LCF algorithm. On the left is shown an image representing the vegetation labelled by single cluster while on the right are shown labelled in red the weeds classified in this phase.

The final step involves selecting the individual clusters identified as potential crop from the vegetation color mask (shown in white in Fig. 56 right) and calculating the local cover fraction by summing along each row. The purpose of this step is to determine the distribution of vegetation along each row and compare these values to the maximum allowable threshold, as specified in the subsequent Section 6.2.4.3. Areas with values exceeding the threshold are identified as critical local vegetation density zones and are segmented and highlighted in purple in Figure 57 on the right.

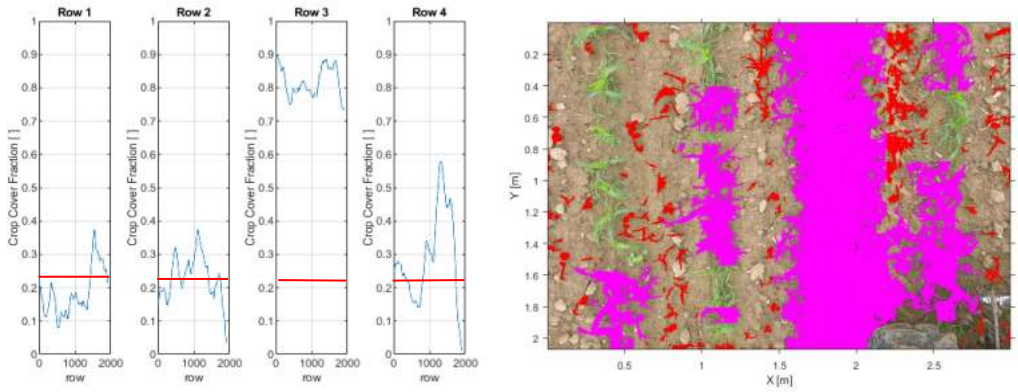

Figure 57. Segmentation of critical areas with LCF method. On the left: Histogram of the LCF measured for each crop-row. The red lines represent the threshold used to identify as highly infested areas those that exceed this threshold. On the right: result of the classification process, red areas represent inter-row weeds detected in the first step of the algorithm and the magenta-colored areas shows zones where the distribution of biomass along the row reaches defined critical levels.

6.2.4.3 Determination of Thresholds

The threshold used in colorimetric segmentation and those required to identify the areas to be treated are determined by running the calibration algorithms on an image of a clear field, where weeds are either absent or manually removed. Additionally, under these conditions, an initial estimate of the crop row positions is made, which will be updated during each successive pass of the treatment.

For segmenting the plant material from the soil, the ExG index is calculated to determine the threshold using Otsu's method. The threshold reflects the crop conditions and typical lighting levels at the time of imaging, so this calibration process should be performed at the beginning of each intervention. For this example, the determined ExG threshold is 60.8, meaning that all pixels with an ExG value greater than this threshold are classified as vegetation.

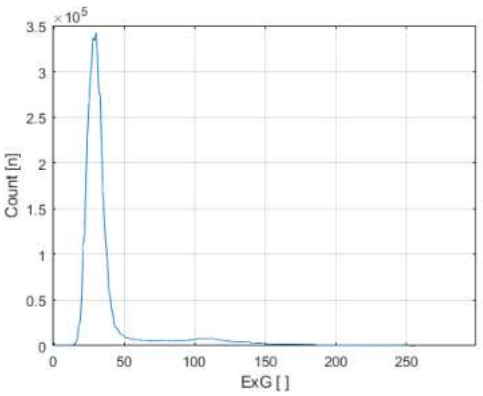

Figure 58. Frequency distribution of ExG single pixel values in the calibration frame.

To determine the thresholds used for treatments, both algorithms are executed, and the output is considered as the typical soil cover level of the crop at the time of the survey. This value is then increased by 5% to account for any minor differences in crop vigor in specific areas of the field and to prevent these variations from affecting the treatment decision.

For the MZ method (see Fig. 59a), the cover fraction is determined for each individual zone. The maximum value among the 8 zones is then selected and increased by 5%, resulting in a value of 0.13 in this example.

For the LCF method (see Fig. 59b), the peak value of the local cover fraction is extracted from all visible rows and similarly increased by 5%, resulting in a value of 0.28.

In conclusion, Figure 59c also illustrates an example of how the crop row positions are determined on the clean field frame.

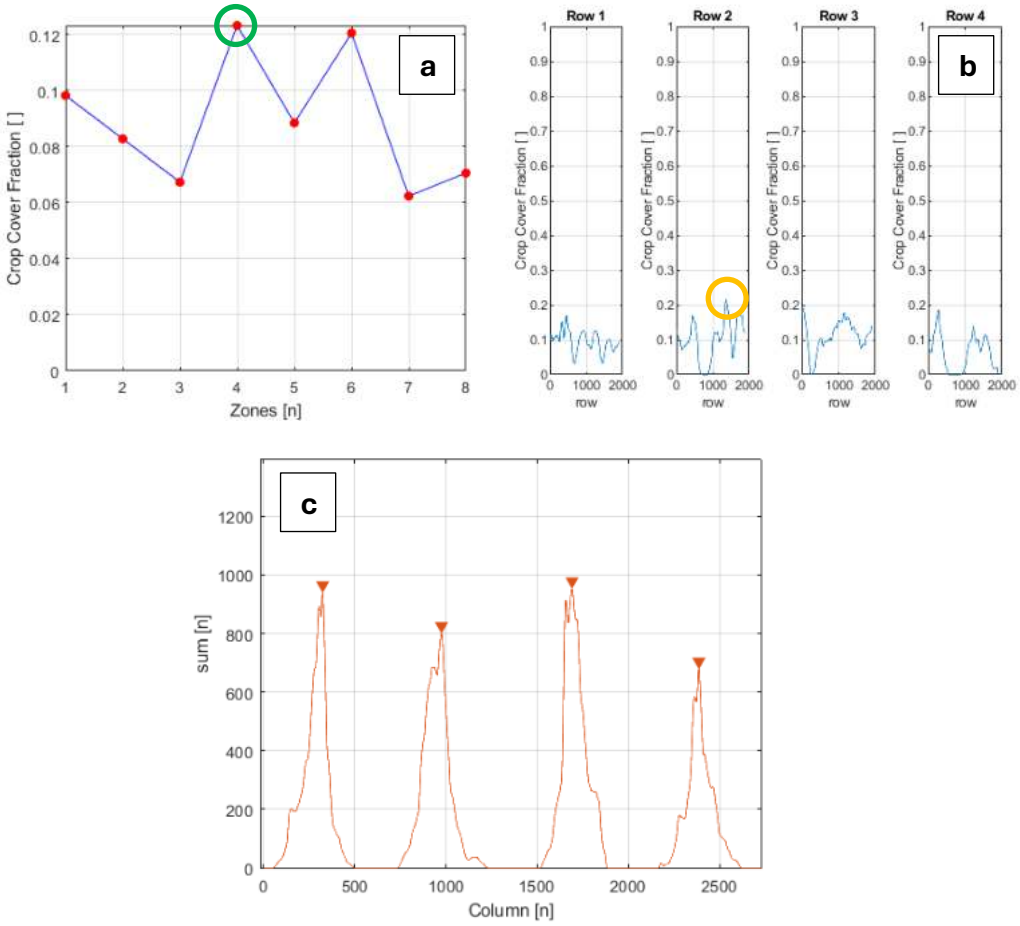

Figure 59. Determination of thresholds used for treatment. (a) FC measured in the 8 areas considered by the MZ method in the clean field image, useful to calculate the threshold used in the treatment. (b) LFC measured in the clean field image used to determine the threshold used in the treatment. The extracted value is highlighted in the green and yellow circles. c) Example of crop row position estimation extraction in the calibration frame where no weeds are present. In this case the positions of the individual rows are easily visible since the weeds are not present. Orange triangles indicate automatically determined peaks i.e. crop row position.

6.2.5 Ground Truth Image Labelling

To evaluate the performance of the algorithms under different infestation conditions, 15 images measuring 3 by 2 m were manually labeled. These images were selected based on three increasing infestation classes (low, medium, and high), classified according to its FC. The images were manually labeled by editing the pixel values, assigning blue (RGB [0, 0, 255]) to the crop pixels and red (RGB [255, 0, 0]) to the weed pixels. The labeled images were then used as ground truth to verify the performance and the impacts of the simulated treatments.

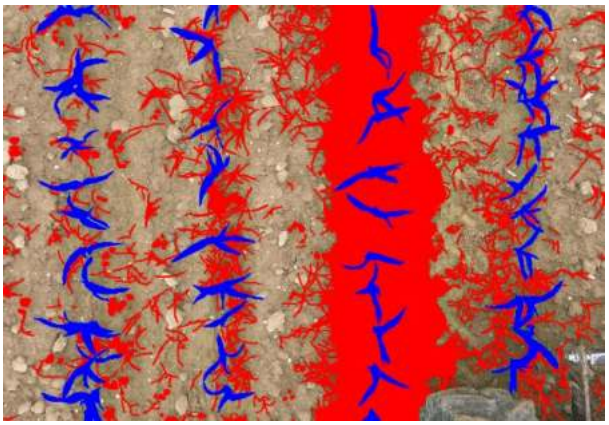

Figure 60. Manually labelled ground truth image. The areas labeled in red represent the weeds while the crop is labeled in blue.

6.2.6 Results Metrics and Environmental Impacts

The performance of the simulated treatments was assessed by calculating sensitivity, specificity, accuracy, and precision indices, evaluating the outcomes by overlaying appropriate binary masks. The treated areas were derived from the algorithm outputs (Treated). By overlapping these with the ground truth masks labeled as weeds, the mask of weeds hit by the treatment was obtained. The labeled images were thus used to generate masks for the crop (Crop) and weeds (Weeds) by segmenting them according to the RGB values used during the labeling process, as described earlier in Section 6.2.5. Below, the logical operations performed to obtain the values used for calculating performance indices and those related to the environmental impact of the operation are summarized in pseudocode.

```
Inputs: Binary Logical Masks (Treated, Crop, Weeds)
Frame Area(Fa) = size(I) rows * size(I) columns
Treated Weeds(TP) = Treated & Weeds
Treated Crop(FP) = Treated & Crop
Untreated Weeds(FN) = Weeds & (~Crop)
Untreated Crop(TN) = Crop & (~Treated)
Treated Area(Ta) = area(Treated)
Treated Soil(Ts) = area(Treated & ~(Crop|Weeds))/Fa
Logical Operators:
& = AND    ~ = NOT    | = OR
```

Figure 61. Pseudocode of the logical operations carried out to evaluate the performance indices of the treatments

The indices used to evaluate performance of the classification results were calculated as indicated below, using the values corresponding to the areas obtained from the combination of the binary masks described earlier. These indices allow for an assessment of the treatment's effectiveness by comparing the algorithm's output with the ground truth data, providing insights into the accuracy, precision, sensitivity, and specificity of the weed management approach.

$$Sensitivity = \frac{TP}{TP + FN} \quad [\ ]$$

$$Specificity = \frac{TN}{FP + TN} \quad [\ ]$$

$$Precision = \frac{TP}{TP + FP} \quad [\ ]$$

$$Accuracy = \frac{TP + TN}{TP + FN + FP + TN} \quad [\ ]$$

The index used to assess the environmental impact of the treatment is based on the determination of the amount of herbicide that misses its target and reaches the soil. This approach was chosen because herbicide that reaches the soil can cause environmental harm through various mechanisms, as discussed in Section 1.5.2. By calculating the amount of herbicide that affects the soil, the value provides a measure of the potential environmental damage that could result from the treatment. This consideration is crucial for understanding and mitigating the broader ecological consequences of herbicide application.

6.2.7 FC-dependent Intervention Modulation

To evaluate the intervention modulation capability of the different methods based on the infestation level in different scenarios, the outputs were compared in terms of sprayed area as the FC values increased. The modulation capability indicates the range of FC values within which the algorithm operates, differentiating it from the UD method where 100% of the surface area would be treated. The comparison highlights how effectively the algorithm reduces the treated area compared to a uniform application, especially in scenarios with varying levels of weed infestation.

6.2.8 Field Capacity Estimation

To assess the real-time applicability of the two algorithms, the field capacity (F_{cap}) was estimated by considering the sampled area in each frame and the average execution time (t_{exec}) measured across all conditions. The field capacity reflects how efficiently the algorithms can process data in real-time, which is crucial for their practical deployment in PA applications.

It should be noted that this value is purely indicative and depends on the performance of the machine on which the algorithms are executed. These values were obtained by running the script in a MATLAB environment using the PC1. Given the type of setup and the potential to further optimize the computation process with more powerful hardware and more efficient programming languages (e.g., C++), there is significant potential for improvement and reduction of the observed computation times in the test.

$$F_{cap} = \frac{(b_L \cdot b_a)}{t_{exec}} \cdot 0.36 \quad \left[\frac{ha}{h}\right]$$

6.3 Results

6.3.1 Ground Truth Images Labelling

Below is a summary of the image labeling process used for evaluating the performance of the different herbicide distribution methods. The images were divided into three distinct groups, corresponding to different levels of ground cover and thus varying intensities of weed infestation.

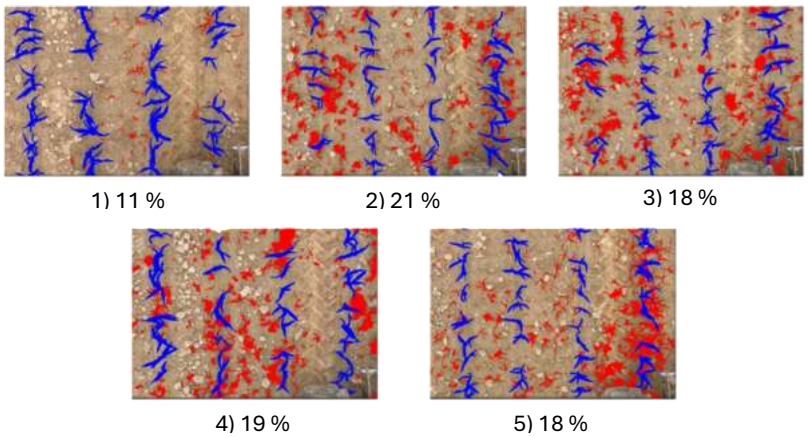

Figure 62. Results labeling on low level of FC images (FC < 22%). The areas labeled in red represent the weeds while the crop is labeled in blue.

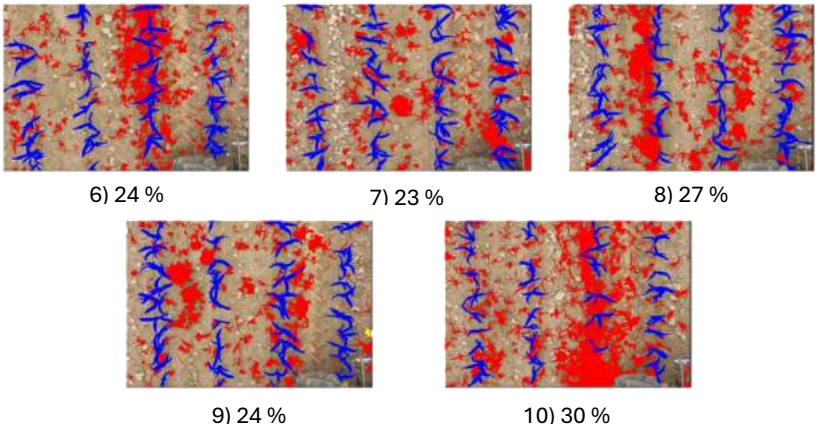

Figure 63. Results labeling on low medium of FC images (22% ≤ FC ≤ 30%). The areas labeled in red represent the weeds while the crop is labeled in blue.

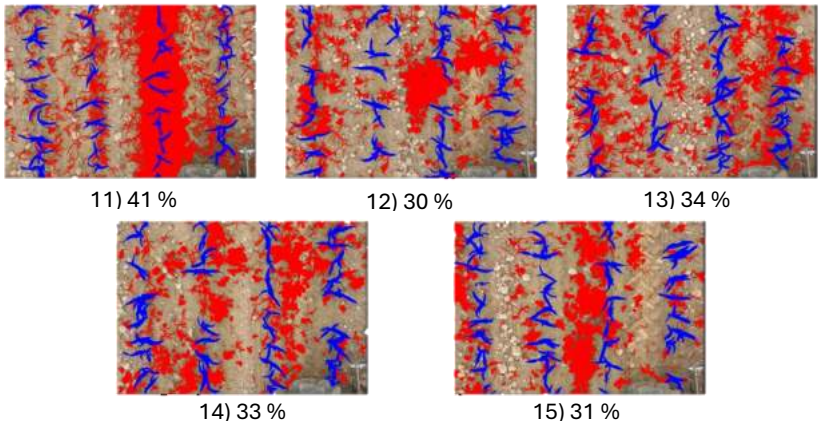

Figure 64. Results labeling on high level of FC images (FC >30%). The areas labeled in red represent the weeds while the crop is labeled in blue.

6.3.2 Treated Area

The results obtained from evaluating the amount of surface areas treated using different simulated methods are quite interesting. Figure 65 presents the average values obtained across all ground cover scenarios for each method, compared with the simulation of uniformly distributed treatment (UD).

The MZ method ensured an average reduction in the amount of herbicide used by 10% compared to the non-localized method, with quantities ranging from 25% to 100% across the different simulations. In contrast, the LFC method achieved a significantly greater reduction, with an average decrease of 45% compared to the non-localized method. In this case, the areas treated across different scenarios varied between 12% and 82%.

This evaluation highlights the different behaviors exhibited by the algorithms across the proposed scenarios. At first look, it appears that the reduction in the amount of herbicide distributed has indeed been achieved. However, these results must be supported by adequate levels of treatment efficacy. Therefore, in the following section, we will assess whether the reduction in the amount of herbicide used has compromised the overall effectiveness of the treatment.

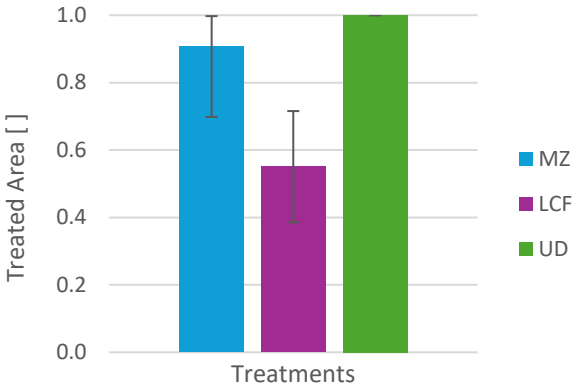

Figure 65. Average percentage of the sampled area treated in the simulations, representative of the amount of herbicide distributed.

6.3.3 Evaluation of Treatment Efficacy

This section presents the indices used to evaluate the performance of the simulated treatment. Specifically, the average values obtained by the different methods across the simulated scenarios are summarized in Figure 66.

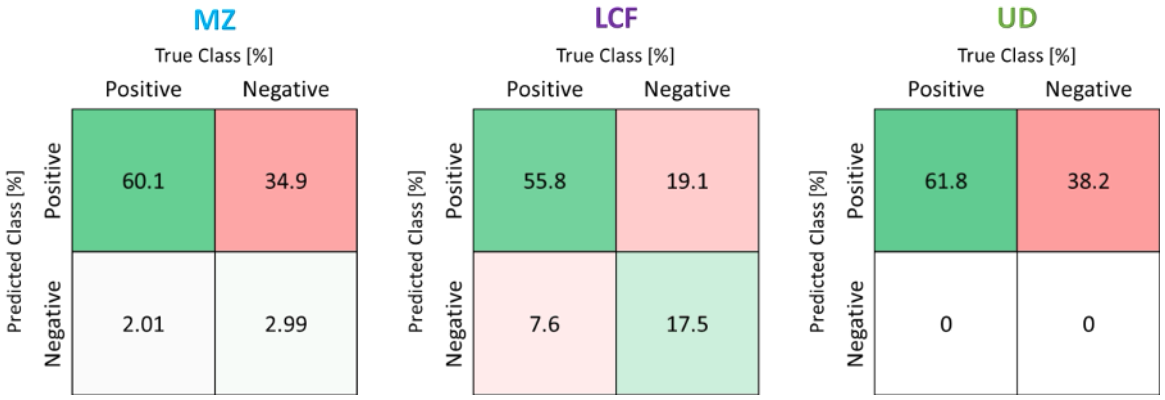

Figure 66. Confusion matrices of treatments based on 2D images. Values are given in percentages

Regarding sensitivity, the UD method has an average value of 1, as it uniformly treats the entire area, inevitably targeting all weeds present within the treated zone. The MZ method, on the other hand, achieves a sensitivity value close to that of the UD method, approximately 0.94, which is higher than the LCF method's average sensitivity value of

0.87. This reduction in sensitivity for the LCF method is due to the decrease in the area treated, which leads to some weeds being missed.

In terms of precision and accuracy, the proposed methods yield higher average values compared to the UD method 0.63 and 0.66 for the MZ method, 0.74 and 0.75 for the LCF method, respectively.

In conclusion, considering the treated area discussed in the previous section, it is evident that the LCF method achieved a 45% reduction in input, though it compromised sensitivity by 14%. This reduction was possible due to the high specificity achieved by the algorithm, which was not observed to be the same with the MZ method. For a more detailed analysis and comparison between the results obtained with these algorithms and those obtained with 3D sensing, refer to Section 8.5.

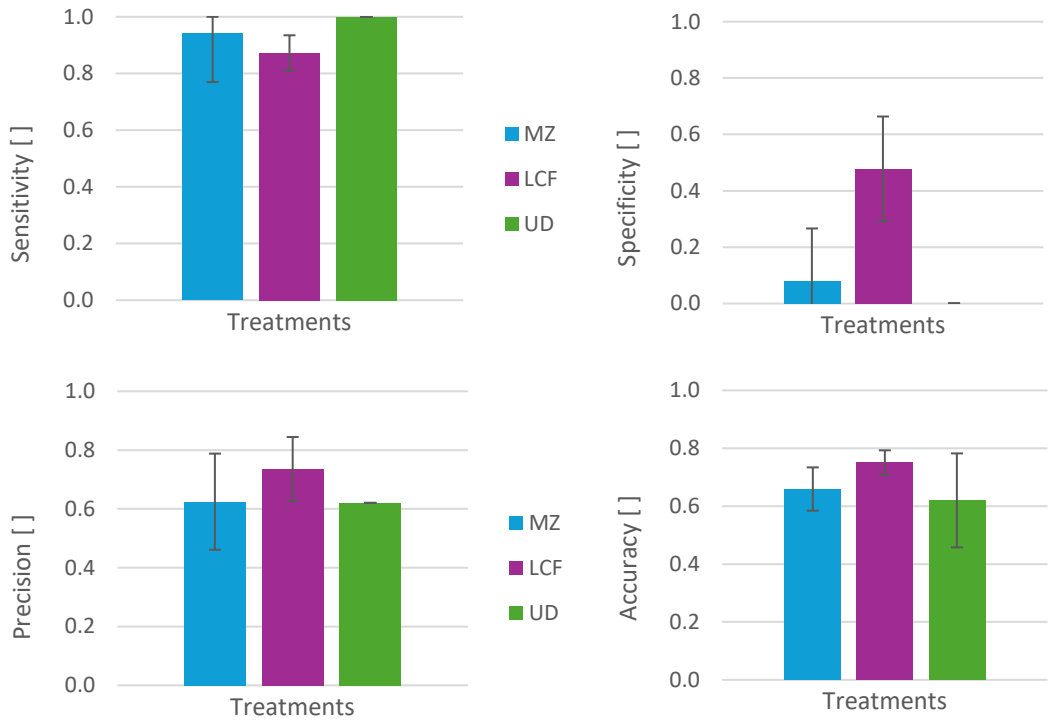

Figure 67. RGB-based algorithm performance indexes summary.

6.3.4 FC-dependent Intervention Modulation

From the analysis of the treated areas across different scenarios, and by examining the curves representing the percentage of treated surface, it becomes evident that the curve for the MZ method reaches saturation at an FC value of 19%. This indicates that,

beyond this FC threshold, the MZ method will tend to treat the entire area, behaving similarly to the UD method under these experimental conditions.

In contrast, the treatment curve for the LCF method shows a more gradual response with the treated area increasing in direct proportion to the rise in FC, without ever reaching saturation under the observed experimental conditions. Consequently, the LCF method offers greater input efficiency, supporting the algorithm's performance as demonstrated in the results.

Given that the experimental conditions did not lead to the saturation point for the LCF method, this level was estimated using the regression line derived from the observed values for the LCF method (see Fig. 69). By calculating the intersection point, it can be estimated that the LCF method would only reach a point of equivalence with the UD method at extremely high infestation levels, characterized by FC values reaching up to 49%.

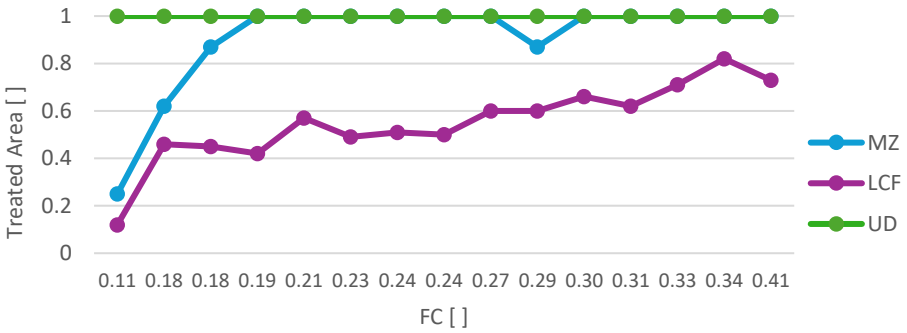

Figure 68. Intervention modulation using RGB-based algorithms.

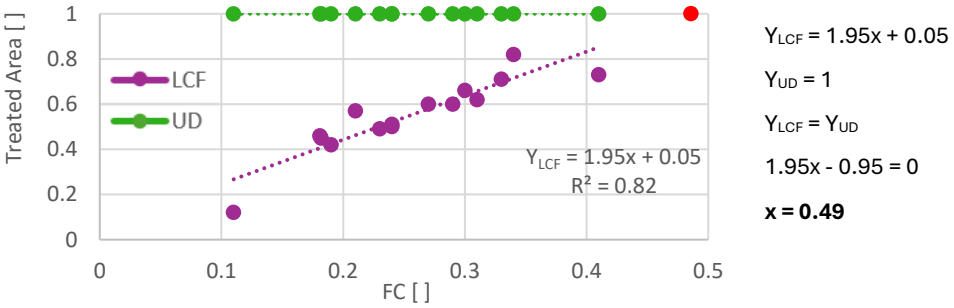

Figure 69. Point of indifference between the LCF and UD method.

Such FC values are indeed very high and generally occur infrequently in typical field conditions at the phenological stage considered in this study, which is when post-emergence herbicide application is usually performed. It is important to note that these infestation levels were primarily reached because no pre-sowing or pre-emergence herbicide treatments were conducted, which would have helped to keep the FC levels within more manageable ranges.

6.3.5 Environmental Impact Index

The results obtained regarding the environmental impact index confirm the effectiveness of the algorithms in reducing the amount of herbicide applied and increasing the precision of its application. Both methods resulted in less product waste by reducing the percentage of off-target distribution, which for the uniformly distributed method was 74%.

In the simulations, the MZ method reduced off-target product application to 66%, representing an 11% reduction compared to the uniformly distributed method. The LCF method performed even better, reducing off-target application to 35%, which corresponds to a 53% reduction in environmental impact compared to the uniform method. Therefore, both methods are suitable for contributing to the reduction of the environmental impact of post-emergence herbicide treatments.

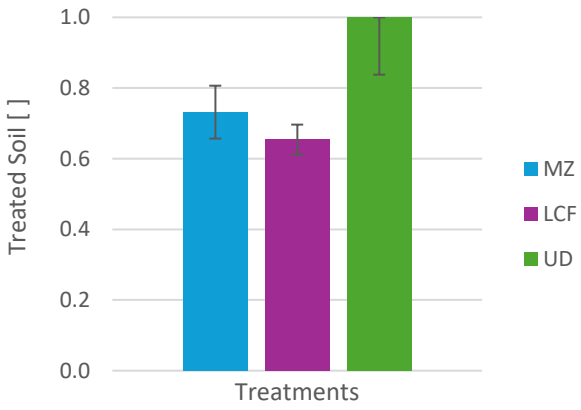

Figure 70. Environmental impact of the spraying operation assessed on the proportion of land sprayed.

6.3.6 Field Capacity Results

The estimated field capacities confirm the potential for real-time application of the algorithms. These capacities refer to a single acquisition module with a working width of 3 m. Typically, sprayers used for these treatments have bars ranging from 12 to 36 m in width. Therefore, the potential field capacity reported can be increased by employing multiple modules in parallel. Furthermore, implementing the algorithms on higher-performance single-board computers and deploying the code using more efficient programming languages (such as C++ or C#) would enable an additional increase in field capacity. This is due to the ability to support higher advancement speeds, thanks to faster execution times.

The results show that the MZ method has a higher field capacity due to its simpler algorithm, which requires less processing time (an average of 0.44 s). Its field capacity is 4.87 ha/h, and it can support a theoretical advancement speed of 16.4 km/h. In contrast, the LCF method has a lower field capacity, at 2.73 ha/h, given the average execution time of 0.8 s, which supports an advancement speed of 9 km/h. Assuming the use of four modules in parallel on a 12 m bar, the estimated average field capacities are 19.5 ha/h for the MZ method and 10.9 ha/h for the LCF method.

Table 1. Field capacity estimation results for MZ and LCF methods.

	[U.M]		MZ	LCF
Execution time	s		0.44 ± 0.02	0.8 ± 0.08
Field capacity	ha/h	1 module	4.87 ± 0.22	2.73 ± 0.27
		4 modules	19.5 ± 0.84	10.9 ± 1.08
Theoretical speed	km/h		16.4 ± 0.14	9 ± 0.5

6.4 Research Objectives Achieved

The two presented algorithms have shown potential for real-time application under field conditions, although there remains the possibility for performance improvement through integration with more advanced platforms. The LCF algorithm demonstrated better capability in modulating the intervention during simulations, leading to a substantial reduction in the amount of herbicide used (−45%) without compromising weed control effectiveness, achieving results like the UD method.

In terms of environmental impact, the LCF method achieved a reduction of approximately 53% compared to the UD method. Statistical analysis has confirmed the significance of these results, which will be further discussed in Section 8.5, which includes a comprehensive statistical analysis and a direct comparison of the 2D and 3D methods outcomes. In conclusion, the developed algorithms and their simulated treatments have proven suitable for real-time field applications due to the following reasons:

- The algorithms achieved sensitivity scores comparable to those of the non-localized method, ensuring the effectiveness of the treatment.
- They reduced the amount of the product used, with the LCF method showing particularly high efficiency in specificity.

- They decreased the environmental impact by reducing the amount of herbicide distributed to the soil.
- They demonstrated the ability to be used at typical operational speeds for such tasks, thus ensuring adequate field capacity for real-time application without compromising the timeliness of the intervention.

7 Laboratory-scale 3D Plant Characterization

The aim of this section is to identify the most significant geometric and morphological characteristics that can be used to make a classification based on these and make it possible to efficiently discriminate a crop from weeds. This analysis focused on the primary crop, *Zea mays L.*, during its early vegetative stages which correspond to those stages of development in which the post-emergency weeding intervention is carried out. Additionally, to assess which parameters are most effective for discrimination, data were also collected on the morphology of various weed species. These included monocotyledons such as *Echinochloa crus-galli L.* and *Lolium perenne L.*, as well as dicotyledons like *Solanum nigrum L.* and *Amaranthus retroflexus L.* These species are commonly found in the region and typically compete with the crop involved in the experiment.

The study specifically targeted the early growth stages of the crop because this period corresponds to the critical time for weed removal (CTWR). This window is crucial for developing an integrated weed management strategy that limits competition and protects crop yield at harvest (Nedeljković et al., 2021). Moreover, accurate characterization during these stages is vital to enable timely post-emergence chemical weed control interventions without harming the crop.

Data collection was managed using a single-axis linear actuator specifically designed for this purpose. This actuator was independently controlled by an Arduino Uno microcontroller, interfaced via USB with the PC1. Using the MATLAB development environment, the PC managed the movement of the sensor along a track positioned above the cultivation trays. This setup ensured extremely high positioning accuracy, allowing for the automatic periodic collection of data across the entire workspace with size 2.2 by 0.8 m. This arrangement facilitated sample revisiting, ensuring data comparability and perfect spatial and temporal alignment.

To carry out the data acquisition, the sensor was mounted on a support attached to the linear actuator, oriented perpendicularly to the cultivation trays, and positioned at a fixed height of approximately 1 m above the ground. This distance was selected as representing an optimal compromise to ensure good spatial resolution, capable of

detecting even the smallest plants for characterization from the early growth stages. It also prevents the plants from growing too close to the sensor, as they approach the minimum measurable limit of the depth sensor, which is 0.5 m.

7.1 Aim of the Experiment

The aims of this experiment are to enhance understanding of using the RGB-D sensor (Kinect V2) for plant characterization in a more complex environment and with many individuals observed at the same time. While the previous test involved observing one individual plant at a time, this experiment focuses on stitching together multiple point clouds. The goal is to better characterize the geometric and morphological traits of the plants involved in the experiment.

7.2 Materials and Methods

7.2.1 Plants Management

Plants were cultivated in greenhouse at the Department of Agricultural and Environmental Sciences, University of Milan (Italy) under controlled conditions: 24/20 °C day/night temperature, 60-75% relative humidity, and a 16-hour photoperiod.

The plants were seeded in six cultivation trays, each measuring 0.6 by 0.4 m. Two of these trays were dedicated to the crop, while the remaining four trays were used for different weed species. The trays were filled with a fertilized growth substrate, adequate to support plant growth throughout the experiment. After sowing, the trays were placed within the support structure of a robotic platform, which manages the movement of the sensor at an approximate distance of 1.1 m above the plants.

7.2.2 Plants Material

The plant material involved in this trial includes maize plants as the main crop and 4 weed species as potential targets that may be present in the field.

Maize was selected as the primary crop for this experiment due to its commercial importance and relevance in both the livestock and food industries. In Italy, maize

cultivation is primarily concentrated in the Po River plain, accounting for more than 88% of the total maize area in the country (ISTAT, 2023).

The variety used in this experiment is the Pioneer® 1817 hybrid, classified as FAO 700 - 133 days, and is typically used for grain, silage, and corn cob mix production. The plants were grown from sowing until the third/fourth leaf stage (VE to V4), reaching a height of between 0.35 and 0.4 m. This relatively tall height for the developmental stage is attributed to greenhouse conditions. The recommended field planting density is 8 - 8.5 plants/m^2 for grain production and 8.1 - 8.6 plants/m^2 for silage production (Corteva). Additionally, the plants were also grown at a higher planting density of approximately 20 plants/m^2. Although this density is much higher than that typically found in the field, it was useful for assessing the segmentation capability in extreme conditions, particularly when the phenological stage surpasses the third leaf and the crop becomes denser.

Figure 71. RGB top-view image of maize plants acquired with the automated platform.

Several weed species were also cultivated to examine their geometric characteristics and test their segmentation using the RGB-D sensor. Given their well-known differences, two monocotyledon and two dicotyledon species were selected, representing some of the most widespread and common weeds in Italian agricultural areas.

The genus *Lolium* belongs to the autumn-winter grasses, originally from Western Asia. These are tufted plants with a height ranging from 0.5 to 0.8 m. *Lolium* is characterized by a shallow root system, erect stems, and very thin, glossy leaf blades. This weed is prevalent in Italian regions and includes various species, among them *L. perenne*, *L. multiflorum*, and *L. rigidum*, all of which hold significant global agricultural importance, serving as both pasture crops and weeds (Matzrafi et al., 2020). Under severe infestation, *L. rigidum* can cause substantial yield losses, exceeding 30% in wheat (Lemerle et al., 1995), while field studies in barley have reported reductions of

up to 85% (Izquierdo et al., 2003). The development of herbicide resistance in *Lolium* populations further complicates control strategies, increasing the risk of yield losses.

The *Echinochloa* genus includes some of the most agriculturally significant weeds (Holm et al., 1977). Among them, *E. crus-galli L.,* commonly known as barnyardgrass, is a particularly notorious weed with a global distribution. It has successfully adapted to a range of temperate regions and anaerobic environments, such as rice fields and wetlands. Its broad ecological tolerance, characterized by its ability to mimic rice, rapid germination, swift growth, and prolific seed production, makes it a highly successful weed in over 60 countries (Barrett, 1983). Various management strategies, including intensive chemical control, are employed to combat infestations in rice production systems across multiple countries (Gibson et al., 2003). It has a tufted growth habit and can reach heights of up to 1.5 m. The plant can colonize a wide variety of agricultural systems, including rice, maize, tomatoes, soybeans, and sugar beets. It is a highly competitive weed that produces many seeds, which remain viable in the soil for a long time. Its staggered emergence makes it a particularly challenging weed to eradicate (Altop K. et al., 2010).

Solanum nigrum L., commonly known as black nightshade, is a widespread agricultural weed belonging to the Solanaceae family. It is an autumnal plant with an erect, highly branched stem capable of reaching a height of up to 0.8 m. This weed typically grows in various soil, posing a significant threat to a range of crops, including maize, sugar beets, grapes, tomatoes, potatoes, sunflowers, and various vegetables worldwide (Holm et al., 1977). Each plant can produce up to hundreds of seeds, which can remain viable in the soil for up to 20 years. This longevity is due to seed dormancy, which prevents germination even under favorable conditions.

The *Amaranthus* genus comprises approximately 70 predominantly annual species with a global distribution. Roughly 40 of these species are native to the Americas, while the rest are indigenous to other continents (Costea et al., 2001). In the Italian flora, there are 21 species from this genus, with the majority considered aliens, and some having become naturalized and invasive (Conti et al., 2005). Various amaranths can have significant ecological and economic impacts (Camarda et al., 2005). These

impacts include intense competition with crops, leading to decreased productivity and crop quality, as well as issues related to toxicity, damage caused by secondary chemicals, or the spread of pathogens (Iamonico, 2010).

A. retroflexus is an annual herbaceous plant belonging to the Amaranthaceae family. It reproduces via seeds and features an erect, woody stem at the base, typically light green in color. The plant commonly reaches a height of 0.8 - 1 m, with a bushy growth habit. The seeds produced by this plant have the unique characteristic of remaining viable in the soil for many years, making it particularly difficult to eradicate.

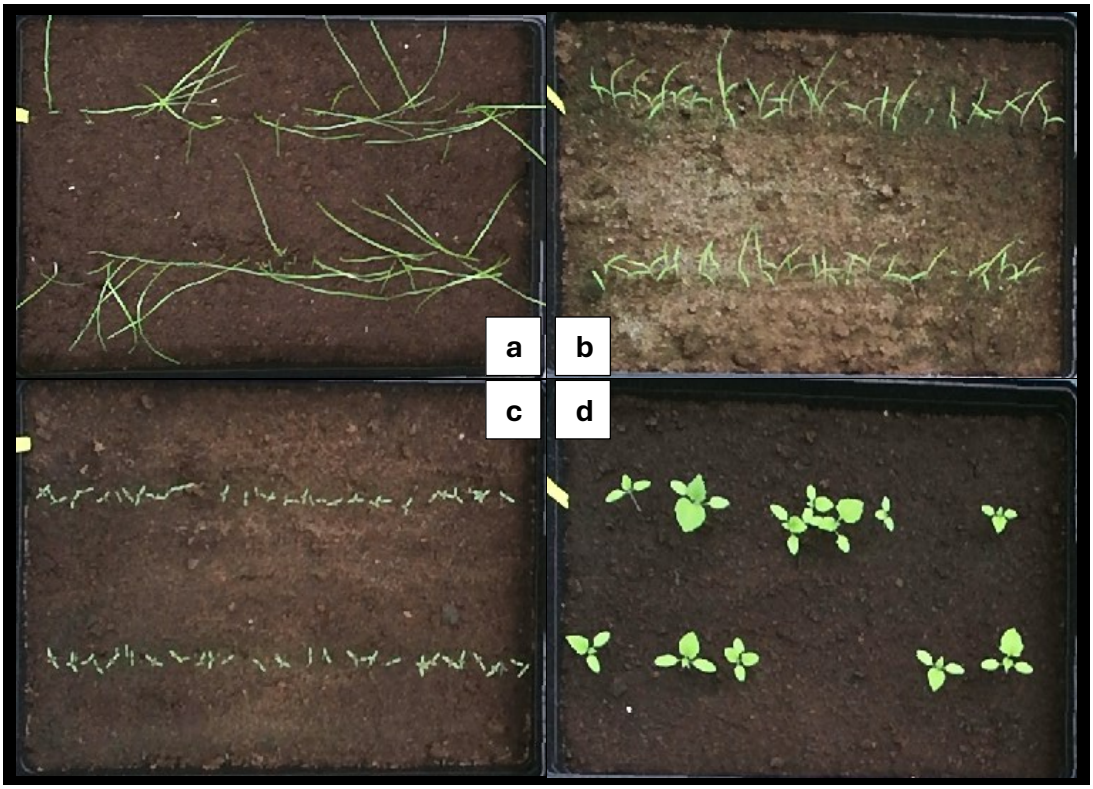

Figure 72. RGB top-view image of weeds plants acquired with the automated platform. a) Lolium, b) Echinochloa, c) Amaranthus, d) Solanum.

7.2.3 Sensor Carrier

The automated management system for the sensor movement was custom-built for the experiment using aluminum profiles (Bosch® Rexroth 20 by 20 mm), which are commonly employed in the construction of structural components for professional prototypes. The motorized sensor platform is a single-degree-of-freedom linear actuator that moves along two rails. The movement is driven by a toothed belt engaged with two aluminum pulleys. The driving pulley, installed at the motor end, is directly

coupled with the motor shaft, providing the necessary power to move the platform along the rails. The second pulley, mounted at the opposite end, is a freely rotating idler supported by a tensioning mechanism that ensures the proper tension of the synchronous belt, preventing slippage. This setup allows for precise and repeatable positioning of the sensor over the workspace.

Figure 73. Overview of the linear actuator with the sensor attached underneath on the moving platform. The two rails and the drive belt are visible.

The actuator used is a stepper motor, a type of motor widely employed in automation and robotics applications where high positioning accuracy is required (Aranjo et al., 2012). The specific stepper motor chosen for the prototype is a NEMA 17 model, which provides an angular resolution of 200 steps per revolution, corresponding to a rotation of 1.8° per step. This stepper motor can handle a maximum current of 1.5 A, making it well-suited for the precise and controlled movement needed in this experiment.

Stepper motors like the NEMA 17 are ideal for applications that demand exact positioning, as they move in discrete steps and can hold their position without the need for feedback systems like encoders. This characteristic ensures that the sensor platform can be accurately positioned along the rails, which is critical for obtaining consistent and reliable data during the plant monitoring process.

To use the motor, a power module (driver) is required, which receives energy from the power supply and controls the motor according to input signals from the microcontroller. The driver used in this setup is the MDD3A model produced by Cytron®, which is compatible with the chosen stepper motor and capable of handling motors with current draws of up to 3 A. This driver is essential for converting the low-power control signals from the microcontroller into the high-power signals needed to drive the stepper motor effectively. Its compatibility with the NEMA 17 stepper motor ensures that the motor can work properly.

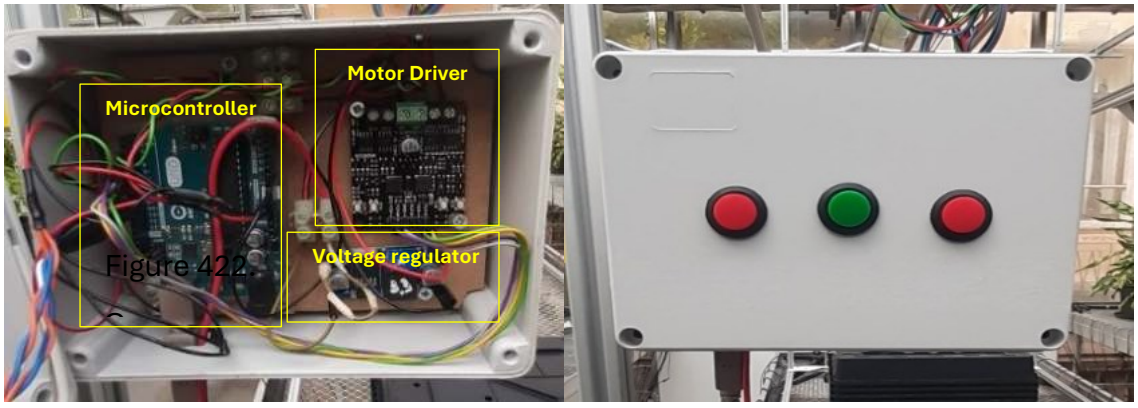

Figure 422.

Figure 74. Components of the control module. On the left are shown the microcontroller, the stepper motor driver and the voltage regulator. On the right: exterior of the assembled control module with buttons for manual control. The red buttons allow the platform to move, the green one to manually acquire images.

The platform can guarantee a displacement resolution of 0.2 mm (K_{conv}), which can be estimated as follows:

- Belt pitch $= 2 \ \frac{mm}{tooth}$
- Pulley tooths $= 20 \ \frac{tooth}{revolution}$

$$Belt \text{ development } = \text{Belt pitch} \cdot \text{ Pulley tooths } [\text{mm/revolution}]$$

- Belt development $= 40 \ \frac{mm}{revolution}$
- Motor resolution $= 200 \ \frac{steps}{revolution}$

$$\text{Displacement resolution } = \frac{\text{Belt development}}{\text{Motor resolution}} \ [\text{mm/step}]$$

- Displacement resolution $= 0{,}2 \ \frac{mm}{step}$

The prototype also requires two sensors known as limit switches. These are contact-activated switches that play a crucial role in preventing the platform from exceeding its predefined travel limits. Additionally, they are essential for the homing process, which is the initial calibration performed every time the machine is started. The limit switches ensure that the carriage does not move beyond its designated range, protecting the mechanical components from potential damage. During the homing process, the carriage moves until it is at this switch, allowing the system to establish a reference position. This process is vital for ensuring that all subsequent movements of the platform are accurate and within the intended operational boundaries. The use of limit switches is a standard safety measure in automated systems, ensuring both the precision and safety of the device.

The execution of the homing routine involves moving the carriage at a reduced speed until the upstream limit switch (home switch) is triggered. This event resets a counter responsible for managing the carriage's position. After the homing operation, the carriage's position can be monitored by checking the counter variable. Each pulse that moves the carriage forward corresponds to a clockwise rotation of the motor and increases the counter variable by 1. Conversely, the variable decreases by 1 if a pulse is generated that causes the carriage to move backward, resulting in counterclockwise motor rotation. By considering the displacement resolution mentioned earlier, it is possible to convert a linear position along the platform's travel into a counter value, which is treated as the target ($Target_{counter}$) to achieve the desired positioning, and vice versa.

$$Target_{counter} = \frac{Target_{metrics}}{K_{conv}}$$

The target value can be sent to the microcontroller, which autonomously generates the necessary pulses to rotate the motor with controlled speed (V_f) and acceleration (a), ensuring smooth movement and stopping of the carriage according to the equations of uniformly accelerated rectilinear motion. The kinematic calculations are performed by the microcontroller using the execution time of the main loop for integration, and spatial variables are measured in units based on the number of steps.

$$\Delta t = loop\ Execution\ time\ [\ s\ ]$$

$$Vf_{(t)} = Vi_{(t)} + (a \cdot \Delta t)\ _{[VMin\ :\ Vf_{(t)}:VMax]}\ \left[\frac{step}{s}\right]$$

$$Brake\ Space = \frac{Vf_{(t)}{}^{2}}{2a}$$

$$Vf_{(t)} = Vi_{(t)} - (a \cdot \Delta t)\ Vf_{\ (t)} = Vi_{(t)} - (a \cdot \Delta t)\ _{[VMin\ :\ Vf_{(t)}:VMax]}\ \left[\frac{step}{s}\right]$$

$$S_{(t)} = 0.5 \cdot\ (a \cdot \Delta t)^2 + Vi_{(t)} \cdot \Delta t + S_0\ \ [\ step\ ]$$

After the homing procedure, the platform can be operated either manually or automatically. In manual mode, the user can move the platform using the buttons on the control module and can trigger an acquisition at any time using the green button.

In automatic mode, the carriage receives instructions regarding its position and movement speed directly from the control station (Master), represented by the PC1. The components of the platform are managed by a microcontroller (Arduino Uno), which is specifically programmed for this purpose and capable of interfacing the platform with the Master via USB. This setup facilitates automated management of the platform missions and RGB-D image acquisition.

The desired positioning is achieved by sending a positional target, quantified in motor steps, from the master. This unit of measurement was chosen to simplify and streamline calculations based on integer values and for data encoding during transmission via USB.

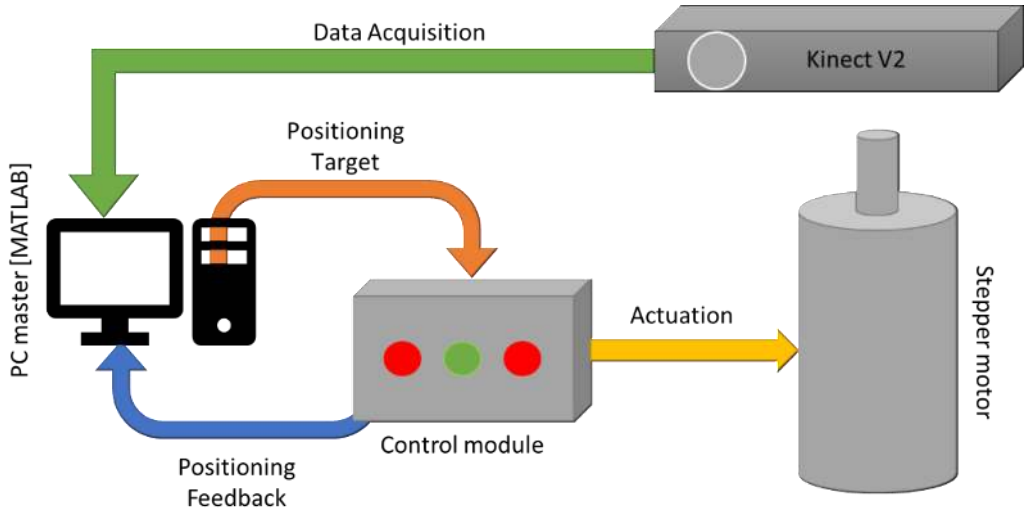

Figure 75. Main components and operating diagram of the automated platform.

The data transmission protocol uses encoding that casts the desired target value, encoded as a 16-bit unsigned integer (*'uint16'*), into two 8-bit unsigned integers (*'uint8'*) suitable for transmission via USB protocol. Below is an example of converting a 16-bit target value of 5000 into two equivalent 8-bit numbers (19 and 136), identified as the most significant byte (MSB) and least significant byte (LSB), respectively. The conversion process is graphically represented in Figure 76.

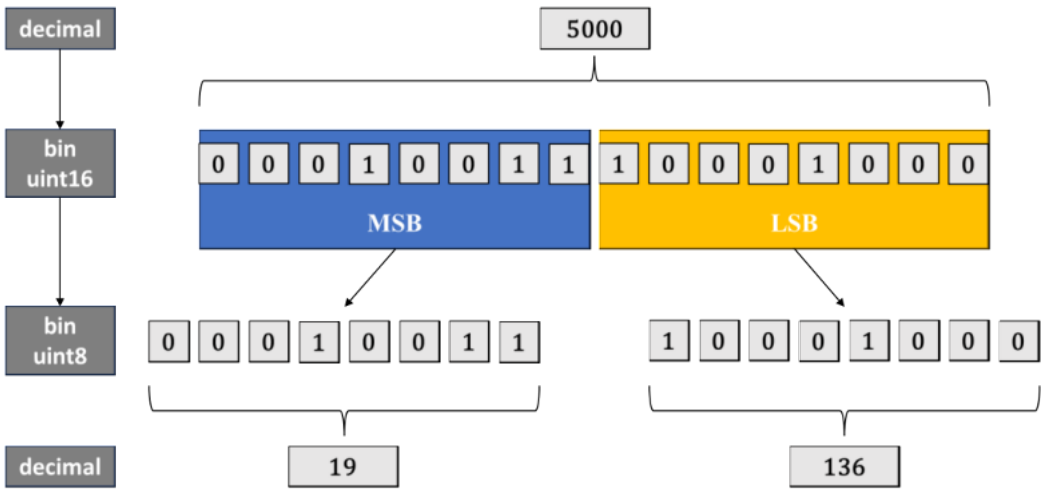

Figure 76. Example of target value casted for sending via serial communication.

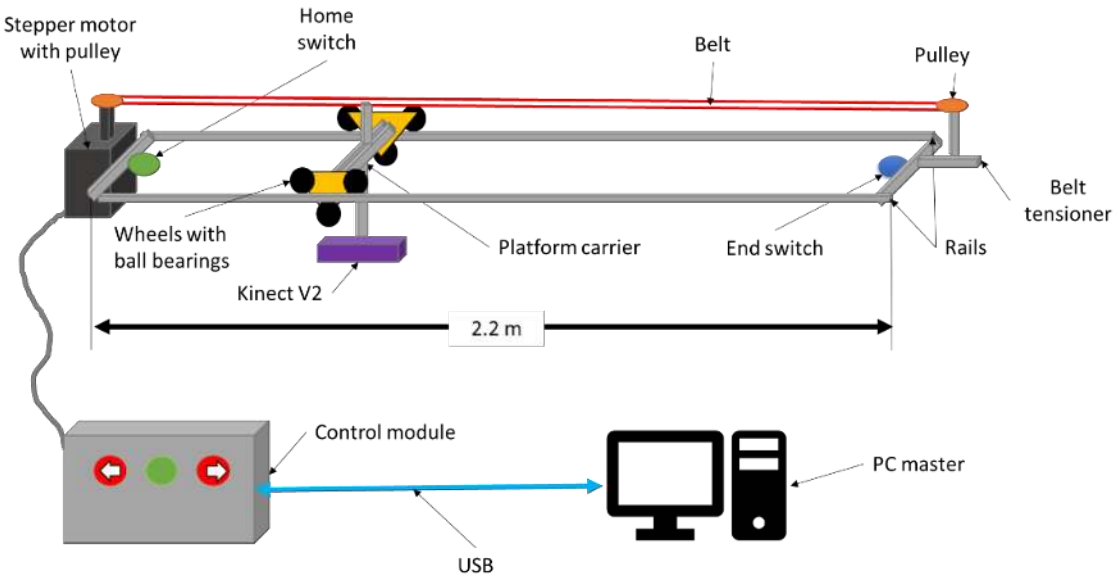

Figure 77. Automated platform components and operational diagram.

Each data acquisition mission involves an initial alignment and the sequential reaching of all pre-set waypoints. Upon reaching each waypoint, a color image and a depth image are captured, which are then converted into a point cloud. A typical acquisition mission requires the platform to reach 10 pre-set waypoints. Once all waypoints have been reached, the platform returns to its homing position. This process ensures that data is collected systematically and accurately at each specified location, allowing for consistent and reliable data acquisition across the entire workspace. The use of multiple waypoints allows for a comprehensive analysis of the plant structure, ensuring that all relevant morphological data are captured for subsequent processing and analysis.

Table 2. List of waypoints of a mission reported in metric unit and the related motor target numbers.

Acquisition [N]	Position [m]	Target [motor step]
1	0.09	450
2	0.27	1350
3	0.46	2300
4	0.64	3200
5	0.82	4100
6	1.01	5050
7	1.18	5900
8	1.37	6850
9	1.56	7800
10	1.74	8700

Here is the pseudocode for the scripts necessary to manage the operational logic of the control module and the master.

```
Control module
Input 1: Max acceleration
Input 2: Max deceleration
Input 3: Max velocity
Input 4: Target

Output 1: Position feedback

if serial available
 - check for a new target
end
 -Positioning error calculation
  while Absolute positioning error > 0
   -Positioning error calculation
    -Instantaneous Velocity
    if Positioning error > 0
     -rotate motor counterclockwise
      -send to master position feedback
    elseif Positioning error < 0
     -rotate motor clockwise
      -send to master position feedback
    else
     -send to master target reached feedback
     -wait until the master has finished
           the acquisition routine
    end
  end
```

```
Master
Input 1: List of waypoints
Input 2: Max acceleration
Input 3: Max deceleration
Input 4: Max velocity
Input 5: Position feedback

Output 1: Target

for each waypoint
 -Send desired position to
platform
 while the platform is moving
  -wait for correct
positioning
 end
  -RGB-D image acquisition
end
Return to home
```

Figure 78. Pseudocode of platform management. On the left: code of the platform control module (slave). On the right: handling of automated control by the master.

It should be noted that in this case, the control technique is open loop, meaning there is no sensor, such as an encoder, used for position feedback. Given the low rolling resistance ensured by the ball bearings, the lightweight nature of the platform and sensor, and thus the minimal torques involved, as well as the short data acquisition mission involving only a 2 m travel distance, this control strategy is deemed appropriate. The steps executed by the motor can be considered accurate and without slippage, which is why position feedback is based solely on the pulses sent from the microcontroller.

7.2.4 Data Processing

As a first step, the analysis involves reducing the noise in the depth channel. To achieve this, the raw point clouds were filtered by eliminating outliers using the method described in Section 3.2.3. Subsequently, a geometric transformation was

applied to each point cloud using MATLAB's *'pctransform'* function. This transformation includes the necessary rotation to convert the sensor's reference frame into the general reference frame (world) and a translation that accounts for the offset due to the sensor's position relative to the origin of the world reference frame. Specifically, this offset is 0.48 m along the X-axis (distance between the sensor and the origin along the X-axis), 1.07 m along the Z-axis (distance between the sensor and the ground in the cultivation tanks), and along the Y-axis by an amount corresponding to the platform's position during data acquisition.

After the roto-translation, the individual point clouds were combined into a single general point cloud through a merging operation using the MATLAB *'pcmerge'* function. This function returns a merged point cloud by applying a box grid filter in regions of overlap, in this experiment the size of the 3D box for the filter set to 2.5 mm.

Morphological parameter extraction was performed by starting from the general point cloud and segmenting clusters that identify individual plants whenever possible. This approach allows for the unique identification of single plants or specific areas, enabling them to be revisited on different acquisition dates. This makes it possible, for example, to identify the emergence time of individual plants, even if emergence occurs at different times.

The segmentation process occurs in two main steps. The first step involves selecting the vegetation by applying the same methodology described in Section 3.2.3 with the method based on colorimetric segmentation, using the ExG index.

Figure 79. Example of color-based vegetation segmentation.

The second step of the segmentation process involves distance-based clustering, which is achieved using the MATLAB function '*pcsegdist*'. This function segments a point cloud into clusters based on a minimum Euclidean distance between points from different clusters and assigns a cluster label to each point. In this case, a threshold of 0.02 m was chosen as the minimum Euclidean distance. Figure 80 provides an example of the clustering of individual maize plants, where the different clusters are represented by distinct colors corresponding to their labels.

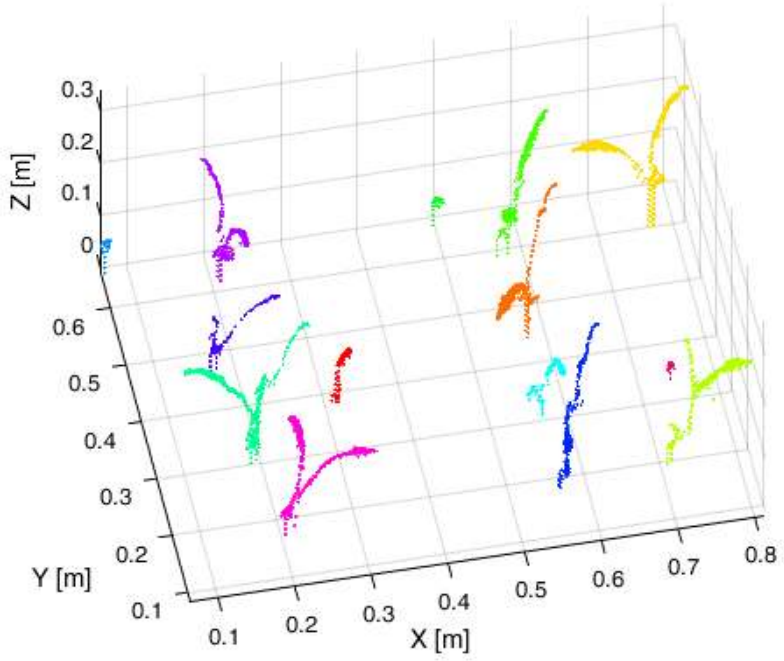

Figure 80. Distance-based individual clustering.

Following the clustering process, several geometric features can be extracted to characterize individual plants. Below is a list of the extracted features:

- Maximum cluster height: The maximum elevation reached by the cluster.
- Average height of the points within the cluster: The mean elevation of all points belonging to the cluster.
- Distribution of points along the Z-axis: The probability distribution of the Z-axis elevations for the points within a cluster, divided into bins of 0.01 m. This distribution helps in understanding how the points are spread across different heights.

- Horizontal shape: The polygon obtained by projecting the points of a single cluster onto the plane defined by the X and Y axes. The points along the outer edges of the projection are selected using the MATLAB function *boundary*.
- Bounding box surface: the surface of the quadrilateral that can ascribe the polygon.

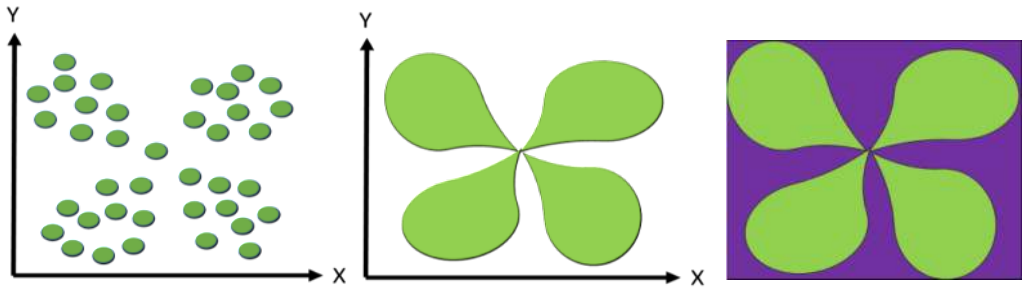

Figure 81. Example of geometric feature extraction. Starting from the left: single segmented cluster in format of point cloud; extraction of the polygon by identifying the boundary of the projection of the points on the X-Y plane with the specific MATLAB boundary function. From this polygon it is possible to extract the surface area or, as visible on the right, it is possible to generate the polygon of its bounding box (in violet) to check shape ratios i.e. for example the relationship between polygon area and bounding box area.

- Vertical shape: The polygon obtained by projecting the points of a single cluster onto the plane defined by the X and Z axes. The points along the outer edges of this projection are selected using the MATLAB boundary function. Before extracting the edges, a rotation around the Z-axis passing through the cluster's centroid is applied so that the maximum Feret diameter (the maximum distance between two points in the cluster on the X-Y plane) is parallel to the X-axis, ensuring that the most significant polygon is extracted, which maximizes the visible area.
- Surface area of the shapes: The area of both the vertical and horizontal polygons.
- Surface area of the bounding box: The area of the quadrilateral that circumscribes the polygon.

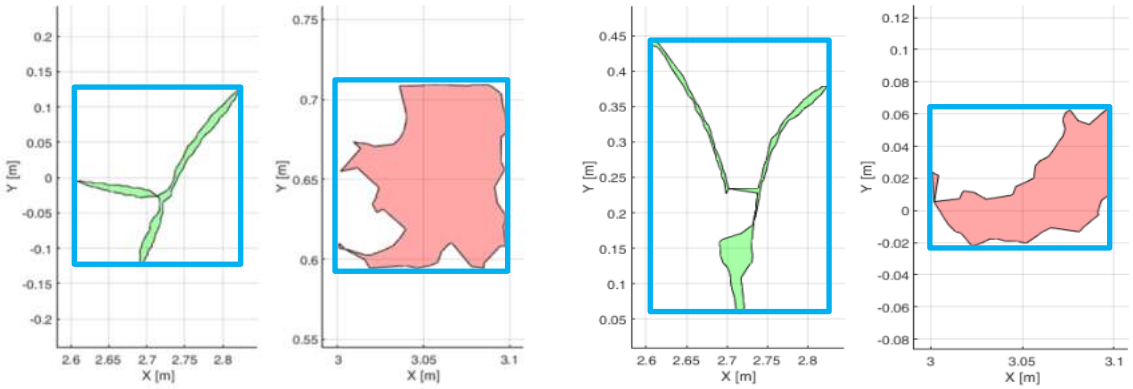

Figure 82. Example of feature extraction output (horizontal polygon (left) and vertical polygon (right) plus bounding-box (indicated in blue) of maize plants and a weed (Lolium perenne L.).

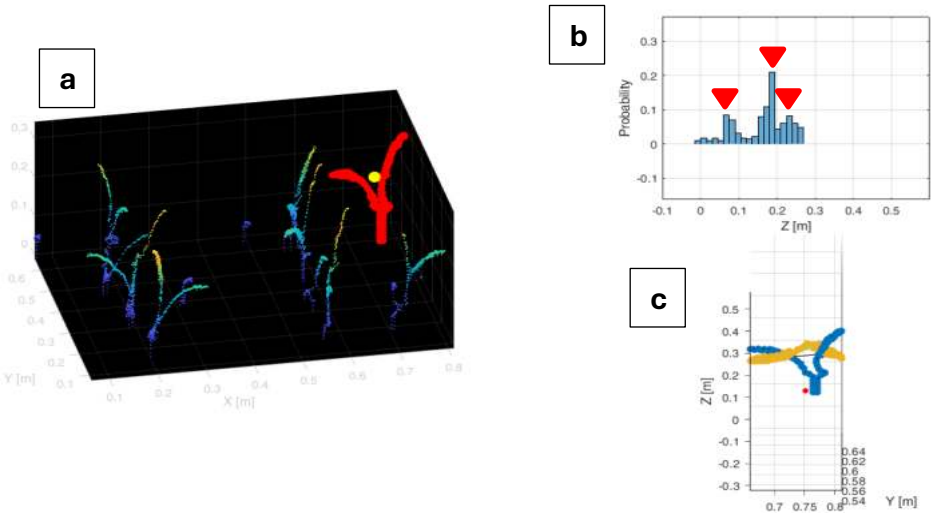

Figure 83. Example of semi-automatic validation interface output. a) example of a point cloud of maize plants segmented with maximum Euclidean distance. the selected point cloud on which feature extraction is taking place is highlighted in red. the yellow point represents the cluster center of gravity. b) distribution of points along the Z axis. The red triangles identify the position of the peaks. c) extraction of the vertical polygon in blue and horizontal in yellow.

The data related to the extracted features, belonging to the different clusters, were validated semi-automatically by developing a user interface. This interface displays the extracted point cloud and highlights each individual cluster to be examined, one at a time. For each isolated cluster, a preview of certain features is provided, such as the centroid position, the vertical and horizontal polygons, the distribution of points along the Z-axis, and the number of days since emergence. The interface also suggests an automatic species classification based on absolute position, which the user must validate by reviewing the displayed information for accuracy.

7.3 Results

7.3.1 Segmented point cloud

This section presents the results obtained from the segmentation and extraction of individual point clouds. The total number of clusters identified and validated during the experiment is 728, distributed among species as follows: 118 maize clusters, 191 Lolium clusters, 142 Solanum clusters, 131 Amaranthus clusters, and 146 Echinochloa clusters.

The following graph displays some point clouds from the different species involved in the experiment, providing a general view of their typical growth dynamics. The plot shows that maize exhibits a higher growth rate in height compared to the other species considered. This parameter has been identified as optimal for use in the discrimination process between crops and weeds, and it will be discussed in detail in Chapter 8.

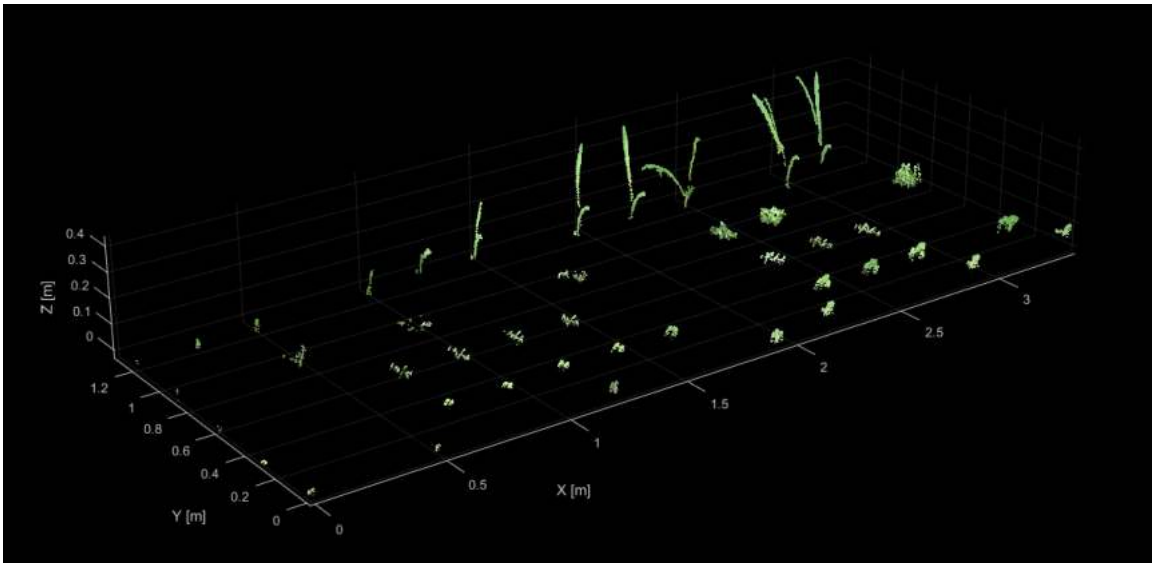

Figure 84. Example of point cloud extraction according to the emergence of the different species involved in the test. The clusters are shifted along the X-axis as a function of time since emergence..

The next Figure shows examples of the extraction of certain morphological parameters carried out on the individual clusters seen above.

Shape polygons obtained from the extraction of the vertical boundary (side-view) and the horizontal boundary (top-view) involving the crop and one of the monocotyledonous weeds in the first 12 days after emergence are shown.

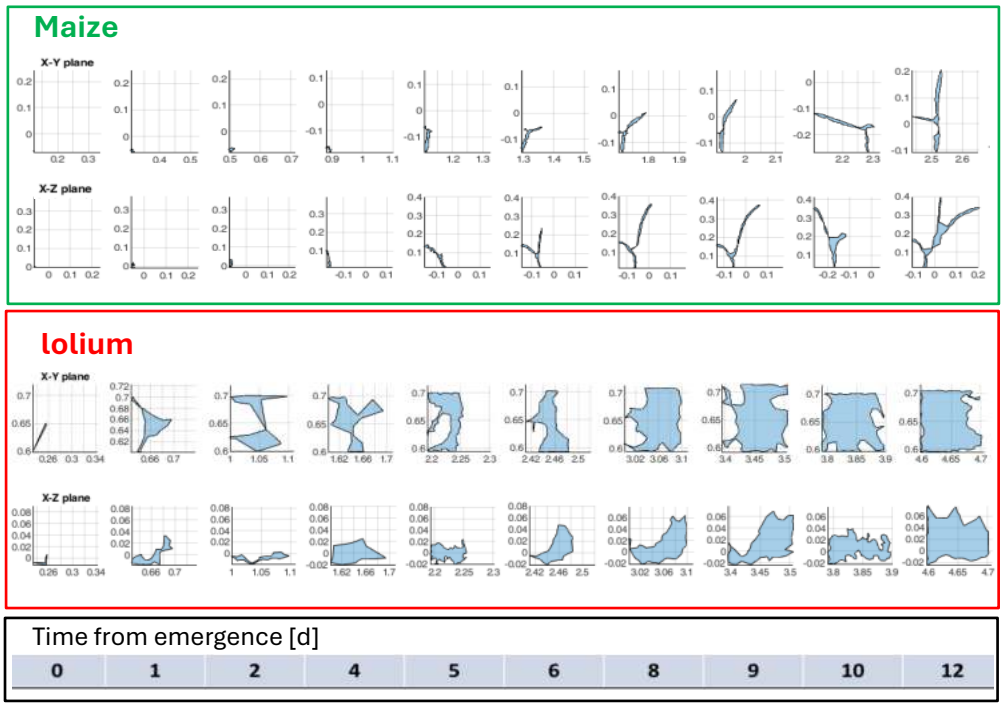

Figure 85. Example of horizontal and vertical shapes extracted in the first 12 days after the emergency for maize and Lolium.

7.3.2 Morphological parameter extraction

The extraction of morphological parameters has yielded interesting results. The mode of the heights within individual clusters, when compared at the same emergence time, becomes significantly different as early as the second day after emergence. This is due to the difference in the growth rate in height between maize and weeds, which can be effectively utilized in the discrimination process. Figure 86 presents the results for the first 12 days after emergence for both maize and weeds. The data for the weeds have been aggregated, as the intention is to achieve a dichotomous classification between the crop and the weeds. Similarly, the analysis of shape coefficients (especially the ratio of the area of the polygon to the bounding box containing it) also produced interesting results for both horizontal and vertical polygons. However, in this case, the discriminative capacity requires a bit more time, approximately 3 or 4 days, since this is the time it takes for maize to develop its first leaves in length, thereby reducing the values of both extent ratios.

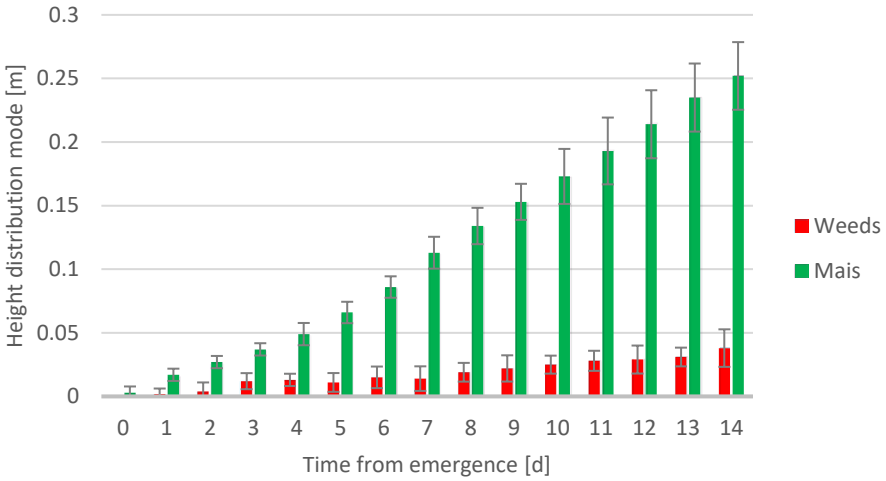

Figure 86. Evolution of height mode in the first 12 days after the emergence measured with depth data.

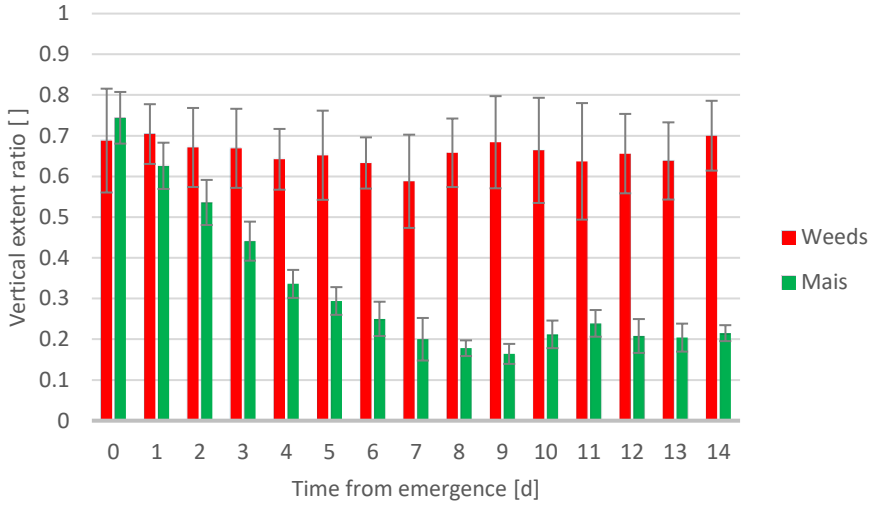

Figure 87. Evolution of vertical extent ratio in the first 12 days after the emergence.

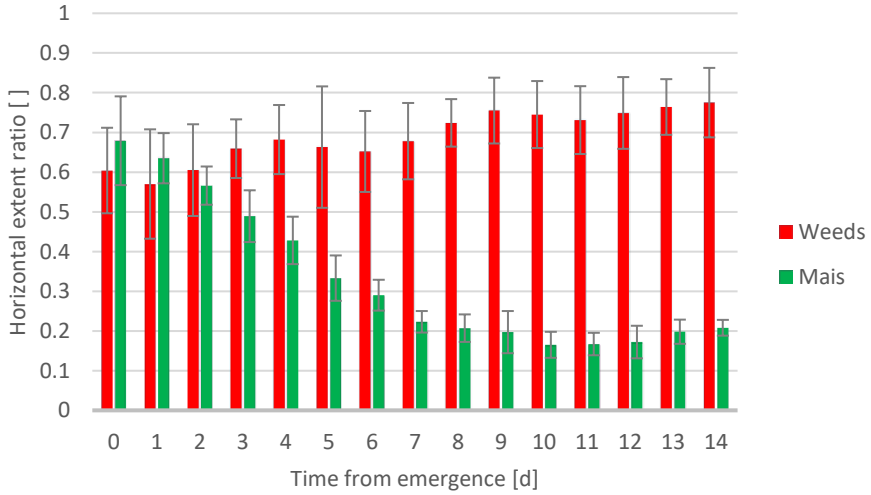

Figure 88. Evolution of horizontal extent ratio in the first 12 days after the emergence.

7.4 Research Objective Achieved

Data extraction and processing yielded satisfactory results. Among the parameters extracted, the trend of cluster heights, particularly the height distribution mode, representing the height where the greatest biomass of a plant is concentrated, proved to be especially promising for integration into real-time discrimination processes.

Regarding the shape extent ratios (obtained from top and lateral views), these also represent valuable variables for understanding plant structure and performing accurate discrimination. However, these variables could present additional challenges in field applications, as some clusters, unlike in this controlled study, may be only partially visible or poorly segmented, potentially compromising their representativeness in terms of shape.

This experiment was the first conducted during the doctoral studies and proved to be highly valuable to gain confidence with the sensor and develop analytical methods based on this type of data. Although not all the extracted features were ultimately used, this experiment provided the foundational basis for the subsequent development of other algorithms presented in the thesis.

8 3D-based Algorithm for Weed Detection in Maize

RGB-based algorithms for weed sensing in maize during the phenological stage of the crop (V3 → V5), it is crucial to effectively control weeds to reduce competition for the rest of the crop cycle. At this stage, especially with significant weed growth, it becomes more challenging to use 2D imaging-based sensing techniques to classify segmented vegetation as either weeds or crops. This task becomes particularly complex when weed presence and development are substantial, as it becomes difficult to accurately extract and distinguish the relevant features of individual plants. The introduction of 3D sensors can make this task less daunting by allowing the use of additional features based on depth data, thus making the classification process more accurate.

The decision was made to use color and height as the main discriminant variables employed by the algorithm for crop detection, considering the results obtained in the previous Section or by referring to similar studies, such as Andujar (Andujar et al., 2016). The integration of the shape feature did not yield the expected results because the segmentation technique used in the field does not allow for a point cloud clustering suitable for this purpose. For this reason, a positional feature was employed, which considers the position of the segmented elements relative to the crop row, like the 2D LFC method described in Section 6.2.4, where crop lines are detected using only the color channel, but in this case adding the depth information.

8.1 Aim of the Experiment

The objective of this section is to develop an algorithm capable of identifying crop positions within a workspace and detecting weeds present in that space. The goal is to evaluate, under field conditions, the impact of 3D sensor integration on the ability to discriminate between crops and weeds. In addition, the collected data will be used to create prescription maps for high-precision post-emergence herbicide spraying on maize.

The experiment involves collecting 3D data in motion by installing a stereo camera (StereoLabs ZED 2i, introduced in Sect. 2.2) on a tractor and developing an algorithm

to improve weed detection, particularly in challenging scenarios characterized by a high weed presence achieved by omitting pre-emergence control operations.

The weeds identified as targets will be used to simulate potential control strategies based on two hypothesized methods of action. One proposed strategy considers all detected weeds as valid targets for treatment (Treat All Weeds - TAW), while the other strategy considers a target valid only if there are more weed points than crop points within the workspace single nozzle (Treat Weeds in Majority - TWM). The aim is to evaluate the outcomes of these different control strategies and compare them with the results that would have been obtained by applying a uniform herbicide distribution.

Furthermore, this work also considers the possibility of a high precision distribution of biostimulant (BlueN®, see Sect. 8.2.8) via foliar application. The goal is to assess the feasibility of site-specific applications to reduce operational costs by minimizing waste due to soil distribution and limiting the undesired effect of promoting weed growth that could occur with non-localized distribution. This operation could be carried out simultaneously with herbicide spraying, as the biostimulant has been tested by the manufacturer in mixtures with various pesticides, fertilizers, and adjuvants. Therefore, a combined application using a dedicated spraying line would be feasible.

To enable on-the-go distribution control, it is essential that the algorithm be developed considering for the execution time required for classification. After conducting several trials, the analytics were developed using binary masks whenever possible, minimizing complexity and the use of point cloud data. MATLAB offers a wide range of dedicated functions for point cloud manipulation, which are very useful but often computationally expensive. For example, the *'pcsegdist'* function, used for distance-based clustering and point counting, is useful for dividing points into clusters to study centroid positions or shape coefficients (as discussed in Sect. 7.2.4). However, it requires computation times that are incompatible with real-time field applications. For example, another function (*'pcnorm'*) is useful for calculating surface normals, which could help recognize maize leaves based on insertion angle and position, but this too demands significant computation time.

8.2 Materials and Methods

8.2.1 Experimental Site

The experimental activity was carried out within a plot of the experimental farm of the University of Milan “A.Menozzi” located in Landriano (PV) (Italy, 45°319 N - 9°265 E). The crop (*Zea mays L.* hybrid P1916 FAO 600) was sown on June 4, 2024 with 0.70 m row spacing and the monitoring was carried out on July 11, 2024 when the crop was at the V3-V4 stage at the right time to execute a post-emergency weeding treatment. No chemical or physical weeding was carried out prior to the survey.

8.2.2 Sensor Management

The 3D sensor was mounted on the rear of the tractor using the three-point hitch, supported by a custom-built structure made from 45 mm Bosch Rexroth aluminum profiles, fixed 90° joints and adjustable joints capable of rotating around an axis. This setup was designed to provide the necessary degrees of freedom for adjusting the sensor's height and positioning it directly above a crop row. This positioning enables the acquisition of both RGB images and depth maps of the area occupied by the crop, including the lateral inter-row spaces, thereby making the system easily scalable. Additionally, one of the rotating joints was designed to allow variation in the sensor's pitch angle relative to the ground, facilitating trials with different angles. Following these trials, the configuration that enabled top-view acquisition, with the sensor maintained parallel to the ground, was chosen. Considering the height development of the plants at the time of data collection, the sensor was installed at an elevation of 1.3 m above the ground, ensuring a minimum distance of 0.5 m between the plants and the sensor.

The data acquisition and processing were conducted using the PC2 through the development of dedicated scripts in MATLAB environment.

Figure 89. Field operational configuration of the sensor assembly support

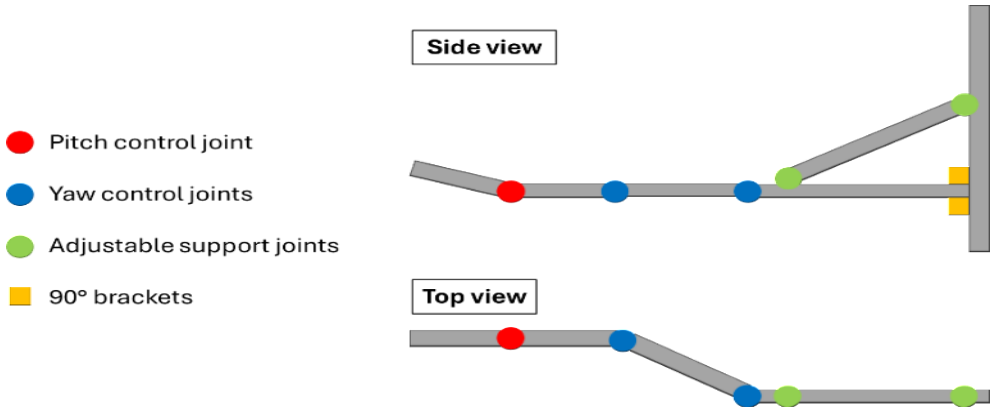

Figure 90. Adjustable sensor support, design diagram.

8.2.3 Crop and Weeds Binary Classification

Building on the premise discussed in previous Section, which established that maize plants, given the same time since emergence, tend to accumulate biomass at relatively higher elevations and at a much faster rate than weeds, especially in the early vegetative growth stages. Moreover, considering that any mechanical operations necessary for soil preparation for planting can also be designed to inhibit weed development and effectively allow the simultaneous emergence of both crops and weeds, it was decided to develop an algorithm based on prior experiences with 2D image processing, where the primary feature identified for separate the inter row vegetation (weeds) from the row vegetation (potential crop) was the crop row position.

In this case, the raw images (color and depth) will undergo pre-processing to clean the data and adjust the axis orientation before being processed for classification.

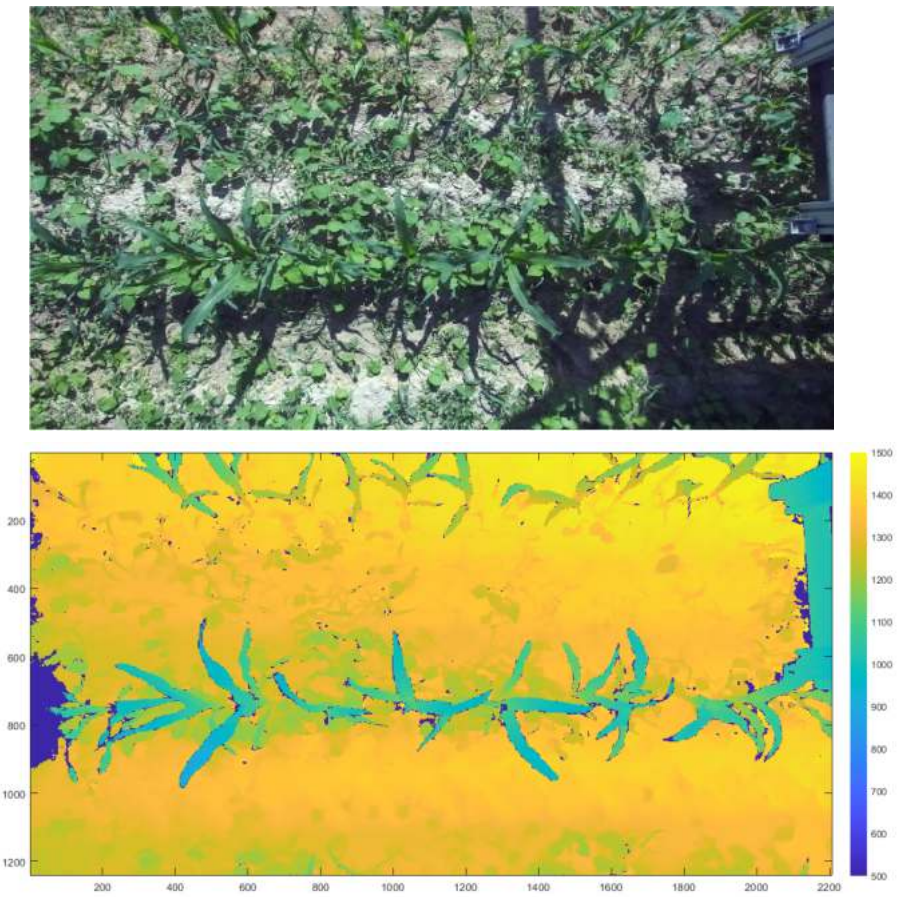

Figure 91. Top image shows an RGB image. Bottom image shows a depth map acquired with Zed 2i in field conditions.

8.2.4 Data Pre-processing

The weed detection algorithm involves a preprocessing phase, where the first step is to transform the raw depth data to achieve the correct orientation of the reference system axes, ensuring that the Z-axis represents the height above the ground. This transformation is accomplished using data from the onboard sensors of the stereo camera, which include an accelerometer, gyroscope, and magnetometer. The output provides pitch and roll values of the sensor, which are used to perform the necessary rotation to restore the correct orientation of the reference axes during the field test. The initial phase of the analysis involves generating a binary mask resulting from colorimetric segmentation (*maskColor*), based on applying a minimum threshold to the ExG vegetation index (described in detail in Sect. 3.2.3) and utilizing a threshold value determined by Otsu's method.

Additionally, the RGB image was used to detect edges by first converting it to grayscale and then using it as input for the '*edge*' function, which is based on the Canny method. This method detects edges by identifying local maxima in the gradient of the grayscale image.

Figure 92. Overlay of the color mask shown in yellow on the RGB image.

The subsequent phase focuses on creating the effective workspace by filtering out all points outside of the area of interest. This is achieved by generating a binary mask ($mask_{WS}$) based on the distance from the center of the frame along the X-Y axes, with the goal of standardizing the sampled area in each frame and excluding certain areas near the edges that are characterized by lower quality due to high noise levels recorded with this setup. Given the optical characteristics of the sensor, the height at which it was installed, and the plant height at the time of measurement, a workspace of 1.5 m along the row axis (X) and 1 m along the Y-axis was chosen. Since the initial location of the row is unknown, the workspace mask is initially generated using arbitrary boundaries, with an added tolerance of 50 mm for the first segmentation (*Ktoll*). The actual $mask_{WS}$ is then recalculated after locating the row, using the matrix of orthogonal distances from the row, referred to as $Dist_Y$.

Within the sampled area, it is necessary to clean the data from noise and potential outliers. For this purpose, a binary mask ($mask_G$) is generated based on the gradient variation of the depth map, excluding points with a total gradient exceeding 250 mm (K_d), a threshold determined as the 95th percentile of the gradient value distribution, excluding values equal to 0. This approach enhances the segmentation capability of

elements at higher elevations. The mask is generated by applying the maximum threshold K_d to the output of the '*imgradient*' function, using the depth map as its input.

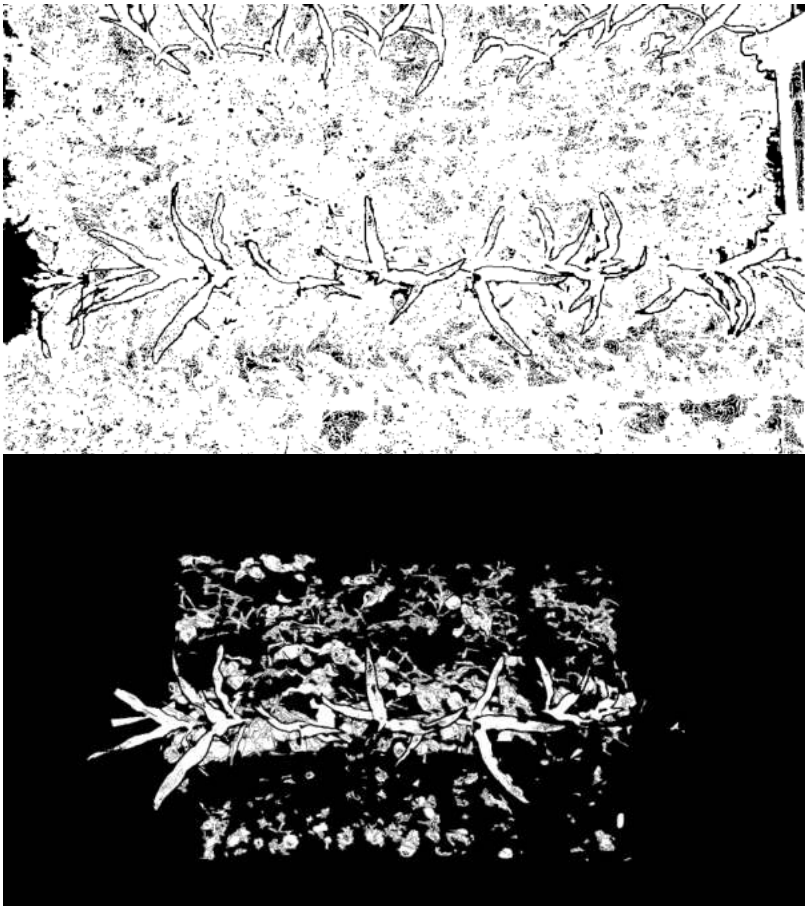

Figure 93. Segmenting with stereo camera. Above is shown the result of applying the gradient filter, below the result of also applying the color mask.

8.2.5 Crop Row Detection

The primary advantage of employing 3D sensors lies in their ability to determine row position information with greater accuracy compared to the method on 2D RGB sensing described in Sect. 6.2.4.1. Previously, with RGB imaging crop row positions could be accurately identified in cases of medium to low infestation levels with adequate level of accuracy. However, as the level of infestation increased, an accurate detection of crop rows with 2D imaging became challenging, requiring the use of the average position estimated in previous frames to make detection more robust. This method, however, is not highly reliable, particularly in compensating for minor misalignments caused by the operator's steering during the survey or by the

imperfect linearity of the sowing rows, which affects trajectory corrections made by the operator during sowing operations.

In this Section, a method is proposed for determining row position, which involves calculating a threshold value using Otsu's method. This threshold is used to separate the upper parts of the vegetation, which is likely predominantly part of the crop, from lower vegetation, which includes both some crop parts and primarily weeds. To calculate this threshold, it is necessary to evaluate the height frequency distribution of the segmented points from the pre-processing phase. The data are discretized into homogeneous height intervals of 20 mm using the *histcounts* function. The segmentation of points that must be considered in the frequency distribution of the heights values is done by multiplying the depth map with a mask obtained by performing a logical AND operation between $mask_{Color}$, $mask_{G}$, and $mask_{WS}$, followed by an appropriate conversion to single precision to match the depth map format. The distribution obtained through this process is used as input for the calculation of the Otsu threshold (OtsuH) using the MATLAB function *otsuthresh*.

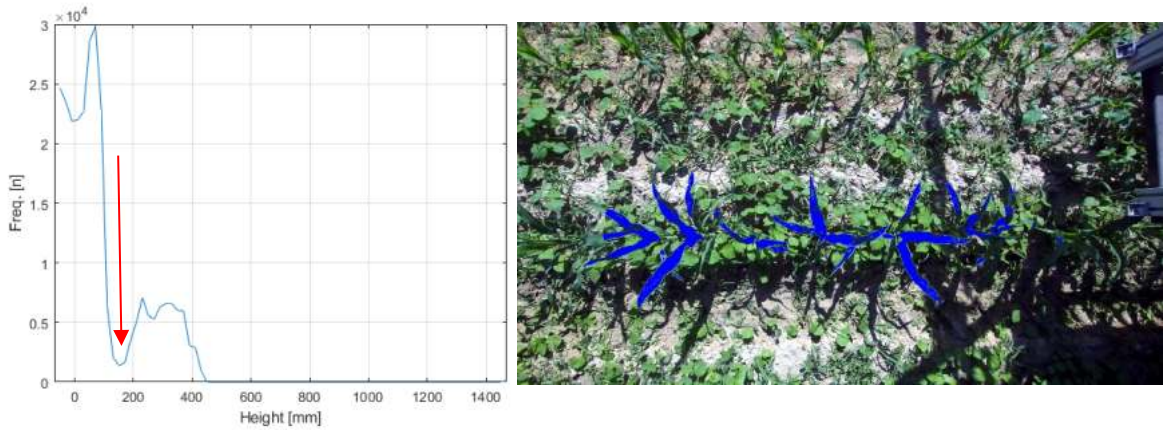

Figure 94. Result of segmentation based on height. Left: height frequency distribution used for threshold calculation using the Otsu's method. The red arrow indicates the threshold identified in this example. Right: overlay of the height-based mask, in blue are showed segmented pixels as high vegetation.

By segmenting the points with a height greater than *OtsuH*, it is possible to accurately estimate the position and orientation of the crop row (*CropLine*) by fitting a straight line using the *polyfit* function. This function takes the X and Y coordinates of the segmented points as input and provides the linear model ($Y = mX + q$) as output. This line is used to determine the current position of the crop row, which is essential for compensating for any misalignment between the camera and the crop, as previously described.

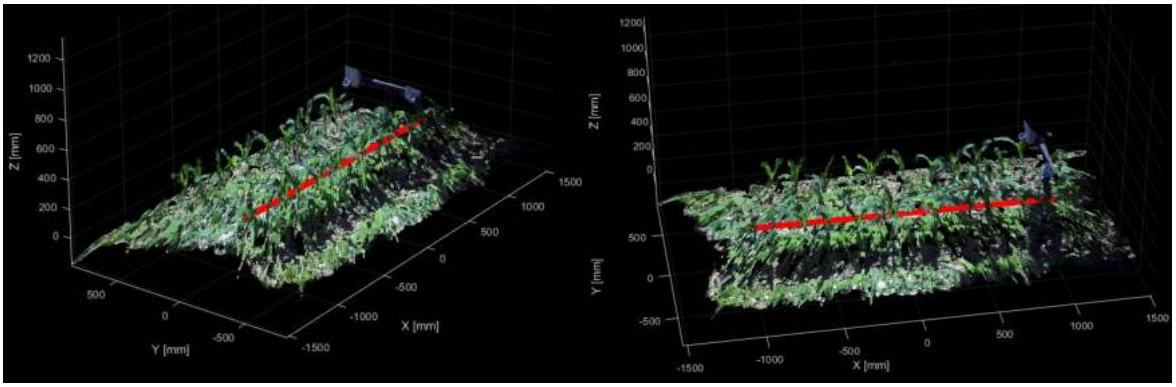

Figure 95. Example of estimating the position of the crop line in a situation of high weed infestation

Determining the position of the crop row is essential for identifying several important features that will be used during the discrimination process. These features include the relative distance of the points from the *CropLine* ($DistY_{rel}$) and the Euclidean distance from the line at the *OtsuH* height ($Dist_{otsu}$). As mentioned earlier, $DistY_{rel}$ is necessary for defining the actual workspace and for determining the operational areas of individual actuators during treatment simulations.

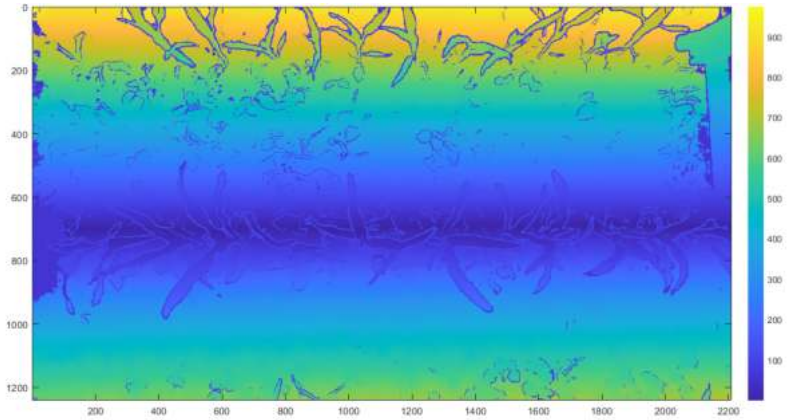

Figure 96. Estimated crop-row distance map.

8.2.6 Detection of the Near Crop Row Volume

The next step involves identifying the vegetation within a specific volume defined by the space located at a distance less than ($0.5 \cdot OtsuH$) and this will be defined as $Near_{Crop}$ vegetation, as indicated by the distance matrix $Dist_{Otsu}$. This volume will likely contain all the parts close to the stem of the crop plants, vegetation with generally higher heights near the center of the row, and some of the taller weeds that are centrally located relative to the crop row.

Identifying this volume using a binary mask ($mask_{VolOtsu}$), where $Dist_{Otsu} < Near_{Crop}$, serves a dual purpose. First, it isolates this volume by disrupting the continuity of blobs

present in the global color and gradient masks, a common occurrence in cases of high infestation, and second, it provides a region for applying the flood fill technique to the segmented blobs in $mask_{high}$, procedure, which will be discussed in more detail in the following section.

Figure 97. Segmentation of the near crop-row volume.

8.2.7 Binary Classification

The classification method involves treating the image regions with heights above *OtsuH* ($mask_{high}$) separately from those below ($mask_{low}$). The high region is processed using both the $mask_G$ and the $mask_{Color}$ previously applied during the pre-processing phase. This approach aims to maximize the segmentation potential offered by the depth channel for high elevations. In contrast, the low region is segmented by applying an additional mask that excludes edges identified in the color channel. Edges in the color channel are chosen for the low region to enhance the segmentation capabilities, particularly for smaller plants. This is because color channel edges are better suited for distinguishing different elements in the scene compared to the depth channel, where small discontinuities are less effectively detected due to their similar heights.

The flood fill technique involves selecting all pixels connected to a specific chosen point. In this case, this technique is employed after individually labeling the blobs present in the $mask_{high}$ using the '*bwconncomp'* function. This function outputs a list of pixels belonging to each individual blob. By selecting the first pixel from each of these lists, its position index is used to expand the selection to all connected pixels in the mask ($floodFill_{WS}$), which results from the logical OR operation between $mask_{high}$ and $mask_{VolOtsu}$.

The blobs thus selected are classified as crop ($mask_{Crop}$), while the remaining blobs are classified as weeds ($mask_{Weed}$). All masks are then filtered by the minimum blob size using the '*bwareafilt*' function, which imposes a minimum area of 25 pixels. This step eliminates potential clusters that are either very small or represent imperfections in the color or depth masks.

Figure 98. Overlay of the points with heights above the Otsu's method threshold, shown in blue and the volume mask of the near crop row volume in magenta. These masks are used as input for the application of the flood fill technique to segment the crop.

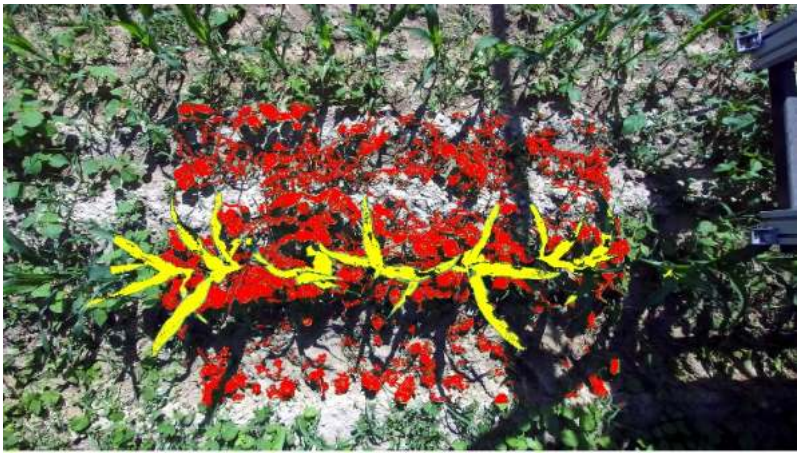

Figure 99. Example of binary crop-weed segmentation. An overlay is shown highlighting pixels classified as crop in yellow and those classified as weeds in red. The highlighted area corresponds to the workspace of 1 m x 1.5 m.

To conclude this section, Table 3 is presented detailing all the steps of the algorithm used for classification. The table shows the description of each step, the inputs used in each step, the conditions imposed and their outputs.

Table 3. Summary of all the steps needed to get the binary classification.

	Operations description	Input	Conditions	Output
1	Definition of the preliminary workspace	raw point cloud	abs(X < 750) & abs(Y < 500 + 50) [mm]	$mask_{XY}$
2	Rotation of points with sensor data orientation feedback	point cloud raw & sensor data	-	transformed point clud
3	Depth gradient calculation and gradient based masking	depth	depth gradient < 250 mm & depth gradient > 0	$mask_{G}$
4	Color mask with ExG and Otsu theresholding	RGB image	EG > Otsu'method threshold	$mask_{Color}$
5	Color to Grayscale and edge calculation	grayscale image	Edge with Canny method	$mask_{Ed}$
6	Histogram counts of the value of green points height inside the workspace with bin step of 20 mm	H matrix, $mask_{Color}$, $mask_{XY}$	H.* single($mask_{Color}$).*single($mask_{XY}$) > 0	histogram counts
7	Calculation of the height threshold with Otsu's method on histogram counts	histogram counts	-	OtsuH
8	Selection of points with height greater than the OtsuH threshold and the regression line	H matrix, $mask_{Color}$, $mask_{XY}$	H > OtsuH	$mask_{high}$, crop row model
9	Calculation of the orthogonal distance from the crop row model	crop row model	-	$DistY_{rel}$
10	Definition of the treatments workspace	$DistY_{rel}$	abs(X<750) & abs($DistY_{rel}$<500) [mm]	$mask_{WS}$
11	Calculation of the Euclidean distance from the cropLine placed at a OtsuH height	crop row model	-	OtsuRowDist
12	Segmentation of points with distance lower than half of OtsuH	OtsuRowDist	OtsuRowDist < 0.5 * OtsuH	$maskVol_{otsu}$
13	Check $mask_{high}$ pixel 8-connectivity and flood fill the connected blob of $maskVol_{otsu}$	$mask_{high}$, $maskVol_{otsu}$	8-connected blob	floodFilled
14	Classify as weeds all the blob with an area greater than 25 pixels that falls into the workspace and with an height less than OtsuH which are not connected with the high parts of the plants	$mask_{low}$, floodFilled, $mask_{WS}$	$mask_{low}$ &~ floodFilled & $mask_{WS}$	$mask_{Weed}$
15	Classify as crop all the floodFilled blob with an area greater than 25 pixels that falls into the workspace	floodFilled, $mask_{WS}$	floodFilled & maskWS	$mask_{Crop}$

8.2.8 Treatments Simulations and Intervention Strategies

The simulation of treatments involves using a section of spray bar of 1 m in length, equipped with 5 fan nozzles with a 20° spray angle. When installed at a height of 0.57 m, these nozzles cover a working area of 0.2 m, as detailed in Figure 100. This setup corresponds to the micro-spraying configuration used in treatment simulations on 2D images. The individual working areas of each nozzle ($mask_{tr(i)}$) were determined by dividing the $mask_{WS}$ into 5 zones based on the distance matrix from the crop line ($distY_{rel}$), as summarized in Table 4.

Table 4. Individual nozzle workspace masks.

Noozle	Workspace
1	$mask_{tr(1)} = (distY_{rel} > -0.5 \,\&\, distY_{rel} < -0.3) \,\&\, mask_{WS}$
2	$mask_{tr(2)} = (distY_{rel} > -0.3 \,\&\, distY_{rel} < -0.1) \,\&\, mask_{WS}$
3	$mask_{tr(3)} = (distY_{rel} > -0.1 \,\&\, distY_{rel} < 0.1) \,\&\, mask_{WS}$
4	$mask_{tr(4)} = (distY_{rel} > 0.1 \,\&\, distY_{rel} < 0.3) \,\&\, mask_{WS}$
5	$mask_{tr(5)} = (distY_{rel} > 0.3 \,\&\, distY_{rel} < 0.5) \,\&\, mask_{WS}$

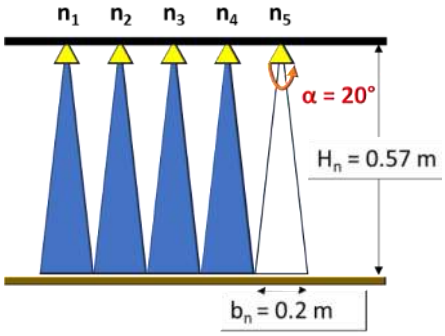

Figure 100. Micro-spraying design used for treatments simulations.

Regarding weed control treatments, two different strategies were hypothesized. The first strategy involves treating all targets identified by the algorithm as weeds (treat all weeds - TAW), representing the standard approach for comprehensive weed control. The second strategy (treat weeds in majority - TWM) applies treatment only when

weeds are detected in quantity exceeding that of the crop within the working area of an individual nozzle. The purpose of implementing this dual control strategy is to assess the impact of modifying the treatment rules on the effectiveness of the intervention.

The treatment, i.e., the areas where an actuator needs to be activated, is determined as a binary digital signal (1 = high or 0 = low). To achieve this, a binary treatment mask ($mask_{trW(i)}$) is generated by combining the working area mask of each individual actuator ($mask_{tr(i)}$) with the weed mask using a logical AND operation. For each nozzle's mask, a column-wise summation is performed by identifying the columns where $sum(mask_{trW(i)}) > 0$. The output of this logical operation functions as a 0-1 signal, which, when synchronized with the forward movement via an encoder, can be used to control solenoid valves.

For the TWM method, in addition to the procedure described above for $mask_{trW(i)}$, the same process is carried out by overlaying the workspace mask of each actuator with the crop mask ($mask_{trC(i)}$) using a logical AND operation. In this case, the signal is generated when $sum(mask_{trW(i)}) > sum(mask_{trC(i)})$, as illustrated in the example provided in Figure 99. The biostimulant treatment is managed according to the condition $sum(mask_{trC(i)}) > 0$. To simulate the treatment and evaluate the results obtained, all areas within the workspace of each individual nozzle that were in a region where the signal was positive, according to the defined rules, were considered as treated and thus assigned a 'true' value. This generated the corresponding mask, with the treated areas indicated in yellow in Figure 102.

To verify the effects of the simulated implementation strategies, a uniformly distributed intervention (UD3D) was simulated.

Table 5. Summary of the actuation rules. When the conditions are met, the signal for the actuators is generated.

	TAW	TMW	Biostimulant
Treatments rules	$sum(mask_{trW(i)}) > 0$	$sum(mask_{trW(i)}) > sum(mask_{trC(i)})$	$sum(mask_{trC(i)}) > 0$

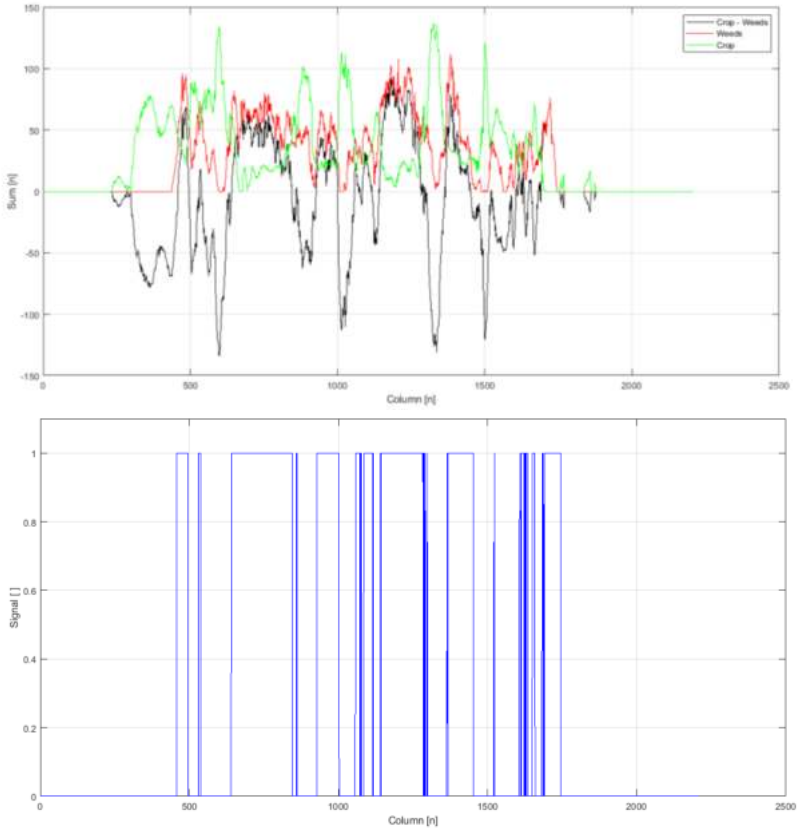

Figure 101. Implementation rules. Above are the sums per column of the masks used to trigger treatments. The crop summation is shown in green and the weed summation in red. The black line indicates the crop-weeds difference and is calculated to generate the implementation signal shown in the figure below in blue. The example for the TMW strategy is shown here. The signal will be true in cases where weeds > crop.

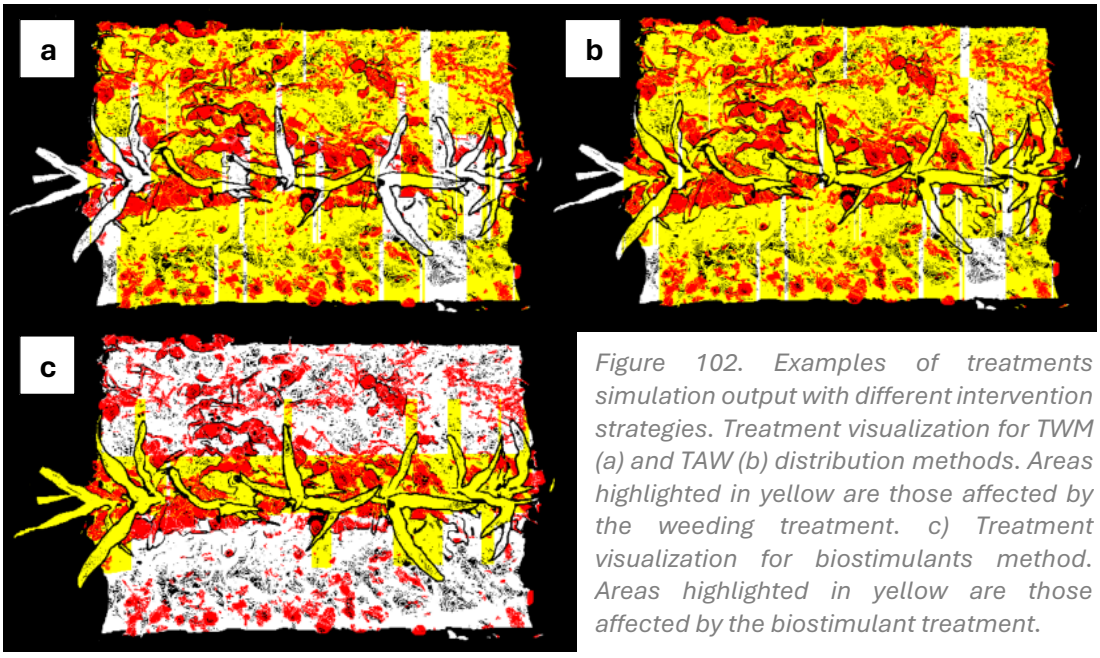

Figure 102. Examples of treatments simulation output with different intervention strategies. Treatment visualization for TWM (a) and TAW (b) distribution methods. Areas highlighted in yellow are those affected by the weeding treatment. c) Treatment visualization for biostimulants method. Areas highlighted in yellow are those affected by the biostimulant treatment.

8.2.9 Results Metrics

The results were evaluated using sensitivity, specificity, precision, and accuracy indices, calculated as described in Section 6.2.6. The amount of product distributed was calculated by considering the amount of surface area covered by the treatment and the impact on the soil by considering the proportion of soil that was treated. The ground truth used for calculating performance indices (*maskCropValid* and *maskWeedValid*, shown in blue and red respectively in Fig. 103) was obtained by manually labeling the binary mask resulting from a logical AND operation between $mask_{WS}$, $mask_{Color}$, and $mask_{G}$. This preliminary step of creating masks for labeling was necessary because the 3D data filtered for workspace and gradient are not directly comparable with the labeling results of the color mask. 3D data lack numerous pixels, and thus, directly labeling the color image, as was done previously for the 2D treatment evaluations in Section 6.2.5, would have led to inaccurate assessments.

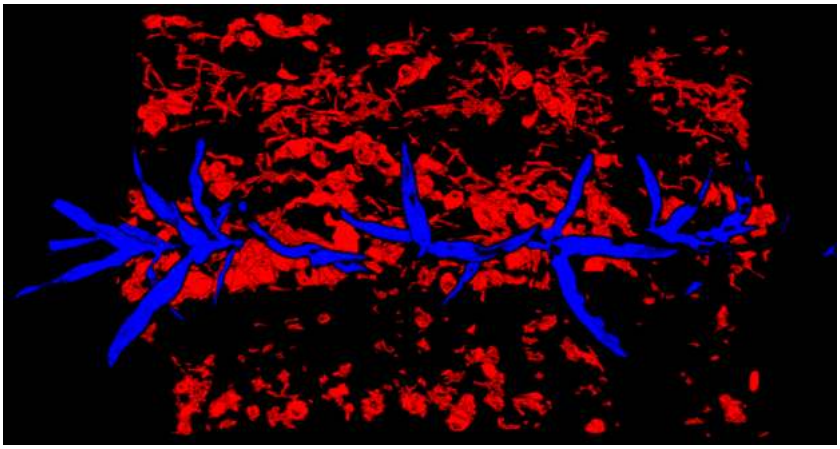

Figure 103. Evaluation of treatment performance. The figure shows an example of ground truth labeled image where the weeds are shown in red and the crop in blue.

Table 6. Method for calculating treatment performance. The table shows the method used to generate the binary masks used for estimates treatment performance.

	TAW	TMW	Biostimulant
TP	$maskTAW_{tr(i)}$ & maskWeedValid	$maskTMW_{tr(i)}$ & maskWeedValid	$maskBIO_{tr(i)}$ & maskCropValid
FP	$maskTAW_{tr(i)}$ & maskCropValid	$maskTMW_{tr(i)}$ & maskCropValid	$maskBIO_{tr(i)}$ & maskWeedValid
TN	~ $maskTAW_{tr(i)}$ & maskCropValid	~ $maskTMW_{tr(i)}$ & maskCropValid	~ $maskBIO_{tr(i)}$ & maskWeedValid
FN	~ $maskTAW_{tr(i)}$ & maskWeedValid	~ $maskTMW_{tr(i)}$ & maskWeedValid	~ $maskBIO_{tr(i)}$ & maskCropValid

8.2.10 Field Capacity Estimation

The work capacity was calculated by considering the average execution time (t_{Ex}) measured for performing the classification and generating the prescription map to be used in real-time. Field capacity is expressed in terms of the surface area analyzed per unit of time, considering the area sampled with a single frame and the sustainable forward speed that can be maintained on average with this configuration. This calculation also considers the effective working width parallel to the direction of travel, WS_x, which is equal to 1.5 m.

$$Va_{sust} = 3.6 \cdot \frac{WS_x}{t_{Ex}} \quad \left[\frac{km}{h}\right]$$

$$Field\ Capacity = 0.36 \cdot \frac{WS_{area}}{t_{Ex}} \quad \left[\frac{ha}{h}\right]$$

8.2.11 Precision Biostimulant Application

The use of 3D sensors enables a more accurate classification of visible vegetation, which opens the possibility of utilizing this data for additional purposes. With the aim of improving the efficiency of other operations, the distribution of biostimulants was considered an intriguing application. Biostimulants enhance the vigor of the plants that receive them, but since they do not specifically target the crop, they risk also promoting the growth of weeds when distributed uniformly.

To illustrate the potential of this approach, a hypothetical scenario was proposed in which a biostimulant is used to simulate a treatment targeting the crop. The focus was on BlueN®, a patented foliar-applied biostimulant distributed by Corteva™ Agriscience, which involves the application of *Methylobacterium symbioticum* SB23 (107 CFU/g) on various crops, including maize. The manufacturer recommends applying it during the phenological stages between V4 and V8 at a dose of 333 g/ha dissolved in a water volume of 80 to 250 L.

Once applied to the foliar tissue, this endophytic bacterium is capable of penetrating through the stomata to colonize the plant tissue. For this reason, it is advised to apply the biostimulant in the morning when the stomata are open. The bacterium is

employed because it can metabolize atmospheric nitrogen, fixing it into a chemically assimilable form for the crop by producing the enzyme nitrogenase, which converts atmospheric nitrogen into ammonium ions, making it available to plant cells. Additionally, within the leaves, the bacterium produces methyllobamine, a natural pinkish pigment that optimizes photosynthetic efficiency by reflecting specific wavelengths (UV). A symbiotic relationship is established between the plant and the bacterium, where the plant provides methanol, a toxic substance for the plant but beneficial for the bacterium. With a single application, the bacterium can reproduce within the plant and spread to newly growing tissues that were not present at the time of treatment.

The advantages of using this biostimulant include enabling the plant to absorb nitrogen fixed by the bacteria regardless of its actual availability in the soil, thereby enhancing and making the plant's photosynthetic activity more efficient. Consequently, the use of this biostimulant allows for a reduction in soil nitrogen fertilization, maximizing nitrogen use efficiency and promoting increased yield and greater yield stability under suboptimal fertilization conditions.

8.3 Results

8.3.1 Binary Classification

The classification algorithm, applied under conditions of medium to high weeds infestation, demonstrated excellent classification capabilities, achieving high scores across all indices. It correctly classified weeds in 99.1% of cases and the crop in 97.5%

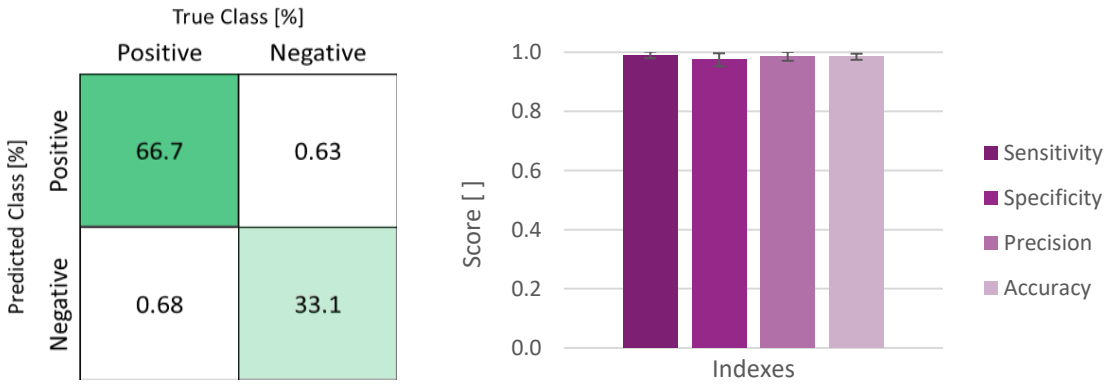

Figure 104. Results of binary classification. On the left: the classifier confusion matrix. On the right: report on the performance indexes.

of cases. Overall, the algorithm accurately identified the correct class at the individual pixel level in 98.5% of the analyzed cases.

8.3.2 Treatments Simulations and Intervention Strategies

The two different distribution strategies based on detection using RGB-D images yielded varying results. The TAW strategy achieved a 100% success rate, aligning with the expected outcome. In contrast, the TWM strategy treated approximately 90% of the targets on average, which was expected given its approach of treating only when more weeds than crops were detected simultaneously. Below are the results in the form of confusion matrices and performance indices for the two strategies simulated in the treatments.

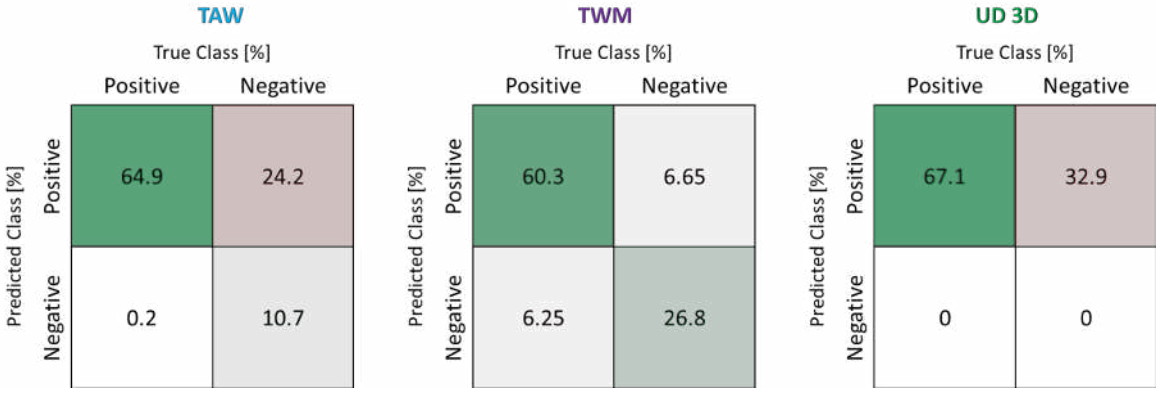

Figure 105. Confusion matrices of results obtained by applying TAW and TWM and UD3D strategies to treatments based on 3d sensor detection

This reduction in treated targets, however, resulted in specificity of 0.81 for TWM, compared to 0.28 for the TAW strategy. The higher specificity of the TWM strategy also positively influenced the precision and accuracy scores, where TWM overall achieved the highest levels across these indices.

It is important to note that, despite the generally higher average score, it should be assessed whether the 10% reduction in treated weeds targets with TMW is acceptable in an operational context aimed at total weed control. This is crucial to prevent the remaining weeds from seeding and contributing to the soil's seed bank.

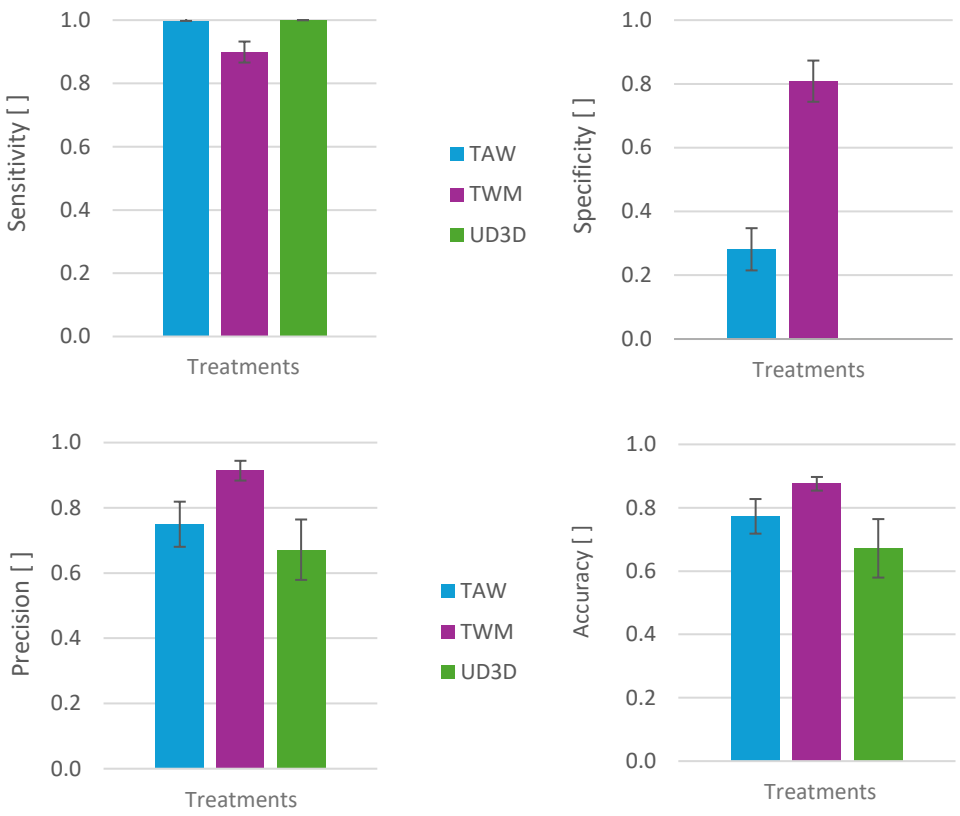

Figure 106. 3D based precision spraying treatments performance indexes results.

The two strategies also yielded different results in indices which directly reflect the environmental impact of the intervention. Both strategies ensured a reduction in the quantity of products distributed compared to the uniform distribution method. On average, this reduction was approximately 26% for the TWM strategy and 17% for TAW, while still maintaining a sensitivity of 1, as previously noted. Similarly, the environmental impact on the soil was reduced, with the TWM strategy achieving an average reduction of 28% in herbicide distribution to the soil, compared to 22% for the TAW strategy.

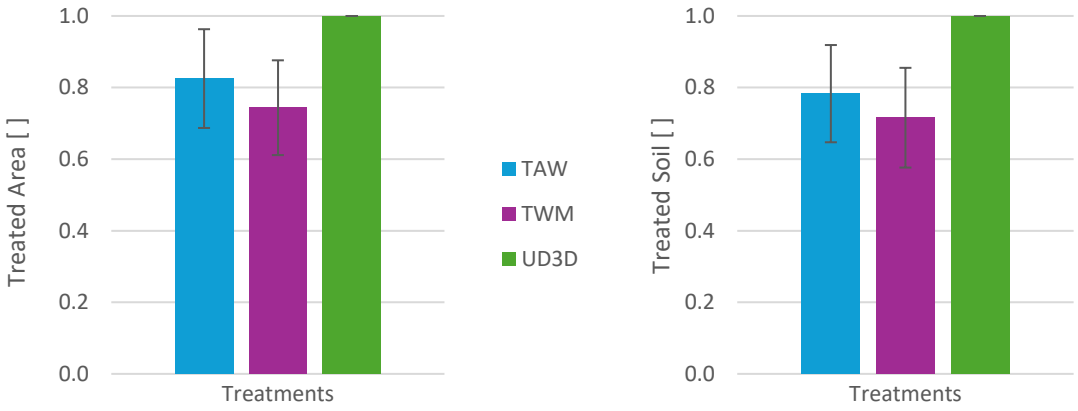

Figure 107. Result of environmental impact of different precision spraying strategies.

8.3.3 Biostimulant distribution

The simulation of the biostimulant treatment yielded excellent results. On average, 99% of the crop surface was reached by the treatment, while only 16% of the soil was treated. The levels of precision and accuracy were comparable to those observed in weed control treatments, while specificity was like that of the TMW weed control strategy, which achieved the best results for this index.

The treatment with biostimulants represents a highly innovative approach and, in the simulations, has shown significant potential for real-world field applications, potentially even in conjunction with site-specific weed control operations. For this type of treatment to be effective, it requires accurate detection capabilities, and in this case, the use of the 3D sensor significantly contributed to achieving the desired outcome.

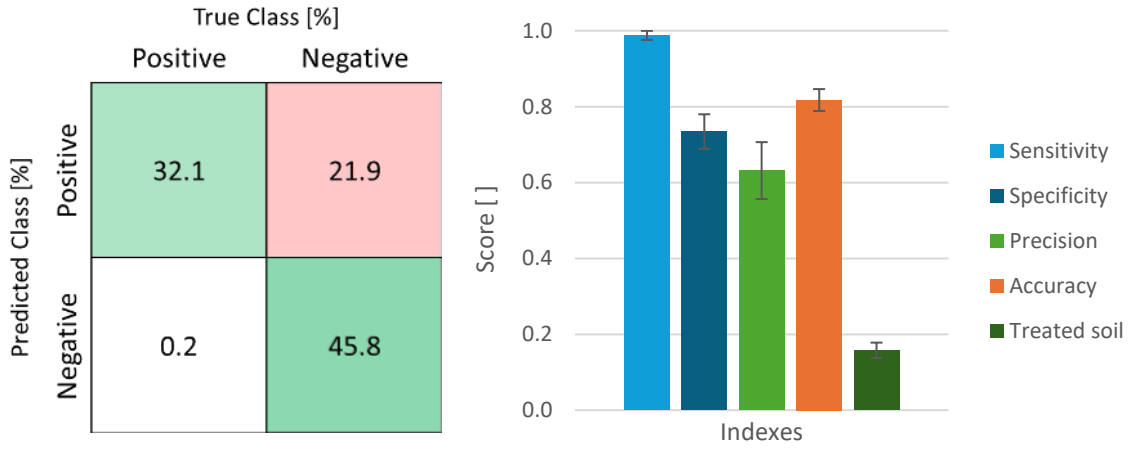

Figure 108. Biostimulant treatment performance index results. On the left: the classifier confusion matrix. On the right: report on the performance indexes.

8.3.4 Field capacity

The estimation of field capacity at the current stage of algorithm development and integration has revealed its potential for field deployment. It is also important to note that there is room for further optimizations, both in terms of code and in terms of the hardware on which it is implemented.

Table 7. Field capacity estimation results for 3D methods.

	U.M		3D
Execution time	s		1.12 ± 0.13
Field capacity	ha/h	1 module	0.45 ± 0.09
Theoretical speed	km/h		4.49 ± 0.33

For instance, integrating the script on a dedicated single-board computer, such as the one suggested by the sensor manufacturer (the ZED Box (powered by the NVIDIA® Jetson Orin processor) would allow for controlling the sensor and deploying the code directly on high-performance hardware. This integration would significantly enhance performance, reducing the algorithm's execution time to a fraction, thanks to the 100 TOPS (Tera Operations per Second) it can process. This would support the typical speeds of site-specific spraying operations in maize, which generally range between 4 and 8 km/h (Karadöl et al., 2020), even if the execution time were halved compared to the current development level, which currently allows for a forward speed of approximately 4.5 km/h, which still represents a very good result.

8.4 Comparability between results obtained with RGB and RGB-D sensors

In this section, a comparison will be made between the results obtained using imaging techniques based on RGB images and those obtained using RGB-D images. The purpose of this analysis is to verify the comparability of the results obtained from the simulated treatments for the two sensing methods under consideration. The test used to verify comparability is the Kruskal-Wallis test with a significance level of 5% (α = 0.05), considering the null hypothesis (H_0) that there are no statistically significant differences between the two groups representing the levels of land cover obtained through 2D and 3D imaging techniques. If the null hypothesis is accepted, it is possible to proceed with subsequent comparative analyses between the results obtained in the treatment simulations.

This preliminary study found no statistically significant differences between the two samples, which can be seen from the *pValue* of 0.86 as verified by the test, and therefore the null hypothesis can be accepted and the FC values observed in the different tests and acquisitions can be considered as coming from a single population, allowing comparative analyses to be conducted.

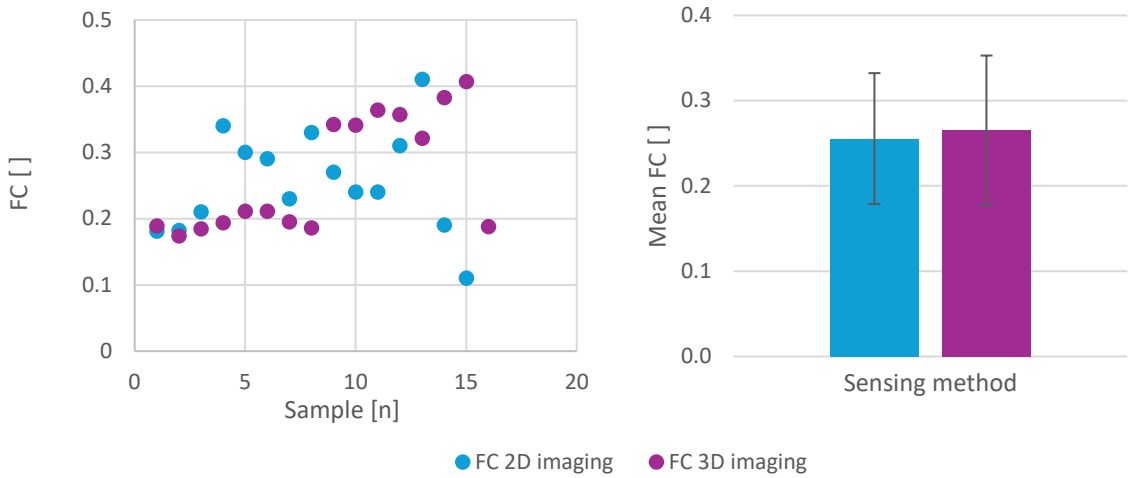

Figure 109. FC levels observed in samples used in experiments involving algorithms developed with 2D and 3D images. Bars represent the average FC of sampled areas. Error bars represent the standard deviation. the standard deviation. Letters indicate statistically significant groups identified by Tukey's post hoc test ($p < 0.05$).

8.5 Significance Test of the Results

After verifying the possibility of comparing the scenarios observed with the two different sensing methods, it was possible to proceed with the comparison of the performance indices that better explain the contribution made by the sensing algorithms and techniques in achieving the objectives of reducing the environmental impact of the precision weeding operation. Given the non-normal distribution of the data considered, Kruskal-Wallis test with a significance level of 5% (α = 0.05) was conducted considering the null hypothesis (H_0) that there are no statistically significant differences between the results obtained with treatment simulations and the related UD treatment.

The first result to be considered is the quantity of herbicide distributed in order to verify the ability of the algorithms to significatively reduce the quantities distributed. In this case, the probability value shows the possibility of rejecting the null hypothesis and thus accepting the alternative that there are statistically significant differences between the groups considered. Since statistically significant differences were detected with the Kruskal-Wallis test, a post hoc analysis was conducted using Tukey's test to further explore pairwise group comparisons. The analysis showed that methods LCF, TAW and TWM used significantly lower quantities of herbicide in treatment simulations.

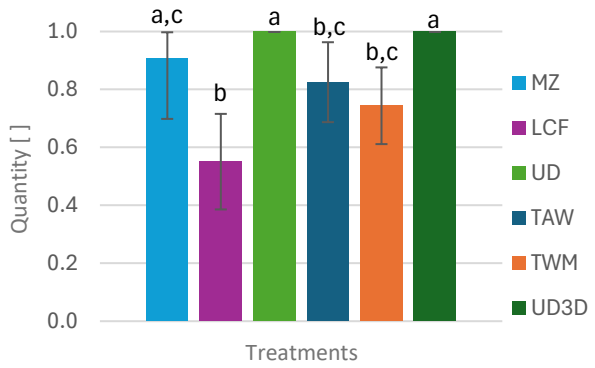

Figure 110. Comparison of the quantity of herbicides distributed estimated in treatment simulations. Bars represent the average amount of herbicide distributed in the simulated treatments. Error bars represent the standard deviation. Letters indicate statistically significant groups identified by Tukey's post hoc test ($p < 0.05$).

After evaluating the quantities distributed for treatments, it is necessary to assess whether the reduction in quantities has significatively affected the quality of the treatment by examining its effectiveness or the capacity of the treatment to treat all the targets. For this purpose, sensitivity has been considered. In this case, the probability value shows the possibility of rejecting the null hypothesis and thus accepting the alternative hypothesis that there are statistically significant differences between the groups considered. Since statistically significant differences were detected with the Kruskal-Wallis test, a post hoc analysis was conducted using Tukey's test to further explore pairwise group comparisons. This statistical analysis indicates that the reduction in distributed products has significantly affected the treatment outcome. In fact, TWM for RGB-D sensing and LCF for RGB have shown

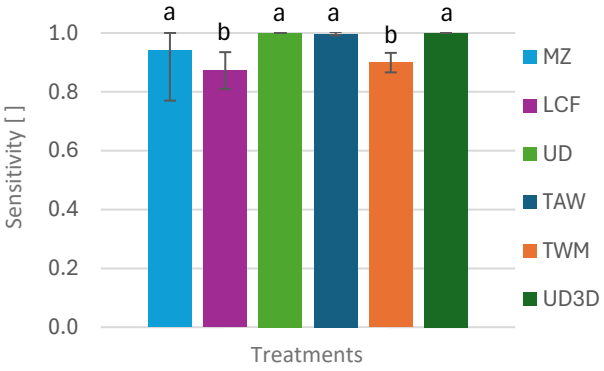

Figure 111. Comparison of the sensitivity estimated in treatment simulations. Comparison of the sensitivity value of the simulated treatments. Error bars represent the standard deviation. Letters indicate statistically significant groups identified by Tukey's post hoc test ($p < 0.05$).

sensitivity levels that are lower than those of UD, and this could adversely affect the outcome of the treatment.

The last statistical analysis involve the environmental impact of the treatment on the soil. The Kruskal-Wallis test shows the possibility of rejecting the null hypothesis and thus accepting the alternative hypothesis that there are statistically significant differences between the groups considered. The Tukey's test indicates that all the developed algorithms significantly reduced the impact compared to the related UD method.

The reduction in the amount of herbicide and environmental impacts has been made possible by the increased specificity demonstrated by the developed algorithms. The best specificity result was achieved with 3D imaging and the TWM intervention strategy. Surprisingly, the LCF method, based on 2D imaging, achieved results comparable to those of 3D imaging-based treatments. The high levels of specificity obtained with this method explain its significant performance in terms of reducing the amount of input.

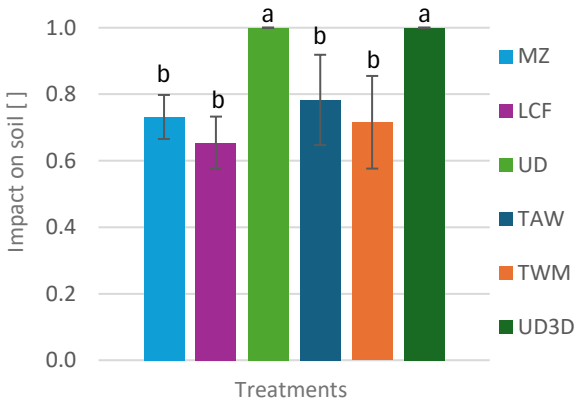

Figure 112. Comparison of the impact on soil estimated in treatment simulations. Error bars represent the standard deviation. Letters indicate statistically significant groups identified by Tukey's post hoc test ($p < 0.05$).

To conclude, it is worth pointing out that the control strategy that performed best overall in achieving the expected goals of significance of input reduction without reducing the ability to hit targets was the RGB-D sensor-based with the TAW strategy and this represents a major achievement.

8.6 Conclusions

The ability to perform classification using 3D sensing effectively enhances the localization of treatments, whether for weed control or the application of biostimulants, as demonstrated in the previous sections.

The observed reduction in the amount of product applied, compared to uniformly distributed treatment, might seem relatively modest (quantified between 20% and 25%) when localized treatment is used. However, it is important to consider that the scenarios analyzed represent situations characterized by very high levels of infestation. For example, the only crop soil coverage assumed values around 5-7% and FC in some cases even exceeded 40 %. Consequently, a consistent reduction in the amount of herbicide applied cannot be expected without compromising sensitivity and thus potentially leaving some weeds untreated. In cases of limited infestation, much higher reductions in the amount applied can be achieved, which, depending on the weed density, could reach up to a 100% reduction compared to the uniformly distributed method in areas where no weeds are present.

It should also be noted that the algorithm based on 3D imaging was developed and optimized to operate under conditions of high infestation. In these conditions, it achieved excellent levels of classification accuracy (as discussed in Sect. 8.3.1). For moderate to low infestation levels, however, a 2D imaging-based algorithm, such as the LCF method, might be sufficient.

The LCF algorithm achieved excellent results that exceeded expectations, even though it does not perform a true binary classification (or rather, it only classifies weeds in the inter-row space that are not directly connected to the crop). Instead, it estimates areas that are likely infested and therefore more likely to require treatment.

Regarding the simulation of treatments, the achievable performance is strongly constrained by the accuracy of the intervention, specifically by the spatial resolution obtainable with the use of commercial nozzles. Although this can be considered a simulation of high precision intervention, it still falls short of matching the classification accuracy achieved by the algorithm. For this reason, to enhance the quality and sustainability levels achievable in treatments, several strategies could be

considered. These include the possibility of innovating the spraying system, such as developing robotic nozzles that can be oriented or equipped with a variable range of action depending on the target. Alternatively, other combined strategies could be hypothesized, such as employing physical methods for weed elimination in the inter-row space while applying precise spraying on the crop row, thereby reducing chemical input.

In conclusion, the RGB-D camera used in this study enabled the development of optimized algorithms for detecting crops and weeds under field conditions. These algorithms were specifically designed to address some of the most challenging scenarios, characterized by high weed density, where detection based solely on RGB images struggles to manage the complexity of field classification tasks.

A potential future development could involve creating an algorithm that adapts based on the local level of weed infestation. Such an algorithm could rely solely on the RGB channel in low-intensity infestation scenarios, while incorporating the depth channel only when it offers a significant advantage.

9 Precision Actuation

9.1 Aim of the Experiment

The purpose of this section is to develop control strategies based on low-cost hardware that can effectively implement the algorithms discussed in previous Chapters. To achieve this, a prototype platform has been developed capable of detecting potential targets using imaging techniques and subsequently simulating the treatment in real-time during the survey. The application explored in this preliminary test is a high-precision patch-spraying technique achieved by controlling eight actuators installed 0.125 m apart (bL_x) on a 1-meter boom, ensuring a spatial resolution of treatment slightly exceeding 122 cm^2 (0.098 m (bL_y) by 0.125 m).

For this experiment, hardware architecture comprising two modules was adopted. The first module (master) is dedicated to image acquisition and processing, represented at this stage of development by the PC1 (see Sect. 2.4) running a script in the MATLAB environment. The second module (slave) is an Arduino Uno board, tasked with controlling the actuators based on instructions received from the master via USB. The data sent from the master is interpreted and converted into digital signals to command the actuators, which in this instance are represented by LEDs.

9.2 Materials and Methods

To construct the prototype, several components were necessary to perform various tasks:

- For image acquisition, the color channel of a Kinect V1 was utilized, which outputs an RGB image with dimensions of 640 by 480 pixels. The images were captured using the Image Acquisition Toolbox in MATLAB.
- To monitor the movement of the machine, an incremental encoder with a resolution of 1024 pulses per revolution (*cpr*) was selected, which is affixed to a wheel of known diameter (wd). The linear resolution for displacement is therefore 0.44 mm, calculated by dividing the circumference of the wheel by the encoder's resolution.

$$Enc_{metr} = \frac{wd \cdot \pi}{cpr} \quad \left[\frac{m}{impulse}\right]$$

The encoder is connected to the microcontroller using digital pins D2 and D3, which can be utilized in interrupt mode. This allows specific functions to be triggered whenever the input signal on either pin changes state (High-Low). During rotation, the encoder generates a High or Low signal that changes state with each rotation corresponding to the sensor's resolution. By monitoring these signals, it is possible to measure the angular rotation of the wheel, determine the direction of rotation, and calculate the distance traveled.

- The actuators used to simulate the operation of the machine, specifically the distribution of treatment, are eight LEDs that have been soldered onto a breadboard for electronic prototyping and connected to the digital outputs of an external multiplexer board (PCA9685). This external module serves to provide 16 PWM channels, as the Arduino Uno board only has 6 digital lines capable of PWM control, which is insufficient for the requirements of this experiment. The multiplexer receives a separate 5V DC power supply to power the LEDs and communicates with the microcontroller via the I^2C protocol, receiving the duty cycle to be generated for each output channel. Additionally, these external modules can be connected in series to expand the capabilities for generating such signals from a single Arduino Uno board.

The instructions for managing the actuation, or the prescription map, are sent from the master via USB in *'uint8'* format and correspond to an area equivalent to that monitored in a single image. This allows the master to continue acquiring and processing images while the slave autonomously executes the last received map.

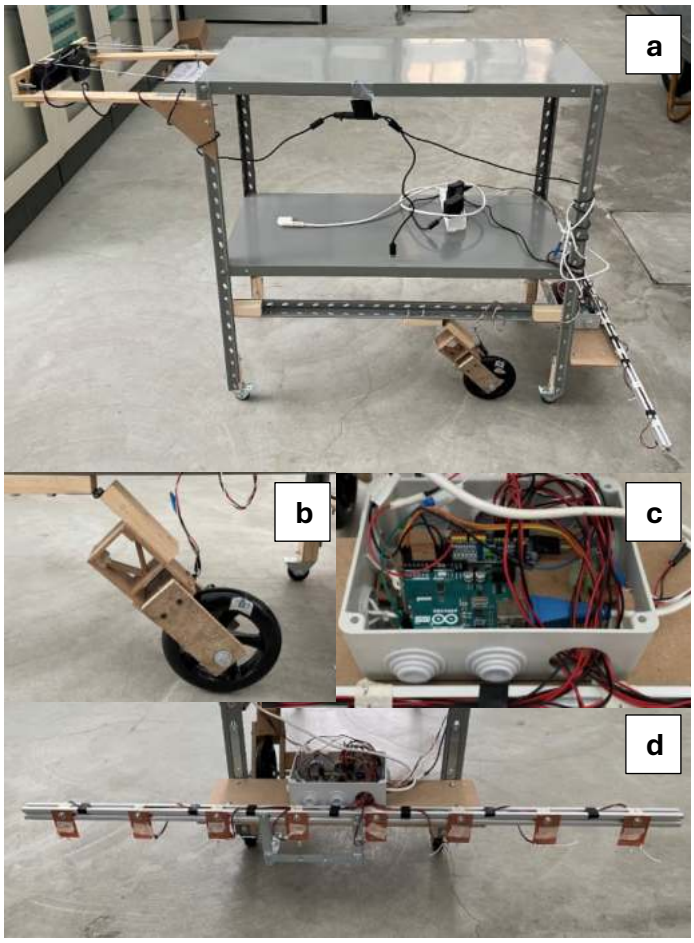

Figure 113. Machine components summary. a) Image of the machine used to make the prescription map and the actuation management in real-time. b) detail of the wheel equipped with encoder to monitor the movement of the machine. c) Details of the microcontroller and PWM multiplexer (PCA9685) used to manage the machine's operating logic. d) Treatment boom with installed LEDs that are driven to display the output of the actuation process.

9.2.1 Calibration Procedures

To operate effectively, the machine requires calibration, which involves determining the values of several fundamental parameters that define its geometric characteristics. This section proposes an innovative method for obtaining these parameters, making the calibration process both accurate and rapid, and allowing for quick reconfiguration if components such as the camera or the number and position of actuators are changed.

The camera used for image acquisition must be calibrated to eliminate lens distortion. The undistortion operation is performed each time an image is captured, producing an output image with dimensions of 630 by 468 pixels. The camera parameters were

estimated using a specific application available in MATLAB called Camera Calibrator App.

The first parameters considered pertain to the characteristics of the boom, specifically the number of nozzles present, their position relative to the camera, and the distance between the boom and the camera's field of view. These parameters are estimated using the following procedure: 8 AprilTags are placed corresponding to the actuators on the boom, carefully arranged in order by ID, positioned perpendicularly beneath each actuator. This allows for the identification of each actuator and assigns a unique identifier to it. Subsequently, the machine is moved in the opposite direction of travel until the markers reach approximately the center of the camera's field of view. During this calibration phase, an image is captured, and the markers are automatically detected using the *readAprilTags* function. This procedure is essential for measuring the distance and position of the nozzles relative to the camera (*Boom distance*).

$$Boom\ Distance = encoder\ impulse \cdot\ Enc_{metr}\ \ [m]$$

Additionally, the positions of the centroids of the identified markers are used to assess their alignment by fitting a line and evaluating its slope. Proper alignment is crucial for validating this phase of the process; excessive misalignment may result from an imperfect trajectory during the movement executed to measure the distance from the boom, rendering the measurement invalid. Similarly, misalignment could also arise from improper positioning of the camera relative to the boom, allowing for corrective actions to be taken.

In addition to measuring the distance from the boom to the camera, this phase serves other purposes. The first is to define the working area of each actuator, and the second is to estimate the metric conversion of individual pixels.

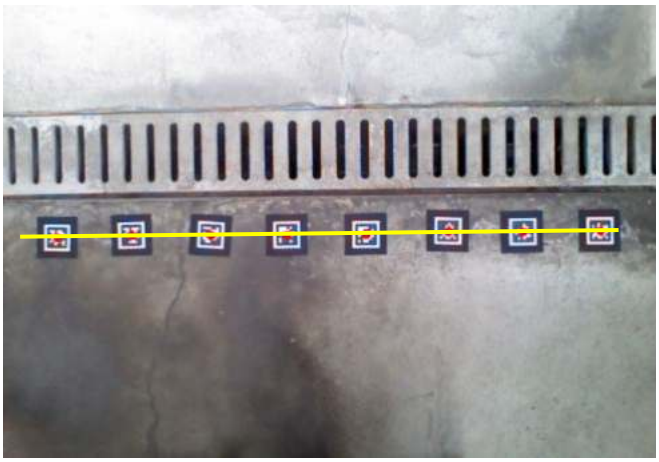

Figure 114. Display of marker detection for individual actuators and verification of correct alignment.

The working area of each actuator, represented by a vertical section of the image, is determined by subdividing the image so that each vertical section contains one of the markers at its center. To achieve this, after identifying the centroids of the markers, the linear distance on X axes from each pixel to the nearest marker is calculated. By identifying the peaks of this variable, the points for placing the vertical lines that separate the individual working areas are determined. Subsequently, to complete the grid that defines the treatment zones, horizontal lines are positioned at equidistant intervals according to the target resolution.

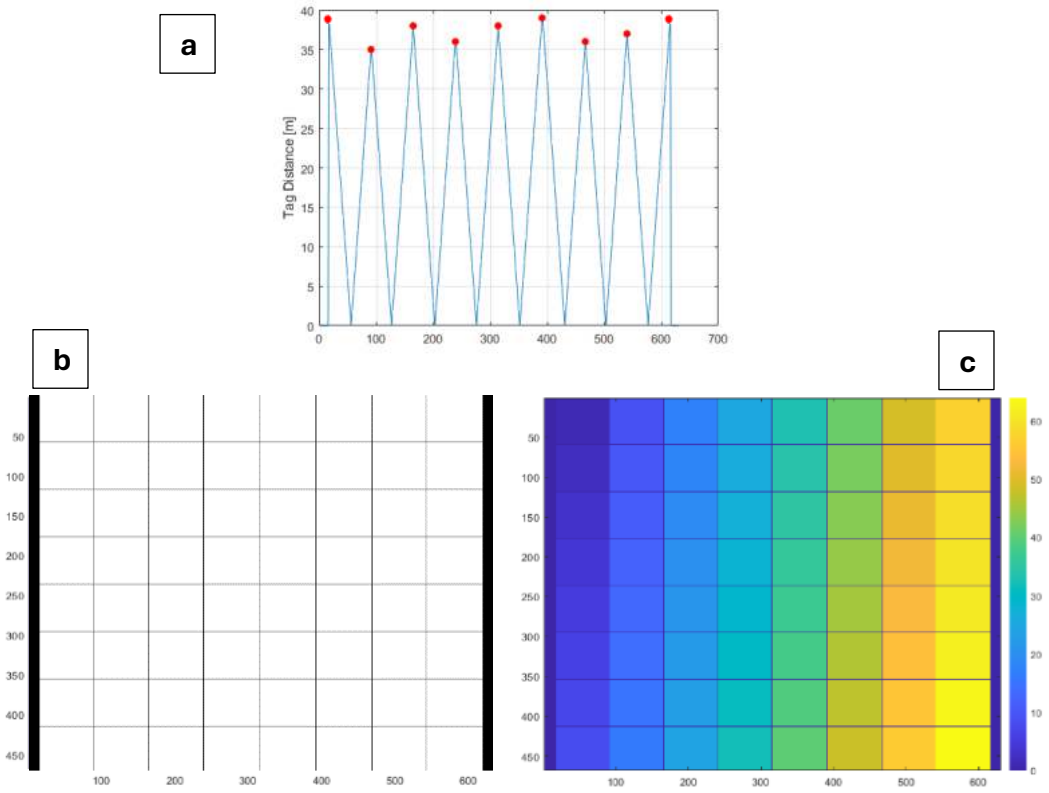

Figure 115. Procedure for segmentation of individual zones. a) Distance from the centroid of the nearest marker. The red dots indicate the points where vertical cuts are made to separate the working space of the individual actuators. b) Binary mask of the useful working space divided into the individual zones obtained by subtracting the vertical lines and the equally spaced horizontal lines used to divide the space of each actuator into 8 equal zones. c) individually labelled zones.

The metric conversion is estimated by considering the area measured in pixels, which is segmented for each marker. By knowing the actual dimensions of the markers, the metric conversion is calculated by dividing the average segmented area of each marker by the known area of the marker.

$$K_{metr} = \frac{mean(MarkerArea_{(pix)})}{MarkerArea_{(metr)}} \quad \left[\frac{pix}{m}\right]$$

This conversion is used to map the working area by converting the pixel coordinates of the image (rows, columns) into metric coordinates (y,x), providing an estimate of the dimensions of the sampled area with each acquisition.

Additionally, it is necessary to convert the distance between the top margin of the image and the fitted line representing the marker positions, expressed in pixels (*fL*), into a linear distance in meters (*Umd*). This conversion aims to evaluate the total space that must be stored by the master, pre-allocating a logical matrix with the same width as the undistorted images and enough rows to store all necessary data in a pre-processed form. This matrix must be capable of containing information regarding the last processed image and all previous images up to the boom, which in this case corresponds to 1080 pixels.

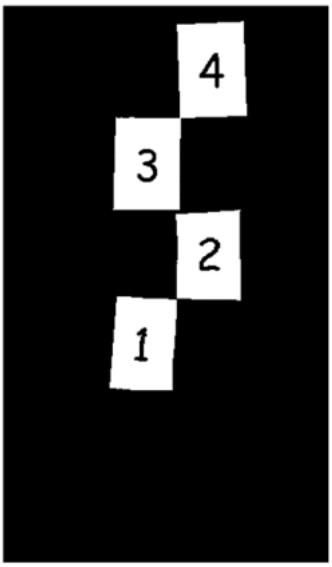

Figure 116. Total spatial memory stored from the master to manage the following prescription map generation.

$$Umd = \frac{fL}{K_{metr}} \ [m]$$

$$Spatial\ Memory = (Boom\ Distance + Umd) \cdot K_{metr} \ [pix]$$

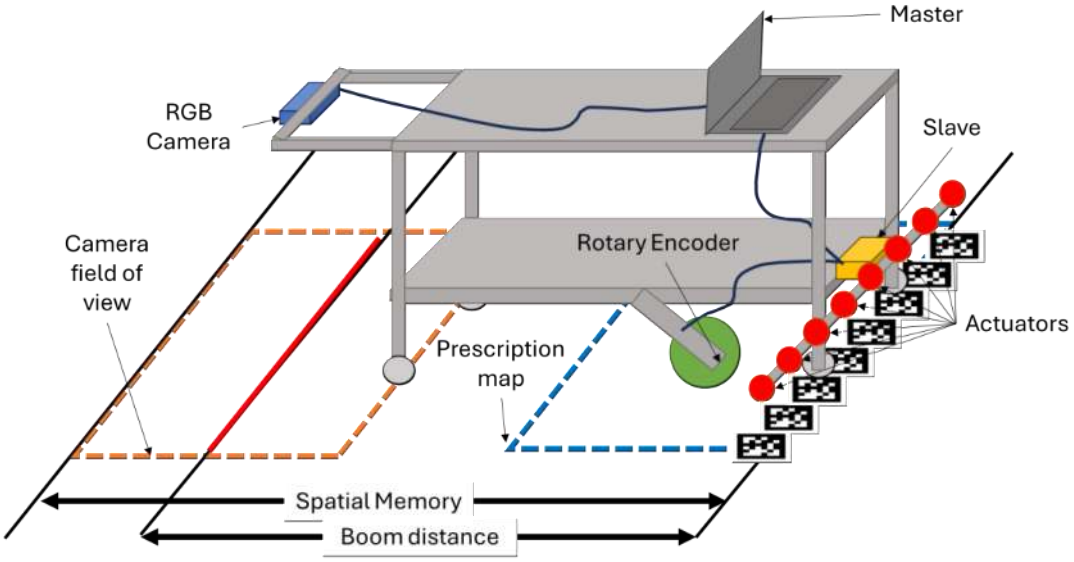

Figure 117. Diagram of the components used to build the machine and significance of key variables for operation. Spatial memory identifies the space that is digitized and maintained in memory for actuation management. The orange dashed line box indicates the area that is sampled in a single acquired image, this is placed upstream in the memory. The blue dashed line box indicates the area that is extracted from memory and sent in the form of instructions that can be managed in parallel by the slave. Boom distance and camera alignment were estimated using graphic markers with an automatic procedure.

9.2.2 Prescription Map Generation

The simplified image processing logic used in this test involves segmenting the white pixels determined by summing the total reflectance across the RGB channels, applying a threshold of 700 as the minimum value. This approach ensures accurate acquisition of the targets represented by numbered sheets of paper.

The generation of prescription maps involves extracting a section from the end of the spatial memory to create the output to be sent to the slave, allowing it to operate in parallel during subsequent acquisition and processing. The data is transmitted to the slave via serial communication, and due to the need for timely transmission and the limited size of the slave's serial buffer, it must be compressed as much as possible.

To achieve this, the working area of each actuator is divided into 8 zones, which in this experimental setup correspond to 0.098 m, resulting in a total of 64 areas per image. These areas are labeled during the calibration phase and subsequently extracted individually for analysis during operation to enhance computational efficiency. In this trial, for each subdivided area of the image, the percentage of 'true' pixels is evaluated; if this exceeds a threshold value of 20%, the area is classified as needing treatment. The information regarding the areas to be treated is compressed using the following procedure:

- Each individual area corresponding to a single actuator is assessed to determine whether treatment is required.
- Areas designated for treatment are marked as 1, while those not requiring treatment are marked as 0.
- The results are combined into a single number in *'uint8'* format, with the first area located at the top of the image representing the MSB of the composed number.
- The *'uint8'* numbers generated for each actuator are subsequently transmitted to the slave via USB.
- The output buffer from the master includes one byte representing the content of the message, followed by 8 bytes containing the instructions for managing the 8 actuators.

Figure 118. Summary of the procedure for converting the prescription map for each individual actuator into a single byte that can be sent via serial to the slave.

9.2.3 Distributed Control Operating Logic

When the slave receives data through the serial port, it extracts the first byte to identify the message content. If this byte equals 0, the slave responds by sending the encoder count as feedback on the machine's movement since the last reset. The encoder count, stored as *'uint16'* in the microcontroller, is split into two bytes for serial transmission.

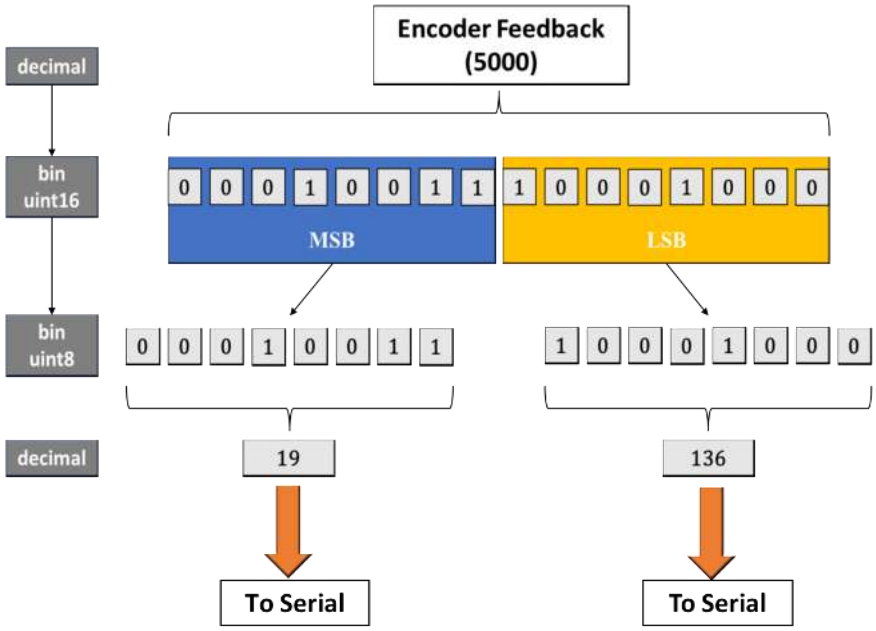

Figure 119. Summary of the procedure for converting the prescription map for each individual actuator into a single byte that can be sent via serial to the slave.

If the first received byte equals 1, it triggers the resetting of the encoder and the downloading of the next 8 bytes from the serial buffer, which will define the treatment map to be executed until a new update. For each actuator, the slave receives a byte that specifies its activation state, with each bit representing whether the actuator should be on or off. After resetting the encoder, the machine's progress is continuously monitored to determine which zone of the map the actuator is currently in. The zone value is calculated by dividing the encoder count by a constant representing the counts corresponding to the length of each area. This value is rounded down to select the appropriate bit from the received data, as bit numbering starts from 0 for the Least Significant Bit (LSB).

The selected bit determines whether the actuator is activated. If the bit is *'true'*, the actuator will be activated. If the zone value exceeds the maximum of 7, the actuation is interrupted, indicating an anomaly, since the refresh rate of the map ensures updates occur before the slave can finish processing the last received data. The master algorithm execution time is about 0.2 s (Ex_{time}), allowing the system to sustain speeds up to 14.2 km/h, well above typical treatment speeds and compatible with the previously discussed 2D and 3D-based detection algorithms.

$$Theoretical\ speed = \frac{b_{Ly}}{Ex_{time}} \quad \left[\frac{m}{s}\right]$$

$$imp2Zone = \frac{b_{Ly}}{Enc_{metr}} \quad \left[\frac{impulse}{zone}\right]$$

$$Selected\ Zone = \quad floor\left(\frac{Encoder\ Impulse}{imp2Zone}\right) \quad [\ zone\ ]$$

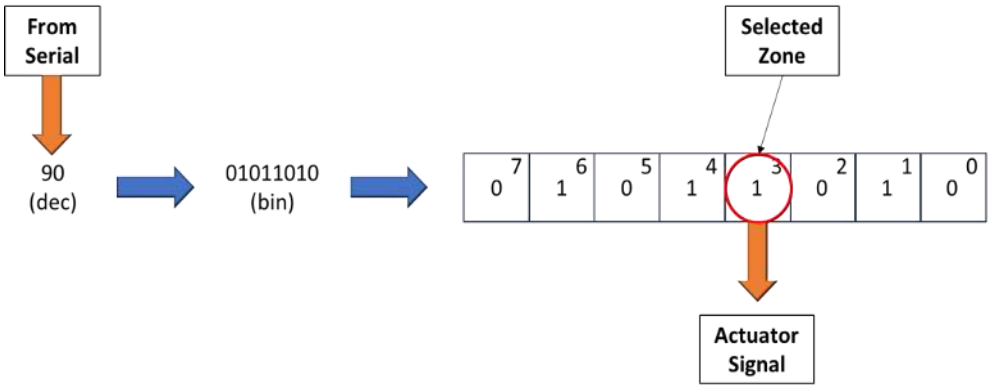

Figure 120. Summary of the procedure for converting data received from the master into signals used to drive the individual actuators within the different zones.

9.2.4 Overall Operating Logic

The overall operational logic of the machine requires the slave to concurrently monitor the movement of the machine and generate the digital signal used to control the actuators according to the instructions received from the master. The master may also request feedback on the movement to ensure accurate synchronization at both levels.

The master is responsible for capturing images and performing the necessary analytics to produce the resulting binary mask. This binary mask is subsequently stored in the main machine memory pre-allocated for the treatments, which is shifted in the opposite direction to the machine's movement based on feedback from the encoder. After that, the tail end of the memory (located closest to the actuators) is extracted and split according to the schema that identifies the individual zones representative of the treatment resolution. The outcome of the intervention map is then compressed and sent to the slave, allowing it to execute the intervention in parallel. The master will wait until the machine has moved a defined minimum distance, as specified by the operator, before triggering the next image acquisition. Below are the algorithms for the operation of the machine at the slave and master levels, presented in pseudocode.

```
Slave Pseudocode (Arduino env.):

On Serial Event{
      if(byte[0]==0){Encoder Value feedback is
      sended to master;}
      else {Encoder Zeroing();
            Map Update();}}
Main loop(){
      - Check for Zone Position;
      - PWM Signal Generation;}
```

Figure 121. Pseudocode representing operation logic management by the slave.

```
Master Pseudocode (MATLAB env.):

While 'true'
      - Image Acquisition
      - Image Undistortion
      - Color segmentation (binary output)
      - Encoder feedback = Displacement 1 (during image processing)
      - Y Traslation of Spatial Memory by Displacement 1
      - Insertion on top Spatial Memory of last binary output
      - Encoder feedback = Displacement 2 (during memory update)
      - Y Traslation of Spatial Memory by Displacement 2
      - Extraction of bottom part of spatial memory
      - Prescription map generation
      - Encoder feedback = Displacement 3 (during map generation)
      - Y Traslation of Spatial Memory by Displacement 3
 While(Encoder feedback < Minimum Displacement Threshold)
 end
end
```

Figure 122. Pseudocode representing operation logic management by the master

9.3 Conclusions and Future Prospectives

The prototype setup has proven suitable for achieving the objectives of the trial. The calibration method employed for the machine yielded excellent results, making the procedure reliable, straightforward, and quick, thus enabling rapid and precise adjustment of the calibration parameters and enhancing the prototype's configurability.

Various missions aimed at generating real-time prescription maps were successfully executed, meeting the initial objectives of the trial. The actuator management strategy devised for simulating treatments proved effective for high-accuracy patch-spraying applications, with the minimum treatable zones being on the order of several hundred square centimeters. However, the system can still be categorized as patch-spraying. This operational scheme was chosen to reduce implementation costs, but it can be

enhanced by increasing complexity and improving accuracy through micro-spraying modifications.

One potential enhancement could involve using a separate board for each actuator, creating a network that utilizes protocols like CAN BUS to send instructions to individual actuators with higher resolution, surpassing the limitations of a single board's serial buffer, which handles all eight actuators.

Another strategy to elevate accuracy would be to replace the Arduino Uno board with a higher-performance microcontroller (e.g., Raspberry Pi), capable of managing other data transmission standards such as ROS. This would allow the master to send the prescription map directly to the slave in image form, achieving a resolution at the pixel level rather than relying on fixed, predetermined areas.

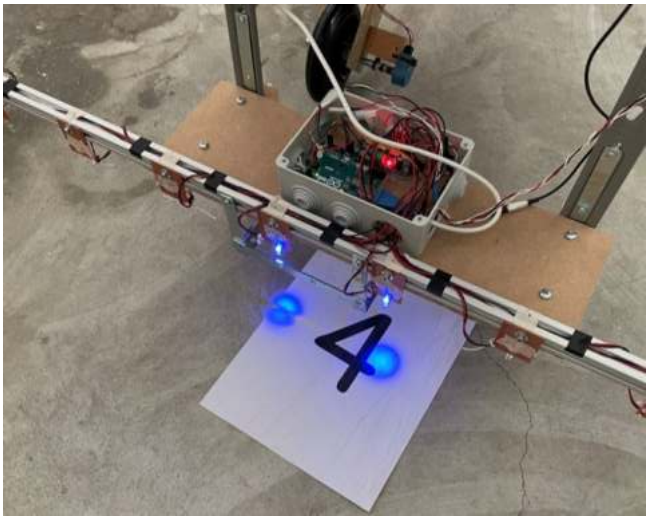

Figure 123. Actuators triggered at a target according to the prescription map generated in real-time.

10 Conclusions

The use of 3D sensors in the agricultural sector can offer a significant contribution to solving complex situations that are more difficult to address with 2D imaging. The ability to measure distances with a high degree of accuracy enables the effective modeling of individual plants.

The application of these sensors in phenotyping has shown considerable potential, both in laboratory-scale experiments and in field trials. In this context, the integration of these sensors in parallel with the development of algorithms capable of reconstructing plant structures, albeit simplified and approximate, in areas occluded by the perspective from above, this type of data has made it possible to satisfactorily estimate the dry matter and thus the biomass of head lettuces, with mean square errors of 0.12 g for the laboratory trial and 1.07 g for the field trial. The different levels of estimation accuracy is mainly due to the different conditions under which the estimation took place. To improve the results obtained at the field scale, the acquisition setup should be optimized by making it more like the laboratory setup, i.e. by bringing the sensor closer to the plants and standardizing the measurement conditions such as shielding the ambient lighting from the sun and replacing it with an artificial lighting system.

This sensing and data processing technique is crucial as it allows for non-destructive, repeatable, and contactless measurements. As a result, it offers the advantage of accurately monitoring the growth dynamics of samples, for instance, to characterize the development of a specific genotype or to assess the effectiveness of treatments applied to the samples. This methodology not only yields more accurate results but also reduces the sample size required for trials, as it avoids destructive measurements, thereby decreasing the space and costs involved.

The results obtained with the ToF sensor (Kinect V2), used in all 3D applications except field weed detection, were satisfactory, although the sensor showed some limitations due to the accuracy of distance measurement in high solar radiation and especially in the alignment between the information coming from the depth channel and the color channel, which most likely represented the greatest limitation, especially in moving

acquisitions. These critical issues were overcome by implementing the stereo camera. The results obtained using the stereo camera were characterized by a higher level of accuracy in both depth and color data. Therefore, the use of this technology for the applications previously tested with the Kinect V2 presents significant opportunities for optimization and improvement in future applications.

As regards the second main topic addressed in this work, relating to site-specific weed control, the introduction of 3D sensing has allowed a more effective identification of weeds within a work area in field conditions, even in scenarios with high weed density, which are particularly difficult to manage using only RGB images.

The results obtained with the analysis of RGB images confirm the possibility to optimize the management of herbicide treatments using algorithms that can correctly interpret the degree and type of soil cover. In particular, the LCF algorithm provided the possibility of obtaining a substantial and significant reduction in the quantities distributed, only partially penalizing the perfect success of the treatment which represents the standard obtained with non-localized distribution.

The classification algorithm which also exploits the depth data guaranteed significant reductions in the quantities distributed without reducing the effectiveness of the intervention and for this reason it proved to be very promising for implementation in open field tests.

The intervention strategy aimed at targeting all objects identified as weeds achieved its goal, yielding results statistically comparable to a uniformly distributed treatment in terms of its ability to target weeds. Furthermore, it ensured a substantial reduction in the impact of the simulated operation.

However, under moderate to low weed infestation conditions, the LCF algorithm, based on RGB imaging, still provided excellent results that exceeded expectations. For these reasons it could be worthwhile, as a future development, with the aim of keeping execution times as low as possible without compromising the quality of the result, to create a hybrid algorithm. This algorithm should use RGB images coming from the stereo camera, and use them as seen with the LCF algorithm in conditions of limited FC, and integrate the depth information only in the areas identified as most

problematic because characterized by high levels of infestation in the second phase of this algorithm only if necessary, as outlined in Section 6.2.4.

To conclude, the topic addressed regarding the implementation which includes both the simulations of the intervention strategies hypothesized in chapter 8 and the management of the actual implementation addressed in chapter 9, has highlighted the criticality linked to the spatial resolution obtainable with the actuators commercial (nozzles). These are not able to support the accuracy obtained in the detection and therefore represent an obstacle to the effective application in the field of these very high precision intervention strategies. For this reason, the possibility of working to optimize the degree of resolution achievable in spraying by investigating possible strategies or technologies that can raise the degree of spatial resolution obtainable in treatment is promising.

Reference

[1] Abdallah, I. S., Atia, M. A. M., Nasrallah, A. K., El-Beltagi, H. S., Kabil, F. F., El-Mogy, M. M., & Abdeldaym, E. A. (2021). Effect of New Pre-Emergence Herbicides on Quality and Yield of Potato and Its Associated Weeds. In Sustainability (Vol. 13, Issue 17, p. 9796). MDPI AG. https://doi.org/10.3390/su13179796

[2] Acharya (Siwakoti), E., & Pokhrel, B. (1970). Ethno-Medicinal Plants Used by Bantar of Bhaudaha, Morang, Nepal. In Our Nature (Vol. 4, Issue 1, pp. 96–103). Nepal Journals Online (JOL). https://doi.org/10.3126/on.v4i1.508

[3] Alptekin, H., Ozkan, A., Gurbuz, R., & Kulak, M. (2023). Management of Weeds in Maize by Sequential or Individual Applications of Pre- and Post-Emergence Herbicides. In Agriculture (Vol. 13, Issue 2, p. 421). MDPI AG. https://doi.org/10.3390/agriculture13020421

[4] Alsalam, B. H. Y., Morton, K., Campbell, D., & Gonzalez, F. (2017). Autonomous UAV with vision based on-board decision making for remote sensing and precision agriculture. In 2017 IEEE Aerospace Conference (pp. 1–12). 2017 IEEE Aerospace Conference. IEEE. https://doi.org/10.1109/aero.2017.7943593

[5] Altop K., E., & Mennan, H. (2010). Genetic and morphologic diversity of Echinochloa crus-galli populations from different origins. In Phytoparasitica (Vol. 39, Issue 1, pp. 93–102). Springer Science and Business Media LLC. https://doi.org/10.1007/s12600-010-0135-3

[6] Anderson, R., Bayer, P. E., & Edwards, D. (2020). Climate change and the need for agricultural adaptation. In Current Opinion in Plant Biology (Vol. 56, pp. 197–202). Elsevier BV. https://doi.org/10.1016/j.pbi.2019.12.006

[7] Aranjo, B., Soori, P. K., & Talukder, P. (2012). Stepper motor drives for robotic applications. In 2012 IEEE International Power Engineering and Optimization Conference. 2012 IEEE International Power Engineering and Optimization Conference (PEOCO). IEEE. https://doi.org/10.1109/peoco.2012.6230890

[8] Araus, J. L., & Cairns, J. E. (2014). Field high-throughput phenotyping: the new crop breeding frontier. In Trends in Plant Science (Vol. 19, Issue 1, pp. 52–61). Elsevier BV. https://doi.org/10.1016/j.tplants.2013.09.008

[9] Andújar, D., Dorado, J., Fernández-Quintanilla, C., & Ribeiro, A. (2016). An Approach to the Use of Depth Cameras for Weed Volume Estimation. In Sensors (Vol. 16, Issue 7, p. 972). MDPI AG. https://doi.org/10.3390/s16070972

[10] Bagagiolo, G., Matranga, G., Cavallo, E., & Pampuro, N. (2022). Greenhouse Robots: Ultimate Solutions to Improve Automation in Protected Cropping Systems - A Review. In Sustainability (Vol. 14, Issue 11, p. 6436). MDPI AG. https://doi.org/10.3390/su14116436

[11] Barrett S. C. H., (1983). *Crop mimicry in weeds*. Economic Botany, 37, 255–282

[12] Bechar, A. (2021). Agricultural Robotics for Precision Agriculture Tasks: Concepts and Principles. In Innovation in Agricultural Robotics for Precision Agriculture (pp. 17–30). Springer International Publishing. https://doi.org/10.1007/978-3-030-77036-5_2

[13] Berge, T. W., Goldberg, S., Kaspersen, K., & Netland, J. (2012). Towards machine vision based site-specific weed management in cereals. In Computers and Electronics in Agriculture (Vol. 81, pp. 79–86). Elsevier BV. https://doi.org/10.1016/j.compag.2011.11.004

[14] Bernardes, M. F. F., Pazin, M., Pereira, L. C., & Dorta, D. J. (2015). Impact of Pesticides on Environmental and Human Health. In Toxicology Studies - Cells, Drugs and Environment. InTech. https://doi.org/10.5772/59710

[15] Bezen, R., Edan, Y., & Halachmi, I. (2020). Computer vision system for measuring individual cow feed intake using RGB-D camera and deep learning algorithms. In Computers and Electronics in Agriculture (Vol. 172, p. 105345). Elsevier BV. https://doi.org/10.1016/j.compag.2020.105345

[16] Brancati, R., Cosenza, C., Niola, V., & Savino, S. (2018). Experimental Measurement of Underactuated Robotic Finger Configurations via RGB-D Sensor. In Mechanisms and Machine Science (pp. 531–537). Springer International Publishing. https://doi.org/10.1007/978-3-030-00232-9_56

[17] Brown, R. B., & Noble, S. D. (2005). Site-specific weed management: sensing requirements— what do we need to see? In Weed Science (Vol. 53, Issue 2, pp. 252–258). Cambridge University Press (CUP). https://doi.org/10.1614/ws-04-068r1

[18] Buelvas, R. M., Adamchuk, V. I., Pouliot, A., Strömvik, M. V., & Whitmore, A. (2019). Development of a quick-install rapid phenotyping system. In 2019 Boston, Massachusetts July 7- July 10, 2019. 2019 Boston, Massachusetts July 7- July 10, 2019. American Society of Agricultural and Biological Engineers. https://doi.org/10.13031/aim.201900130

[19] Bumgarner, N. R., Miller, W. S., & Kleinhenz, M. D. (2012). Digital Image Analysis to Supplement Direct Measures of Lettuce Biomass. HortTechnology hortte, 22(4): 547-555. https://doi.org/10.21273/HORTTECH.22.4.547

[20] Busi, R., Vila-Aiub, M. M., Beckie, H. J., Gaines, T. A., Goggin, D. E., Kaundun, S. S., Lacoste, M., Neve, P., Nissen, S. J., Norsworthy, J. K., Renton, M., Shaner, D. L., Tranel, P. J., Wright, T., Yu, Q., & Powles, S. B. (2013). Herbicide-resistant weeds: from research and knowledge to future needs. In Evolutionary Applications (Vol. 6, Issue 8, pp. 1218–1221). Wiley. https://doi.org/10.1111/eva.12098

[21] Camarda I, Brundu G, Celesti Grapow L, Viegi L & Blasi C. 2005 – Le specie esotiche invasive. In: Scoppola A & Blasi C. (eds.), Stato delle Conoscenze sulla flora vascolare d'Italia, Pp 23-28. Palombi & Partner, Roma.

[22] Chauhan, B. S. (2020). Grand Challenges in Weed Management. In Frontiers in Agronomy (Vol. 1). Frontiers Media SA. https://doi.org/10.3389/fagro.2019.00003

[23] Chéné, Y., Rousseau, D., Lucidarme, P., Bertheloot, J., Caffier, V., Morel, P., Belin, É., & Chapeau-Blondeau, F. (2012). On the use of depth camera for 3D phenotyping of entire plants. In Computers and Electronics in Agriculture 82: 122–127. https://doi.org/10.1016/j.compag.2011.12.007

[24] Christensen, S., Søgaard, H. T., Kudsk, P., Nørremark, M., Lund, I., Nadimi, E. S., & Jørgensen, R. (2009). Site-specific weed control technologies. In Weed Research (Vol. 49, Issue 3, pp. 233–241). Wiley. https://doi.org/10.1111/j.1365-3180.2009.00696.x

[25] Cortignani, R., Buttinelli, R., & Dono, G. (2022). Farm to Fork strategy and restrictions on the use of chemical inputs: Impacts on the various types of farming and territories of Italy. In Science of The Total Environment (Vol. 810, p. 152259). Elsevier BV. https://doi.org/10.1016/j.scitotenv.2021.152259

[26] Conti F, Abbate G, Alessandrini A & Blasi C. (eds.) 2005. An annotated checklist of the italian vascular flora. Palombi & Partner, Roma.

[27] Costea M, Sanders A & Waines G. (2001). Preliminary results toward a revision of the Amaranthus hybridus species complex (Amaranthaceae). Sida 19: 931–974.

[28] Cozzolino, Eugenio & Bilotto, Maurizio & Leone, Vincenzo & Zampella, Luigi & Petriccione, Milena & Cerrato, Domenico & Morra, Luigi. (2015). Produzione e qualità di melone retato su pacciamatura in Mater -Bi®. Colture Protette. Retrieved from https://www.researchgate.net/publication/277774347

[29] Dhanaraju, M., Chenniappan, P., Ramalingam, K., Pazhanivelan, S., & Kaliaperumal, R. (2022). Smart Farming: Internet of Things (IoT)-Based Sustainable Agriculture. In Agriculture (Vol. 12, Issue 10, p. 1745). MDPI AG. https://doi.org/10.3390/agriculture12101745

[30] Dewar, A. M. (2009). Weed control in glyphosate-tolerant maize in Europe. In Pest Management Science (Vol. 65, Issue 10, pp. 1047–1058). Wiley. https://doi.org/10.1002/ps.1806

[31] Dobbs, A. M., Ginn, D., Skovsen, S. K., Bagavathiannan, M. V., Mirsky, S. B., Reberg-Horton, C. S., & Leon, R. G. (2022). New directions in weed management and research using 3D imaging. In Weed Science (Vol. 70, Issue 6, pp. 641–647). Cambridge University Press (CUP). https://doi.org/10.1017/wsc.2022.56

[32] Duckett T., Pearson S., Blackmore S., Grieve B., Agricultural Robotics: The Future of Robotic Agriculture; UK-RAS White papers, UK-RAS (2018) ISSN 2398-4414

[33] Esposito, M., Crimaldi, M., Cirillo, V., Sarghini, F., & Maggio, A. (2021).Drone and sensor technology for sustainable weed management: a review.In Chemical and Biological Technologies in Agriculture (Vol. 8, Issue 1). Springer Science and Business Media LLC. https://doi.org/10.1186/s40538-021-00217-8

[34] Fabula, J. V., & Sharda, A. (2021). Field evaluation of turn compensation feature of pulse width modulation (PWM) equipped agricultural sprayer. In 2021 ASABE Annual International Virtual Meeting, July 12-16, 2021. 2021 ASABE Annual International Virtual Meeting, July 12-16, 2021. American Society of Agricultural and Biological Engineers. https://doi.org/10.13031/aim.202101190

[35] Fankhauser, P., Bloesch, M., Rodriguez, D., Kaestner, R., Hutter, M., & Siegwart, R. (2015). Kinect v2 for mobile robot navigation: Evaluation and modeling. In 2015 International Conference on Advanced Robotics (ICAR). 2015 International Conference on Advanced Robotics (ICAR). IEEE. https://doi.org/10.1109/icar.2015.7251485

[36] Farooq, N., Abbas, T., Tanveer, A., & Jabran, K. (2020). Allelopathy for Weed Management. In Reference Series in Phytochemistry (pp. 505–519). Springer International Publishing. https://doi.org/10.1007/978-3-319-96397-6_16

[37] Feng, A., Zhang, M., Sudduth, K. A., Vories, E. D., & Zhou, J. (2019). Cotton Yield Estimation from UAV-Based Plant Height. In Transactions of the ASABE (Vol. 62, Issue 2, pp. 393–404). American Society of Agricultural and Biological Engineers (ASABE). https://doi.org/10.13031/trans.13067

[38] Fernández-Quintanilla, C., Dorado, J., Andújar, D., & Peña, J. M. (2020). Site-Specific Based Models. In Decision Support Systems for Weed Management (pp. 143–157). Springer International Publishing. https://doi.org/10.1007/978-3-030-44402-0_7

[39] Francesca, N., Guarcello, R., Craparo, V., Moschetti, G., Settanni, L., Gaglio, R. (2019). Microbial ecology of retail ready-to-eat escarole and red chicory sold in Palermo City, Italy. In Journal of Food Quality and Hazards Control, 6 (2): 45-52, https://doi.org/10.18502/jfqhc.6.2.954

[40] Friedli, M., Kirchgessner, N., Grieder, C., Liebisch, F., Mannale, M., & Walter, A. (2016). Terrestrial 3D laser scanning to track the increase in canopy height of both monocot and dicot crop species under field conditions. In Plant Methods, 12 (1). Springer Science and Business Media LLC. https://doi.org/10.1186/s13007-016-0109-7

[41] Fue, K., Porter, W., Barnes, E., & Rains, G. (2020). An Extensive Review of Mobile Agricultural Robotics for Field Operations: Focus on Cotton Harvesting. In Agri Engineering (Vol. 2, Issue 1, pp. 150–174). MDPI AG. https://doi.org/10.3390/agriengineering2010010

[42] Gai, J., Tang, L., Steward, B. (2016). Plant localization and discrimination using 2d+3d computer vision for robotic intra-row weed control. In: Proceedings of the ASABE Annual International Meeting. Paper No. 162460814, St. Joseph, Mich.: ASABE: 1-15, https://doi.org/10.13031/aim.20162460814

[43] Gai, J., Tang, L., Steward, B.L. (2020). Automated crop plant detection based on the fusion of color and depth images for robotic weed control. Journal of Field Robotics, 37 (1): 35-52, https://doi.org/10.1002/rob.21897

[44] Gai, J., Xiang, L., & Tang, L. (2021). Using a depth camera for crop row detection and mapping for under-canopy navigation of agricultural robotic vehicle. In Computers and Electronics in Agriculture (Vol. 188, p. 106301). Elsevier BV. https://doi.org/10.1016/j.compag.2021.106301

[45] Ganesan, T., Jayarajan, N., & Sureshkumar, P. (2023). Review on the Real-time Implementation of IoT-enabled UAV in Precision Agriculture and the Overview of Collision Avoidance Strategies. In Philippine Journal of Science (Vol. 152, Issue 3). Science and Technology Information Institute. https://doi.org/10.56899/152.03.29

[46] Gebbers, R., & Adamchuk, V. I. (2010). Precision Agriculture and Food Security. In Science (Vol. 327, Issue 5967, pp. 828–831). American Association for the Advancement of Science (AAAS). https://doi.org/10.1126/science.1183899

[47] Gerhards, R., & Oebel, H. (2006). Practical experiences with a system for site-specific weed control in arable crops using real-time image analysis and GPS-controlled patch spraying. In Weed Research (Vol. 46, Issue 3, pp. 185–193). Wiley. https://doi.org/10.1111/j.1365-3180.2006.00504.x

[48] Gerhards, R., Andújar Sanchez, D., Hamouz, P., Peteinatos, G. G., Christensen, S., & Fernandez-Quintanilla, C. (2022). Advances in site-specific weed management in agriculture—A review. In Weed Research (Vol. 62, Issue 2, pp. 123–133). Wiley. https://doi.org/10.1111/wre.12526

[49] Gharde, Y., Singh, P. K., Dubey, R. P., & Gupta, P. K. (2018). Assessment of yield and economic losses in agriculture due to weeds in India. In Crop Protection (Vol. 107, pp. 12–18). Elsevier BV. https://doi.org/10.1016/j.cropro.2018.01.007

[50] Giacomelli, G.A., Ling, P.P., & Kole, J. (1998). Determining Nutrient Stress in Lettuce Plants with Machine Vision Technology. HortTechnology horttech, 8(3): 361-365. https://doi.org/10.21273/HORTTECH.8.3.361

[51] Gibson, K. D., Fischer, A. J., Foin, T. C., & Hill, J. E. (2002). Implications of delayed Echinochloa spp. germination and duration of competition for integrated weed management in water-seeded rice. In Weed Research (Vol. 42, Issue 5, pp. 351–358). Wiley. https://doi.org/10.1046/j.1365-3180.2002.00295.x

[52] Gnanavel, I. (2015). Eco-Friendly Weed Control Options for Sustainable Agriculture. In Science International (Vol. 3, Issue 2, pp. 37–47). Science International. https://doi.org/10.17311/sciintl.2015.37.47

[53] Golbach, F., Kootstra, G., Damjanovic, S., Otten, G., van de Zedde, R. (2015). Validation of plant part measurements using a 3D reconstruction method suitable for high-throughput seedling phenotyping. In Machine Vision and Applications, 27 (5): 663–680. https://doi.org/10.1007/s00138-015-0727-5

[54] Gregorio, E., & Llorens, J. (2021). Sensing Crop Geometry and Structure. In Progress in Precision Agriculture (pp. 59–92). Springer International Publishing. https://doi.org/10.1007/978-3-030-78431-7_37

[55] Gullino, M.L., Gilardi, G., Garibaldi, A. (2019). Ready-to-Eat Salad Crops: A Plant Pathogen's Heaven. Plant disease, 103 (9): 2153-2170, https://doi.org/10.1094/PDIS-03-19-0472-FE

[56] Heo, K.-S., & Lim, K.-T. (2004). Antioxidative Effects of Glycoprotein Isolated from Solanum nigrum L. In Journal of Medicinal Food (Vol. 7, Issue 3, pp. 349–357). Mary Ann Liebert Inc. https://doi.org/10.1089/jmf.2004.7.349

[57] Holm, L. G., Plucknett, D. L., Pancho, J. V., & Herberger, J. P. (1977). *Echinochloa crus-galli L.* In: *The world's worst weeds* (pp. 32- 40). Honolulu, HI, USA: University Press of Hawaii

[58] Hu, Y., Wang, L., Xiang, L., Wu, Q., Jiang, H. (2018). Automatic non-destructive growth measurement of leafy vegetables based on Kinect Sensors. In Sensors, 18 (3), 806. https://doi.org/10.3390/s18030806

[59] Huang, Y., Reddy, K. N., Fletcher, R. S., & Pennington, D. (2017). UAV Low-Altitude Remote Sensing for Precision Weed Management. In Weed Technology (Vol. 32, Issue 1, pp. 2–6). Cambridge University Press (CUP). https://doi.org/10.1017/wet.2017.89

[60] Hunter, J. E., III, Gannon, T. W., Richardson, R. J., Yelverton, F. H., & Leon, R. G. (2019). Integration of remote-weed mapping and an autonomous spraying unmanned aerial vehicle for site-specific weed management. In Pest Management Science (Vol. 76, Issue 4, pp. 1386–1392). Wiley. https://doi.org/10.1002/ps.5651

[61] Hütt, C., Bolten, A., Hüging, H., & Bareth, G. (2022). UAV LiDAR Metrics for Monitoring Crop Height, Biomass and Nitrogen Uptake: A Case Study on a Winter Wheat Field Trial. In PFG – Journal of Photogrammetry, Remote Sensing and Geoinformation Science (Vol. 91, Issue 2, pp. 65–76). Springer Science and Business Media LLC. https://doi.org/10.1007/s41064-022-00228-6

[62] Iamonico D., *life-strategy and invasiveness of Amaranthus retroflexus L. in central Italy: preliminary remarks*. Botanica serbica 34 (2): 137-145 (2010)

[63] Iqbal, S., Tahir, S., Dass, A., Bhat, M. A., & Rashid, Z. (2020). Bio-efficacy of Pre-emergent Herbicides for Weed Control in Maize: A Review on Weed Dynamics Evaluation. In Journal of Experimental Agriculture International (pp. 13–23). Science domain International. https://doi.org/10.9734/jeai/2020/v42i830565

[64] Izquierdo, J., Recasens, J., Fernández-Quintanilla, C., & Gill, G. (2003). Effects of crop and weed densities on the interactions between barley and Lolium rigidum in several Mediterranean locations. In Agronomie (Vol. 23, Issue 7, pp. 529–536). EDP Sciences. https://doi.org/10.1051/agro:2003028

[65] Jain, L. K. (2022). Growth and productivity of maize (Zea mays L.) as influenced by organic weed and nutrient management practices in Western Rajasthan. In Annals of plant and soil research (Vol. 24, Issue 1, pp. 59–64). Gramya Krishi Vikas Samiti. https://doi.org/10.47815/apsr.2022.10124

[66] James, T. K., Rahman, A., & Trolove, M. (2007). Optimising time of planting and herbicide aplication for control of problem weeds in maize. In New Zealand Plant Protection (Vol. 60, pp. 183–188). New Zealand Plant Protection Society. https://doi.org/10.30843/nzpp.2007.60.4598

[67] Jebeli, M., Bilesan, A., & Arshi, A. (2017). A study on validating KinectV2 in comparison of Vicon system as a motion capture system for using in Health Engineering in industry. In Nonlinear Engineering (Vol. 6, Issue 2). Walter de Gruyter GmbH. https://doi.org/10.1515/nleng-2016-0017

[68] Jin, Y., Liu, J., Xu, Z., Yuan, S., Li, P., & Wang, J. (2021). Development status and trend of agricultural robot technology. In International Journal of Agricultural and Biological Engineering (Vol. 14, Issue 3, pp. 1–19). International Journal of Agricultural and Biological Engineering (IJABE). https://doi.org/10.25165/j.ijabe.20211404.6821

[69] Jung, D.-H., Park, S. H., Han, X. Z., & Kim, H.-J. (2015). Image Processing Methods for Measurement of Lettuce Fresh Weight. Journal of Biosystems Engineering, 40(1): 89–93. https://doi.org/10.5307/JBE.2015.40.1.089

[70] Karadöl, H., Aybek, A., & Üçgül, M. (2020). Implementation of Patch Spraying Application to the Weed Areas Detected in Corn Lands. In Tarım Bilimleri Dergisi. Ankara University Faculty of Agriculture. https://doi.org/10.15832/ankutbd.495903

[71] Karkee, M., Bhusal, S., & Zhang, Q. (2021). Sensors II: 3D Sensing Techniques and Systems. In Agriculture Automation and Control (pp. 39–77). Springer International Publishing. https://doi.org/10.1007/978-3-030-70400-1_3

[72] Klopfenstein, T. J., Erickson, G. E., & Berger, L. L. (2013). Maize is a critically important source of food, feed, energy and forage in the USA. In Field Crops Research (Vol. 153, pp. 5–11). Elsevier BV. https://doi.org/10.1016/j.fcr.2012.11.006

[73] Kőmíves, P. M., Pilishegyi, P., Novák, N., Nagy, A. S., & Köröspartí, P. (2019). The Role of the Higher Education in the Development of the Agriculture. In International Journal of Information and Education Technology (Vol. 9, Issue 9, pp. 607–612). EJournal Publishing. https://doi.org/10.18178/ijiet.2019.9.9.1275

[74] Kudsk, P., & Streibig, J. C. (2003). Herbicides – a two-edged sword*. In Weed Research (Vol. 43, Issue 2, pp. 90–102). Wiley. https://doi.org/10.1046/j.1365-3180.2003.00328.x

[75] Kurtser, P., & Lowry, S. (2023). RGB-D datasets for robotic perception in site-specific agricultural operations—A survey. In Computers and Electronics in Agriculture (Vol. 212, p. 108035). Elsevier BV. https://doi.org/10.1016/j.compag.2023.108035

[76] Lachat, E., Macher, H., Landes, T., & Grussenmeyer, P. (2015). Assessment and Calibration of a RGB-D Camera (Kinect v2 Sensor) Towards a Potential Use for Close-Range 3D Modeling. In Remote Sensing 7 (10), 13070–13097. MDPI AG. https://doi.org/10.3390/rs71013070

[77] Lati, R. N., Filin, S., & Eizenberg, H. (2013). Estimation of Plants' Growth Parameters via Image-Based Reconstruction of Their Three-Dimensional Shape. In Agronomy Journal, 105(1): 191–198. Wiley. https://doi.org/10.2134/agronj2012.0305

[78] Le Louëdec, J., & Cielniak, G. (2021). 3D shape sensing and deep learning-based segmentation of strawberries. In Computers and Electronics in Agriculture (Vol. 190, p. 106374). Elsevier BV. https://doi.org/10.1016/j.compag.2021.106374

[79] Lemerle, D., Verbeek, B., & Coombes, N. (1995). Losses in grain yield of winter crops from Lolium rigidum competition depend on crop species, cultivar and season. In Weed Research (Vol. 35, Issue 6, pp. 503–509). Wiley. https://doi.org/10.1111/j.1365-3180.1995.tb01648.x

[80] Liaqat, W., Barutçular, C., Farooq, M. U., Ahmad, H., Jan, M. F., Ahmad, Z., Nawaz, H., & Li, M. (2022). Climate change in relation to agriculture: A review. In Spanish Journal of Agricultural Research (Vol. 20, Issue 2, p. e03R01). Instituto Nacional de Investigacion y Tecnologia Agraria y Alimentaria (INIA). https://doi.org/10.5424/sjar/2022202-17742

[81] Li, L., Mu, X., Jiang, H., Chianucci, F., Hu, R., Song, W., et al. (2023). Review of ground and aerial methods for vegetation cover fraction (fCover) and related quantities estimation: definitions, advances, challenges, and future perspectives. ISPRS J. Photogrammetry Remote Sens. 199, 133–156. https://doi.org/10.1016/j.isprsjprs.2023.03.020

[82] (1) Lin, G., Huang, P., Wang, M., Xu, Y., Zhang, R., & Zhu, L. (2022). An Inverse Kinematics Solution for a Series-Parallel Hybrid Banana-Harvesting Robot Based on Deep Reinforcement Learning. In Agronomy (Vol. 12, Issue 9, p. 2157). MDPI AG. https://doi.org/10.3390/agronomy12092157

[83] (2) Lin, C., Hu, F., Peng, J., Wang, J., & Zhai, R. (2022). Segmentation and Stratification Methods of Field Maize Terrestrial LiDAR Point Cloud. In Agriculture (Vol. 12, Issue 9, p. 1450). MDPI AG. https://doi.org/10.3390/agriculture12091450

[84] Liu, K., Dong, X., & Qiu, B. (2018). Analysis of cotton height spatial variability based on UAV-LiDAR. In International Journal of Precision Agricultural Aviation (Vol. 1, Issue 1, pp. 72–76). International Journal of Precision Agricultural Aviation. https://doi.org/10.33440/j.ijpaa.20200303.79

[85] Liu, H., Bruning, B., Garnett, T., & Berger, B. (2020). Hyperspectral imaging and 3D technologies for plant phenotyping: From satellite to close-range sensing. In Computers and Electronics in Agriculture (Vol. 175, p. 105621). Elsevier BV. https://doi.org/10.1016/j.compag.2020.105621

[86] Losio, M.N., Pavoni, E., Bilei, S., Bertasi, B., Bove, D., Capuano, F., Farneti, S., Blasi, G., Comin, D., Cardamone, C., Decastelli, L., Delibato, E., De Santis, P., Di Pasquale, S., Gattuso, A., Goffredo, E., Fadda, A., Pisanu, M., De Medici, D. (2015). Microbiological survey of raw and ready-to-eat leafy green vegetables marketed in Italy. International Journal of Food Microbiology, 210: 88-91, https://doi.org/10.1016/j.ijfoodmicro.2015.05.026

[87] Lou, L., Liu, Y., Han, J., & Doonan, J. H. (2014). Accurate Multi-View Stereo 3D Reconstruction for Cost-Effective Plant Phenotyping. In Lecture Notes in Computer Science (pp. 349–356). Springer International Publishing. https://doi.org/10.1007/978-3-319-11755-3_39

[88] Lou, M., Lu, J., Wang, L., Jiang, H., Zhou, M., (2022). Growth parameter acquisition and geometric point cloud completion of lettuce. Frontiers in Plant Science. 13:947690. https://doi.org/10.3389/fpls.2022.947690

[89] Lowenberg-DeBoer, J., Huang, I. Y., Grigoriadis, V., & Blackmore, S. (2019). Economics of robots and automation in field crop production. In Precision Agriculture (Vol. 21, Issue 2, pp. 278–299). Springer Science and Business Media LLC. https://doi.org/10.1007/s11119-019-09667-5

[90] Maciel, G. M., Gallis, R. B. de A., Barbosa, R. L., Pereira, L. M., Siquieroli, A. C. S., & Peixoto, J. V. M. (2020). Image phenotyping of lettuce germplasm with genetically diverse carotenoid levels. In Bragantia (Vol. 79, Issue 2, pp. 224–235). FapUNIFESP (SciELO). https://doi.org/10.1590/1678-4499.20190519

[91] Matzrafi, M., Preston, C., & Brunharo, C. A. (2020). Review: evolutionary drivers of agricultural adaptation in Lolium spp. In Pest Management Science (Vol. 77, Issue 5, pp. 2209–2218). Wiley. https://doi.org/10.1002/ps.6219

[92] Meyer, G. E., & Neto, J. C. (2008). Verification of color vegetation indices for automated crop imaging applications. In Computers and Electronics in Agriculture (Vol. 63, Issue 2, pp. 282–293). Elsevier BV. https://doi.org/10.1016/j.compag.2008.03.009

[93] Mohd Ghazi, R., Nik Yusoff, N. R., Abdul Halim, N. S., Wahab, I. R. A., Ab Latif, N., Hasmoni, S. H., Ahmad Zaini, M. A., & Zakaria, Z. A. (2023). Health effects of herbicides and its current removal strategies. In Bioengineered (Vol. 14, Issue 1). Informa UK Limited. https://doi.org/10.1080/21655979.2023.2259526

[94] Monta, M., & Namba, K. (n.d.). Three-dimensional sensing system for agricultural robots. In Proceedings 2003 IEEE/ASME International Conference on Advanced Intelligent Mechatronics (AIM 2003) (Vol. 2, pp. 1216–1221). 2003 IEEE/ASME International Conference on Advanced Intelligent Mechatronics (AIM 2003). IEEE. https://doi.org/10.1109/aim.2003.1225516

[95] Monteiro A., & Santos S. (2022). Sustainable Approach to Weed Management: The Role of Precision Weed Management. Agronomy, 12(1): 118. https://doi.org/10.3390/agronomy12010118

[96] Mortensen, A. K., Lisouski, P., & Ahrendt, P. (2016). Weight prediction of broiler chickens using 3D computer vision. In Computers and Electronics in Agriculture (Vol. 123, pp. 319–326). Elsevier BV. https://doi.org/10.1016/j.compag.2016.03.011

[97] Mortensen, A.K., Bender, A., Whelan, B., Barbour, M.M., Sukkarieh, S., Karstoft, H., Gislum, R. (2018). Segmentation of lettuce in coloured 3D point clouds for fresh weight estimation. Computers and Electronics in Agriculture, 154: 373-381, https://10.1016/j.compag.2018.09.010

[98] Moysiadis, V., Sarigiannidis, P., Vitsas, V., & Khelifi, A. (2021). Smart Farming in Europe. In Computer Science Review (Vol. 39, p. 100345). Elsevier BV. https://doi.org/10.1016/j.cosrev.2020.100345

[99] Na, M. H., Cho, W. H., Kim, S. K., & Na, I. S. (2022). Automatic Weight Prediction System for Korean Cattle Using Bayesian Ridge Algorithm on RGB-D Image. In Electronics (Vol. 11, Issue 10, p. 1663). MDPI AG. https://doi.org/10.3390/electronics11101663

[100] Nedeljković, D., Knežević, S., Božić, D., & Vrbničanin, S. (2021). Critical Time for Weed Removal in Corn as Influenced by Planting Pattern and PRE Herbicides. In Agriculture (Vol. 11, Issue 7, p. 587). MDPI AG. https://doi.org/10.3390/agriculture11070587

[101] Nguyen, T. T., Slaughter, D. C., Maloof, J. N., & Sinha, N. (2016). Plant phenotyping using multi-view stereo vision with structured lights. In J. Valasek & J. A. Thomasson (Eds.), SPIE Proceedings (Vol. 9866, p. 986608). SPIE Commercial + Scientific Sensing and Imaging. SPIE. https://doi.org/10.1117/12.2229513

[102] Nicola, S., Hoeberechts, J., Fontana, E., Saglietti, D. (2003). Cultural technique influences on post-harvest quality of rocket (Eruca sativa Mill.) Acta Horticulturae, 604: 685-690, https://doi.org/10.17660/ActaHortic.2003.604.85

[103] Nicola, S., Fontana, E. (2014). Fresh-Cut Produce Quality. Implications for a Systems Approach. In: Postharvest Handling: A Systems Approach, pp. 217-273. Ed. Elsevier Inc. https://doi.org/10.1016/B978-0-12-408137-6.00009-0

[104] Oerke, E.-C. (2005). Crop losses to pests. In The Journal of Agricultural Science (Vol. 144, Issue 1, pp. 31–43). Cambridge University Press (CUP). https://doi.org/10.1017/s0021859605005708

[105] Pant, C., Sah, S. K., Marahatta, S., & Dhakal, S. (2021). Weed Dynamics In No-Till Maize System And Its Management: A Review. In Agronomy Journal of Nepal (Vol. 5, pp. 168–177). Nepal Journals Online (JOL). https://doi.org/10.3126/ajn.v5i01.44838

[106] Partel, V., Charan Kakarla, S., & Ampatzidis, Y. (2019). Development and evaluation of a low-cost and smart technology for precision weed management utilizing artificial intelligence. In Computers and Electronics in Agriculture (Vol. 157, pp. 339–350). Elsevier BV. https://doi.org/10.1016/j.compag.2018.12.048

[107] Paruelo, J. M., Lauenroth, W. K., & Roset, P. A. (2000). Estimating Aboveground Plant Biomass Using a Photographic Technique. In Journal of Range Management (Vol. 53, Issue 2, p. 190). JSTOR. https://doi.org/10.2307/4003281

[108] Pauli, D., Andrade-Sanchez, P., Carmo-Silva, A. E., Gazave, E., French, A. N., Heun, J., Hunsaker, D. J., Lipka, A. E., Setter, T. L., Strand, R. J., Thorp, K. R., Wang, S., White, J. W., & Gore, M. A. (2016). Field-Based High-Throughput Plant Phenotyping Reveals the Temporal Patterns of Quantitative Trait Loci Associated with Stress-Responsive Traits in Cotton. In G3 Genes|Genomes|Genetics (Vol. 6, Issue 4, pp. 865–879). Oxford University Press (OUP). https://doi.org/10.1534/g3.115.023515

[109] Paulus, S. (2019). Measuring crops in 3D: using geometry for plant phenotyping. In Plant Methods (Vol. 15, Issue 1). Springer Science and Business Media LLC. https://doi.org/10.1186/s13007-019-0490-0

[110] Patrignani, A., & Ochsner, T. E. (2015). Canopeo: A Powerful New Tool for Measuring Fractional Green Canopy Cover. In Agronomy Journal (Vol. 107, Issue 6, pp. 2312–2320). Wiley. https://doi.org/10.2134/agronj15.0150

[111] Peles, F., Sipos, P., Kovács, S., Győri, Z., Pócsi, I., & Pusztahelyi, T. (2021). Biological Control and Mitigation of Aflatoxin Contamination in Commodities. In Toxins (Vol. 13, Issue 2, p. 104). MDPI AG. https://doi.org/10.3390/toxins13020104

[112] Peng, Y., Liu, J., Xie, B., Shan, H., He, M., Hou, G., & Jin, Y. (2021). Research Progress of Urban Dual-arm Humanoid Grape Harvesting Robot. In 2021 IEEE 11th Annual International Conference on CYBER Technology in Automation, Control, and Intelligent Systems (CYBER). 2021 IEEE 11th Annual International Conference on CYBER Technology in Automation, Control, and Intelligent Systems (CYBER). IEEE. https://doi.org/10.1109/cyber53097.2021.9588266

[113] Pereyra-Irujo, G. A., Gasco, E. D., Peirone, L. S., & Aguirrezábal, L. A. N. (2012). GlyPh: a low-cost platform for phenotyping plant growth and water use. In Functional Plant Biology (Vol. 39, Issue 11, p. 905). CSIRO Publishing. https://doi.org/10.1071/fp12052

[114] Pérez-Ruíz, M., Slaughter, D. C., Fathallah, F. A., Gliever, C. J., & Miller, B. J. (2014). Co-robotic intra-row weed control system. In Biosystems Engineering (Vol. 126, pp. 45–55). Elsevier BV. https://doi.org/10.1016/j.biosystemseng.2014.07.009

[115] Peteinatos, G. G., Reichel, P., Karouta, J., Andújar, D., & Gerhards, R. (2020). Weed Identification in Maize, Sunflower, and Potatoes with the Aid of Convolutional Neural Networks. In Remote Sensing (Vol. 12, Issue 24, p. 4185). MDPI AG. https://doi.org/10.3390/rs12244185

[116] Popescu, D., Stoican, F., Stamatescu, G., Ichim, L., & Dragana, C. (2020). Advanced UAV–WSN System for Intelligent Monitoring in Precision Agriculture. In Sensors (Vol. 20, Issue 3, p. 817). MDPI AG. https://doi.org/10.3390/s20030817

[117] Priyanka P. Chandak (2017), Smart Farming System Using Data Mining, In International Journal of Applied Engineering Research, Volume 12, Number 11. https://doi.org/10.22214/ijraset.2022.45739

[118] Rasmussen, J., Nielsen, J., Garcia-Ruiz, F., Christensen, S., & Streibig, J. C. (2013). Potential uses of small unmanned aircraft systems (UAS) in weed research. In B. Lotz (Ed.), Weed Research (Vol. 53, Issue 4, pp. 242–248). Wiley. https://doi.org/10.1111/wre.12026

[119] Remondino, F., Barazzetti, L., Nex, F., Scaioni, M., & Sarazzi, D. (2012). UAV photogrammetry for mapping and 3d modeling – current status and future perspectives. In The International Archives of the Photogrammetry, Remote Sensing and Spatial Information Sciences: Vol. XXXVIII-1/C22 (pp. 25–31). Copernicus GmbH. https://doi.org/10.5194/isprsarchives-xxxviii-1-c22-25-2011

[120] Reynolds, M., Dobos, J., Peel, L., Weyrich, T., & Brostow, G. J. (2011). Capturing Time-of-Flight data with confidence. In CVPR 2011. 2011 IEEE Conference on Computer Vision and Pattern Recognition (CVPR). IEEE. https://doi.org/10.1109/cvpr.2011.5995550

[121] Riemens M., Sønderskov M., Moonen A.-C., Storkey J., & Kudsk P. (2022). An Integrated Weed Management framework: A pan-European perspective. European Journal of Agronomy, 133: 126443). https://doi.org/10.1016/j.eja.2021.126443

[122] Revilla, P., Alves, M. L., Andelković, V., Balconi, C., Dinis, I., Mendes-Moreira, P., Redaelli, R., Ruiz de Galarreta, J. I., Vaz Patto, M. C., Žilić, S., & Malvar, R. A. (2022). Traditional Foods From Maize (Zea mays L.) in Europe. In Frontiers in Nutrition (Vol. 8). Frontiers Media SA. https://doi.org/10.3389/fnut.2021.683399

[123] Riomoros, I., Guijarro, M., Pajares, G., Herrera, P. J., Burgos-Artizzu, X. P., & Ribeiro, A. (2010). Automatic image segmentation of greenness in crop fields. In 2010 International Conference of Soft Computing and Pattern Recognition. 2010 International Conference of Soft Computing and Pattern Recognition (SoCPaR). IEEE. https://doi.org/10.1109/socpar.2010.5685936

[124] Ronchetti, G. (2020). UAV surveys for crop monitoring and management in Precision Agriculture

[125] Rose, J., Paulus, S., & Kuhlmann, H. (2015). Accuracy Analysis of a Multi-View Stereo Approach for Phenotyping of Tomato Plants at the Organ Level. In Sensors, 15 (5), 9651–9665, MDPI AG, https://doi.org/10.3390/s150509651

[126] Rose, J., Kicherer, A., Wieland, M., Klingbeil, L., Töpfer, R., & Kuhlmann, H. (2016). Towards Automated Large-Scale 3D Phenotyping of Vineyards under Field Conditions. In Sensors (Vol. 16, Issue 12, p. 2136). MDPI AG. https://doi.org/10.3390/s16122136

[127] Sabov, A., & Kruger, J. (2008). Identification and correction of flying pixels in range camera data. In Proceedings of the 24th Spring Conference on Computer Graphics. SCCG08: Spring Conference on Computer Graphics. ACM. https://doi.org/10.1145/1921264.1921293

[128] Saini, R.K., Ko, E.Y., Keum, Y.-S. (2017). Minimally processed ready-to-eat baby-leaf vegetables: Production, processing, storage, microbial safety, and nutritional potential. Food Reviews International, 33 (6): 644-663, https://doi.org/10.1080/87559129.2016.1204614

[129] Sampaio, G. S., Silva, L. A., & Marengoni, M. (2021). 3D Reconstruction of Non-Rigid Plants and Sensor Data Fusion for Agriculture Phenotyping. In Sensors (Vol. 21, Issue 12, p. 4115). MDPI AG. https://doi.org/10.3390/s21124115

[130] Scarfone, A., Picchio, R., del Giudice, A., Latterini, F., Mattei, P., Santangelo, E., & Assirelli, A. (2021). Semi-Automatic Guidance vs. Manual Guidance in Agriculture: A Comparison of Work Performance in Wheat Sowing. In Electronics (Vol. 10, Issue 7, p. 825). MDPI AG. https://doi.org/10.3390/electronics10070825

[131] Scavo, A., Abbate, C., & Mauromicale, G. (2019). Plant allelochemicals: agronomic, nutritional and ecological relevance in the soil system. In Plant and Soil (Vol. 442, Issues 1–2, pp. 23–48). Springer Science and Business Media LLC. https://doi.org/10.1007/s11104-019-04190-y

[132] Scavo, A., & Mauromicale, G. (2020). Integrated Weed Management in Herbaceous Field Crops. In Agronomy (Vol. 10, Issue 4, p. 466). MDPI AG. https://doi.org/10.3390/agronomy10040466

[133] Sharma, N., & Rayamajhi, M. (2022). Different Aspects of Weed Management in Maize (Zea mays L.): A Brief Review. In G. Kocsy (Ed.), Advances in Agriculture (Vol. 2022, pp. 1–10). Hindawi Limited. https://doi.org/10.1155/2022/7960175

[134] Shaw, D. R. (2005). Remote sensing and site-specific weed management. In Frontiers in Ecology and the Environment (Vol. 3, Issue 10, pp. 526–532). Wiley. https://doi.org/10.1890/1540-9295(2005)003[0526:rsaswm]2.0.co;2

[135] Shiferaw, B., Prasanna, B. M., Hellin, J., & Bänziger, M. (2011). Crops that feed the world 6. Past successes and future challenges to the role played by maize in global food security. In Food Security (Vol. 3, Issue 3, pp. 307–327). Springer Science and Business Media LLC. https://doi.org/10.1007/s12571-011-0140-5

[136] Shockley, J. M., Dillon, C. R., & Shearer, S. A. (2019). An economic feasibility assessment of autonomous field machinery in grain crop production. In Precision Agriculture (Vol. 20, Issue 5, pp. 1068–1085). Springer Science and Business Media LLC. https://doi.org/10.1007/s11119-019-09638-w

[137] Skoczeń, M., Ochman, M., Spyra, K., Nikodem, M., Krata, D., Panek, M., & Pawłowski, A. (2021). Obstacle Detection System for Agricultural Mobile Robot Application Using RGB-D Cameras. In Sensors (Vol. 21, Issue 16, p. 5292). MDPI AG. https://doi.org/10.3390/s21165292

[138] Slaughter, D. C., Giles, D. K., & Downey, D. (2008). Autonomous robotic weed control systems: A review. In Computers and Electronics in Agriculture (Vol. 61, Issue 1, pp. 63–78). Elsevier BV. https://doi.org/10.1016/j.compag.2007.05.008

[139] Stafford, J. V. (2000). Implementing Precision Agriculture in the 21st Century. In Journal of Agricultural Engineering Research (Vol. 76, Issue 3, pp. 267–275). Elsevier BV. https://doi.org/10.1006/jaer.2000.0577

[140] Stephens, R. J. (1982). Effects of Weed Infestation on Crop Yield and Quality. In Theory and Practice of Weed Control (pp. 1–14). Macmillan Education UK. https://doi.org/10.1007/978-1-349-86066-1_1

[141] Swinton, S. M. (2005). Economics of site-specific weed management. In Weed Science (Vol. 53, Issue 2, pp. 259–263). Cambridge University Press (CUP). https://doi.org/10.1614/ws-04-035r2

[142] Tackenberg, O. (2007). A new method for non-destructive measurement of biomass, growth rates, vertical biomass distribution and dry matter content based on digital image analysis. Annals of botany, 99(4), 777-783, https://doi.org/10.1093/aob/mcm009

[143] Terence, S., & Purushothaman, G. (2020). Systematic review of Internet of Things in smart farming. In Transactions on Emerging Telecommunications Technologies (Vol. 31, Issue 6). Wiley. https://doi.org/10.1002/ett.3958

[144] Thorp, K. R., Gore, M. A., Andrade-Sanchez, P., Carmo-Silva, A. E., Welch, S. M., White, J. W., & French, A. N. (2015). Proximal hyperspectral sensing and data analysis approaches for field-based plant phenomics. In Computers and Electronics in Agriculture (Vol. 118, pp. 225–236). Elsevier BV. https://doi.org/10.1016/j.compag.2015.09.005

[145] Tomasi N., Pinton R., Dalla Costa L., Cortella G., Terzano R., Mimmo T., Scampicchio M., Cesco S. (2015). New 'solutions' for floating cultivation system of ready-to-eat salad: A review. Trends in Food Science & Technology, 46: 267-276, https://doi.org/10.1016/j.tifs.2015.08.004

[146] Tona E., Calcante A., & Oberti R. (2017). The profitability of precision spraying on specialty crops: a technical–economic analysis of protection equipment at increasing technological levels. Precision Agriculture, 19(4): 606–629. https://doi.org/10.1007/s11119-017-9543-4

[147] Torres-Sánchez, J., López-Granados, F., De Castro, A. I., & Peña-Barragán, J. M. (2013). Configuration and Specifications of an Unmanned Aerial Vehicle (UAV) for Early Site Specific Weed Management. In D. Abbott (Ed.), PLoS ONE (Vol. 8, Issue 3, p. e58210). Public Library of Science (PLoS). https://doi.org/10.1371/journal.pone.0058210

[148] Tripodi, P., Nicastro, N., & Pane, C. (2022). Digital applications and artificial intelligence in agriculture toward next-generation plant phenotyping. In D. Cammarano (Ed.), Crop & Pasture Science (Vol. 74, Issue 6, pp. 597–614). CSIRO Publishing. https://doi.org/10.1071/cp21387

[149] Trognitz, F., Hackl, E., Widhalm, S., & Sessitsch, A. (2016). The role of plant–microbiome interactions in weed establishment and control. In G. Muyzer (Ed.), FEMS Microbiology Ecology (Vol. 92, Issue 10, p. fiw138). Oxford University Press (OUP). https://doi.org/10.1093/femsec/fiw138

[150] Tudi, M., Daniel Ruan, H., Wang, L., Lyu, J., Sadler, R., Connell, D., Chu, C., & Phung, D. T. (2021). Agriculture Development, Pesticide Application and Its Impact on the Environment. In International Journal of Environmental Research and Public Health (Vol. 18, Issue 3, p. 1112). MDPI AG. https://doi.org/10.3390/ijerph18031112

[151] United Nations Department of Economic and Social Affairs, Population Division (2022). World Population Prospects 2022: Summary of Results. UN DESA/POP/2022/TR/NO. 3.

[152] Urrea, C., & Muñoz, J. (2013). Path Tracking of Mobile Robot in Crops. In Journal of Intelligent & Robotic Systems (Vol. 80, Issue 2, pp. 193–205). Springer Science and Business Media LLC. https://doi.org/10.1007/s10846-013-9989-1

[153] van Bussel, L. M., Kuijsten, A., Mars, M., & van ‘t Veer, P. (2022). Consumers’ perceptions on food-related sustainability: A systematic review. In Journal of Cleaner Production (Vol. 341, p. 130904). Elsevier BV. https://doi.org/10.1016/j.jclepro.2022.130904

[154] van Henten, E. J., Bac, C. W., Hemming, J., & Edan, Y. (2013). Robotics in protected cultivation. In IFAC Proceedings Volumes (Vol. 46, Issue 18, pp. 170–177). Elsevier BV. https://doi.org/10.3182/20130828-2-sf-3019.00070

[155] Vázquez-Arellano, M., Griepentrog, H., Reiser, D., & Paraforos, D. (2016). 3-D Imaging Systems for Agricultural Applications—A Review. In Sensors (Vol. 16, Issue 5, p. 618). MDPI AG. https://doi.org/10.3390/s16050618

[156] Vijayakumar, V., Ampatzidis, Y., Schueller, J. K., & Burks, T. (2023). Smart spraying technologies for precision weed management: A review. In Smart Agricultural Technology (Vol. 6, p. 100337). Elsevier BV. https://doi.org/10.1016/j.atech.2023.100337

[157] Virlet, N., Sabermanesh, K., Sadeghi-Tehran, P., & Hawkesford, M. J. (2017). Field Scanalyzer: An automated robotic field phenotyping platform for detailed crop monitoring. In Functional Plant Biology (Vol. 44, Issue 1, p. 143). CSIRO Publishing. https://doi.org/10.1071/fp16163

[158] Walter, A., Liebisch, F., & Hund, A. (2015). Plant phenotyping: from bean weighing to image analysis. In Plant Methods (Vol. 11, Issue 1, p. 14). Springer Science and Business Media LLC. https://doi.org/10.1186/s13007-015-0056-8

[159] Wang, X., Kang, H., Zhou, H., Au, W., & Chen, C. (2022). Geometry-aware fruit grasping estimation for robotic harvesting in apple orchards. In Computers and Electronics in Agriculture (Vol. 193, p. 106716). Elsevier BV. https://doi.org/10.1016/j.compag.2022.106716

[160] Westwood, J. H., Charudattan, R., Duke, S. O., Fennimore, S. A., Marrone, P., Slaughter, D. C., Swanton, C., & Zollinger, R. (2018). Weed Management in 2050: Perspectives on the Future of Weed Science. In Weed Science (Vol. 66, Issue 3, pp. 275–285). Cambridge University Press (CUP). https://doi.org/10.1017/wsc.2017.78

[161] Xiang, L., & Wang, D. (2023). A review of three-dimensional vision techniques in food and agriculture applications. In Smart Agricultural Technology (Vol. 5, p. 100259). Elsevier BV. https://doi.org/10.1016/j.atech.2023.100259

[162] Xie, D., Chen, L., Liu, L., Chen, L., & Wang, H. (2022). Actuators and Sensors for Application in Agricultural Robots: A Review. In Machines (Vol. 10, Issue 10, p. 913). MDPI AG. https://doi.org/10.3390/machines10100913

[163] Xu, K., Li, H., Cao, W., Zhu, Y., Chen, R., & Ni, J. (2020). Recognition of Weeds in Wheat Fields Based on the Fusion of RGB Images and Depth Images. In IEEE Access (Vol. 8, pp. 110362–110370). Institute of Electrical and Electronics Engineers (IEEE). https://doi.org/10.1109/access.2020.3001999

[164] Yohannes, H. (2015). A Review on Relationship between Climate Change and Agriculture. In Journal of Earth Science & Climatic Change (Vol. 07, Issue 02). OMICS Publishing Group. https://doi.org/10.4172/2157-7617.1000335

[165] Yong Chen, Xiaojun Jin, Lie Tang, Jun Che, Yanxia Sun, & Jun Chen. (2013). Intra-row weed recognition using plant spacing information in stereo images. In 2013 Kansas City, Missouri, July 21 - July 24, 2013. 2013 Kansas City, Missouri, July 21 - July 24, 2013. American Society of Agricultural and Biological Engineers. https://doi.org/10.13031/aim.20131592292

[166] You, A., Sukkar, F., Fitch, R., Karkee, M., & Davidson, J. R. (2020). An Efficient Planning and Control Framework for Pruning Fruit Trees. In 2020 IEEE International Conference on Robotics and Automation

(ICRA). 2020 IEEE International Conference on Robotics and Automation (ICRA). IEEE. https://doi.org/10.1109/icra40945.2020.9197551

[167] Yu, J.-K., & Moon, Y.-S. (2021). Corn Starch: Quality and Quantity Improvement for Industrial Uses. In Plants (Vol. 11, Issue 1, p. 92). MDPI AG. https://doi.org/10.3390/plants11010092

[168] Zakaria, Z. A., Gopalan, H. K., Zainal, H., Mohd. Pojan, N. H., Morsid, N. A., Aris, A., & Sulaiman, Mohd. R. (2006). Antinociceptive, Anti-inflammatory and Antipyretic Effects of Solanum nigrum Chloroform Extract in Animal Models. In Yakugaku ZASSHI (Vol. 126, Issue 11, pp. 1171–1178). Pharmaceutical Society of Japan. https://doi.org/10.1248/yakushi.126.1171

[169] Zhang, F., Prisacariu, V., Yang, R., & Torr, P. H. S. (2019). GA-Net: Guided Aggregation Net for End-To-End Stereo Matching. In 2019 IEEE/CVF Conference on Computer Vision and Pattern Recognition (CVPR). 2019 IEEE/CVF Conference on Computer Vision and Pattern Recognition (CVPR). IEEE. https://doi.org/10.1109/cvpr.2019.00027

[170] Zhang, D., Mansaray, L. R., Jin, H., Sun, H., Kuang, Z., & Huang, J. (2018). A universal estimation model of fractional vegetation cover for different crops based on time series digital photographs. In Computers and Electronics in Agriculture (Vol. 151, pp. 93–103). Elsevier BV. https://doi.org/10.1016/j.compag.2018.05.030

[171] Zhang, Y., Li, M., Li, G., Li, J., Zheng, L., Zhang, M., Wang, M., 2022. Multi-phenotypic parameters extraction and biomass estimation for lettuce based on point clouds. Measurement 204, 112094. https://doi.org/10.1016/j.measurement.2022.112094

[172] Zhao, J., Yang, Y., Zheng, H., & Dong, Y. (2020). Global Agricultural Robotics Research and Development: Trend Forecasts. In Journal of Physics: Conference Series (Vol. 1693, Issue 1, p. 012227). IOP Publishing. https://doi.org/10.1088/1742-6596/1693/1/012227

[173] Zhou, K., Meng, X., & Cheng, B. (2020). Review of Stereo Matching Algorithms Based on Deep Learning. In Computational Intelligence and Neuroscience (Vol. 2020, pp. 1–12). Hindawi Limited. https://doi.org/10.1155/2020/8562323

[174] Zohaib, A., Abbas, T., & Tabassum, T. (2016). Weeds Cause Losses in Field Crops through Allelopathy. In Notulae Scientia Biologicae (Vol. 8, Issue 1, pp. 47–56). Society of Land Measurements and Cadastre from Transylvania. https://doi.org/10.15835/nsb819752

Sitography

[1] https://www.corteva.it/prodotti-e-soluzioni/biologicals/BlueN.html

[2] https://climate.ec.europa.eu/climate-change/consequences-climate-change_it

[3]https://www.monarchtractor.com/it/experiences/autonomy-trial-sustainable farming

[4]https://learn.microsoft.com/it-it/windows/apps/design/devices/kinect-for-windows

[5] https://www.stereolabs.com/en-it/products/zed-2

[6] https://www.arduino.cc/

[7] https://april.eecs.umich.edu/software/apriltag

[8]https://www.marketsandmarkets.com/Market-Reports/agricultural-robot-market-173601759.html?gad_source=1&gclid=CjwKCAjwy8i0BhAkEiwAdFaeGJR3fZF17lMy4WAijdikm6-d49v-G82VSrcgoSHEwaGU0MmF8nJHnhoC0b4QAvD_BwE

[9] https://www.corteva.it/prodotti-e-soluzioni/sementi/mais/P1817.html

[10] https://www.hracglobal.com/

[11]https://agronotizie.imagelinenetwork.com/difesaediserbo/2023/11/23/fitofarmaci-il-parlamento-europeo-ferma-il-dimezzamento/80685

[12] http://www.fao.org/3/a-i6874e.pdf

[13] www.weedscience.org

[14] https://sustainabledevelopment.un.org/content/documents/Agenda21.pdf